



Delft University of Technology

Tracking Schooling Fish in Three Dimensions Experiments at the Rotterdam Zoo

Muller, K.

DOI

[10.4233/uuid:12905cc1-b9e7-4bff-972d-19bea5cf4fdf](https://doi.org/10.4233/uuid:12905cc1-b9e7-4bff-972d-19bea5cf4fdf)

Publication date

2023

Document Version

Final published version

Citation (APA)

Muller, K. (2023). *Tracking Schooling Fish in Three Dimensions: Experiments at the Rotterdam Zoo*. [Dissertation (TU Delft), Delft University of Technology]. <https://doi.org/10.4233/uuid:12905cc1-b9e7-4bff-972d-19bea5cf4fdf>

Important note

To cite this publication, please use the final published version (if applicable). Please check the document version above.

Copyright

Other than for strictly personal use, it is not permitted to download, forward or distribute the text or part of it, without the consent of the author(s) and/or copyright holder(s), unless the work is under an open content license such as Creative Commons.

Takedown policy

Please contact us and provide details if you believe this document breaches copyrights. We will remove access to the work immediately and investigate your claim.

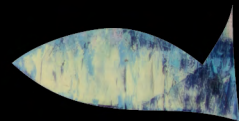
Tracking Schooling Fish in Three Dimensions

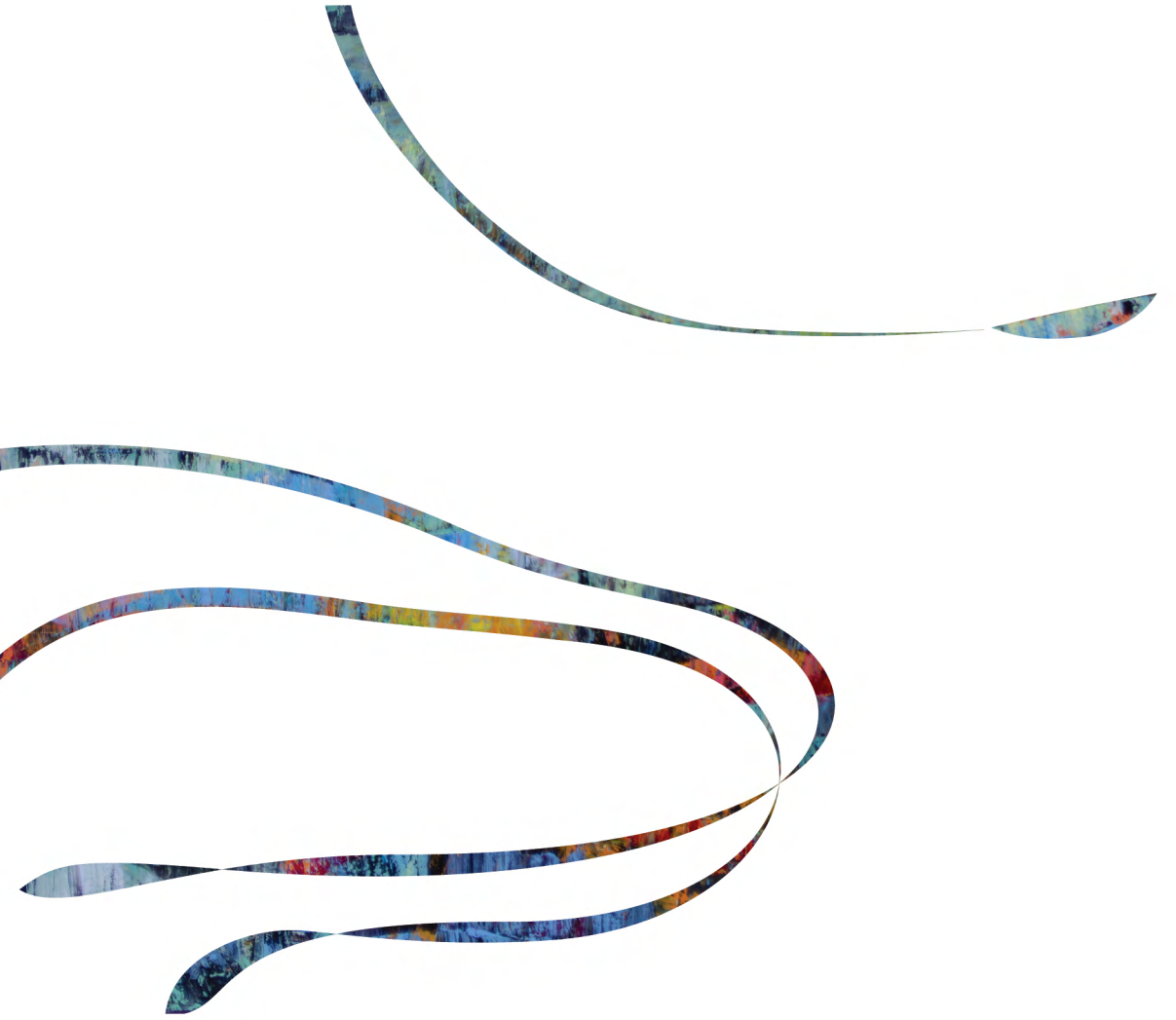
Tracking Schooling Fish in Three Dimensions

Koen Muller

*Experiments at the
Rotterdam Zoo*

Koen Muller





**TRACKING SCHOOLING FISH IN
THREE DIMENSIONS**

EXPERIMENTS AT THE ROTTERDAM ZOO

TRACKING SCHOOLING FISH IN THREE DIMENSIONS

EXPERIMENTS AT THE ROTTERDAM ZOO

Proefschrift

ter verkrijging van de graad van doctor
aan de Technische Universiteit Delft,
op gezag van de Rector Magnificus prof. dr. ir. T.H.J.J. van der Hagen
voorzitter van het College voor Promoties,
in het openbaar te verdedigen op dinsdag 5 september 2023 om 12:30 uur

door

Koen MULLER

Master of Science in Mechanical Engineering,
Technische Universiteit Delft, Nederland,
geboren te Wageningen, Nederland.

Dit proefschrift is goedgekeurd door de promotoren.

Samenstelling promotiecommissie:

Rector Magnificus,	voorzitter
Dr. D.S.W. Tam	Technische Universiteit Delft, promotor
Prof. dr. ir. J. Westerweel	Technische Universiteit Delft, promotor
Prof. dr. C.K. Hemelrijk	Rijksuniversiteit Groningen, promotor

Onafhankelijke leden:

Prof. dr. B. Thiria	ESPCI Paris
Prof. dr. ir. F.T. Muijres	Wageningen University & Research
Prof. dr. ir. F. Scarano	Technische Universiteit Delft
Dr. A. Corbetta	Technische Universiteit Eindhoven

Overige leden:

Prof. dr. ir. R. Pecnik	Technische Universiteit Delft, reservelid
-------------------------	---



Keywords: Schooling Fish, Three-Dimensional Tracking, Collective Behavior, Animal Locomotion, Biological Fluid-Dynamics, Field Experiments

Printed by: Gildeprint

Front & Back: Sardientje '19

Copyright © 2023 by K. Muller

ISBN 978-94-6419-878-2

An electronic version of this dissertation is available at
<http://repository.tudelft.nl/>.

To my wonderful wife and our beloved son who have supported me with happiness, joy,
and adventure during critical moments while working on this thesis.

*The prince says that the world will be saved by beauty! And I maintain that the reason he
has such playful ideas is that he is in love.*

Fyodor Dostoevsky, *The Idiot*

CONTENTS

Summary	xi
Samenvatting	xiii
1 Introduction	1
1.1 Collective Animal Locomotion	2
1.2 The Dynamic Schooling of Fish	3
1.2.1 Schooling Behavior of Fish	3
1.2.2 Fluid Mechanics of Schooling Fish	3
1.2.3 Development of Agent-Based Schooling Models	5
1.2.4 Extraction of Social Forces and Experimental Work	6
1.3 Previous Work on Animal Tracking	7
1.3.1 Swarming Dynamics in the Lab and the Field	7
1.3.2 A Paradigm Shift for Birds Flocking in the Field	7
1.3.3 The Lack of Large Scale Three-Dimensional Tracking Data	9
1.4 Experiments at the Rotterdam Zoo	9
1.4.1 The Diergaarde Blijdorp Oceanium	9
1.4.2 Harengula, Predator and Cohabitant Species	10
1.5 Outline of this Thesis	11
References	13
2 Measurement Technique and Camera Calibration	27
2.1 Flexible Camera Calibration Techniques	27
2.2 Camera Setup and Calibration Procedure	28
2.2.1 Image Processing	29
2.2.2 Distortion Correction	29
2.2.3 Camera Calibration and Projective Geometry	32
2.2.4 Single Camera Calibration	32
2.2.5 Multiple Camera Calibration	33
2.3 Assessment of the Calibration Method	34
2.3.1 Intrinsic and Extrinsic Camera Parameters	34
2.3.2 Convergence and Robustness	34
2.3.3 Spatial Accuracy of the Camera Calibration	37
2.4 Application to Field Experiments	38
2.5 Conclusion	40
References	43

3	Volumetric Tracking of Fish in a Large School	47
3.1	Animal Tracking and Volumetric Imaging Fluids	48
3.2	Imaging an Underwater Environment.	50
3.2.1	Data Acquisition and Image Quality	50
3.2.2	Fish Image Data	50
3.3	Image Processing	52
3.3.1	Background Removal	54
3.3.2	Multi-Resolution Image Contrast	54
3.3.3	Ellipse Image Convolution	55
3.3.4	Image Segmentation and Identification	58
3.3.5	Contrast Maximization.	59
3.3.6	Camera Tracking.	61
3.4	Correspondence Matching and Triangulation.	61
3.4.1	Linking Stereoscopic Correspondences	61
3.4.2	F-Focal Correspondence Matching	64
3.4.3	Cost-Function Optimization	66
3.5	Three-Dimensional Time-Resolved Tracking	68
3.5.1	Branching and Smoothing of Feasible Trajectories	68
3.5.2	Splitting and Merging of Feasible Trajectories	71
3.5.3	Cost-Function Optimization	71
3.6	Object Reconstruction and Post-Processing.	73
3.6.1	Quadric Reconstruction	75
3.6.2	Cleaning and Filtering of Trajectories	75
3.7	Performance Assessment	76
3.7.1	Parameters of Main Input	76
3.7.2	Coin Toss: Probability Tracking into the Next Frame	78
3.7.3	Track-Length Distribution and Tracking Efficacy.	79
3.8	Conclusions.	80
	References	83
4	Inner Structure and Kinematics of Three-Dimensional Fish Schools	89
4.1	Tracking Data Acquired at the Rotterdam Zoo.	90
4.1.1	Measurements at the Oceanium Aquarium	90
4.1.2	Milling, Predatory Escape, Shoaling, and Foraging	91
4.2	School Shape and Distribution of Fish	96
4.2.1	School Center of Mass, Semi-Axes and Local Fish Density	96
4.2.2	Inner Distribution of Fish in the School	99
4.2.3	Variability in School Shape and Bimodal Fish Distribution.	101
4.3	Kinematics of Fish Schooling	102
4.3.1	Velocity, Polarization, Angular Momentum, and Dilation	103
4.3.2	Kinematic Decomposition and Partition in Kinetic Energy.	105
4.3.3	Variability and Distribution of Kinetic Energy	109
4.4	Shape, Kinematics, and Local State Variables	112
4.4.1	Kinematic State, Fish Velocity, Polarization, and Density.	113
4.4.2	School Geometry, Fish Velocity, Polarization, and Density	113

4.5	Summary and Conclusions	114
	References	117
5	Conclusions and Recommendations	121
5.1	Outlook to Future Work	123
5.2	Scientific Contribution and Impact	125
A	Appendix	127
A.1	Optical Distortion Across an Interface	127
A.2	Relative Camera Positions from Calibrated Views	127
A.3	Projected Area of a Planar Object	128
A.4	Magnification of the Distortion Map	128
A.5	Point Triangulation and Skewness	129
	References	130
B	Appendix	131
B.1	Patching a Background Image.	131
B.2	Image Smoothing and Differentiation Filters	132
B.3	Shape Parameters from the Ellipse Contour.	133
B.4	Manipulations to an Ellipse Contour	134
B.5	Distance Functions on the Ellipse Contour	134
B.6	Clustering of Stereoscopic Correspondences	135
B.7	Iterative Cost-Function Solution	137
B.8	Quadric Reconstruction by Dual-Space Geometry	140
	References	145
C	Appendix	147
C.1	Data Descriptor: Camera Calibration	147
C.2	Data Descriptor: Processed Tracking	147
C.3	Principal Semi-Axes and Bounding Ellipsoid	154
C.4	Moments of the Radial Fish Density Distribution	154
C.5	Distribution of Velocity inside the School	156
	References	165
	Acknowledgements	167
	Curriculum Vitæ	169
	List of Publications	171

SUMMARY

This thesis describes methods and first analyses to study the shape and motion of a large school of approximately 2000 *Harengula clupeiola* (false herring) in three-dimensional space. This school of fish was present at the large-scale and publicly accessible ocean aquarium of the Rotterdam zoo, in the Netherlands known as Diergaarde Blijdorp, from spring 2017 to summer 2020.

Nature presents a broad range of length scales in which collective behavior emerges in living systems, ranging from the bio-active convection of bacteria within the thickness of a hair to the large-scale aerial display of starlings flying in a gigantic flock. Chapter 1 introduces an overall motivation to study the collective behavior of schooling fish in three dimensions from a fluid-mechanics background, at the interface between biology, physics, and engineering. We review seminal experimental and modeling work on fish schools and the current state-of-the-art in the camera tracking of animals in three dimensions. Finally, the fully climate-controlled semi-natural habitat at the large-scale ocean aquarium of the Rotterdam zoo is described, which includes a multitude of co-habitant species such as sharks and sea turtles.

Obtaining accurate fish tracking data from the large-scale ocean aquarium requires a camera calibration that is accurate and consistent over multiple views. Chapter 2 describes a flexible calibration technique that combines tools developed in computer vision with non-linear camera mappings used in experimental fluid mechanics. We successfully calibrate a four-camera setup over a large measurement volume of $\sim 10 \times 25 \times 6 \text{ m}^3$ while using a much smaller calibration target that is randomly positioned at different orientations with a team of divers. Imaging from air to water, the camera calibration supports linear ray-tracing and applies projective geometry in the presence of significant distortions across the optical refractive interface. The accuracy and robustness of the developed methods are demonstrated, and a measurement error within one centimeter is achieved covering several tens of meters.

Imaging a school of false herrings inside a complex underwater environment faces several challenges. Chapter 3 presents the image processing and tracking algorithms to follow fish in three dimensions over a large distance. Necessary steps to remove artifacts in the image background are explained and a series of image convolution filters identify elliptical projections of fish over multiple scales. Subsequently, the framework of projective geometry fully integrates the ellipse identification with the linear ray-tracing to robustly match corresponding fish between multiple views. An integer assignment is used to find the matched correspondences that best fit the individual camera views in the presence of large occlusions. This integer assignment is extended to make recursive adjustments in fish trajectories and integrates recent advances from experimental fluid mechanics to perform time-resolved tracking. The performance and implementation of the tracking algorithms are quantified. High tracking reliability is achieved, which provides extraction of relatively long tracking sequences.

Over the course of four years, a total of six measurement weeks were performed to obtain the full three-dimensional tracking data of the large school of fish. Chapter 4 starts with a qualitative overview of the behavior of the schooling fish that freely swim in the relatively unconstrained semi-natural habitat. Subsequently, we perform quantitative analyses of the school shape and internal distribution of fish. Time series for the evolution of the local fish density, the school volume and aspect ratio(s), and the moments of the radial fish distribution are presented. The variation in the local fish density does not simply scale with the school volume, instead, a constant lower bound is reached at higher volumes. Moreover, the internal distribution of fish in the school reveals a bimodality where the fish either cluster in a cohesive group or redistribute towards the boundary, suggesting a predator attack. Next, we investigate the kinematics of the school. Time series for the local polarization, the velocity of the center of gravity, angular momentum, and volumetric dilation are discussed, including their shortcomings. From the kinematic decomposition, three kinematic parameters are derived for milling (rotation), foraging (translation), and dilation (radial motion), which together partition the kinetic energy. We find that for an increase in milling the motion of the school becomes increasingly cylindrical and that the dilation approaches a pure expansion when evading the predator. Finally, we discuss several interconnections between the school shape, kinematics, and local state variables. Together these suggest a dependency between the fish velocity, the local density, and polarization.

Chapter 5 summarizes the main conclusions of the current work and makes several recommendations for future research. Unlocking the third dimension to analyze the shape and kinematics of swimming schools of fish contributes to future research beyond the laboratory environment and in the field.

SAMENVATTING

Dit proefschrift beschrijft methodiek en eerste analyses om vorm en beweging van een grote school van ongeveer 2000 *Harengula clupeola* (valse haring) te bestuderen in de driedimensionale ruimte. Deze school vissen was aanwezig in het grootschalige en openbare zee aquarium van de Rotterdamse dierentuin, in Nederland bekend als Diergaarde Blijdorp, vanaf voorjaar 2017 tot zomer 2020.

In de natuur bestaat een breed scala aan lengteschalen waarin collectief gedrag zich voordoet in levende systemen, variërend van bioactieve convectie van bacteriën in de dikte van een haar tot grootschalige zwermen spreeuwen in een spectaculaire luchtshow. Hoofdstuk 1 introduceert een algehele motivatie om het collectieve gedrag van vissen en het zwemmen in scholen te bestuderen vanuit de invalshoek van de stromingsleer, op het snijvlak van biologie, natuurkunde en techniek. We beschouwen zowel voorgaand experimenteel onderzoek als het modelleren voor scholende vissen en huidig onderzoek in het optisch volgen van dieren in drie dimensies. Tot slot wordt het volledig geklimatiseerde semi-natuurlijke habitat van het grootschalige zee aquarium in de dierentuin van Rotterdam beschreven, waarin een veelvoud aan diersoorten zoals haaien en zeeschildpadden rondzwemt.

Het verkrijgen van nauwkeurige meetdata voor het volgen van vissen in het grootschalige zee aquarium vereist een camera kalibratie die nauwkeurig en consistent is over meerdere aanzichten. Hoofdstuk 2 beschrijft een flexibele camera kalibratie techniek welke methoden uit de digitale optica combineert met niet-lineaire camera modellen uit de experimentele stromingsleer. We bereiken een succesvolle kalibratie voor een vier-camera systeem over een groot meetvolume van $\sim 10 \times 25 \times 6 \text{ m}^3$ terwijl er een veel kleiner kalibratie object wordt gebruikt dat gepositioneerd wordt onder verschillende oriëntaties met een groep duikers. Voor het filmen van lucht naar water wordt lijnmeetkunde en projectieve geometrie toegepast in bijzijn van vervormingen langs het optisch brekende grensvlak. De nauwkeurigheid en robuustheid van de ontwikkelde methoden wordt gedemonstreerd en er wordt een meetfout binnen één centimeter bereikt over een afstand van enkele tientallen meters.

Het filmen van een school valse haringen in een complexe onderwater omgeving staat voor een aantal uitdagingen. Hoofdstuk 3 presenteert de beeld verwerking methoden en tracking-algoritmen voor het volgen van vissen in drie dimensies over grote afstand. Benodigde stappen om achtergrond artefacten te verwijderen worden uitgelegd en een reeks beeldconvolutiefilters identificeert ovaal vormige projecties van vissen over verschillende groottes. Vervolgens integreert het raamwerk van de projectieve geometrie de vis detectie volledig met de lijnmeetkunde om overeenkomende aanzichten van vissen op robuuste wijze met elkaar te verbinden. Een geheel getal toewijzing wordt gebruikt om de overeenkomsten te vinden die het best in verhouding staan tot de individuele camerabeelden in aanwezigheid van grote oclusies. Deze geheel getal toewijzing wordt uitgebreid op grond van recursieve aanpassingen van vis trajecten en integreert

recente vorderingen uit de experimentele stromingsleer om de tijd opgeloste tracking uit te voeren. De prestaties en implementatie van de tracking-algoritmen worden gekwantificeerd. Er wordt een hoge volgbetrouwbaarheid bereikt, waardoor relatief lange vis trajecten kunnen worden geëxtraheerd.

Over het verloop van vier jaar zijn zes meetweken uitgevoerd om de volledig driedimensionale data van de grote school vissen te verkrijgen. Hoofdstuk 4 begint met een kwalitatief overzicht voor het gedrag van de scholende vissen die vrijuit zwemmen in het relatief onbegrensde semi-natuurlijke habitat. Vervolgens voeren we kwantitatieve analyses uit aan de vorm van de school en de interne verdeling van vissen. Tijdsreeksen voor de ontwikkeling van de lokale visdichtheid, het volume van de school, aspectverhouding(en), en de momenten van de radiale visverdeling worden gepresenteerd. De variatie in lokale visdichtheid schaaft niet simpelweg met het volume van de school, in plaats daarvan wordt er een constante ondergrens bereikt bij hogere volumes. Bovendien onthult de interne verdeling van de vissen een bimodaliteit, waar de vissen clusteren in een samenhangende groep of zich herverdelen naar de grens van de school, hetgeen een aanval van een roofdier suggereert. Daarna bestuderen we de kinematica van de school. Tijdsreeksen voor de lokale polarisatie, de snelheid van het zwaartepunt, impulsmoment en de volumetrische dilatatie worden besproken, inclusief hun tekortkomingen. Vanuit de kinematische ontleding worden drie kinematische parameters afgeleid voor het malen (draaien), foerageren (transleren), en dilatatie (radiale beweging), die samen de kinetische energie verdelen. Voor een toename in malen vinden we dat de beweging van de school cilindrischer wordt, en dat de dilatatie een pure verwijding benadert wanneer de school een roofdier ontvlucht. Tenslotte bespreken we verschillende onderlinge verbanden tussen de school vorm, kinematica en lokale toestandsvariabelen. Samen suggereren deze een afhankelijkheid tussen de vissnelheid, de lokale visdichtheid en polarisatie.

Hoofdstuk 5 vat de belangrijkste conclusies van het huidige werk samen en geeft verschillende aanbevelingen voor toekomstig onderzoek. De ontsluiting van de derde dimensie om de vorm en beweging van zwemmende scholen vis te analyseren draagt bij aan toekomstig onderzoek buiten de laboratoriumomgeving en in het veld.

1

INTRODUCTION

... “In the case of all things which have several parts and in which the totality is not, as it were, a mere heap, but the whole is something beside the parts, there is a cause; for even in bodies contact is the cause of unity in some cases, and in others viscosity or some other such quality.” ...

— Aristotle, *Metaphysics VIII-p6*, 350 B.C.E

The sudden expansion and wave propagation through a gigantic school of oceanic fish escaping a predator is a startling display of collective animal behavior. Such massive, impressive, mesmerizing, and rapidly shape-shifting fish schooling aggregations are abundant. Sardines, herring, and anchovies may school in vast numbers that can extend over several square kilometers [1, 2] from coastal waters [3] deep into the open waters of the pelagic ocean [4, 5]. Likewise, jellyfish gather in enormous oceanic blooms [6], antarctic krill swarm in colossal assembles [7], and oceanic eels aggregate in large groups down to abyssal depths [8]. Formations of such animal collectives continue to captivate scientists in many disciplines including biologists, mathematicians, physicists, and fluid-dynamicists in particular.

The emergence of rapid information transfer as commonly observed in schools of fish [9] and flocks of birds [10, 11] is possibly the most astounding view of animals moving in a group. With propagation speeds far exceeding that of the individuals, early conjectures have hypothesized that birds in a flock must possess some form of telepathic ability [12]. Such propositions are nowadays refuted [11]. Nonetheless, animal groups may behave like a ‘collective mind’ [13] or ‘super-organism’, where the sensory input of many eyes facilitates the alarmed collective response and decision-making or ‘wisdom of the crowd’ for animal taxes [9–11, 14]. Studying the bewildering complexity of moving animal groups is central to understanding the underlying collective animal behavior — and the collective locomotion of schooling fish for the current thesis.

1.1. COLLECTIVE ANIMAL LOCOMOTION

From the bio-active convection of a suspension of micro-organisms within the thickness of a hair [15–18] up to the large aerial display of a flock of starlings spanning several hundreds of meters [19–21], collective behavior is a ubiquitous phenomenon in nature [22–28]. How can it be that fish in a school, birds in a flock, insects in a swarm, or sheep in a herd can maneuver through complex environments and coordinate in unison, but rarely collide with one another? As is illustrated in Figure 1.1 such examples cover many length scales [29], which the emerging collective locomotion may yield surprising results from a fluid-mechanics background.

For example, at the small scale (left Figure 1.1), whether it be a mixture of micro-tubules in a nematic ordered phase [17] or a dense suspension of bacteria [16], the emerging bio-convection likely originates from the physical hydrodynamic force dominated by viscosity [30]. In contrast with flows at the micro-scale, the coherent motion in bacterial suspensions [31–34] may resemble large-scale three-dimensional turbulent flows, even when the suspension is confined in two dimensions. At the large scale, on the other hand (right Figure 1.1), whether it be midges in a swarm [35, 36], fish in school [27], starlings in a flock [19, 20], sheep in a herd [37], or humans in a crowd [38–40], the collective locomotion likely originates from decisions by individuals engaged in social interaction. At increasing social cohesion, such groups may display a strongly correlated system and act like a fluid dominated by apparent viscous (and elastic) forces, again in contrast to what one may expect from the fluid inertia at large-scale convection.

From a ‘microscopic’ perspective the local social interactions among animals in a group offer a mechanism to transfer the motion or ‘momentum’ from one individual to another, similar to an isolated system of interacting particles. Unlike physical forces, social forces between individuals do not require the action of one individual on the other to be balanced by an equal and opposite reaction. Moreover, the self-propelled nature of the group constituents presents a highly dissipative system far away from equilibrium. Even the simplest such systems organize from disorder to order [41] manifesting different phase transitions [42–44] and have provided the foundation for continuum theory [45, 46] and hydrodynamics of flocking [47]. Here the non-conservative forces and interactions among members may violate concepts central to mechanics [48].

From a ‘macroscopic’ perspective one can investigate the group dynamics of the animal collective. In physics, the linear and angular momenta for a collection of interacting particles are conserved. Although subject to Newtonian mechanics, moving animal groups do not need to follow such conservation laws which are clearly breached on net collective locomotion (translation, rotation, *etc.*). On the other hand, in analogy to fluid dynamics [49], the conservation of mass is at the foundation of transport equations in modeling traffic flow [50]. Here the nonlinear hyperbolic and dispersed wave propagation [51] may underlie traffic jam formation and contrast expectations from Bernoulli in a simple pipe flow. Such phenomena of emergent flows are intriguing, with new, hidden conservation laws on discovery in the case of moving animal groups [52].

What exactly determines the internal structure of a moving animal group? What underlies the almost ‘solid’ group cohesion in contrast with the ‘fluid’ collective coordination? How does collective behavior emerge from the underlying social and physical interactions? Learning from fish schools has great potential to contribute to the bio-

mimicry for robotic schooling [53], including the design of mechanical model systems without cognition [54, 55]. New insight may contribute to crowd-control [40] such as the modeling of pedestrians' walkways and corridors [56, 57] and to understanding mosh-pits and crowd dynamics in concert halls [38, 39] as well as cycling in pelotons [58, 59]. Such research into the spontaneous emergence and physics of living fluids [16] may perhaps one day bring us engineering of 'functional- and/or smart' fluid-dynamics of active suspensions and (human) crowds [60, 61].

1.2. THE DYNAMIC SCHOOLING OF FISH

From a biological perspective, the collective schooling of fish is thought to be an effective survival strategy. For example, the selfish herd hypothesis [62] assumes that individuals seek shelter inside available space of the animal aggregation to minimize the risk of predation and is an active area of research [37, 63, 64]. Another hypothesis is that schooling is used to create a confusion effect [65, 66]. Here the collective animal locomotion confuses the predator in identifying and targeting a single prey. For example, a school of fish may disorient a predator on a collective turn, acting like a 'mechanical mirror'.

1.2.1. SCHOOLING BEHAVIOR OF FISH

Schooling fish may be roughly divided into two types of social behavior: obligate schoolers and facultative schoolers [67]. Obligate schoolers live permanently in large aggregations. Such schools may form oceanic 'bait-balls' such as circular and torus-like motion which is often referred to as milling and is a well-documented natural behavior [24, 27, 68, 69]. Facultative schoolers may school on and off, from time to time. For example, the collaborative hunting in groups of jack and sailfish [70–72].

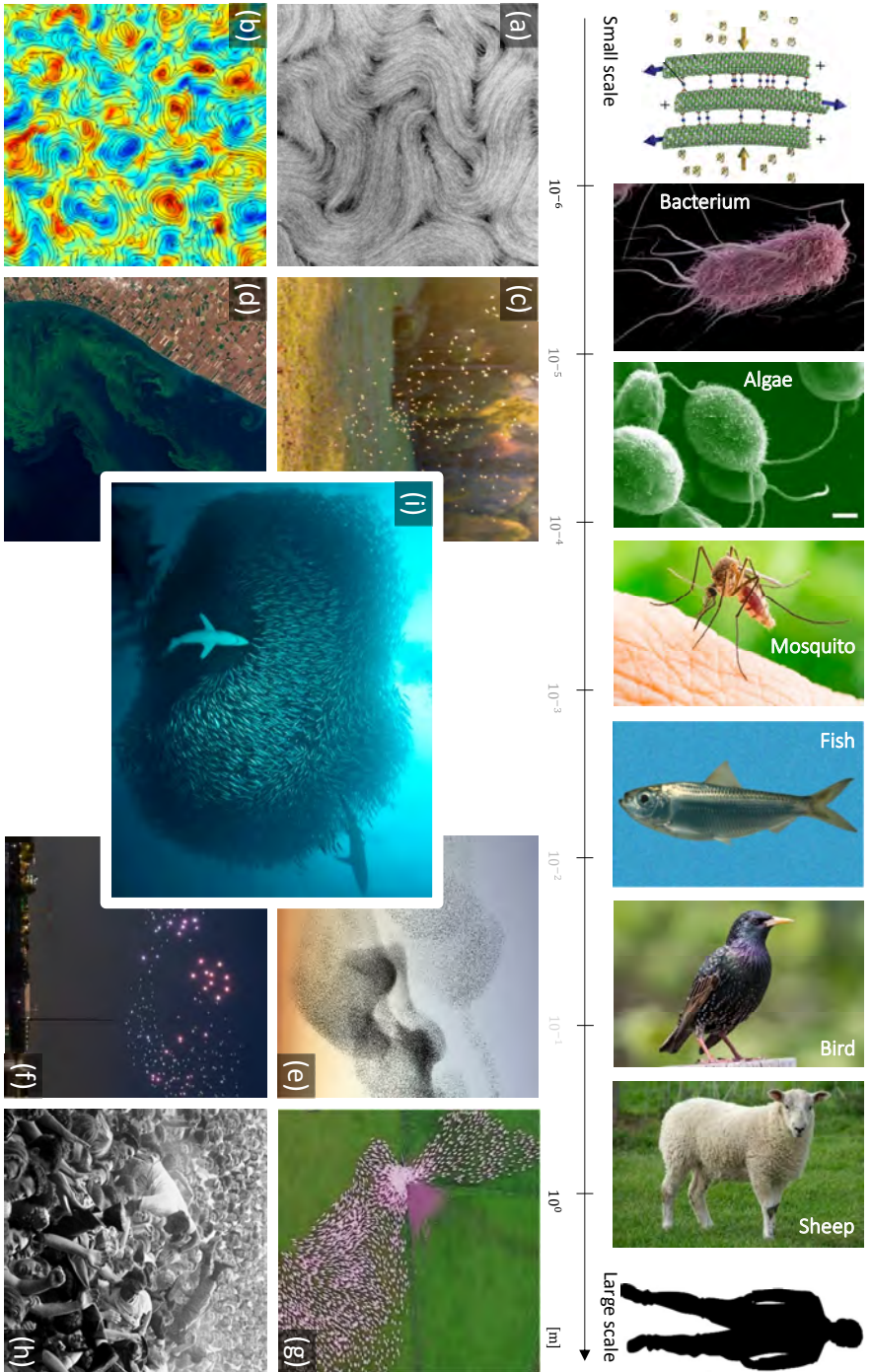
Pitcher and Wyche [73] qualitatively described the behavior of a school of 250 sandeels in presence of mackerel fish and classified predator evasion strategies [65, 74]. These included: 'avoid', 'herd', 'vacuole', 'hourglass', 'split', 'join', and 'flash expansion', next to other behaviors such as 'cruising', see Figure 1.2a. Influential work by Magurran and Pitcher [75] similarly studied a small group of 10–50 sweat water minnows interacting with a pike. Here further evasion strategies included: 'compact', 'approach', 'skittering', 'fountain', 'group jump', 'confusion', and 'hide'.

A strict taxonomy in the schooling behavior is not always possible [76]. This is perhaps best illustrated in the Venn diagram of Figure 1.2b by the intersection of 'shoaling' and 'schooling'. Together with qualitative descriptions of different fish schools [73, 75, 77], these works first studied the variability in the associated schooling behavior, and as well routed their interconnection [75, 78], see Figure 1.2c.

1.2.2. FLUID MECHANICS OF SCHOOLING FISH

Most fish that display a schooling behavior swim by undulating their body [79, 80]. This swimming stroke leads to the shedding of vortices from the caudal fin and creates for-

Picture references Figure 1.1. Above the scale bar: Microtubule, Yeomans [17]; Bacterium (*E. coli*), cdc.gov; Green algae (*C. reinhardtii*), physicsworld.com; Mosquito, whitehorse.vic.gov.au; Fish (*H. clupeiola*), bio-geodb.stri.si.edu; Bird (*S. vulgaris*), eastsideadubon.org; Sheep, animals.fandom.com; Human, freepik.com. Below the scale bar: a) Gompper *et al.* [18], b) Wensink *et al.* [32], c) insights.workwave.com d) newsweek.com e) champ-magazine.com f) studiodrft.com g) madlyodd.com h) theparisreview.org i) i.imgur.com



ward propulsion by an inverted von Karman wake, or jet stream. Therefore, in addition to behavioral aspects, the surrounding fluid at interaction with the fish biomechanics may play a decisive role.

For example, it has been shown that a blind fish can coordinate with others [81], in which the sensory input from the lateral line is considered to be crucial [82, 83]. Weihs [84] first pointed out that fish in a school may configure in crystalline structures to make optimal energetic usage of each other's vortex wake. Early conjectures in favor of vortex flow-induced energy savings trace back to Breder [85] for milling fish schools. However, experimental evidence pointed against and could not confirm such mechanisms directly from experimental observation [86].

Simulations on the fluid dynamics of infinite fish schools have provided novel evidence of such energy-saving configurations [87]. Such reductions in energy expenditure have as well been verified experimentally regardless of the internal schooling configuration [88], see also [89, 90] and references therein. Moreover, recent studies integrating machine learning methods with computational fluid dynamics have shown that different internal configurations reduce the cost of swimming through elaborate vortex-catching strategies [91, 92]. Such strategies have also been demonstrated experimentally using bio-mimetic experiments with robotic fish [93] showing an increased swimming efficiency upon synchronized tail-beat [94].

Perhaps the non-trivial nature of the hydrodynamics is best demonstrated by the 'swimming' of a dead fish trapped in the vortex wake of an object [95]. In the natural environment, such interactions with the surrounding fluid may include the wake drafting of dolphins in a group [96–98]. Thereby the dynamics of the fluid can have a dramatic impact on the dynamics of animal aggregations. For example, recent simulations on schooling fish have shown that the inclusion of hydrodynamic aspects [99] influences the schooling dynamics and adds to behavioral noise inside the school. More dramatically, for birds inside a flock, it has been shown that a reduction of the lift-force at bank-angle [100] induces a collective down draft [101–103] which significantly contributes to the flocking dynamics.

1.2.3. DEVELOPMENT OF AGENT-BASED SCHOOLING MODELS

Breder [104] first proposed that social interactions among fish could be captured in 'force-like' rules reminiscent of electrostatics. These interactions included a phenomenological attraction and repulsion among the group members. In application to computer graphics Reynolds [105] popularized such a distributed behavioral model and simulated a large number of 'Boids' displaying a plethora of flocking motions. Modeling such an effective interaction force is central to the development of realistic models that explain different school shapes and structures [65, 74, 77]. Today such interactions are known as 'social forces' and provide the backbone for agent-based modeling of fish schools [22, 27] and birds in a giant flock [103] as well as animal groups in general [23, 24, 26].

Huth and Wissel [106] first validated a behavioral schooling model in three spatial dimensions [107] with seminal experimental work [108–110]. In the absence of a designated leader, their model presented three phenomenological rules: (1) a long-range attraction, (2) a near-field repulsion, and (3) parallel orientation (alignment) at an intermediate range, together with a 'dead-angle' zone behind the fish, see also [111, 112]. In a

following study, Couzin *et al.* [113] quantified the global translation and rotational order by the total angular momentum and polarization for such a model. Their work revealed four behavioral states: (1) ‘swarming’, (2) ‘torus’, (3) a dynamic ‘parallel’, and (4) highly ‘parallel’ motion while exploring the model parameters.

The design of social forces offers a framework to study various behavioral traits as observed in natural schooling behavior [27, 73, 75]. For example, the size and form of the body of the fish [114] influences the internal density and spatial sorting [115]. Moreover, modifications to such local interaction rules have provided an explanation for frontal density in real fish schools [116] and the resulting oblong school shape observed in empirical data [117]. Further efforts in model development include decision trees [118], the application of Newtonian mechanics [119], the effect of informed individuals in a school [120], alignment and neutral zones [121], sensory perception [122], pursuit and escape [123, 124], variable speed [125], and an abundance of models not reviewed here.

Whether or not (instantaneous) social forces accurately capture social interactions may be debated. Social forces may, for example, poorly capture the latency between group members while the actual decision-making engaged in social interaction may be drawn differently over time. Moreover, schooling models are yet to bring a comprehensive explanation for the milling dynamics observed in the natural environment [24, 27, 68, 69]. Recent progress has been made augmenting a few simple behavioral rules to a minimal ‘Vicsek-like’ milling model [126], including the effect of uninformed individuals [127] and latency among group members [128]. Such new models based on different schooling mechanisms [129] motivate the need for real-world empirical data to validate against.

1.2.4. EXTRACTION OF SOCIAL FORCES AND EXPERIMENTAL WORK

Hunter [130] performed the first empirical work on the sensory-motor response of a single jack mackerel against external perturbations. Constructing models from [131], and validating models with observation data [107] is not at all a trivial exercise. Therefore, identifying the decision rules [132] by comparison with experimental data has gathered high levels of interest for the past decades.

Experimental work by Katz *et al.* [133] spatially mapped the effective ‘social force’ for 2 and 3 golden shiners. These social forces were deduced from the measured instantaneous acceleration in two dimensions up to 30 fish. A simultaneous study by Herbert-Read *et al.* [134] extracted social rules between small groups of 8 to 10 mosquito fish using neural networks and nonlinear function estimation on the relative position, velocity, and acceleration. These studies found similar force maps characterized by repulsive, attractive, and turning forces in front, behind, and to the side of a focal fish, see also preceding work on surf scoters [135]. Facing a rapidly growing body of work on extracting social rules we limit the current review, see for example [136–138] and many (valuable) related studies, with evolutionary evidence even drawn from the fossil record [139].

The interest in experimental data on schooling fish goes beyond the estimation of social forces. For example, by estimating the visual field [140] and performing a network analysis [141] previous studies have investigated the transfer of information, or ‘Trafalgar effect’ [142], and have applied recent progress in statistical concepts such as transfer entropy [143]. Another interest is the ability of a school to navigate complex environ-

ments. Here it has been shown that fish can collectively sense a gradient in variable lighting conditions [144, 145]. Furthermore, to investigate the response of a predator to virtual prey [146] recent laboratory experiments have even extended the application of virtual reality [147].

In addition to the local interactions between individuals [148], studies of schooling fish have also focused on identifying the global fish schooling dynamics and variability. Tunström *et al.* [149] performed quantitative laboratory experiments on the variability of the dynamics of schooling fish and identified three distinct states: (1) rotation, (2) polarized school, and (3) swarming. Such analyses are relevant in characterizing different schooling mechanisms [99, 113, 150, 151]. However, most experimental laboratory work, including recent advances [152], has focused on two dimensions. Despite a few early studies [117, 153], the availability of three-dimensional tracking data has only recently shown an increase in the lab [154, 155] and the field [156].

1.3. PREVIOUS WORK ON ANIMAL TRACKING

Tracking animals in three dimensions is central to the study of collective animal locomotion. Such data are of the greatest value to the development of accurate and realistic schooling models, but gathering such experimental data represents an enormous challenge. In particular, non-intrusive and three-dimensional imaging techniques have gained much popularity in numerous applications in recent years. Such data are not only of interest to biologists but also to statistical physicists [19, 21, 157], among others.

1.3.1. SWARMING DYNAMICS IN THE LAB AND THE FIELD

Insects, for example, provide a perfect model system to study swarming dynamics in the laboratory and acquire velocity and acceleration statistics [35, 158, 159]. Controlled lab experiments have demonstrated the emergence of visco-elastic properties by applying mechanical spectroscopy [160, 161]. In addition, recent laboratory work on midges suggests that interactions between insects and the internal cohesion of the swarm may originate from acoustics signals [162]. Such novel insights have as well contributed to a perspective of a ‘thermodynamics’ of swarming midges [163] presenting an ‘equation of state’ for the swarm properties.

In addition, the swarming of midges is a model system for fieldwork as well. Here, experiments have shown that interactions between midges are of metric range [36], providing a distinct feature for the disorganized swarming dynamics. Such field data have shown that the cohesion of wild swarms, despite their chaotic dynamics, are fully correlated and poised critical [164]; with recent insight into the dynamic scaling of insect swarms [165].

1.3.2. A PARADIGM SHIFT FOR BIRDS FLOCKING IN THE FIELD

The development of tracking methods in the field [166–168] and the reliable tracking of several thousands of birds in a giant flock [169] have opened the door to collecting unprecedented empirical flocking data [170, 171]. Such data have proven their contribution. For example, Ballerini *et al.* [172] found that starlings in a flock continuously interact with seven of their closest neighbors, hence supporting evidence that the inter-

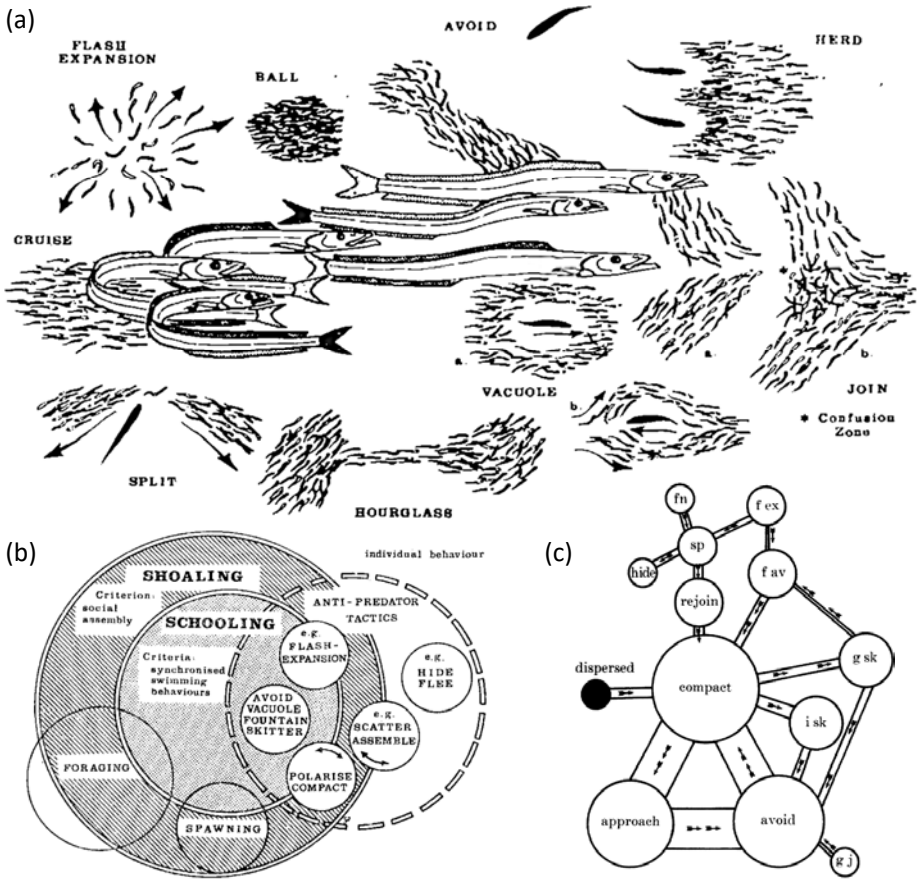


Figure 1.2: Classification and interconnection for fish schooling dynamics. a) Behavioral aspects of fish schooling, adopted from Pitcher and Wyche [73]. b) Venn diagram summarizing the different types of behavior for fish schools, adopted from Pitcher [76]. c) Interconnections between different schooling behaviors, adopted from Magurran and Pitcher [75].

action range is topological rather than metric. In addition, Cavagna *et al.* [173] revealed that fluctuations through a large flock of starlings are scale-free as the correlation length scales with the flock size, hence the flock appears to truly act as a whole.

Moreover, the availability of such tracking data from the field have revealed novel conservation laws governing the collective behavior [52]. This has been pivotal in the understanding of long-range signal propagation [157, 174], spontaneous changes in the travel direction of a flock [175], the criticality of the flock [176, 177], as well as the relative diffusion of birds [178], among many other results. The availability of such aerial observation data has also provided new insight into wave propagation in flocks during predator strike [10, 11]. Moreover, the abundance of the data collected helped classify the flow of different flocking events [179] in similarity to seminal work on fish [78].

Such methods have also been applied to investigate the roosting behavior of chimney

swifts [180]. Moreover, recent developments on portable field equipment have looked at the relation between wing beat and collective flight in jackdaw flocks [181], investigated the collective turns [182], revealed a ‘behavior plasticity’ for mobbing and transit flight of jackdaws [183], and shown the formation of long-term pairs or ‘social bonds’ [184]. Most recently these authors obtained in-plane social forces from three-dimensions tracking data as well [185].

1.3.3. THE LACK OF LARGE SCALE THREE-DIMENSIONAL TRACKING DATA

Beyond the lab environment, Nøttestad and Axelsen [186] first deployed a multi-beam sonar technique to study an Atlantic herring school escaping from a killer whale and distinguished a collective diving mode. Other such contributions include the three-dimensional structure and morphology of giant oceanic schools [4, 5], the propagation of large waves through anchovy schools [9, 187], planar fish velocimetry from acoustic video of predator escapes [188], killer whale tail slaps to stun prey [189], and the compacting of a school on predation [190]. Only most recent field experiments have observed 60000 wild-caught oceanic herring in a $12 \times 12 \times 12 \text{ m}^3$ arena with simulated predator attacks [191] including planar ultrasound velocimetry [192].

Despite early work by Cullen *et al.* [193], Pitcher [194], and Van Long *et al.* [195], only a few studies have proceeded to track schooling fish in three dimensions in a laboratory setting [117, 153, 155, 196–198] with limited results due to constraints on the scale and the number of fish. In addition to laboratory scale experiments [199, 200] few experimental works are present at large-scale in a relatively unconstrained environment [201]. All-in-all, to our best knowledge, no studies exist to date that performed the time-resolved three-dimensional tracking of realistically sized schools of fish consisting of a few thousand individuals in an unconstrained habitat. This will be the central theme and contribution of the current thesis — a first result for a realistically sized school as is shown in the middle of Figure 1.1i.

1.4. EXPERIMENTS AT THE ROTTERDAM ZOO

This thesis is an experimental study. The goal of this thesis is to extract quantitative tracking data of a large school of ± 2000 *Harengula clupeola* (false herring, *Clupeidae* family) in three dimensions at the large public ocean aquarium of the Rotterdam zoo. This large ocean aquarium is a unique facility that spans $20 \times 20 \times 6 \text{ m}^3$ in length, width, and depth (height), and by its size is relatively unconstrained to the fish. To date, only a few studies have attempted quantitative measurement of schooling fish at such large length scales [192, 201]. The number of fish is substantially more than previous experimental and laboratory work in two [133, 134, 141, 149, 199, 200] and three dimensions [117, 153, 155, 196–198] which have been limited to a few 10–100 of individuals.

1.4.1. THE DIERGAARDE BLIJDORP OCEANIUM

The ‘Diergaarde Blijdorp Oceanium’ of the Rotterdam zoo is a large-scale ocean aquarium (oceanarium) that reproduces a semi-natural habitat off the coast of Florida. The tank includes multiple cohabiting fish species and is optically accessible via a large window, see Figure 1.3. The climate in the tank is fully controlled; the lighting conditions

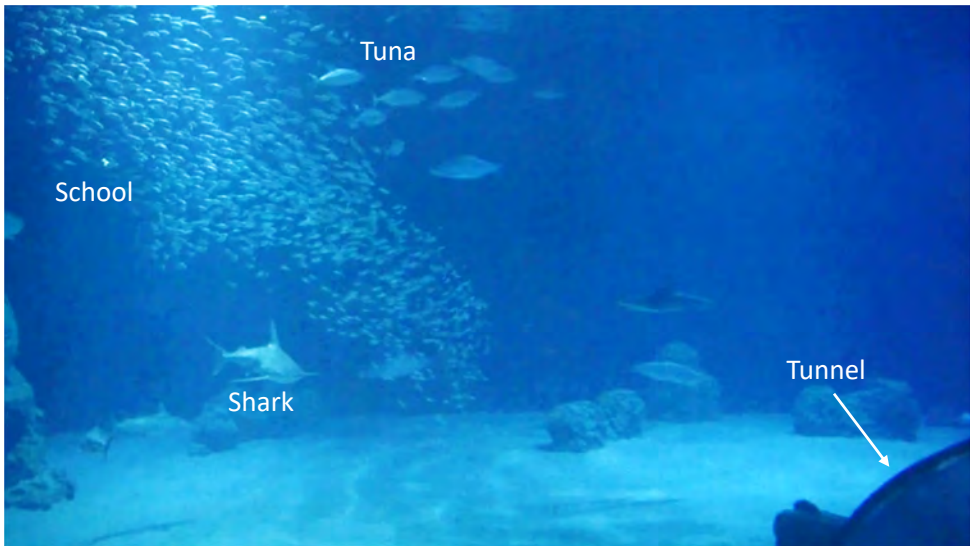


Figure 1.3: The Oceanium aquarium at the Rotterdam zoo. Left, a large school of harengula (obligate schoolers) at varying (optical) densities surrounded by predator fish, all in a relatively unconstrained environment. Middle, a trespassing shark (solitary predator) and a group of hunting tuna fish (facultative schoolers). Right, the publicly accessible underwater tunnel.

simulate the day- and nighttime cycle as well as long-term effects for the yearly seasons. These include changes in the summer and winter water temperatures, oxygen saturation, and salinity, which affect the water quality and turbidity levels.

The water flow in the tank is clockwise when viewed from the top. Interestingly, the harengula swim counter-clockwise and thereby against the flow in the tank. This is consistently reported by the curators for the current and past fish schools that have been present at the Rotterdam zoo. A blower that simulates a minor wind shear produces water waves on the surface. This is used to obscure the ceiling for the visitor experience during opening hours, which otherwise is visible from the publicly accessible underwater tunnel (Figure 1.3).

As the Oceanium aquarium simulates the day- and nighttime cycle by its lighting conditions, the activity of the fish changes during the day. In particular, in line with observations from the curators, we find little predation in the morning and an increasing number of attacks towards the evening as the fish become increasingly agitated. Furthermore, control over long-term seasonal effects may be used to stimulate breeding conditions. This may as well affect the fish activity and predation pressure. It is noteworthy that all fish present in the tank seem undisturbed by visitors during opening hours and show little response to camera flashes coming from the underwater tunnel.

1.4.2. HARENGULA, PREDATOR AND COHABITANT SPECIES

The large school of harengula in Figure 1.3 forms a milling-type configuration in the absence of predation. This is a well-documented behavior found in the natural environ-

ment [24, 27, 68, 69] where the fish are also observed to be swimming in a cylindrical motion. When interacting with predators and cohabiting species the school in the Rotterdam zoo displays many different schooling behaviors such as ‘flash expansion’, ‘split’, ‘herd’, ‘vacuole’, and ‘cruise’, and many more of those reported in [73, 75, 77, 186].

In total, we have imaged two consecutive schools of ± 2000 harengula which were collected and flown in off the coast of Florida in February 2017 and 2018 and released into the fish tank after a ± 4 month quarantine. The harengula are of typical dimension ~ 15 cm and with a swimming speed of ~ 30 cm/s at a characteristic tail-beat of ~ 10 Hz. The harengula are obligate schoolers and are thought to navigate primarily on vision. However, the school also remains cohesive in the dark presumably because of the lateral line [82, 83]. Furthermore, from visual observation, the fish occasionally release excrement when stressed which may act as an olfaction agent [202]. Such behavioral aspects we will not further consider in this thesis.

There are multiple species of fish that actively engage with the harengula school, posing a constant threat. First of all, there are several species of predatory shark (7–12) in the tank, including blacknose sharks (*Carcharhinus acronotus*), sandbar sharks (*Carcharhinus plumbeus*), blacktip sharks (*Carcharhinus limbatus*), ranging between 1–2.5 m in length. Next, there are facultative schoolers that may hunt in small groups including 8–11 horse-eye jack (*Caranx latus*), 5–10 yellowfin tuna-fish (*Thunnus albacares*), 3 barracudas (*Sphyraena barracuda*), 5 tarpon fish (*Megalops atlanticus*), and greater amberjack (*Seriola dumerili*); for the most important selection see Figure 1.4.

The predator fish are fed three times a week. The harengula, on the other hand, are continuously fed with a feeding machine that allows us to control their preferred position in the tank. In total we imaged about 1500–2500 fish as ± 500 fish are lost a year by the fish life expectancy. The predators typically attack at the front or back of the school relative to the observation behind the large window (not the overall swimming direction), swimming either with or against the flow and tracing the boundaries of the semi-natural habitat.

In addition, there are cohabitant species in the tank. The most important ones include 3 Atlantic nurse sharks (*Ginglymostoma cirratum*), a black-chin guitarfish (*Rhinobatos cemiculus*), a southern stingray (*Hypanus americanus*), a black- and Nassau grouper (*Mycteroperca bonaci*; *Epinephelus striatus*), a hawksbill (*Eretmochelys imbricata*) and 2 green sea turtles (*Chelonia mydas*). These may also interact with the harengula fish. For example, the school strongly responds to the flipper of the turtle’s swimming stroke. Finally, there are multiple subtropical fish that reside in the coral structures at the walls of the ocean aquarium. These do not actively engage with the school.

1.5. OUTLINE OF THIS THESIS

In the first part of this thesis, we introduce methods to perform quantitative measurements of the position and velocity of the fish. Starting with Chapter 2, we present the measurement technique to perform three-dimensional imaging over a large distance inside the ocean aquarium. Following, in Chapter 3, we explain different challenges to image processing in a complex underwater environment, we present the application of automated tracking algorithms to track and triangulate fish, and we characterize the performance of the implementation. In the second part of this thesis, we unfold different

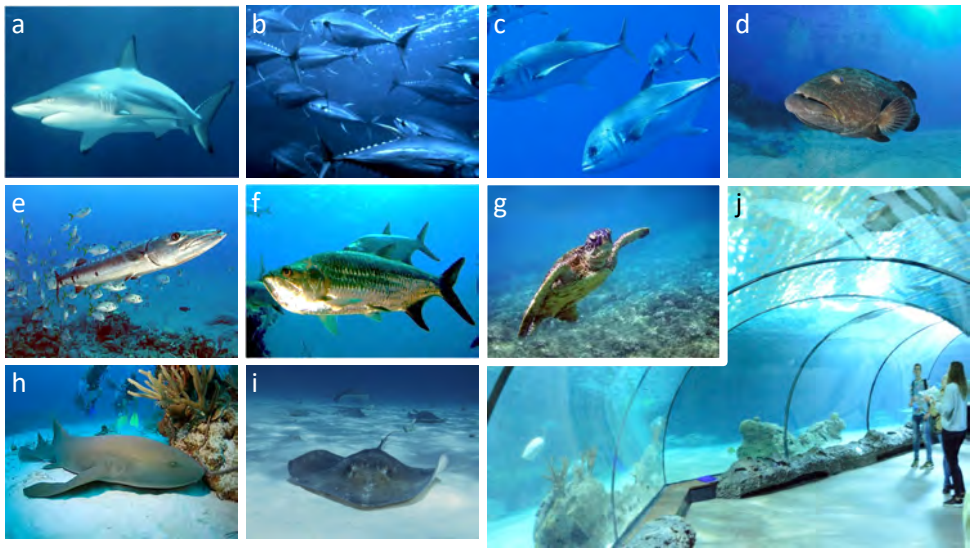


Figure 1.4: Predator fish and cohabitant species. a) Blacktip shark (*Carcharhinus limbatus*). b) Yellowfin tuna-fish (*Thunnus albacares*). c) Horse-eye jack (*Caranx latus*). d) Black grouper (*Mycteroperca bonaci*). e) Barracuda (*Sphyraena barracuda*). f) Tarpon (*Megalops atlanticus*). g) Green sea turtle (*Chelonia mydas*). h) Atlantic nurse shark (*Ginglymostoma cirratum*). i) Southern stingray (*Hypanus americanus*). j) A picture taken from the publicly accessible underwater tunnel at the bottom of the Oceanium aquarium. The pictures (a)–(i) are adopted from <https://en.wikipedia.org>.

quantitative analyses from the obtained tracking data. In Chapter 4, we first present the tracking data obtained for different observed schooling behaviors. Subsequently, we present descriptive statistics to analyze the geometry and kinematics of the school and lay the foundation for further analysis of the three-dimensional tracking data. In Chapter 5, we summarize the main conclusions of this thesis and provide several recommendations for future work. All detail can be found in the appendices.

REFERENCES

- [1] N. C. Makris, P. Ratilal, D. T. Symonds, S. Jagannathan, S. Lee, and R. W. Nero, *Fish Population and Behavior Revealed by Instantaneous Continental Shelf-Scale Imaging*, *Science* **323**, 1734 (2006).
- [2] N. C. Makris, P. Ratilal, S. Jagannathan, Z. Gong, M. Andrews, I. Bertatos, O. R. Godø, R. W. Nero, and J. M. Jech, *Critical Population Density Triggers Rapid Formation of Vast Oceanic Fish Shoals*, *Science Reports* **323**, 1734 (2009).
- [3] A. Bertrand, F. Gerlotto, S. Bertrand, M. Gutiérrez, L. Alza, A. Chipollini, E. Díaz, P. Espinoza, J. Ledesma, R. Quesquén, S. Peraltila, and F. Chavez, *Schooling behaviour and environmental forcing in relation to anchoveta distribution: An analysis across multiple spatial scales*, *Progress in Oceanography* **79**, 264 (2008).
- [4] F. Gerlotto and J. Paramo, *The three-dimensional morphology and internal structure of clupeid schools as observed using vertical scanning multibeam sonar*, *Aquatic Living Resources* **16**, 113 (2003).
- [5] J. Paramo, F. Gerlotto, and C. Oyarzun, *Three dimensional structure and morphology of pelagic fish schools*, *Journal of Applied Ichthyology* **26**, 853 (2010).
- [6] W. M. Hamner and M. N. Dawson, *A review and synthesis on the systematics and evolution of jellyfish blooms: Advantageous aggregations and adaptive assemblages*, in *Hydrobiologia*, Vol. 616 (2009) pp. 161–191.
- [7] W. M. Hamner and P. P. Hamner, *Behavior of Antarctic krill (*Euphausia superba*): schooling, foraging, and antipredatory behavior*, *Can. J. Fish. Aquat. Sci.* **57**, 192 (2000).
- [8] A. B. Leitner, J. M. Durden, C. R. Smith, E. D. Klingberg, and J. C. Drazen, *Synbranchid eel swarms on abyssal seamounts: Largest aggregation of fishes ever observed at abyssal depths*, *Deep-Sea Research Part I: Oceanographic Research Papers* (2020), 10.1016/j.dsr.2020.103423.
- [9] F. Gerlotto, S. Bertrand, N. Bez, and M. Gutierrez, *Waves of agitation inside anchovy schools observed with multibeam sonar: a way to transmit information in response to predation*, *ICES Journal of Marine Science* **63**, 1405 (2006).
- [10] A. Procaccini, A. Orlandi, A. Cavagna, I. Giardina, F. Zoratto, D. Santucci, F. Chiarotti, C. K. Hemelrijk, E. Alleva, G. Parisi, and C. Carere, *Propagating waves in starling, *Sturnus vulgaris*, flocks under predation*, *Animal Behaviour* **82**, 759 (2011).
- [11] C. K. Hemelrijk, A. Costanzo, H. Hildenbrandt, and C. Carere, *Damping of waves of agitation in starling flocks*, *Behavioral Ecology and Sociobiology* **73** (2019), 10.1007/s00265-019-2734-4.
- [12] E. Selous, *Thought Transference (or What?) in Birds*, *Nature* **122**, 263 (1931).

- [13] I. D. Couzin, *Collective minds*, *Nature* **445**, 715 (2007).
- [14] D. Grunbaum, *Schooling as a strategy for taxis in a noisy environment*, *Evolutionary Ecology* **12**, 503 (1998).
- [15] S. Ramaswamy, *The mechanics and statistics of active matter*, *Annual Review of Condensed Matter Physics* **1**, 323 (2010).
- [16] D. L. Koch and G. Subramanian, *Collective Hydrodynamics of Swimming Microorganisms: Living Fluids*, *Annual Review of Fluid Mechanics* **43**, 637 (2011).
- [17] J. M. Yeomans, *Active matter: Playful topology*, *Nature Materials* **13**, 1004 (2014).
- [18] G. Gompper, R. G. Winkler, T. Speck, A. Solon, C. Nardini, F. Peruani, H. Löwen, R. Golestanian, U. B. Kaupp, L. Alvarez, T. Ki rboe, E. Lauga, W. C. Poon, A. Desimone, S. Muiños-Landin, A. Fischer, N. A. Söker, F. Cichos, R. Kapral, P. Gaspard, M. Ripoll, F. Sagues, A. Doostmohammadi, J. M. Yeomans, I. S. Aranson, C. Bechinger, H. Stark, C. K. Hemelrijk, F. o. J. Nedelec, T. Sarkar, T. Aryaksama, M. Lacroix, G. Duclos, V. Yashunsky, P. Silberzan, M. Arroyo, and S. Kale, *The 2020 motile active matter roadmap*, *Journal of Physics Condensed Matter* **32** (2020), 10.1088/1361-648X/ab6348.
- [19] T. Feder, *Statistical physics is for the birds*, *Physics Today* **60**, 28 (2007).
- [20] A. Cavagna and I. Giardina, *The seventh starling*, *Significance* **5**, 62 (2008).
- [21] A. Cavagna and I. Giardina, *Bird flocks as condensed matter*, *Annual Review of Condensed Matter Physics* **5**, 183 (2014).
- [22] J. K. Parrish, S. V. Viscido, and D. Grünbaum, *Self-organized fish schools: An examination of emergent properties*, *Biological Bulletin* **202**, 296 (2002).
- [23] I. D. Couzin and J. Krause, *Self-Organization and Collective Behavior in Vertebrates*, *Advances in the Study of Behavior* **32**, 1 (2003).
- [24] D. J. T. Sumpter, *The principles of collective animal behaviour*, *Philosophical Transactions of the Royal Society B: Biological Sciences* **361**, 5 (2006).
- [25] M. Moussaid, S. Garnier, G. Theraulaz, and D. Helbing, *Collective information processing and pattern formation in swarms, flocks, and crowds*, *Topics in Cognitive Science* **1**, 469 (2009).
- [26] T. Vicsek and A. Zafeiris, *Collective motion*, *Physics Reports* **517**, 71 (2012).
- [27] U. Lopez, J. Gautrais, I. D. Couzin, and G. Theraulaz, *From behavioural analyses to models of collective motion in fish schools*, *Interface Focus* **2**, 693 (2012).
- [28] N. T. Ouellette, *A physics perspective on collective animal behavior*, *Physical Biology* **19** (2022), 10.1088/1478-3975/ac4bef.
- [29] T. Vicsek, *A question of scale*, *Nature* **411**, 421 (2001).

- [30] K. Drescher, J. Dunkel, L. H. Cisneros, S. Ganguly, and R. E. Goldstein, *Fluid dynamics and noise in bacterial cell-cell and cell-surface scattering*, Proceedings of the National Academy of Sciences **108**, 10940 (2011).
- [31] C. Dombrowski, L. Cisneros, S. Chatkaew, R. E. Goldstein, and J. O. Kessler, *Self-concentration and large-scale coherence in bacterial dynamics*, Physical Review Letters **93**, 2 (2004).
- [32] H. H. Wensink, J. Dunkel, S. Heidenreich, K. Drescher, R. E. Goldstein, H. Lowen, and J. M. Yeomans, *Meso-scale turbulence in living fluids*, Proceedings of the National Academy of Sciences **109**, 14308 (2012).
- [33] J. Dunkel, S. Heidenreich, K. Drescher, H. H. Wensink, M. Bär, and R. E. Goldstein, *Fluid dynamics of bacterial turbulence*, Physical Review Letters **110**, 1 (2013).
- [34] G. Duclos, R. Adkins, D. Banerjee, M. S. E Peterson, M. Varghese, I. Kolvin, A. Baskaran, R. A. Pelcovits, T. R. Powers, A. Baskaran, F. Toschi, M. F. Hagan, S. J. Streichan, V. Vitelli, D. A. Beller, and Z. Dogic, *Topological structure and dynamics of three-dimensional active nematics*, Science **367**, 1120 (2020).
- [35] D. H. Kelley and N. T. Ouellette, *Emergent dynamics of laboratory insect swarms*, Scientific Reports **3**, 1 (2013).
- [36] A. Attanasi, A. Cavagna, L. Del Castello, I. Giardina, S. Melillo, L. Parisi, O. Pohl, B. Rossaro, E. Shen, E. Silvestri, and M. Viale, *Collective Behaviour without Collective Order in Wild Swarms of Midges*, PLoS Computational Biology **10**, 1 (2014).
- [37] A. J. King, A. M. Wilson, S. D. Wilshin, J. Lowe, H. Haddadi, S. Hailes, and A. J. Morton, *Selfish-herd behaviour of sheep under threat*, Current Biology **22**, 561 (2012).
- [38] J. L. Silverberg, M. Bierbaum, J. P. Sethna, and I. Cohen, *Collective motion of humans in mosh and circle pits at heavy metal concerts*, Physical Review Letters **110**, 1 (2013).
- [39] A. Bottinelli and J. L. Silverberg, *When dense crowds act like soft solids*, (2019).
- [40] N. T. Ouellette, *Flowing crowds*, Science **363**, 27 (2019).
- [41] T. Vicsek, A. Czirók, E. Ben-Jacob, I. Cohen, and O. Shochet, *Novel Type of Phase Transition in a System of Self-Driven Particles*, Physical Review Letters **75**, 1226 (1995).
- [42] G. Grégoire, H. Chaté, and Y. Tu, *Moving and staying together without a leader*, Physica D: Nonlinear Phenomena **181**, 157 (2003).
- [43] G. Grégoire and H. Chaté, *Onset of Collective and Cohesive Motion*, Physical Review Letters **92**, 4 (2004).
- [44] M. R. D'Orsogna, Y. L. Chuang, A. L. Bertozzi, and L. S. Chayes, *Self-propelled particles with soft-core interactions: Patterns, stability, and collapse*, Physical Review Letters **96**, 1 (2006).

- [45] J. Toner and Y. Tu, *Long-Range Order in a Two-Dimensional Dynamical XY Model: How Birds Fly Together*, Physical Review Letters **75** (1995), 10.1103/PhysRevLett.75.4326.
- [46] J. Toner and Y. Tu, *Flocks, herds, and schools: A quantitative theory of flocking*, Physical Review E **58**, 4829 (1998).
- [47] J. Toner, Y. Tu, and S. Ramaswamy, *Hydrodynamics and phases of flocks*, Annals of Physics **318**, 170 (2005).
- [48] Y. Tu, J. Toner, and M. Ulm, *Sound Waves and the Absence of Galilean Invariance in Flocks*, Physical Review Letters **80**, 4819 (1998).
- [49] M. J. Lighthill and G. B. Whitham, *On kinematic waves I. Flood movement in long rivers*, Proceeding of the Royal Society A **255**, 281 (1955).
- [50] M. J. Lighthill and G. B. Whitham, *On kinematic waves II. A theory of traffic flow on long crowded roads*, Proceeding of the Royal Society A **229**, 317 (1955).
- [51] G. B. Whitham, *Linear and Nonlinear Waves*, 2nd ed. (WILEY, New York, 1974).
- [52] A. Attanasi, A. Cavagna, L. Del Castello, I. Giardina, T. S. Grigera, A. Jelić, S. Melillo, L. Parisi, O. Pohl, E. Shen, and M. Viale, *Information transfer and behavioural inertia in starling flocks*, Nature physics **10**, 691 (2014).
- [53] F. Berlinger, M. Gauci, and R. Nagpal, *Implicit coordination for 3D underwater collective behaviors in a fish-inspired robot swarm*, Sci Robot **6**, 1 (2021).
- [54] J. Deseigne, O. Dauchot, and H. Chaté, *Collective motion of vibrated polar disks*, Physical Review Letters **105**, 1 (2010).
- [55] M. Workamp, G. Ramirez, K. E. Daniels, and J. A. Dijksman, *Symmetry-reversals in chiral active matter*, Soft Matter **14**, 5572 (2018).
- [56] M. Moussaïd, D. Helbing, and G. Theraulaz, *How simple rules determine pedestrian behavior and crowd disasters*, PNAS **108**, 6884 (2011).
- [57] A. Corbetta, J. A. Meeusen, C. M. Lee, R. Benzi, and F. Toschi, *Physics-based modeling and data representation of pairwise interactions among pedestrians*, Physical Review E **98** (2018), 10.1103/PhysRevE.98.062310.
- [58] B. Blocken, T. van Druenen, Y. Toparlar, F. Malizia, P. Mannion, T. Andrienne, T. Marchal, G. J. Maas, and J. Diepens, *Aerodynamic drag in cycling pelotons: New insights by CFD simulation and wind tunnel testing*, Journal of Wind Engineering and Industrial Aerodynamics **179**, 319 (2018).
- [59] J. Belden, M. M. Mansoor, A. Hellum, S. R. Rahman, A. Meyer, C. Pease, J. Pacheco, S. Koziol, and T. T. Truscott, *How vision governs the collective behaviour of dense cycling pelotons*, Journal of the Royal Society Interface **16** (2019), 10.1098/rsif.2019.0197.

- [60] N. T. Ouellette, *The Most Active Matter of All*, *Matter* **1**, 297 (2019).
- [61] N. T. Ouellette and D. M. Gordon, *Goals and Limitations of Modeling Collective Behavior in Biological Systems*, *Frontiers in Physics* **9** (2021), 10.3389/fphy.2021.687823.
- [62] W. D. Hamilton, *Geometry for the Selfish Herd*, *J. theor. Biol* **31**, 295 (1971).
- [63] S. V. Viscido, M. Millery, and D. S. Wettheywz, *The Dilemma of the Selfish Herd: The Search for a Realistic Movement Rule*, *J. theor. Biol* **217**, 183 (2002).
- [64] D. W. Sankey, R. F. Storms, R. J. Musters, T. W. Russell, C. K. Hemelrijk, and S. J. Portugal, *Absence of “selfish herd” dynamics in bird flocks under threat*, *Current Biology* **31**, 3192 (2021).
- [65] B. L. Partridge, *The Structure and Function of Fish Schools*, **246**, 114 (1982).
- [66] H. Kunz, T. Züblin, and C. K. Hemelrijk, *On prey grouping and predator confusion in artificial fish schools*, in *Proc. 10th Int. Conf. Artificial Life* (2006).
- [67] C. Breder, *On the survival value of fish schools*, *Zoologica: New York Zoological Society* **52**, 25 (1967).
- [68] J. K. Parrish and L. Edelstein-Keshet, *Complexity, Pattern, and Evolutionary Trade-Offs in Animal Aggregation*, *Science* **284**, 99 (1999).
- [69] J. Delcourt, N. W. Bode, and M. Denoël, *Collective vortex behaviors: Diversity, proximate, and ultimate causes of circular animal group movements*, *Quarterly Review of Biology* **91**, 1 (2016).
- [70] P. F. Major, *Predator-Prey Interactions in Two Schooling Fishes, *Caranx Ignobilis* and *Stolephorus Purpurues**, *Anim. Behav* **26**, 760 (1978).
- [71] P. Domenici, A. D. Wilson, R. H. Kurvers, S. Marras, J. E. Herbert-Read, J. F. Steffensen, S. Krause, P. E. Viblanc, P. Couillaud, and J. Krause, *How sailfish use their bills to capture schooling prey*, *Proceedings of the Royal Society B: Biological Sciences* **281** (2014), 10.1098/rspb.2014.0444.
- [72] R. H. Kurvers, S. Krause, P. E. Viblanc, J. E. Herbert-Read, P. Zaslansky, P. Domenici, S. Marras, J. F. Steffensen, M. B. Svendsen, A. D. Wilson, P. Couillaud, K. M. Boswell, and J. Krause, *The Evolution of Lateralization in Group Hunting Sailfish*, *Current Biology* **27**, 521 (2017).
- [73] T. J. Pitcher and C. J. Wyche, *Predator-avoidance behaviours of sand-eel schools: why schools seldom split*, in *Predators and prey in fishes*, Vol. 2 (Springer, Dordrecht, 1983) pp. 193–204.
- [74] E. Shaw, *Schooling Fishes: The school, a truly egalitarian form of organization in which all members of the group are alike in influence, offers substantial benefits to its participants*, *American Scientist* **66**, 166 (1978).

- [75] A. E. Magurran and T. J. Pitcher, *Provenance, shoal size and the sociobiology of predator-evasion behaviour in minnow shoals*, Proc. R. Soc. Lond. **229**, 439 (1987).
- [76] T. J. Pitcher, *Heuristics Definitions of Fish Shoaling Behavior*, Animal Behavior, 611 (1982).
- [77] T. J. Pitcher and J. K. Parrish, *Functions of Shoaling Behaviour in Teleost*, 2nd ed., edited by T. J. Pitcher, Vol. 7 (Chapman & Hall, London, 1993) pp. 364–438.
- [78] A. E. Magurran, *The Adaptive Significance of Schooling as an Anti-predator Defence in Fish*, Ann. Zool. Fennici **27**, 51 (1990).
- [79] M. J. Lighthill, *Hydromechanics of Aquatic Animal Propulsion*, Annual Review of Fluid Mechanics **1**, 413 (1969).
- [80] M. S. Triantafyllou, G. D. Weymouth, and J. Miao, *Biomimetic Survival Hydrodynamics and Flow Sensing*, Annual Review of Fluid Mechanics **48**, 1 (2016).
- [81] T. J. Pitcher, B. L. Partridge, and C. S. Wardle, *A blind fish can school*, Science **194**, 963 (1976).
- [82] B. L. Partridge and T. J. Pitcher, *The Sensory Basis of Fish Schools: Relative Roles of Lateral Line and Vision**, J. Comp. Physiol **135**, 315 (1980).
- [83] K. Faucher, E. Parmentier, C. Becco, N. Vandewalle, and P. Vandewalle, *Fish lateral system is required for accurate control of shoaling behaviour*, Animal Behaviour **79**, 679 (2010).
- [84] D. Weihs, *Hydrodynamics of Fish Schooling*, Nature **241**, 290 (1973).
- [85] C. M. Breder, *Vortices and fish schools*, in *N. Y. Zool. Soc.* (1965) pp. 97–114.
- [86] B. L. Partridge and T. J. Pitcher, *Evidence Against a Hydrodynamics Function for Fish Schools*, Nature **279** (1979), 10.1038/279418a0.
- [87] C. K. Hemelrijk, D. A. P. Reid, H. Hildenbrandt, and J. T. Padding, *The increased efficiency of fish swimming in a school*, Fish and Fisheries **16**, 511 (2015).
- [88] S. Marras, S. S. Killen, J. Lindström, D. J. McKenzie, J. F. Steffensen, and P. Domenici, *Fish swimming in schools save energy regardless of their spatial position*, Behavioral Ecology and Sociobiology **69**, 219 (2015).
- [89] I. Ashraf, R. Godoy-Diana, J. Halloy, B. Collignon, and B. Thiria, *Synchronization and collective swimming patterns in fish (*Hemigrammus bleheri*)*, Journal of the Royal Society Interface **13**, 1 (2016).
- [90] I. Ashraf, H. Bradshaw, T. T. Ha, J. Halloy, R. Godoy-Diana, and B. Thiria, *Simple phalanx pattern leads to energy saving in cohesive fish schooling*, PNAS **114**, 9599 (2017).

- [91] S. Verma, G. Novati, and P. Koumoutsakos, *Efficient collective swimming by harnessing vortices through deep reinforcement learning*, PNAS **115**, 5849 (2018).
- [92] S. Verma, C. Papadimitriou, N. Lüthen, G. Arampatzis, and P. Koumoutsakos, *Optimal sensor placement for artificial swimmers*, Journal of Fluid Mechanics **884**, 1 (2019).
- [93] L. Li, M. Nagy, J. M. Graving, J. Bak-Coleman, G. Xie, and I. D. Couzin, *Vortex phase matching as a strategy for schooling in robots and in fish*, Nature Communications **11** (2020), 10.1038/s41467-020-19086-0.
- [94] L. Li, S. Ravi, G. Xie, and I. D. Couzin, *Using a robotic platform to study the influence of relative tailbeat phase on the energetic costs of side-by-side swimming in fish*, Proceedings of the Royal Society A: Mathematical, Physical and Engineering Sciences **477** (2021), 10.1098/rspa.2020.0810.
- [95] D. N. Beal, F. S. Hover, M. S. Triantafyllou, J. C. Liao, and G. V. Lauder, *Passive propulsion in vortex wakes*, Journal of Fluid Mechanics **549**, 385 (2006).
- [96] R. McNeill Alexander, *Hitching a lift hydrodynamically-in swimming, flying and cycling*, Journal of Biology **3**, 1 (2004).
- [97] D. Weihs, *The hydrodynamics of dolphin drafting*, Journal of Biology **3**, 1 (2004).
- [98] S. R. Noren, G. Biedenbach, J. V. Redfern, and E. F. Edwards, *Hitching a ride: The formation locomotion strategy of dolphin calves*, Functional Ecology **22**, 278 (2008).
- [99] A. Filella, F. Nadal, C. Sire, E. Kanso, and C. Eloy, *Model of Collective Fish Behavior with Hydrodynamic Interactions*, Physical Review Letters **120**, 1 (2018).
- [100] I. L. Bajec and F. H. Heppner, *Organized flight in birds*, Animal Behaviour **78**, 777 (2009).
- [101] H. Hildenbrandt, C. Carere, and C. K. Hemelrijk, *Self-organized aerial displays of thousands of starlings: A model*, Behavioral Ecology **21**, 1349 (2010).
- [102] C. K. Hemelrijk and H. Hildenbrandt, *Some causes of the variable shape of flocks of birds*, PLoS ONE **6**, 1 (2011).
- [103] C. K. Hemelrijk and H. Hildenbrandt, *Schools of fish and flocks of birds: Their shape and internal structure by self-organization*, Interface Focus **2**, 726 (2012).
- [104] C. M. Breder, *Equations Descriptive of Fish Schools and Other Animal Aggregations*, Ecology **35**, 361 (1954).
- [105] C. W. Reynolds, *Flocks, Herds, and Schools: A Distributed Behavioral Model*, Computer Graphics **21**, 25 (1987).
- [106] A. Huth and C. Wissel, *The simulation of the movement of fish schools*, Journal of Theoretical Biology **156**, 365 (1992).

- [107] A. Huth and C. Wissel, *The simulation of fish schools in comparison with experimental data*, *Ecological Modelling* **75**, 135 (1994).
- [108] T. J. Pitcher and B. L. Partridge, *Fish School Density and Volume*, *Marine Biology* **54**, 383 (1979).
- [109] B. L. Partridge, T. Pitcher, M. J. Cullen, and J. Wilson, *The Three-Dimensional Structure of Fish Schools**, *Behav. Ecol. Sociobiol.* **6**, 277 (1980).
- [110] B. L. Partridge, *Internal Dynamics and the Interrelations of Fish in Schools*, *Journal of Comparative Physiology. A* **144**, 313 (1981).
- [111] I. Aoki, *A Simulation Study on the Schooling Mechanism in Fish*, *Bulletin of the Japanese Society of Scientific Fisheries* **48**, 1081 (1982).
- [112] I. Aoki, *Internal Dynamics of Fish Schools in Relation to Inter-fish Distance*1*, *Bulletin of the Japanese Society of Scientific Fisheries* **50**, 751 (1984).
- [113] I. D. Couzin, J. Krause, R. James, G. D. Ruxton, and N. R. Franks, *Collective Memory and Spatial Sorting in Animal Groups*, *J. theor. Biol* **218**, 1 (2002).
- [114] H. Kunz and C. K. Hemelrijk, *Artificial fish schools: collective effects of school size, body size, and body form*. *Artificial Life* **9**, 237 (2003).
- [115] C. K. Hemelrijk and H. Kunz, *Density distribution and size sorting in fish schools: An individual-based model*, *Behavioral Ecology* **16**, 178 (2005).
- [116] C. K. Hemelrijk and H. Hildenbrandt, *Self-organized shape and frontal density of fish schools*, *Ethology* **114**, 245 (2008).
- [117] C. K. Hemelrijk, H. Hildenbrandt, J. Reinders, and E. J. Stamhuis, *Emergence of Oblong School Shape: Models and Empirical Data of Fish*, *Ethology* **116**, 1099 (2010).
- [118] S. Geuron, S. A. Levin, and D. I. Rubenstein, *The Dynamics of Herds: From Individuals to Aggregations*, *J. theor. Biol* **182**, 85 (1996).
- [119] H.-S. Niwa, *Newtonian Dynamical Approach to Fish Schooling*, *J. theor. Biol* **181**, 47 (1996).
- [120] I. D. Couzin, J. Krause, N. R. Franks, and S. A. Levin, *Effective leadership and decision-making in animal groups on the move*, *Letters to Nature* **433**, 513 (2005).
- [121] S. V. Viscido, J. K. Parrish, and D. Grünbaum, *Factors influencing the structure and maintenance of fish schools*, *Ecological Modelling* **206**, 153 (2007).
- [122] B. H. Lemasson, J. J. Anderson, and R. A. Goodwin, *Collective motion in animal groups from a neurobiological perspective: The adaptive benefits of dynamic sensory loads and selective attention*, *Journal of Theoretical Biology* **261**, 501 (2009).
- [123] P. Romanczuk, I. D. Couzin, and L. Schimansky-Geier, *Collective motion due to individual escape and pursuit response*, *Physical Review Letters* **102** (2009), 10.1103/PhysRevLett.102.010602.

- [124] D. Strömbom, *Collective motion from local attraction*, Journal of Theoretical Biology **283**, 145 (2011).
- [125] S. Mishra, K. Tunström, I. D. Couzin, and C. Huepe, *Collective dynamics of self-propelled particles with variable speed*, Physical Review E - Statistical, Nonlinear, and Soft Matter Physics **86**, 1 (2012).
- [126] A. Costanzo and C. K. Hemelrijk, *Spontaneous emergence of milling (vortex state) in a Vicsek-like model*, Journal of Physics D: Applied Physics **51**, 1 (2018).
- [127] A. Costanzo, *Milling-induction and milling-destruction in a Vicsek-like binary-mixture model*, EPL **125** (2019), 10.1209/0295-5075/125/20008.
- [128] A. Costanzo, E. Van Haeringen, and C. K. Hemelrijk, *Effect of time-delayed interactions on milling: A minimal model*, EPL **138**, 1 (2022).
- [129] R. Bastien and P. Romanczuk, *A model of collective behavior based purely on vision*, Science Advances **6**, 1 (2020).
- [130] J. R. Hunter, *Communication of Velocity Changes in Jack Mackerel (Trachurus Symmetricus) Schools*, Animal Behaviour **17**, 507 (1969).
- [131] M. A. Doustari and N. Sannomiya, *A simulation study on schooling behaviour of fish in a water tank*, International Journal of Systems Science **26**, 2295 (1995).
- [132] J. H. Tien, S. A. Levin, and D. I. Rubenstein, *Dynamics of fish shoals: identifying key decision rules*, Evolutionary Ecology Research **6**, 555 (2004).
- [133] Y. Katz, K. Tunström, C. C. Ioannou, C. Huepe, I. D. Couzin, S. A. Levin, I. D. C. Designed, and I. D. C. Performed, *Inferring the structure and dynamics of interactions in schooling fish*, PNAS **108**, 18720 (2011).
- [134] J. E. Herbert-Read, A. Perna, R. P. Mann, T. M. Schaerf, D. J. T. Sumpter, A. J. W. Ward, and H.-R. Performed, *Inferring the rules of interaction of shoaling fish*, PNAS **108**, 18726 (2011).
- [135] R. Lukeman, Y. X. Li, and L. Edelstein-Keshet, *Inferring individual rules from collective behavior*, Proceedings of the National Academy of Sciences of the United States of America **107**, 12576 (2010).
- [136] M. Romenskyy, J. E. Herbert-Read, A. J. Ward, and D. J. Sumpter, *Body size affects the strength of social interactions and spatial organization of a schooling fish (Pseudomugil signifer)*, Royal Society Open Science **4**, 1 (2017).
- [137] J. E. Herbert-Read, E. Rosén, A. Szorkovszky, C. C. Ioannou, B. Rogell, A. Perna, I. W. Ramnarine, A. Kotrschal, N. Kolm, J. Krause, and D. J. Sumpter, *How predation shapes the social interaction rules of shoaling fish*, Proceedings of the Royal Society B: Biological Sciences **284** (2017), 10.1098/rspb.2017.1126.
- [138] M. I. Kent, R. Lukeman, J. T. Lizier, and A. J. Ward, *Speed-mediated properties of schooling*, Royal Society Open Science **6** (2019), 10.1098/rsos.181482.

- [139] N. Mizumoto, S. Miyata, and S. C. Pratt, *Inferring collective behaviour from a fossilized fish shoal*, Proceedings of the Royal Society B: Biological Sciences **286**, 1 (2019).
- [140] A. Strandburg-Peshkin, C. R. Twomey, N. W. Bode, A. B. Kao, Y. Katz, C. C. Ioannou, S. B. Rosenthal, C. J. Torney, H. S. Wu, S. A. Levin, and I. D. Couzin, *Visual sensory networks and effective information transfer in animal groups*, Current Biology **23** (2013), 10.1016/j.cub.2013.07.044.
- [141] S. B. Rosenthal, C. R. Twomey, A. T. Hartnett, H. S. Wu, and I. D. Couzin, *Revealing the hidden networks of interaction in mobile animal groups allows prediction of complex behavioral contagion*, Proceedings of the National Academy of Sciences of the United States of America **112**, 4690 (2015).
- [142] J. E. Treherne and W. A. Foster, *Group Transmission of Predator Avoidance Behaviour in a Marine Insect: The Trafalgar Effect*, Anim. Behav **29**, 911 (1981).
- [143] V. Lecheval, L. Jiang, P. Tichit, C. Sire, C. K. Hemelrijk, and G. Theraulaz, *Social conformity and propagation of information in collective u-turns of fish schools*, Proceedings of the Royal Society B: Biological Sciences **285**, 1 (2018).
- [144] A. Berdahl, C. J. Torney, C. C. Ioannou, J. J. Faria, and I. D. Couzin, *Emergent Sensing of Complex Environments by Mobile Animal Groups*, Science **339**, 574 (2013).
- [145] J. G. Puckett, A. R. Pokhrel, and J. A. Giannini, *Collective gradient sensing in fish schools*, Scientific Reports **8**, 1 (2018).
- [146] C. C. Ioannou, V. Guttal, and I. D. Couzin, *Predatory Fish Select for Coordinated Collective Motion in Virtual Prey*, Science **337**, 1210 (2012).
- [147] J. R. Stowers, M. Hofbauer, R. Bastien, J. Griessner, P. Higgins, S. Farooqui, R. M. Fischer, K. Nowikovskiy, W. Haubensak, I. D. Couzin, K. Tessmar-Raible, and A. D. Straw, *Virtual reality for freely moving animals*, Nature Methods **14**, 995 (2017).
- [148] C. Becco, N. Vandewalle, J. Delcourt, and P. Poncin, *Experimental evidences of a structural and dynamical transition in fish school*, Physica A: Statistical Mechanics and its Applications **367**, 487 (2006).
- [149] K. Tunstrøm, Y. Katz, C. C. Ioannou, C. Huepe, M. J. Lutz, and I. D. Couzin, *Collective States, Multistability and Transitional Behavior in Schooling Fish*, PLoS Computational Biology **9**, 1 (2013).
- [150] J. Gautrais, C. Jost, and G. Theraulaz, *Key behavioural factors in a self-organised fish school model*, Ann. Zool. Fennici **45**, 415 (2008).
- [151] D. S. Calovi, U. Lopez, S. Ngo, C. Sire, H. Chaté, and G. Theraulaz, *Swarming, schooling, milling: Phase diagram of a data-driven fish school model*, New Journal of Physics **16**, 1 (2014).

- [152] J. Jhavar, R. G. Morris, U. R. Amith-Kumar, M. Danny Raj, T. Rogers, H. Rajendran, and V. Guttal, *Noise-induced schooling of fish*, *Nature Physics* **16**, 488 (2020).
- [153] S. V. Viscido, J. K. Parrish, and D. Grünbaum, *Individual behavior and emergent properties of fish schools: a comparison of observation and theory*, Source: *Marine Ecology Progress Series* **273**, 239 (2004).
- [154] I. Watts, M. Nagy, R. I. Holbrook, D. Biro, and T. Burt de Perera, *Validating two-dimensional leadership models on three-dimensionally structured fish schools*, *Royal Society Open Science* **4** (2017), 10.1098/rsos.160804.
- [155] M. Romenskyy, J. E. Herbert-Read, C. C. Ioannou, A. Szorkovszky, A. J. Ward, and D. J. Sumpter, *Quantifying the structure and dynamics of fish shoals under predation threat in three dimensions*, *Behavioral Ecology* **31**, 311 (2020).
- [156] A. J. Ward, T. M. Schaerf, J. E. Herbert-Read, L. Morrell, D. J. Sumpter, and M. M. Webster, *Local interactions and global properties of wild, free-ranging stickleback shoals*, *Royal Society Open Science* **4** (2017), 10.1098/rsos.170043.
- [157] A. Cavagna, I. Giardina, and T. S. Grigera, *The physics of flocking: Correlation as a compass from experiments to theory*, *Physics Reports* **728**, 1 (2018).
- [158] J. G. Puckett, D. H. Kelley, and N. T. Ouellette, *Searching for effective forces in laboratory insect swarms*, *Scientific Reports* **4**, 1 (2014).
- [159] R. Ni and N. T. Ouellette, *Velocity correlations in laboratory insect swarms*, *European Physical Journal: Special Topics* **224**, 3271 (2015).
- [160] R. Ni and N. T. Ouellette, *On the tensile strength of insect swarms*, *Physical Biology* **13** (2016), 10.1088/1478-3975/13/4/045002.
- [161] K. Van Der Vaart, M. Sinhuber, A. M. Reynolds, and N. T. Ouellette, *Mechanical spectroscopy of insect swarms*, *Science Advances* **5**, 1 (2019).
- [162] D. Gorbonos, R. Ianculescu, J. G. Puckett, R. Ni, N. T. Ouellette, and N. S. Gov, *Long-range acoustic interactions in insect swarms: An adaptive gravity model*, *New Journal of Physics* **18**, 1 (2016).
- [163] M. Sinhuber, K. van der Vaart, Y. Feng, A. M. Reynolds, and N. T. Ouellette, *An equation of state for insect swarms*, *Scientific Reports* **11** (2021), 10.1038/s41598-021-83303-z.
- [164] A. Attanasi, A. Cavagna, L. Del Castello, I. Giardina, S. Melillo, L. Parisi, O. Pohl, B. Rossaro, E. Shen, E. Silvestri, and M. Viale, *Finite-size scaling as a way to probe near-criticality in natural swarms*, *Physical Review Letters* **113**, 1 (2014).
- [165] A. Cavagna, D. Conti, C. Creato, L. Del Castello, I. Giardina, T. S. Grigera, S. Melillo, L. Parisi, and M. Viale, *Dynamic scaling in natural swarms*, *Nature Physics* **13**, 914 (2017).

- [166] A. Cavagna, I. Giardina, A. Orlandi, G. Parisi, A. Procaccini, M. Viale, and V. Zdravkovic, *The STARFLAG handbook on collective animal behaviour: Part I, empirical methods*, Tech. Rep. (2008).
- [167] A. Cavagna, I. Giardina, A. Orlandi, G. Parisi, and A. Procaccini, *The STARFLAG handbook on collective animal behaviour: Part II, three-dimensional analysis*, Tech. Rep. (2008).
- [168] D. H. Theriault, N. W. Fuller, B. E. Jackson, E. Bluhm, D. Evangelista, Z. Wu, M. Betke, and T. L. Hedrick, *A protocol and calibration method for accurate multi-camera field videography*, *Journal of Experimental Biology* **217**, 1843 (2014).
- [169] A. Attanasi, A. Cavagna, L. Del Castello, I. Giardina, A. Jelić, S. Melillo, L. Parisi, F. Pellacini, E. Shen, E. Silvestri, and M. Viale, *GReTA-A Novel Global and Recursive Tracking Algorithm in Three Dimensions*, *IEEE Transactions on Pattern Analysis and Machine Intelligence* **37**, 2451 (2015).
- [170] A. Cavagna, A. Cimorelli, I. Giardina, A. Orlandi, G. Parisi, A. Procaccini, R. Santagati, and F. Stefanini, *New statistical tools for analyzing the structure of animal groups*, *Mathematical Biosciences* **214**, 32 (2008).
- [171] M. Ballerini, N. Cabibbo, R. Candelier, A. Cavagna, E. Cisbani, I. Giardina, A. Orlandi, G. Parisi, A. Procaccini, M. Viale, and V. Zdravkovic, *Empirical investigation of starling flocks: a benchmark study in collective animal behaviour*, *Animal Behaviour* **76**, 201 (2008).
- [172] M. Ballerini, N. Cabibbo, R. Candelier, A. Cavagna, E. Cisbani, I. Giardina, V. Lecomte, and A. Orlandi, *Interaction ruling animal collective behavior depends on topological rather than metric distance: Evidence from a field study*, *PNAS* **105**, 1232 (2008).
- [173] A. Cavagna, A. Cimorelli, I. Giardina, G. Parisi, R. Santagati, F. Stefanini, and M. Viale, *Scale-free correlations in starling flocks*, *PNAS* **107**, 11865 (2010).
- [174] A. Cavagna, I. Giardina, T. S. Grigera, A. Jelic, D. Levine, S. Ramaswamy, and M. Viale, *Silent flocks: Constraints on signal propagation across biological groups*, *Physical Review Letters* **114**, 1 (2015).
- [175] A. Attanasi, A. Cavagna, L. Del Castello, I. Giardina, A. Jelic, S. Melillo, L. Parisi, O. Pohl, E. Shen, and M. Viale, *Emergence of collective changes in travel direction of starling flocks from individual birds' fluctuations*, *Journal of the Royal Society Interface* **12**, 1 (2015).
- [176] W. Bialek, A. Cavagna, I. Giardina, T. Mora, E. Silvestri, M. Viale, and A. M. Walczak, *Statistical mechanics for natural flocks of birds*, *PNAS*, 1 (2012).
- [177] W. Bialek, A. Cavagna, I. Giardina, T. Mora, O. Pohl, E. Silvestri, M. Viale, and A. M. Walczak, *Social interactions dominate speed control in poising natural flocks near criticality*, *Proceedings of the National Academy of Sciences of the United States of America* **111**, 7212 (2014).

- [178] A. Cavagna, S. M. Duarte Queirós, I. Giardina, F. Stefanini, and M. Viale, *Diffusion of individual birds in starling flocks*, Proceedings of the Royal Society B: Biological Sciences **280** (2013), 10.1098/rspb.2012.2484.
- [179] R. F. Storms, C. Carere, F. Zoratto, and C. K. Hemelrijk, *Complex patterns of collective escape in starling flocks under predation*, Behavioral Ecology and Sociobiology **73** (2019), 10.1007/s00265-018-2609-0.
- [180] D. J. Evangelista, D. D. Ray, S. K. Raja, and T. L. Hedrick, *Three-dimensional trajectories and network analyses of group behaviour within chimney swift flocks during approaches to the roost*, Proceedings of the Royal Society B: Biological Sciences **284**, 1 (2017).
- [181] H. Ling, G. E. McIvor, G. Nagy, S. MohaimenianPour, R. T. Vaughan, A. Thornton, and N. T. Ouellette, *Simultaneous measurements of three-dimensional trajectories and wingbeat frequencies of birds in the field*, Journal of the Royal Society Interface **15** (2018), 10.1098/rsif.2018.0653.
- [182] H. Ling, G. E. McIvor, J. Westley, K. van der Vaart, R. T. Vaughan, A. Thornton, and N. T. Ouellette, *Behavioural plasticity and the transition to order in jackdaw flocks*, Nature Communications **10** (2019), 10.1038/s41467-019-13281-4.
- [183] H. Ling, G. E. McIvor, J. Westley, K. Van Der Vaart, J. Yin, R. T. Vaughan, A. Thornton, and N. T. Ouellette, *Collective turns in jackdaw flocks: Kinematics and information transfer*, Journal of the Royal Society Interface **16** (2019), 10.1098/rsif.2019.0450.
- [184] H. Ling, G. E. McIvor, K. van der Vaart, R. T. Vaughan, A. Thornton, and N. T. Ouellette, *Costs and Benefits of Social Relationships in the Collective Motion of Bird Flocks*, Nature Ecology and Evolution **3**, 943 (2019).
- [185] H. Ling, G. E. McIvor, K. Van Der Vaart, R. T. Vaughan, A. A. Thornton, and N. T. Ouellette, *Local interactions and their group-level consequences in flocking jackdaws*, Proceedings of the Royal Society B: Biological Sciences **286** (2019), 10.1098/rspb.2019.0865.
- [186] L. Nøttestad and B. E. Axelsen, *Herring schooling manoeuvres in response to killer whale attacks*, Canadian Journal of Zoology **77**, 1540 (1999).
- [187] B. Erik Axelsen, L. Nøttestad, A. Fernö, A. Johannessen, and O. Arve Misund, *'Await' in the Pelagic: Dynamic Trade-off Between Reproduction and Survival within a Herring School Splitting Vertically During Spawning*, Source: Marine Ecology Progress Series **205**, 259 (2000).
- [188] N. O. Handegard, K. M. Boswell, C. C. Ioannou, S. P. Leblanc, D. B. Tjøstheim, and I. D. Couzin, *The dynamics of coordinated group hunting and collective information transfer among schooling prey*, Current Biology **22**, 1213 (2012).
- [189] P. Domenici, R. S. Batty, and T. Similä, *Spacing of wild schooling herring while encircled by killer whales*, Journal of Fish Biology **57**, 831 (2000).

- [190] P. Domenici, *Kinematics of killer whale tail-slaps*, *The Journal of Experimental Biology*, 283 (2000).
- [191] G. Rieucau, A. De Robertis, K. M. Boswell, and N. O. Handegard, *School density affects the strength of collective avoidance responses in wild-caught Atlantic herring *Clupea harengus*: A simulated predator encounter experiment*, *Journal of Fish Biology* **85**, 1650 (2014).
- [192] G. Rieucau, A. J. Holmin, J. C. Castillo, I. D. Couzin, and N. O. Handegard, *School level structural and dynamic adjustments to risk promote information transfer and collective evasion in herring*, *Animal Behaviour* **117**, 69 (2016).
- [193] J. M. Cullen, E. Shaw, and H. A. Baldwin, *Methods for Measuring the Three-dimensional Structure of Fish Schools*, *Animal Behaviour* **8**, 534 (1965).
- [194] T. J. Pitcher, *The Three-Dimensional Structure of Schools in the Minnow, *Phoxinus Phoxinus* (L.)*, *Anim. Behav.* **21**, 673 (1973).
- [195] L. Van Long, T. Aoyama, and T. Inagaki, *A Stereo Photographic Method for Measuring the Spatial Position of Fish*, *Bulletin of the Japanese Society of Scientific Fisheries* **51**, 183 (1985).
- [196] S. Butail and D. A. Paley, *Three-dimensional reconstruction of the fast-start swimming kinematics of densely schooling fish*, *Journal of the Royal Society Interface* **9**, 77 (2012).
- [197] J. Delcourt, M. Denoël, M. Ylief, and P. Poncin, *Video multitracking of fish behaviour: A synthesis and future perspectives*, *Fish and Fisheries* **14**, 186 (2013).
- [198] S. H. Wang, J. Zhao, X. Liu, Z.-M. Qian, Y. Liu, and Y. Q. Chen, *3D Tracking Swimming Fish School with Learned Kinematic Model Using LSTM Network*, in *International Conference on Acoustics, Speech and Signal Processing (ICASSP)* (IEEE, New Orleans, LA, USA, 2017) pp. 1068–1072.
- [199] P. Domenici and R. S. Batty, *Escape behaviour of solitary herring (*Clupea harengus*) and comparisons with schooling individuals*, *Marine Biology* **128**, 29 (1997).
- [200] S. Marras and P. Domenici, *Schooling Fish Under Attack Are Not All Equal: Some Lead, Others Follow*, *PLoS ONE* **8**, 1 (2013).
- [201] S. Marras, R. S. Batty, and P. Domenici, *Information transfer and antipredator maneuvers in schooling herring*, *Adaptive Behavior* **20**, 44 (2011).
- [202] C. C. Hemmings, *Olfaction and Vision in Fish Schooling*, *J. Exp. Biol* **45**, 449 (1966).

2

MEASUREMENT TECHNIQUE AND CAMERA CALIBRATION

Obtaining accurate experimental data from Lagrangian tracking and tomographic velocimetry requires an accurate camera calibration consistent over multiple views. Established calibration procedures are often challenging to implement when the length scale of the measurement volume exceeds that of a typical laboratory experiment. Here, we combine tools developed in computer vision and non-linear camera mappings used in experimental fluid mechanics, to successfully calibrate a four-camera setup that is imaging inside a large tank of dimensions $\sim 10 \times 25 \times 6 \text{ m}^3$. The calibration procedure uses a planar checkerboard that is arbitrarily positioned at unknown locations and orientations. The method can be applied to any number of cameras. The parameters of the calibration yield direct estimates of the positions and orientations of the four cameras as well as the focal-lengths of the lenses. These parameters are used to assess the quality of the calibration. The calibration allows us to perform accurate and consistent linear ray-tracing, which we use to triangulate and track fish inside the large tank.

2.1. FLEXIBLE CAMERA CALIBRATION TECHNIQUES

New studies in biophysics and fluid mechanics require the quantitative imaging of large-scale field experiments. Such studies include the large-scale Lagrangian tracking of bats and bird flocks [3, 4], super-large-scale particle image velocimetry measurements using natural snowfall [5] and recent advancements in tomographic-PIV [6].

Obtaining reliable two- and three-dimensional imaging data in these large field experiments is challenging and requires a camera calibration that is accurate down to the smallest physical length-scale of interest. Non-linear polynomial camera mappings [7–10] are often used in laboratory experiments [11], but their application at length-scales

Parts of this chapter have been published in Muller *et al.* [1] and is freely available through Tam and Muller [2]

beyond that of the laboratory is, in practice, limited. First, the size of the calibration target is limited, such that it only covers a small portion of the measurement. Second, the absence of conventional laboratory equipment, providing access to the measurement volume, does not support the accurate spatial positioning of the target, required in conventional calibration procedures.

In the present work, we combine the pinhole camera model [12] with non-linear polynomial camera mappings used in experimental fluid mechanics [7] to perform a multiple camera calibration over a large-scale measurement volume inside the tank of the aquarium located in the Rotterdam zoo. Our method integrates the use of the pinhole camera model with a non-linear camera mapping to correct for optical distortion across refractive interfaces [13]. Our approach uses the framework of projective geometry in computer vision [14] and applies advanced self-calibration techniques [15, 16].

Here we apply the planar checkerboard calibration technique by Zhang [17], see also: [18–22]. This approach eliminates the need to accurately position the calibration target, as required in conventional calibration procedures. Instead, the checkerboard calibration target is moved to arbitrary and unknown positions and orientations, here with the help of a team of divers. Second, by sequentially acquiring multiple calibration images while freely moving the calibration target, we achieve a camera calibration that spans over length scales much larger than the calibration target itself. This approach yields an accurate calibration over the measurement volume with a characteristic length scale on the order of several tens of meters.

We process the camera calibration in steps [23]. First, we correct for optical distortions [24] by rectifying the curved lines of the checkerboard images [25, 26]. Secondly, we perform a calibration based on a single view for each camera following Zhang [17]. Finally, we combine the single views and find the positions and orientations of the cameras over multiple views [27] and optimize the calibration for spatial accuracy and consistency between the different views.

The camera calibration yields accurate results. To assess the validity of the camera calibration, we compare the estimated effective focal-length obtained from it against the true value of the focal-length of the lenses. We quantify the spatial accuracy of the camera calibration, by computing the skewness of optical rays associated with the multiple views. Our calibration allows us to use linear ray-tracing [28] to track and triangulate multiple fish swimming over the entire visual depth of the tank. The method is versatile and can be implemented in field experiments over large length scales and for measurement volumes that are challenging to access experimentally.

2.2. CAMERA SETUP AND CALIBRATION PROCEDURE

We image inside the large tank of the aquarium in the Rotterdam zoo in a measurement volume of dimensions $\sim 10 \times 25 \times 6 \text{ m}^3$ (see Figure 2.1). We use a set of four 5.5 megapixel sCMOS cameras (LAVISION, GmbH) with wide-angle lenses of focal-length $f_{\text{lens}} = 24 \text{ mm}$ (NIKKOR AF-24mm) that cause significant variations in magnification over the large depth-of-field of $\text{DOF} \approx 25 \text{ m}$ [29].

The camera setup is positioned behind an acrylic window of thickness $\sim 50 \text{ cm}$. Optical distortions in the image plane are due to refraction at the water ($n_{\text{water}} = 1.363$) / acrylic ($n_{\text{acryl}} = 1.51$) and the acrylic/air ($n_{\text{air}} = 1.0003$) interfaces [30], where n is the re-

fractive index. The optical access is limited to the acrylic window, which constrains the spacing between the cameras to $\Delta H \approx 1 \text{ m}$ in height and $\Delta W \approx 6 \text{ m}$ in width, and limits the relative angles between the cameras from 5° to 20° (Figure 2.1).

To calibrate the camera setup we image a planar checkerboard calibration target of dimensions $1.5 \times 1.8 \text{ m}^2$ with 5×6 tiles [27] that are of area $A_{\text{tile}} = 30 \times 30 \text{ cm}^2$. This calibration target is moved within the aquarium by a team of divers that swim with the checkerboard under arbitrary and unknown positions and orientations throughout the aquarium.

2.2.1. IMAGE PROCESSING

The different images of the calibration target are processed to identify the curves and the nodes corresponding to the gridlines and intersections between the tiles of the checkerboard (Figure 2.2). In our application, using a checkerboard calibration target is advantageous over using a pattern of dots. This is because the image gradient obtained from a checkerboard determines grid points more accurately and robustly over the large depth-of-field of our experiment.

The calibration images are converted to the image gradient using a Savitsky-Golay image differentiation approach [31] to mark locations on the gridlines between the tiles. For each image, we then fit a set of polynomial curves $\gamma_i(t)$ to the $I = 9$ gridlines between the tiles of the checkerboards using the local intensity values from the image gradient. These fitting curves are written as $\gamma_i(t) = \sum_k \mathbf{a}_i^k t^{k-1}$, where \mathbf{a}_i^k are two dimensional vectors. Here the parameter t varies within the interval $t \in [0, 1]$ over the checkerboard image, such that $\gamma_i(t = 0)$ and $\gamma_i(t = 1)$ correspond to the beginning and end-points of the gridline of the checkerboard image, see the lines on Figure 2.2. At last, we find the $J = 20$ intersections between all the gridlines as a set of nodes \mathbf{x}_j in the image plane of each camera. Here $\mathbf{x}_j = [x_j \ y_j]^T$ with $(\bullet)^T$ the vector transpose, where the numbering $j = 1 \cdots J$ is consistent between the different camera views [27], see Figure 2.2.

2.2.2. DISTORTION CORRECTION

Following the path of an optical ray for a single camera in Figure 2.2, the linear path is refracted across the air/water interface [13]. This causes optical distortions in the image plane for each camera and therefore we rectify the image plane by dewarping the optical distortion. The coordinates $\mathbf{x} = [x \ y]^T$ in the image plane are mapped to distortion-corrected image coordinates $\hat{\mathbf{x}} = [\hat{x} \ \hat{y}]^T$ by determining a distortion mapping $\hat{\mathbf{x}} = m(\mathbf{x})$. Given the imaged medium (water) is linear, this mapping ensures that co-linear points positioned along a line in object space project as co-linear points in the dewarped image and therefore support linear ray-tracing. For moderate optical distortions, a polynomial distortion map [7] is sufficient. In this study, we write the distortion map as:

$$\hat{\mathbf{x}} = \mathbf{x} + \sum_k \mathbf{c}_k \phi^k(\mathbf{x}) = \mathbf{x} + \mathbf{c}_1 x^2 + \mathbf{c}_2 x y + \mathbf{c}_3 y^2 + \mathbf{c}_4 x^3 + \mathbf{c}_4 x^2 y + \mathbf{c}_5 x y^2 + \mathbf{c}_6 y^3 \quad (2.1)$$

The distortion map is determined by rectifying the curved gridlines in the N original calibration images. We follow Devernay and Faugeras [26] and minimize the percentage of deflection along the gridlines. We consider the nodes \mathbf{x}_j^n along a particular grid-

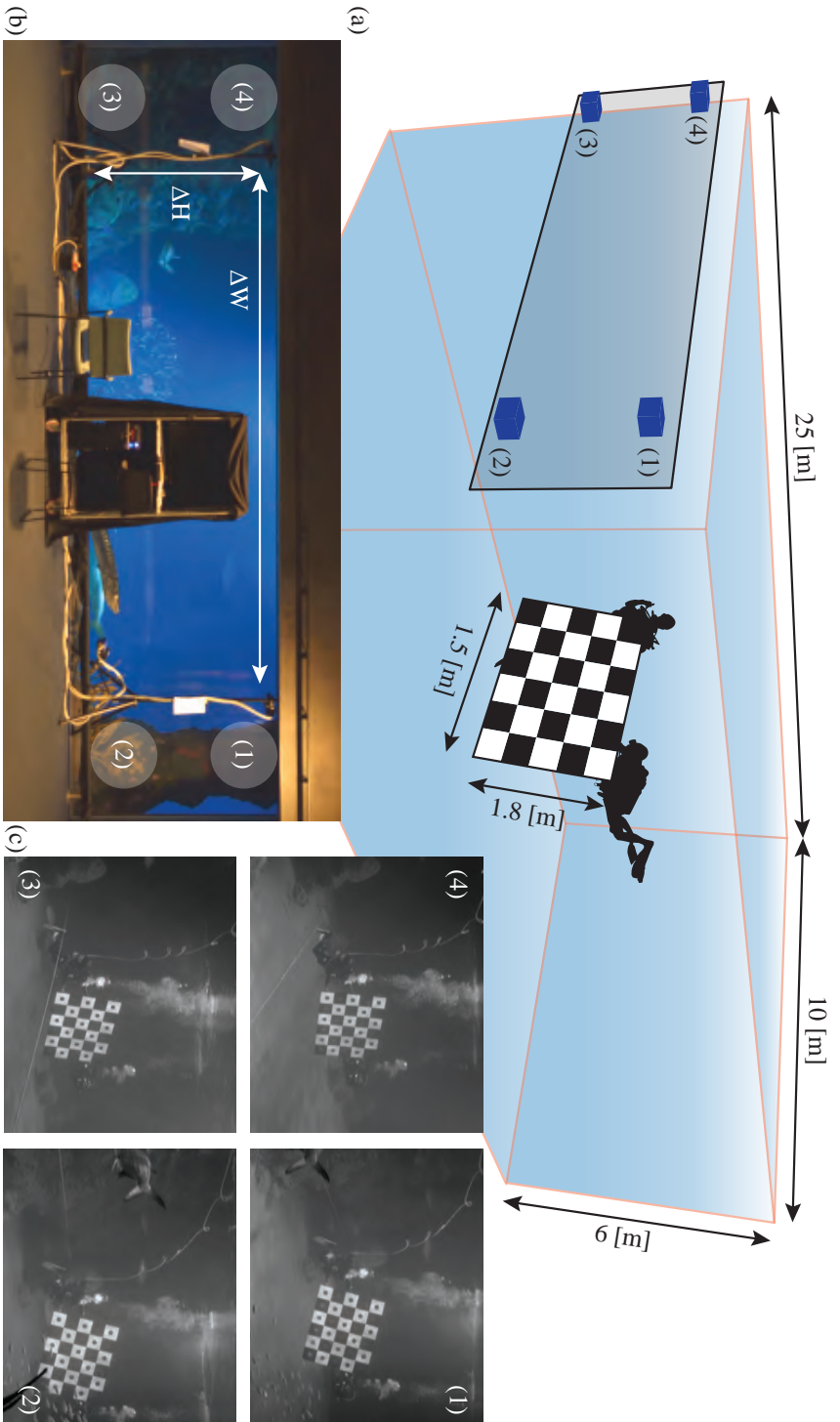


Figure 2.1: The four-camera setup at the Rotterdam zoo. a) Schematic representation of the large measurement volume of $\sim 10 \times 25 \times 6 \text{ m}^3$ along the DOF $\approx 25 \text{ m}$, including the flat checkerboard of dimensions $1.5 \times 1.8 \text{ m}^2$ that is positioned by a team of divers. b) Optical access through the large window spanning $2 \times 8 \text{ m}^2$ including the camera setup at a relative spacing of $\Delta H \approx 1 \text{ m}$ by $\Delta W \approx 6 \text{ m}$. c) An example of calibration images acquired while positioning the checkerboard.

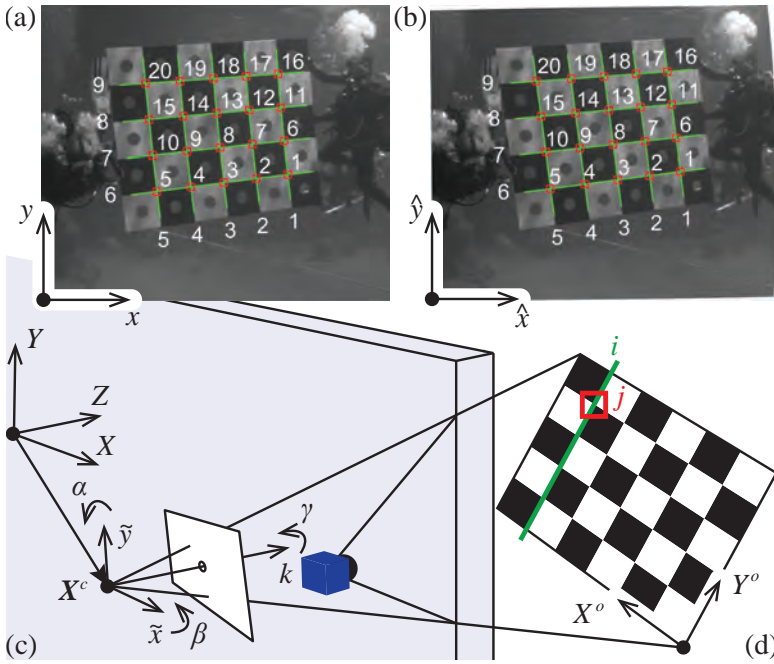


Figure 2.2: Image processing and the geometry of the optical path. a) Processed calibration image with the identified gridlines fitted as second-order polynomial curves (green lines) and the nodes at the gridline intersections (red squares). The gridlines are numbered from $i = 1$ to 9 and the nodes from $j = 1$ to 20. b) The dwarped calibration image corresponding to (a) in which the gridlines are rectified for minor optical distortion using the mapping of Equation 2.1. Supplementary-Figure A.1 provides an example of dewarping for severe optical distortion. c) The geometry of the optical path where the optical rays are refracted across the air-water interface (neglecting the acrylic window for simplicity) and the positioning of the (virtual-)camera coordinate system $[\tilde{x} \ \tilde{y} \ k]^T$ with camera center \mathbf{X}^c with respect to the world coordinates $[X \ Y \ Z]^T$. d) The local coordinate system X^o & Y^o and the indexing i for the gridlines and j for the locations of the nodes.

line $\gamma_i^n(t)$ and their images $\hat{\mathbf{x}}_j^n$ and $\hat{\gamma}_i^n(t)$ in the dwarped image-plane through the map $m(\mathbf{x})$. We fit a straight line $\hat{\ell}_i^n$ through the nodes $\hat{\mathbf{x}}_j^n$ and compute the point-line distance $d(\hat{\mathbf{x}}_j^n, \hat{\ell}_i^n)$. The parameters \mathbf{c}_k defining the distortion map are then determined by solving a minimization problem over all gridlines in all calibration images:

$$\min_{\mathbf{c}_k} \sum_{i,n} \sum_{\substack{\text{nodes } j \\ \text{along } \hat{\gamma}_i}} \frac{d(\hat{\mathbf{x}}_j^n, \hat{\ell}_i^n)^2}{\|\hat{\gamma}_i^n(1) - \hat{\gamma}_i^n(0)\|^2}. \quad (2.2)$$

This minimization problem can be solved efficiently using a steepest descent algorithm and numeric integration techniques described in Boyd and Vanderberghe [32]. This approach directly extends to larger optical distortions requiring more elaborate distortion models (see Appendix A.1 for the air/water interface and Supplementary-Figure A.1). An example of a dwarped image can be found in Figure 2.2.

2.2.3. CAMERA CALIBRATION AND PROJECTIVE GEOMETRY

We consider a physical point in the object domain \mathbf{X} of coordinates $\mathbf{X} = [X \ Y \ Z]^T$ in a world coordinate system and its projected image $\hat{\mathbf{x}} = [\hat{x} \ \hat{y}]^T$ in the dewarped image-plane of a single camera. The calibration is defined by the mapping function F , such that $\hat{\mathbf{x}} = F(\mathbf{X})$. Our method uses the framework of projective geometry to express the mapping function F and implicitly assumes a pinhole camera model. In the following, we outline the main notations used in projective geometry; a more complete introduction can be found in Hartley and Zisserman [14].

We make use of augmented vectors to represent points in both the image plane and the object domain. The coordinates in the dewarped image-plane $\hat{\mathbf{x}}$ are augmented to the ray-tracing vector $\tilde{\mathbf{x}}$ such that $\tilde{\mathbf{x}} = [k\hat{x} \ k\hat{y} \ k]^T$, where k is a scaling parameter in direction of the principle optical axis. The associated inverse function that projects $\tilde{\mathbf{x}}$ back to $\hat{\mathbf{x}}$ is defined as the projection $p(\tilde{\mathbf{x}}) = [\hat{x} \ \hat{y}]^T/k = \hat{\mathbf{x}}$. Similarly, the world coordinates \mathbf{X} are augmented to a homogeneous vector as $\tilde{\mathbf{X}} = [X \ Y \ Z \ 1]^T$ [14]. Using augmented vectors a geometric transformation, consisting of a rotation and a translation, is simply written as a matrix multiplication $[R \ \mathbf{t}]\tilde{\mathbf{X}}$, where R is a rotation matrix and \mathbf{t} is a translation vector.

With these notations, the mapping function can be written in the following form that is widely used in projective geometry [14]:

$$\hat{\mathbf{x}} = F(\mathbf{X}) = p(K[R \ \mathbf{t}]\tilde{\mathbf{X}}). \quad (2.3)$$

Here K is the 3×3 camera calibration matrix and $[R \ \mathbf{t}]$ is a 3×4 matrix, with R the 3×3 rotation matrix, and \mathbf{t} the 3×1 translation vector. The matrix K in Equation 2.3 has the following form:

$$K = \begin{bmatrix} \alpha_x & s & p_x \\ 0 & \alpha_y & p_y \\ 0 & 0 & 1 \end{bmatrix}, \quad (2.4)$$

where $\alpha_x = fr_x$ and $\alpha_y = fr_y$ are scale factors, with f the focal-length of the lens in millimeters (mm) and r_x and r_y the pixel pitch of the sCMOS sensor in pixel-per-millimeter (px/mm). s is the pixel skew, characterizing the angle between the x and the y pixel axes, and $[p_x \ p_y]^T$ are the coordinates of the principal point at the intersection between the optical axis and the dewarped image-plane [14]. The elements of K are often referred to as the intrinsic camera parameters, representing the characteristic properties of the camera itself [14], while $[R \ \mathbf{t}]$ are referred to as the extrinsic parameters representing the position of the camera with respect to the world coordinate system (Figure 2.2).

Together, K , R , and \mathbf{t} define the mapping function F of Equation 2.3 and have to be determined for each of the cameras separately. In the following, we use the superscript $c = 1 \cdots 4$ and the notations K^c , R^c , and \mathbf{t}^c , when we distinguish explicitly between the different cameras. We omit the superscript for clarity when no distinction between the cameras is needed; the details of the algorithms can be found in Appendix A.

2.2.4. SINGLE CAMERA CALIBRATION

First, the camera matrix K is determined for each of the four separate cameras by calibrating a single camera using the method developed by Zhang [17]. We consider a local coordinate system $\mathbf{X}^o = [X^o \ Y^o \ Z^o]^T$ attached to the planar checkerboard in the object

domain, where $Z^o = 0$ corresponds to the plane of the checkerboard. In this coordinate system, the J nodes at the intersections between the gridlines have known coordinates $\mathbf{X}_j^o = [X_j^o \ Y_j^o \ 0]^T$. The nodes \mathbf{X}_j^o are mapped to their images $\hat{\mathbf{x}}_j^n$ following the formalism used in Equation 2.3. This transformation can be written as $p(K[R^n \ \mathbf{t}^n]\tilde{\mathbf{X}}_j^o)$, where the rotation matrix R^n and translation vector \mathbf{t}^n characterize the position of the checkerboard in the object domain. Geometrically, this corresponds to a rotation and translation of the checkerboard plane in the object domain, followed by a projection on the image plane. The camera calibration matrix K and the positioning of the checkerboard by R^n and \mathbf{t}^n are determined following Zhang [17] and are refined by minimizing the following functional:

$$\min_{K, R^n, \mathbf{t}^n} \sum_{j,n} \left\| \hat{\mathbf{x}}_j^n - p(K[R^n \ \mathbf{t}^n]\tilde{\mathbf{X}}_j^o) \right\|^2. \quad (2.5)$$

2.2.5. MULTIPLE CAMERA CALIBRATION

To complete the calibration over the multiple cameras, we determine the rotation R^c and the translation \mathbf{t}^c representing the position of each of the cameras in the world coordinate system. R^c and \mathbf{t}^c correspond to the extrinsic camera parameters described in Section 2.2.3 and a first estimate is deduced directly from the calibration of single cameras performed in the previous step. Selecting two different calibrated cameras, we use the Kabsch algorithm [33] to estimate the relative positions of the two cameras by comparing the positions of the checkerboards by $R^{n,c}$ and $\mathbf{t}^{n,c}$ for these two views. Considering all camera pairs, we determine the relative positions between all the views and deduce a first estimate for R^c and \mathbf{t}^c ; see Appendix A.2 for detail. Next, for each of the N calibration images, we estimate position R^n and \mathbf{t}^n of the checkerboard in the world coordinate system. We do this by averaging the position estimates $R^{n,c}$ and $\mathbf{t}^{n,c}$ obtained from the four separate single-camera calibrations.

In the last step, we compute the final values for K^c , R^c , and \mathbf{t}^c by minimizing the reprojection errors from all cameras and calibration images, and using as initial conditions the camera matrices K^c obtained from Section 2.2.4, the positions R^c and \mathbf{t}^c obtained from the Kabsch algorithm and the estimates of the checkerboard positions R^n and \mathbf{t}^n . We define the reprojection error $\varepsilon_j^{n,c}$ for each of the N calibration images and in each camera view as:

$$\varepsilon_j^{n,c} = \frac{1}{\sqrt{\hat{\mathcal{A}}_j^{n,c}}} \left\| \hat{\mathbf{x}}_j^{n,c} - p \left(K^c [R^c \ \mathbf{t}^c] \begin{bmatrix} R^n & \mathbf{t}^n \\ \mathbf{0}^T & 1 \end{bmatrix} \tilde{\mathbf{X}}_j^o \right) \right\|. \quad (2.6)$$

The reprojection error $\varepsilon_j^{n,c}$ is normalized by $\hat{\mathcal{A}}_j^{n,c}$, which is the area in pixels of a single tile on the checkerboard projection in the dewarped image-plane (see Appendix A.3). Hence, $\varepsilon_j^{n,c}$ provides a measure of the error relative to the size of the checkerboard. This error is relatively independent of the location of the calibration target within the large depth of field and the positions of the cameras, and therefore, independent of the apparent size of the checkerboard in the image plane. The final parameters for the calibration function F for each view are obtained from the minimization of the following summation:

$$\min_{K^c, R^c, \mathbf{t}^c, R^n, \mathbf{t}^n} \sum_c \sum_{j,n} \left(\varepsilon_j^{n,c} \right)^2. \quad (2.7)$$

The resulting camera calibration is shown in Figure 2.3.

2.3. ASSESSMENT OF THE CALIBRATION METHOD

In the following, we evaluate the performance of the calibration. First, we report the extrinsic and intrinsic camera parameters from Table 2.1 and discuss their physical interpretation. Second, we assess the robustness and convergence of the method as a function of the number of calibration images used. Third, we study the spatial accuracy of the calibration and identify the sources of error.

2.3.1. INTRINSIC AND EXTRINSIC CAMERA PARAMETERS

First, we consider the numerical values of the extrinsic camera parameters obtained from calibration, see Table 2.1. As discussed in Section 2.2.3, these parameters characterize the spatial position and orientation of each camera. The reconstructed positions of the cameras are in agreement with the experimental setup, with cameras 4 and 1 positioned above cameras 3 and 2, and cameras 4 and 3 positioned on the left-hand side while cameras 1 and 2 are located on the right-hand side (as shown in Figure 2.1), see Table 2.1. Furthermore, the relative distances between cameras are also in agreement with the experimental scene as we find the horizontal distance between cameras $\Delta W \approx 5.6 \text{ m}$ and a vertical distance between cameras $\Delta H \approx 1.2 \text{ m}$, as deduced from Table 2.1. Likewise, the reconstructed camera orientations are consistent with the cameras on the right-hand side oriented with a positive angle α , while the cameras on the left-hand side are oriented with a comparable negative angle α .

In addition to reconstructing the position of the camera, the calibration procedure reconstructs the intrinsic camera properties, which we compare to the specification of the instrumentation. The coefficients of the camera calibration matrix K of Equation 2.4 are provided for each camera in Table 2.1. We focus on the values of the focal-length of the lenses and deduce an effective focal-length f_{eff} directly from the coefficients as:

$$f_{\text{eff}} = \sqrt{\frac{\alpha_x \alpha_y \tilde{J} \tilde{n}^2}{r^2}}, \quad (2.8)$$

where r is the resolution of the camera sensor (px/mm), which is known from the camera specifications, \tilde{J} represents a correction factor for the image expansion due to optical distortion (see Appendix A.4) and $\tilde{n} = n_{\text{air}}/n_{\text{water}}$ corrects for the magnification due to refraction at the air/water interface. Our calibration yields values for the effective focal-length of the four cameras of $f_{\text{eff}} = 23.73 \pm 0.82 \text{ mm}$. This reconstruction of the focal-length lies within 1–2% of the actual focal-length $f_{\text{lens}} = 24 \text{ mm}$ of the lenses that were used. Hence, we find that both the extrinsic and intrinsic camera parameters deduced from our calibration procedure are in agreement with the dimensions and characteristics of our experimental setup.

2.3.2. CONVERGENCE AND ROBUSTNESS

The camera calibration is obtained by minimizing the sum of the squared reprojection errors $\varepsilon_j^{n,c}$ over all four cameras, all N calibration images, and all nodes on the checkerboard, see Equation 2.7. The camera calibration converges to low values for $\varepsilon_j^{n,c}$ see

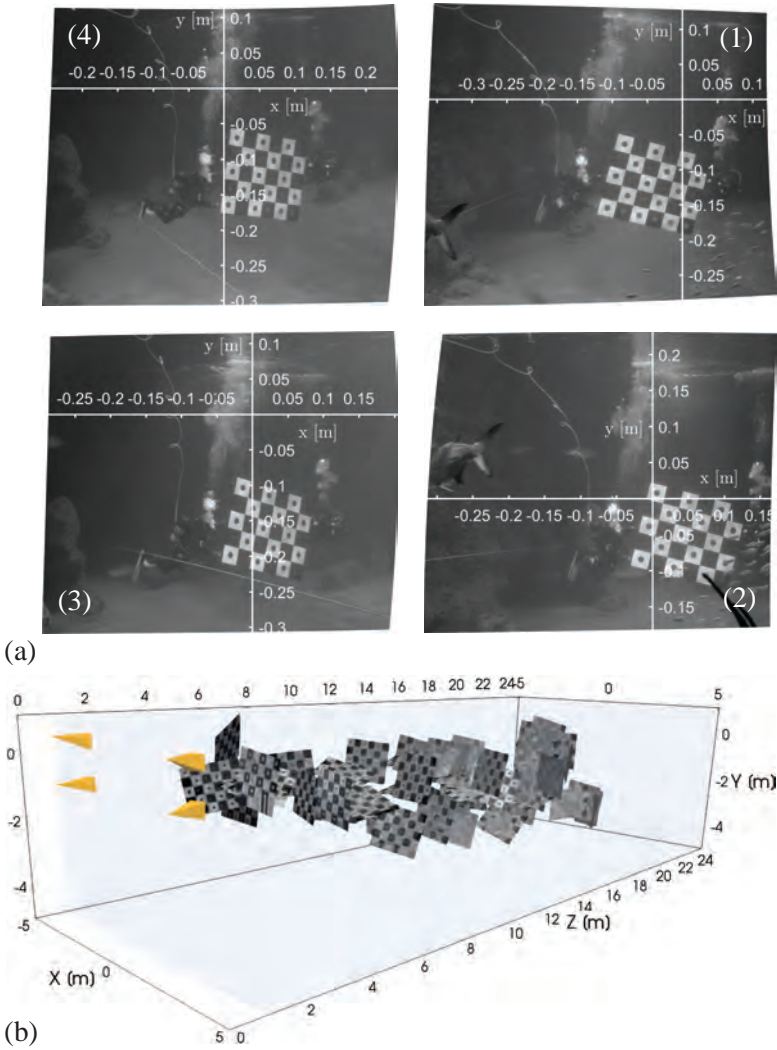


Figure 2.3: The resulting camera calibration. a) The calibrated views that include physical scales on a reference plane at $k = 1 m$ in the depth of field for each view. b) Three-dimensional reconstruction of a random selection of checkerboards used for the calibration, in yellow the reconstructed (virtual-)cameras in front of the acrylic window of Figure 2.1.

Camera		1	2	3	4
\tilde{J}	[-]	0.97	0.98	0.93	0.96
α_x	[px]	5166.3	5245.8	4982.9	5116.0
α_y	[px]	5056.3	5240.5	4941.3	5050.2
s	[px]	-48.5	-63.5	-189.4	-249.5
p_x	[px]	1888.8	1655.0	1419.6	1237.0
p_y	[px]	1488.0	980.0	1530.5	1552.8
X^c	[m]	2.873	2.878	-2.872	-2.87848
Y^c	[m]	0.617	-0.616	-0.658	0.657
Z^c	[m]	0.010	-0.010	0.009	-0.009
α	[°]	9.02	14.00	-13.04	-11.51
β	[°]	-5.18	-3.93	2.56	-5.19
γ	[°]	-2.45	-0.81	-2.29	0.76
f_{eff}	[mm]	23.91	24.66	22.67	23.68
$\varepsilon_j^{n,c}$	[%]	1.84	1.85	2.08	1.95
		± 1.57	± 1.64	± 1.72	± 1.54
$(\varepsilon_j^{n,c})^*$	[px]	1.63	1.72	1.85	1.84
		± 1.49	± 1.62	± 1.59	± 1.60
N	[#]	176	153	197	186

Table 2.1: Numerical values of the calibration parameters. From top to bottom: the expansions factor of the distortion mapping \tilde{J} , the intrinsic camera properties from the matrix K , the extrinsic camera positions X , Y and Z and orientations in pitch-yaw-roll angles α , β , and γ , see Figure 2.1 and Figure 2.2. The effective focal-lengths f_{eff} deduced from K with Equation 2.8, the reprojection errors $\varepsilon_j^{n,c}$ in percentage and equivalent pixel-dimensions $(\bullet)^*$, and the total number of calibration images N used for each camera.

Table 2.1. Here, the average normalized reprojection error is on the order of $\varepsilon_j^{n,c} \sim 2\%$ of the size of a checkerboard tile, which corresponds to an error of less than 1 *cm*.

The camera calibration requires a minimum of two non-coplanar checkerboard images [17]. Increasing the number of calibration images increases the sampling of the measurement volume and, therefore, improves the reliability of the calibration. We further characterize the performance of the method as a function of the number of calibration images used, by randomly selecting different subsets of checkerboard images.

We first consider the effective focal-length f_{eff} of Equation 2.8 deduced from the matrix K to characterize the quality of the position in space of the checkerboards and the cameras. In Figure 2.4, we select different subsets of calibration images ranging from $N = 2$ to $N = 50$ images and compute f_{eff} from the associated calibration. Figure 2.4a represents the ratio between f_{eff} and f_{lens} as a function of N . With a low number of $N = 2$ to 10 calibration images, the ratio $f_{\text{eff}}/f_{\text{lens}}$ is far from one and the focal-length is under- and overestimated by 50 %, indicating an unreliable calibration. Increasing the number of calibration images to $N = 15$ shows that the estimated focal-length f_{eff} approaches f_{lens} and represents a clear improvement of the calibration. Further increasing

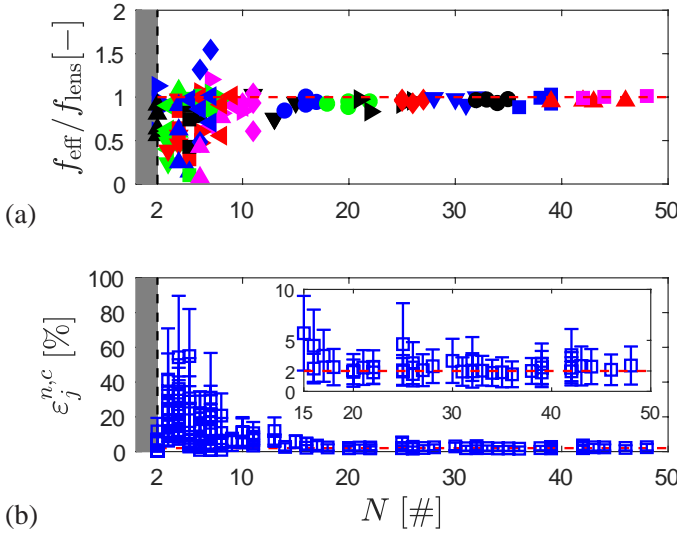


Figure 2.4: Quality assessment of the camera calibration procedure for different subsets of randomly selected calibration images. a) The ratio in estimated focal-length and the true focal-length of the used lenses $f_{\text{eff}}/f_{\text{lens}}$ as a function of the number of calibration images N . Different symbols and colors indicate different selections of images. b) Averaged reprojection errors $\epsilon_j^{n,c}$ for each camera as a function of N . The error bars indicate the standard deviation of the error per camera.

N beyond $N = 15$, the ratio $f_{\text{eff}}/f_{\text{lens}}$ does not significantly converge further (Figure 2.4a).

Secondly we consider the reprojection errors $\epsilon_j^{n,c}$ in Figure 2.4b. For a low number of $N = 2$ to 10 calibration images, the average reprojection error is as high as $\epsilon_j^{n,c} \sim 50$ to 60%. Increasing the number of calibration images from $N = 15$ to 50 shows an additional decrease of the normalized reprojection error from $\epsilon_j^{n,c} \sim 5$ to 2%, see Figure 2.4b and inset. This shows that 15 calibration images are sufficient to achieve a valid calibration. Further increasing the number of calibration images improves the convergence for the camera calibration while the ratio $f_{\text{eff}}/f_{\text{lens}}$ remains at a value close to 1.

2.3.3. SPATIAL ACCURACY OF THE CAMERA CALIBRATION

By inverting the camera matrix \mathcal{K} , one can directly associate an optical ray in the object domain to a point in the dewarped image-plane. For an ideal calibration, the four optical rays associated with the images of the same point on each of the four cameras should intersect at a unique location in the object domain. In practice, the four optical rays are skew lines and do not intersect at a single point. Here, we characterize the spatial accuracy of our camera calibration by estimating the skewness among the four optical rays.

For this, we use the nodes identified at gridline intersections on the N calibration images. We proceed by evaluating the four optical rays associated with each node of each calibration image. We then triangulate the location of each node by finding the point \mathbf{X}_j^n in the object domain that minimizes the sum of the squared distances from the point to the four optical rays. We report for each node the skewness s_j^n as the average distance from the triangulated location \mathbf{X}_j^n to the four optical rays (see Appendix A.5 for more detail).

The calibration images were acquired over the entire depth of the tank and used to characterize the spatial accuracy, by reporting the skewness as a function of the position

along the Z -axis of the world coordinate system, see Figure 2.5a. We find the skewness to be mostly uniform over the large depth of the measurement volume $Z = 5$ to $25m$. Our calibration yields a high spatial accuracy characterized by an average skewness of less than 1 cm . Only a slight increase in the skewness can be observed towards the back of the aquarium, although the average skewness still remains below 1 cm . This small increase is due to the decrease in spatial resolution and the decrease in angles between the optical path from the different views.

The variation in skewness over the height and width of the tank is represented in Figure 2.5b and c. Figure 2.5b is a map of the skewness in a XY -plane at the front of the aquarium, while Figure 2.5c provides a similar map at the back of the aquarium. Both are qualitatively similar and the skewness remains small over the depth of the tank. For reference, Figure 2.5d and e show the sampling density, which indicates the number of checkerboard images that were used at a location to compute the calibration. It is noteworthy that the center of the tank was better sampled than the sides and the bottom. We find that the skewness, and hence the spatial accuracy, is relatively constant over a large part of the measurement volume, but increases towards the edges of the tank. This is likely a result of the lower sampling away from the camera center, as well as unresolved optical distortions at the edges of the image plane.

2.4. APPLICATION TO FIELD EXPERIMENTS

We demonstrate the effectiveness of the calibration method by three-dimensional measurements in the large aquarium at the Rotterdam Zoo. We begin by focusing on an element that is easily identifiable on each camera view and shows that we can accurately triangulate the position. We end our validation by tracking the three-dimensional position of fish of various sizes that are freely swimming over the depth of the tank.

Large predatory fish in the aquarium, such as sharks, swim through the entire aquarium. They provide a good target to evaluate the robustness of the camera calibration as their sharply tipped fins provide easily recognizable and well-defined features. Figure 2.6 shows how accurately such features can be triangulated with our calibration method. We first identify the vertex of the right-hand side pectoral fin of a shark on each camera view. Similar to Section 2.3.3, we directly associate the vertices, identified on each of the four images, with four optical rays in the object domain. We triangulate the position of the vertex and find a skewness of only 0.35 cm , which demonstrates the accuracy of the method. This small skewness is illustrated in Figure 2.6 where, for each camera view, the optical rays associated with the other camera views are projected on the image plane onto the epipolar lines [14]. The epipolar lines intersect nearly perfectly at the identified vertex of the shark fin. The inset in Figure 2.6 presents a closeup view from which one can infer the reprojection error from the slight skew between the optical rays. This associated reprojection error is of only 1.11 px .

Further, we demonstrate that our calibration supports the tracking of several fish simultaneously over large distances by tracking a small group of six tuna fish, see Figure 2.7. By triangulation, we reconstruct the three-dimensional time-resolved position of the group, see Figure 2.7b. Using an in-house automated tracking code, we track the group of six individual fish (tuna) swimming away from the cameras over a large distance of 7 m . Together with the triangulated shark fin, this experiment demonstrates the

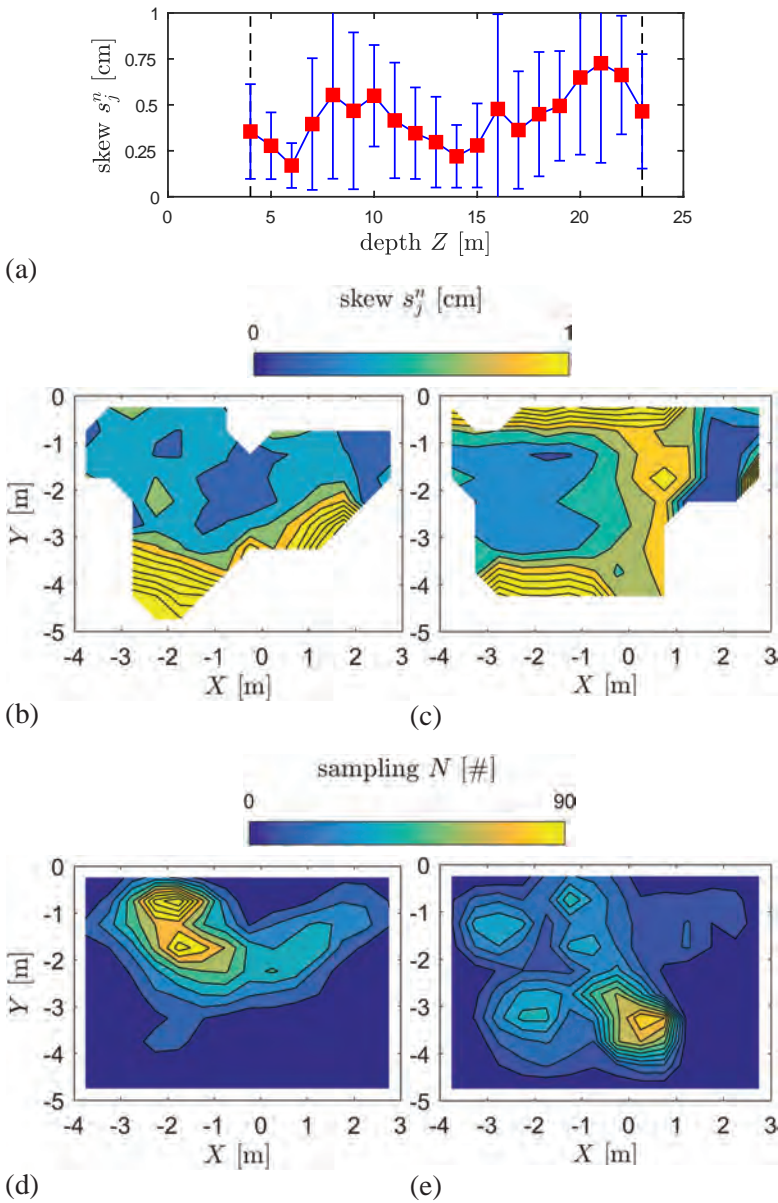
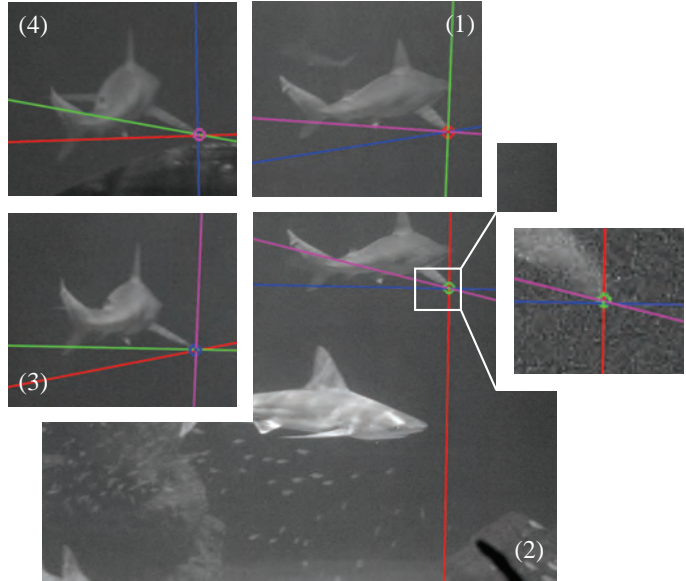


Figure 2.5: Spatial accuracy of the camera calibration. a) The average back-projection error in [cm] over the depth of the tank Z . b) The back-projection error over the width and height of the measurement volume at the front of the tank from $Z = 4$ to $Z = 17$ m. c) The back-projection error at the back of the tank from $Z = 17$ to $Z = 24$ m. d and e) The sampling density of checkerboards associated with (b) and (c), respectively.

Figure 2.6: Triangulation of the vertex of a shark fin. For each camera view: the point corresponding to the vertex of the shark fin is identified with a marker, while the three lines correspond to the epipolar lines associated with the three markers of the remaining three camera views. The color coding is consistent across the multiple views, for example, the vertex on camera 1 is identified with a red marker and the epipolar lines associated with this point in camera 2,3,4 are red. Likewise, the vertex on camera 1 is identified with a red marker and the epipolar lines associated with this point in camera 2,3,4 are respectively represented in green, blue, and magenta. The inset on camera 2 zooms on the vertex of the fin and shows that the epipolar lines intersect at pixel accuracy.



robustness and accuracy of the calibration and its potential use in large-scale field experiments. The calibration supports accurate triangulation over a large distance along the depth of field. This makes it of interest to further applications for the tracking of particles [34, 35], birds [4], insects [36], fish and other animals, and the study of fluid motion using tomographic methods [37] for large scale field experiments.

2.5. CONCLUSION

Here, we have described and characterized a versatile, accurate, and robust calibration method, which supports the three-dimensional tracking and triangulation of multiple fish. Our method is of particular interest to large-scale field experiments; when spatial access to the measurement volume is limited and laboratory equipment to precisely position the target cannot be installed. The method does not require a large calibration target to be moved with known displacements. Rather, we use a freely moving checkerboard calibration target, which is much smaller than the measurement volume itself. The calibration mapping uses the framework of projective geometry, which assumes linear ray-tracing. It combines a pinhole camera model for linear ray-tracing, with non-linear camera mappings commonly used in experimental fluid mechanics to correct for optical distortion. All the algorithms necessary for the implementation of the calibration method are described here with details provided in Appendix A.

The calibration method has been implemented to obtain an accurate and consistent multiple-view camera calibration in the large-scale aquarium of the Rotterdam Zoo. Here, the calibration target was positioned arbitrarily by a team of divers. We have char-

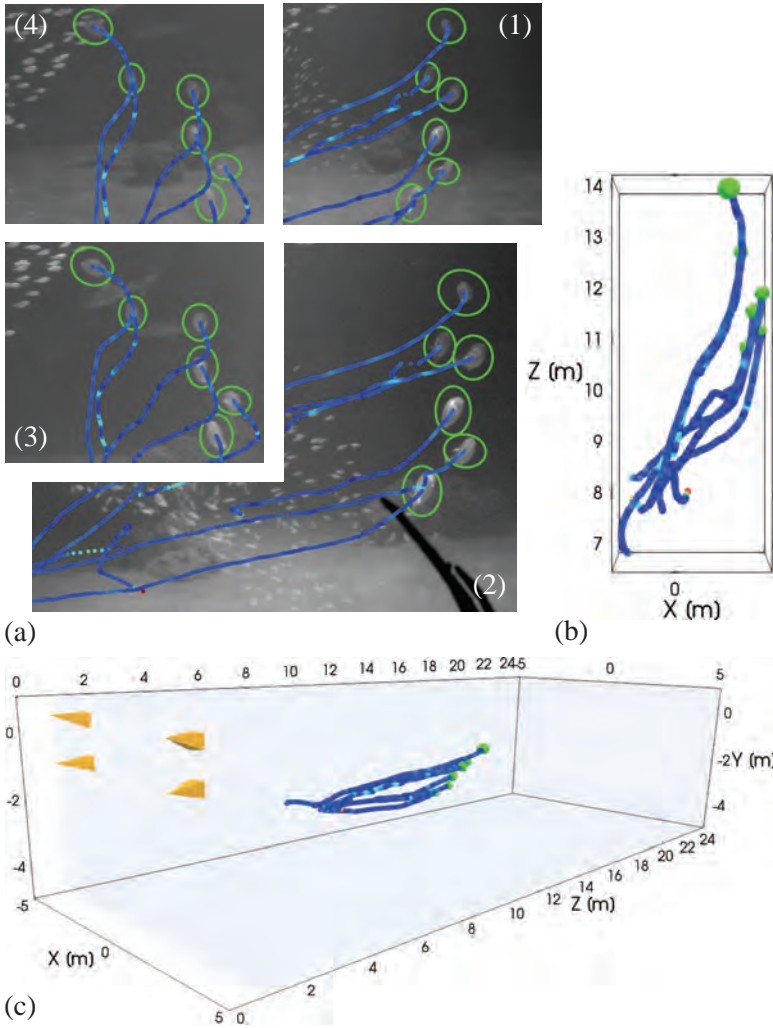


Figure 2.7: Tracking and triangulation of a group of tuna fish inside the measurement volume. a) The group of tracked tuna fish in the image plane. b) Top view of the tuna fish swimming over a distance of $\sim 7\text{ m}$ within the depth of the tank. c) The three-dimensional reconstruction of the fish swimming in object space including the camera position of Figure 2.3. In all visualizations, the color code of the tracks corresponds to the linear velocity in object space.

acterized the spatial accuracy of the calibration to be less than 2% of the size of a checkerboard tile, corresponding to 1 *cm* over the entire measurement volume that spans several tens of meters. When correcting for the difference in the refractive index of air and seawater, we find that our method reconstructs both the camera position and the intrinsic properties of the camera such as the focal-lengths of the lenses. Selecting different subsets of calibration images in a quality assessment, we show that in our case 15 calibration images are sufficient to achieve a valid calibration. Increasing the number of checkerboard images and better sampling the measurement volume further improves spatial accuracy. The resulting camera calibration allows accurate imaging and three-dimensional tracking over a large measurement volume, here with application to biological fluid mechanics and the tracking of fish.

REFERENCES

- [1] K. Muller, C. K. Hemelrijk, J. Westerweel, and D. S. Tam, *Calibration of multiple cameras for large-scale experiments using a freely moving calibration target*, Experiments in Fluids **61** (2020), 10.1007/s00348-019-2833-z.
- [2] D. Tam and K. Muller, *Open-source package for the Calibration of Multiple Cameras for Large-Scale Experiments Using a Freely Moving Calibration Target*, (2019).
- [3] D. H. Theriault, N. W. Fuller, B. E. Jackson, E. Bluhm, D. Evangelista, Z. Wu, M. Betke, and T. L. Hedrick, *A protocol and calibration method for accurate multi-camera field videography*, Journal of Experimental Biology **217**, 1843 (2014).
- [4] A. Attanasi, A. Cavagna, L. Del Castello, I. Giardina, A. Jelić, S. Melillo, L. Parisi, F. Pelacini, E. Shen, E. Silvestri, and M. Viale, *GReTA-A Novel Global and Recursive Tracking Algorithm in Three Dimensions*, IEEE Transactions on Pattern Analysis and Machine Intelligence **37**, 2451 (2015).
- [5] M. Toloui, S. Riley, J. Hong, K. Howard, L. P. Chamorro, M. Guala, and J. Tucker, *Measurement of atmospheric boundary layer based on super-large-scale particle image velocimetry using natural snowfall*, Experiments in Fluids **55**, 1736 (2014).
- [6] C. Jux, A. Sciacchitano, J. F. Schneiders, and F. Scarano, *Robotic volumetric PIV of a full-scale cyclist*, Experiments in Fluids **59**, 1 (2018).
- [7] S. M. Soloff, R. J. Adrian, and Z. C. Liu, *Distortion compensation for generalized stereoscopic particle image velocimetry*, Measurement Science and Technology **8**, 1441 (1997).
- [8] B. Wieneke, *Stereo-PIV using self-calibration on particle images*, Experiments in Fluids **39**, 267 (2005).
- [9] B. Wieneke, *Volume self-calibration for 3D particle image velocimetry*, Experiments in Fluids **45**, 549 (2008).
- [10] B. Wieneke, *Improvements for volume self-calibration*, Measurement Science and Technology **29** (2018), 10.1088/1361-6501/aacd45.
- [11] M. Kühn, K. Ehrenfried, J. Bosbach, and C. Wagner, *Large-scale tomographic particle image velocimetry using helium-filled soap bubbles*, Experiments in Fluids **50**, 929 (2011).
- [12] R. Y. Tsai, *A Versatile Camera Calibration Technique for High-Accuracy 3D Machine Vision Metrology Using Off-the-Shelf TV Cameras and Lenses*, IEEE Journal on Robotics and Automation **3**, 323 (1987).
- [13] J. Belden, *Calibration of multi-camera systems with refractive interfaces*, Experiments in Fluids **54** (2013), 10.1007/s00348-013-1463-0.
- [14] R. Hartley and A. Zisserman, *Multiple view geometry in computer vision*, 2nd ed. (Cambridge University Press, Cambridge, 2004).

- [15] T. Svoboda, D. Martinec, and T. Pajdla, *A convenient multicamera self-calibration for virtual environments*, Presence: Teleoperators and Virtual Environments **14**, 407 (2005).
- [16] R. Shen, I. Cheng, and A. Basu, *Multi-Camera Calibration Using a Globe*, in *8th Workshop on omnidirectional vision (OMNIVIS, Marseille, France, 2008)*.
- [17] Z. Zhang, *A flexible new technique for camera calibration*, IEEE Transactions on Pattern Analysis and Machine Intelligence **22**, 1330 (2000).
- [18] Z. Zhang, *A Flexible New Technique for Camera Calibration*, Tech. Rep. 2 (FEBRUARY, 1975) (1998).
- [19] Z. Zhang, *Flexible camera calibration by viewing a plane from unknown orientations*, in *Proceedings of the Seventh IEEE International Conference on Computer Vision*, Vol. 1 (IEEE, Kerkyra, Greece, 1999) pp. 666–673.
- [20] P. Sturm and S. Maybank, *On Plane-Based Camera Calibration: A General Algorithm, Singularities, Applications*, in *Proceedings. 1999 IEEE Computer Society Conference on Computer Vision and Pattern Recognition (Cat. No PR00149)* (IEEE, Fort Collins, United States, 1999) pp. 432–437.
- [21] J. F. Menudet, J. M. Becker, T. Fournel, and C. Mennessier, *Plane-based camera self-calibration by metric rectification of images*, Image and Vision Computing **26**, 913 (2008).
- [22] J.-Y. Bouguet, *Camera Calibration Toolbox for Matlab*, (2015).
- [23] J. Heikkila and O. Silven, *Four-step camera calibration procedure with implicit image correction*, in *Proceedings of the IEEE Computer Society Conference on Computer Vision and Pattern Recognition* (1997) pp. 1106–1112.
- [24] J. G. Fryer and D. C. Brown, *Lens distortion for close-range photogrammetry*, Photogrammetric Engineering & Remote Sensing **52**, 51 (1986).
- [25] B. Prescott and G. F. Mclean, *Line-Based Correction of Radial Lens Distortion*, Graphical Models and Image Processing **59**, 39 (1997).
- [26] F. Devernay and O. Faugeras, *Straight lines have to be straight*, Machine Vision and Applications **13**, 14 (2001).
- [27] A. Geiger, F. Moosmann, Car, and B. Schuster, *Automatic camera and range sensor calibration using a single shot*, in *Proceedings - IEEE International Conference on Robotics and Automation* (2012) pp. 3936–3943.
- [28] T. L. Hedrick, *Software techniques for two- and three-dimensional kinematic measurements of biological and biomimetic systems*, Bioinspiration and Biomimetics **3** (2008), 10.1088/1748-3182/3/3/034001.
- [29] R. Adrian and J. Westerweel, *Particle Image Velocimetry* (Cambridge University Press, Cambridge, 2011).

- [30] A. Sedlazeck and R. Koch, *Perspective and non-perspective camera models in underwater imaging - Overview and error analysis*, in *Outdoor and large-scale real-world scene analysis*, Vol. 37 (Springer, Berlin, 2012) pp. 212–242.
- [31] P. Meer and I. Weiss, *Smoothed differentiation filters for images*, *Journal of Visual Communication and Image Representation* **3**, 58 (1992).
- [32] S. Boyd and L. Vanderberghe, *Convex Optimization*, 1st ed., 471 (Cambridge University Press, Cambridge, 2004).
- [33] W. Kabsch, *A discussion of the solution for the best rotation to relate two sets of vectors*, *Acta Cryst.* **32**, 922 (1976).
- [34] D. Schanz, A. Schröder, S. Gesemann, and B. Wieneke, *'Shake the box': Lagrangian particle tracking in densely seeded flows at high spatial resolution*, in *9th International Symposium on Turbulence and Shear Flow Phenomena*, Vol. 3 (Melbourne, 2015).
- [35] D. Schanz, S. Gesemann, and A. Schröder, *Shake-The-Box: Lagrangian particle tracking at high particle image densities*, *Experiments in Fluids* **57**, 1 (2016).
- [36] K. Van Der Vaart, M. Sinhuber, A. M. Reynolds, and N. T. Ouellette, *Mechanical spectroscopy of insect swarms*, *Science Advances* **5**, 1 (2019).
- [37] G. E. Elsinga, F. Scarano, B. Wieneke, and B. W. Van Oudheusden, *Tomographic particle image velocimetry*, *Experiments in Fluids* **41**, 933 (2006).

3

VOLUMETRIC TRACKING OF FISH IN A LARGE SCHOOL

In this chapter, we introduce the methodology for time-resolved volumetric tracking of fish in a large school, over a large distance. Our approach combines new developments from tracking animals in the field with techniques from experimental fluid mechanics to track passive tracers in a flow. In particular, we include the directional dependent projection of the fish in the different camera views and present a full integration of projective geometry starting from the image processing. This makes the three-dimensional tracking robust against variations in the reprojection error and other errors from the calibration, here imaging at limited camera angles and baselines. We present all the steps involved to identify fish images on the different camera views, in a complex underwater environment. We match fish across different viewing angles and compute a best-fit object triangulation, taking into account the presence of large occlusions from solitary predators. Subsequently, we integrate the fish tracking in the different camera views with the tracking in the object domain to optimize for trajectories that remain in a best-fit correspondence. Finally, we characterize the reliability of our tracking methods. We investigate the operating conditions in terms of the image density by a 'fish-image-per-pixel' and time resolution by a 'fish-swim-per-frame'. We study the probability of tracking individual fish into the next frame and extract a tracking efficacy metric that quantifies the percentage of the school that remains tracked over a number of frames. Our methods are scalable for any number of views and for tracking large ensembles of objects over large distances. The current work applies equally to the general tracking of (bio-)active particles such as microorganisms. It contributes to the tracking of elongated objects with directional dependence. All algorithmic detail is given in the appendices.

Parts of this chapter have contributed to Buchner *et al.* [1] for the tracking of bio-active micro-algae in a suspension.

3.1. ANIMAL TRACKING AND VOLUMETRIC IMAGING FLUIDS

The application of automated video tracking to reconstruct the time-resolved, three-dimensional motion of animal groups has gained much attention in recent years in the study of collective animal behavior. For example, the three-dimensional tracking of swarming insects such as fruit flies [2–6] and midges [7, 8], zooplankton and the surrounding fluid [9], the swimming of Antarctic krill in schools [10], the collective flight of bats [11–13], and in particular, the highly organized maneuvering of birds in a giant flock [14, 15]. Such studies are of widespread interest in bio- and soft matter physics and include contributions such as open-source toolbox implementations [16], and online available data sets [17].

Only a few existing studies have performed the fully three-dimensional tracking of animal groups in a large-scale field experiment [13, 15, 18]. Such contributions are not only challenged by the number of animals to track but also the increasing dimensions of the group, and new methods are continuously developed [19–21]. Interestingly, despite few available works in a limited laboratory setting [22–26], the application of three-dimensional imaging remains absent for realistically sized fish schools in an underwater environment within the order of a few thousands of individuals.

Whether it be the tracking of particles in a cell [27, 28] or passive tracers carried with the turbulent motion of a fluid [29], image-based particle tracking techniques are at the heart of three-dimensional imaging in experimental fluid mechanics [30, 31]. The past decades have seen an acceleration in the development of three-dimensional particle tracking algorithms [32–35] with different algorithmic strategies [36–38], tomographic particle image velocimetry [39–41], the time-resolved tracking of dense suspensions [42, 43], the extraction of accurate velocimetry data [44, 45], new iterative matching schemes [46], application of learning methods [47], open-source implementation [48], real-time tracking [49], and recent improvements [50–52]. Altogether, with the increasingly greater availability of computational resources and improved camera equipment, such different implementations have largely extended early photogrammetric work [53–55].

In particular, the accurate tracking of large collections of 10000 to 100000 particles in a suspension has been much popularized with the introduction of the ‘Shake-the-Box’ algorithm [42, 43]. This work outlines an elaborate ‘Lagrangian particle tracking’ methodology starting from advances in three-dimensional particle tracking [32–35] and motion-enhanced tomographic methods [56–58] to remove so-called ‘ghost-particle’ reconstructions [59] that decorrelate over time. Different from tomographic techniques [39, 40], which are based on an object intensity value reconstruction [60], the ‘shaking’ approach builds forward on iterative particle triangulation schemes [61] that bypass voxelization of empty volumes of space, and ease the fitting of trajectories [34, 35] to include the time-domain in the object position.

This approach, its extension [51, 62] and related works [46, 48, 52] have particularly focused accurate tracking of particle images at high image densities ranging from 0.05 up to a reported 0.125 ‘particle-per-pixel’ (ppp). Such image densities are of most importance to sample the smallest length-scale in the fluid and are much greater than early works [53–55] below ≤ 0.005 ppp, while extending beyond tomographic methods [39, 40], which are reported reliable up to ~ 0.05 ppp. However, implementations extensively rely on subpixel accurate (self-)calibration techniques [63–65], typically below

0.4 pixels, and the augmentation of an optical transfer function [66] to correct non-uniformity in focus, and astigmatism of the underlying optics, and their application beyond the lab environment remains scarce [67].

On the other hand, existing works in animal tracking have focused on large-scale applications [13, 15, 18] and resolving occlusions [4, 11, 12] using integer programming. Resolving occlusions is vital to the extraction of long time series over large distances as animals are likely to cluster together for long time periods. Disregarding questions of the resolution, such as pixel-by-pixel particle projections [30] against full animal silhouettes [14], the tracking of animals in the field [13, 15, 18] may yet be regarded successful at a considerably lower optical density than in fluid mechanics [43, 51, 52] by visual comparison. Furthermore, algorithmic implementation [4, 11, 12] and architectures [15] are yet limited in advanced trajectory smoothing and differentiation techniques.

In this work, we combine advances from experimental fluid mechanics [43] with methodology from the field [15] to track the motion of a large school of ± 2000 *Harengula clupeiola* (false herring) in three dimensions. Starting from the image processing, we fully integrate the framework of projective geometry [68] using dual-space geometry [69]. This naturally embeds an optical transfer [66] for a pinhole camera and includes the directional (anisotropic) projection of the fish by their position and orientation, without the need to fulfill (in-practical) calibration requirements. In this way, we normalize the resolution of the images in the presence of considerable optical density. We show that our approach relaxes restrictive constraints on subpixel reprojection errors to a ‘sub-fish’ correspondence that is free to extend over several pixels and allows the inclusion of known errors from the calibration.

Imaging underwater inside the large ocean aquarium at the Rotterdam zoo, we explain all steps to remove and suppress background artifacts. We use smoothing and differentiation methods common to image-processing [70] to identify and extract the elliptical fish images over multiple scales [71] using a cascade of simple generic image filters [72]. Subsequently, we match fish between views and use an integer assignment [2, 15] to find a best-fit object triangulation in face of missing data from large occlusion by predator fish. We then simultaneously track fish in the image plane and object space. We extend our solution strategy to track fish that remain in a best-fit correspondence and integrate a generic trajectory model [43, 48]. We demonstrate that tracking fish forward, backward, and again forward in time is crucial to the extraction of long trajectories. Finally, we explain the steps in post-processing the tracking data.

The goal of this chapter is to extract reliable fish tracking data from imaging inside a large-scale underwater environment. Therefore we end this chapter by characterizing the performance of our tracking methods. First, we quantify the variation in the reprojection error and the extraction of long trajectory time series against the main input parameters from the image processing. Secondly, we compute the probability of tracking into the next frame and present boundaries in tracking reliability in terms of ‘fish-image-per-pixel’ and a ‘fish-swim-per-frame’. Finally, we extract a single ‘tracking efficacy’ parameter [30] for the percentage of the school that remains tracked and present an overview of the quality of the fish tracking. The methods described here are as well applicable to tracking bio-active microorganisms in a suspension [1] and contribute to tracking ellipsoidal objects in a fluid.

3.2. IMAGING AN UNDERWATER ENVIRONMENT

Using the fully calibrated setup of sCMOS cameras described in Chapter 2, we image a large school of ± 2000 *Harengula clupeiola* (false herring) inside the large ‘Oceanium’ aquarium at the Rotterdam zoo. The cameras are synchronized through a programmable timing unit (PTU, LAVISION GmbH) and image at limited camera angles and baselines (down to $\sim 5^\circ$ and ~ 1 m). Typical images acquired by the different views for a milling fish school are found in Figure 3.1a and snapshots for a rapid escape in Figure 3.1b.

Multiple artifacts are present in the images. Such include a non-uniform illumination throughout the measurement volume, a complex image background composed of a sand floor, rocks and reflections at the water surface, and multiple species of fish with varying sizes and shapes. We first analyze these artifacts and associated image quality in greater detail.

3.2.1. DATA ACQUISITION AND IMAGE QUALITY

All data acquisition has been carried out in the dark to minimize reflections on the window that provides the optical access (Chapter 2). To capture the rich dynamics displayed by the fish, the image data have different frame rates. The frame rate, in turn, influences the exposure time and thereby the dynamic range and signal-to-noise ratio for the recordings. Hence, all recordings do not have optimal and predetermined image contrast as is common practice in ‘Particle Image Velocimetry’ [30].

LIGHTING CONDITIONS

The calibration of Chapter 2 corrects the optical distortion across the air/glass/water interfaces and compensates for the lighting on the image sensor (Appendix A.4). However, several other sources of non-uniformity in the lighting conditions remain present. The aquarium is illuminated from above and includes multiple sources of LED light that can be influenced by the net power frequency of 50 Hz. Moreover, the refraction of light by surface waves causes uneven illumination below the water surface. This results in light rays that are swept through the measurement domain and range in strength by the water turbidity, see the orange marking in Figure 3.1a.

COMPLEX BACKGROUND

Imaging inside the Ocean aquarium presents challenges compared to a controlled laboratory experiment. In Figure 3.1a we label several complex background artifacts. Firstly, we mark multiple rocks by the yellow dashes which compose a stationary background where bright reflections may later result in spurious fish identifications. Secondly, the sand on the floor of the tank appears bright, while the surrounding walls in the back of the tank appear dark and drastically affect the image contrast. Finally, water waves present surface reflections and project bright spots on the sand floor, see the blue marking in view (3), and as well illuminate part of the patterned ‘sea bed’ in view (4).

3.2.2. FISH IMAGE DATA

The harengula are among the smallest fish inside the aquarium besides other larger fish. In Figure 3.2 we present an elaborate overview of recorded fish images. Due to the com-

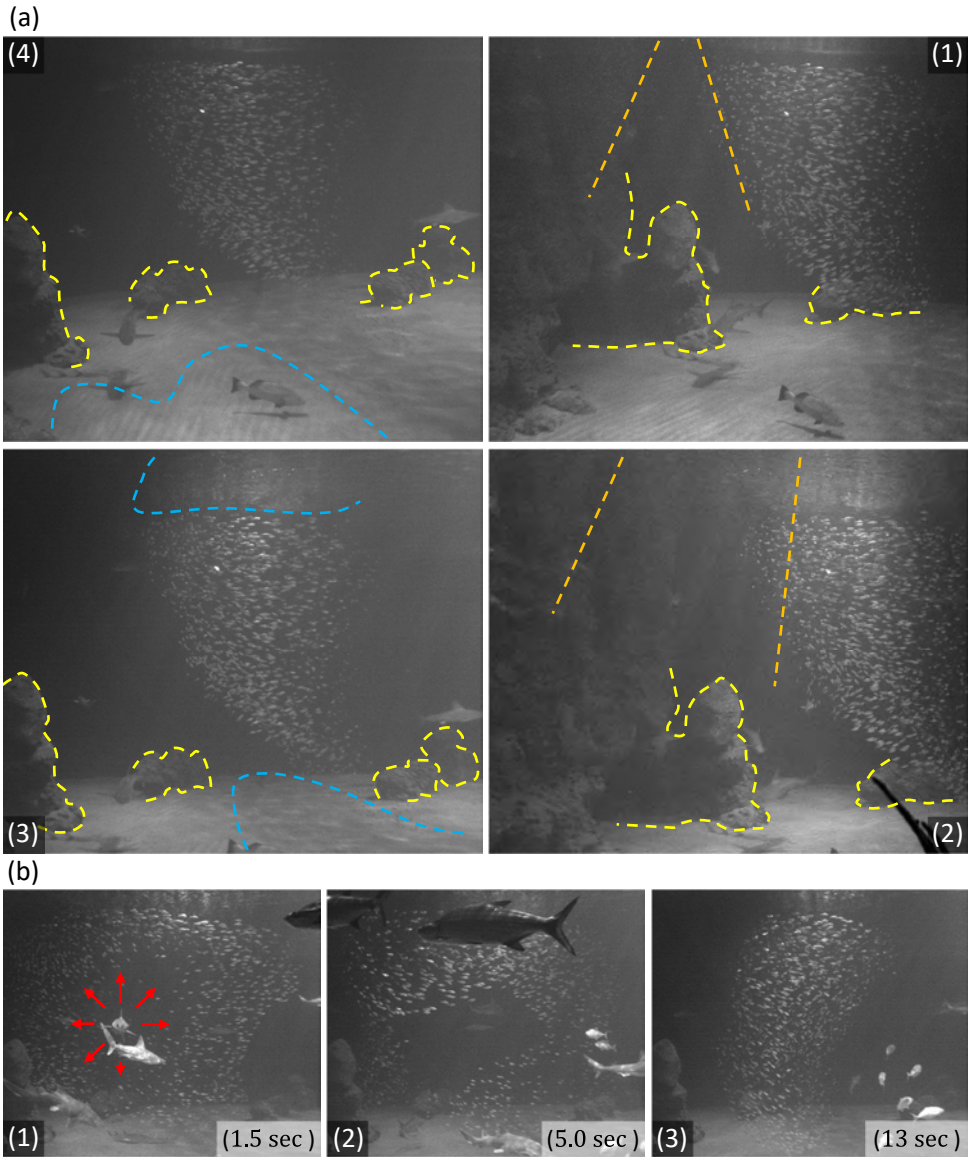


Figure 3.1: Typical imaging inside the fish tank. a) The four camera views imaging a milling fish school. In yellow we mark several objects (rocks and wall silhouettes) in the background (views 1 to 4), in blue we highlight reflections at the ground and the water surface (views 3 and 4), in orange we indicate the (faint) light-rays coming from illumination above the tank (views 1 and 2). b) Three snapshots for a camera (3) imaging an escape to a predator attack at $t = 0$. From left to right we highlight in snapshot (1) a shark attack where the fish rapidly fan outward (red arrows), (2) the fish rejoining (with a tarpon occluding the top part of the school), and (3) the school rejoining into a circular mill with a small group of hunting tuna fish.

plex lighting conditions, the images contain reflections and shadows that are difficult to deal with.

FISH AS ANISOTROPIC PARTICLE IMAGES

In Figure 3.2a, we present fish images zoomed in from the snapshots of Figure 3.1b. Overall the fish appear as bright ‘particle’ image projections from strong specular reflections on their scales. However, unlike conventional particle images [30], the fish image projection is elongated with an inherent anisotropy in the direction of swimming.

We find a large variation in the fish image projected area by the fish position and orientation for the different wide-angle lenses of Chapter 2. See for example the large (parallel) projection upfront in Figure 3.2a-3, in relation to, the much smaller (aligned) projection in the back of Figure 3.2a-4. Furthermore, Figure 3.2a-1 and a-7 particularly underline that there is no uniform contrast inside the tank, and fish may (almost) disappear in the image background (Figure 3.2a-4).

Moreover, there is a large variation in the optical density of the fish projection. We express a local image source density in ‘fish-image-per-pixel’ (fipp) by the number of occupied pixels against the image resolution [30]. This ranges from sparse fish groups ≤ 0.01 fipp in Figure 3.2a-1 to dens fish packing ~ 0.5 fipp in Figure 3.2a-5, and beyond completely filling the image (see also Figure 1.3 in Chapter 1). This sets a clear challenge to extracting reliable tracking data in three dimensions.

SPATIAL AND TEMPORAL RESOLUTION

We further investigate the spatial and temporal resolution. In Figure 3.2b-1 and b-2, we present two close-up views of the directional dependent fish projection. The minimum pixel resolution covers 3–7 pixels for the fish images in the back of the tank. This results in a high spatial resolution over the entire fish tank, ranging above a typical 21–49 pixels in front of the cameras.

Furthermore, to obtain sufficient temporal resolution we sample at a frame rate of 20 to 70 *Hz* to keep the fish displacement within its body-length. Expressing the image displacement as a ‘fish-swim-per-frame’ (fspf) by the projected fish body we keep its value in the range of $\sim 1/5$ fspf. This results in a high time resolution, examples are shown in Figure 3.2b-3 to b-5, with a RGB-colored overlay in Figure 3.2b-6.

OTHER FISH SPECIES

In Figure 3.2c we present several examples of sharks, tarpon fish, barracudas, sea turtles, and tuna fish, as introduced in Chapter 1. These fish constantly interact with the school and challenge the image processing in Section 3.3. They present complex body reflections that vary with position and pose, for example, a sea turtle flapping its fin in Figure 3.2c-3. Furthermore, curious barracuda and grouper fish may appear at the auditorium window and block a camera in Figure 3.2c-8. Such events lead to the temporary loss of a camera view during data acquisition.

3.3. IMAGE PROCESSING

Before we perform the time-resolved tracking in three dimensions we identify the fish in the different camera views. First, we subtract a background image for each recording

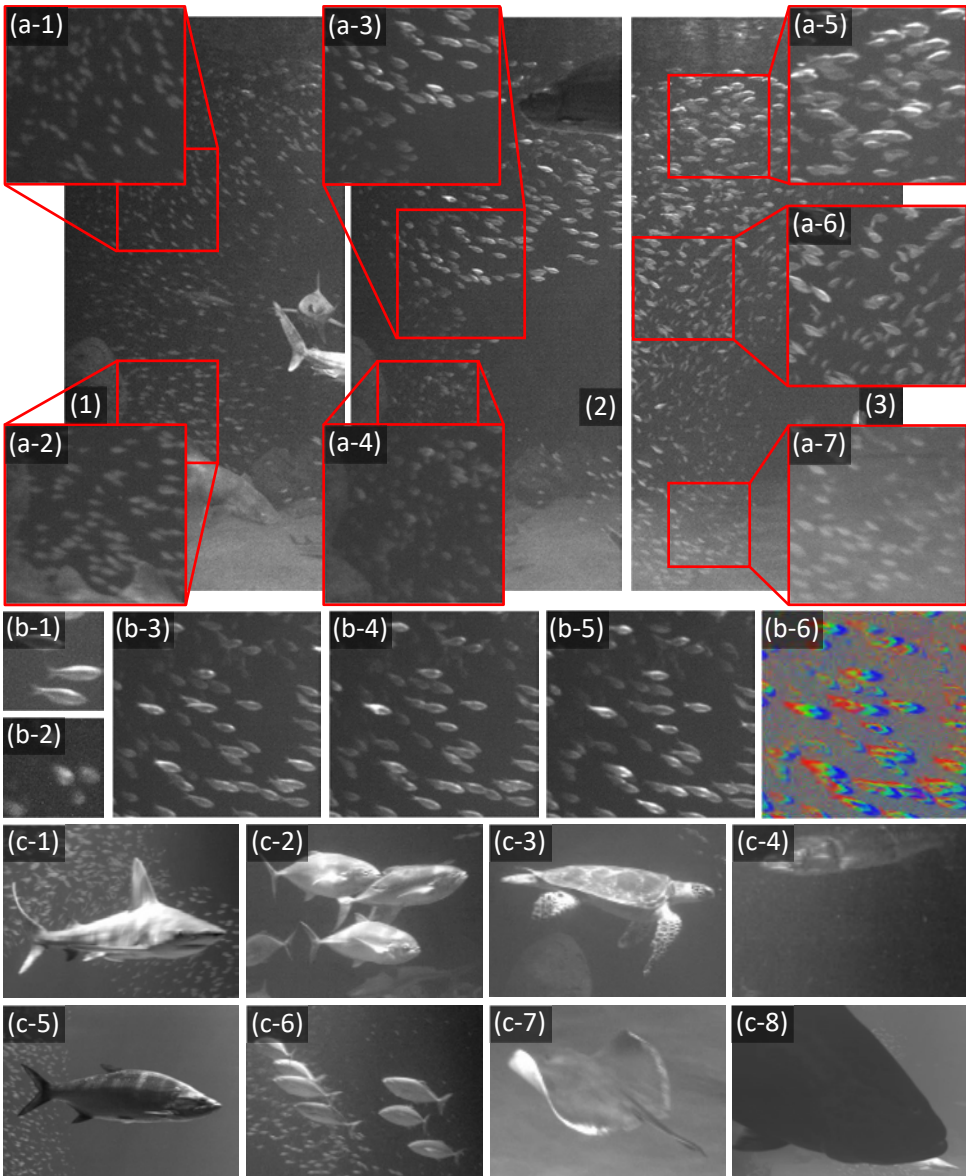


Figure 3.2: Typical fish image data and quality. a) Details of the snapshots (1)–(3) of Figure 3.1b with the harengula swimming: away from the cameras (a-1) at the back of the tank (a-2), upfront and parallel to the cameras in the foreground (a-3), towards the camera views aligned with the depth of field at the bottom in the back (a-4), dens optical projection at the top (a-5) and sparse in the middle (a-6), and with low contrast against the sand floor (a-7). b) Fish image quality of the harengula at high image resolution. Fish image projection swimming parallel (b-1) and towards the camera view (b-2). Three consecutive image frames of a sparse fish group (b-3) to (b-5) showing the temporal resolution plotted in RGB-color overlay in (b-6); in a continuous fish image overlap. c) Several images of predators and other species as introduced in Chapter 1 leading to substantial occlusions: close-up of a blacktip shark (c-1), a horse-eye jack (c-2), a sea turtle (c-3), a barracuda looming at the water surface (c-4), a tarpon (c-5), a group of tuna-fish (c-6), a stingray close to the floor (c-7), and a grouper fish (c-8) — fully blocking the camera view.

to remove stationary background artifacts and enhance the image contrast over multiple length scales. Secondly, we approximate elongated fish images with an ellipse shape and derive several criteria for classification. Subsequently, we extract robust fish identification by maximizing the image contrast over multiple length scales. We end this section by performing tracking in the camera image.

3.3.1. BACKGROUND REMOVAL

To model the static elements in the fish tank that contribute to the image background, we perform a background image removal for the different camera views. As the lighting conditions change during the course of the day (to mimic a natural habitat) and since the fish are always present in the tank, we cannot capture a still background image prior to imaging and therefore need to define it from the image data.

We construct a background image B_{ij} for the pixel indices i and j by recursively averaging the image data I_{ij}^n over the frames n for each camera. To ensure that fish do not trace a swept projection along their swimming path, we suppress artifacts that move in the image foreground by segmentation of the successive background updates, see Appendix B.1. Finally, we fit the patched image background B_{ij} to the input image I_{ij}^n and find the best subtraction S_{ij}^n in the presence of varying illumination from the light above the tank. The resulting progression is shown in Figure 3.3a–c.

3.3.2. MULTI-RESOLUTION IMAGE CONTRAST

We enhance the image contrast over a range of length scales using two techniques from image processing. This allows us to take into account the variation in the projected area by distance and orientation towards the camera for the multiple sizes and shapes of fish swimming in the measurement volume.

MEXICAN HAT IMAGE FILTER

Firstly, we filter the background subtracted image S_{ij}^n of Figure 3.3c using a convolution filter that enhances image contrast for projections of a specific length scale σ in pixel dimension (px). For this purpose, we keep the image resolution fixed and introduce a multi-resolution wavelet image convolution kernel h_{mex} that is shaped like a Mexican hat for the local pixel neighborhood ij^* centered at the pixel index ij .

We derive the shape of the Mexican hat by taking the Laplacian of a Gaussian (LoG) convolution kernel of width σ :

$$h_{\text{mex}} = -\nabla^2 \left[\frac{\sigma^2}{2} \exp \left(-\frac{\|\mathbf{x}_{ij^*}\|^2}{\sigma^2} \right) \right] = \exp \left(-\frac{\|\mathbf{x}_{ij^*}\|^2}{\sigma^2} \right) - 2 \frac{\|\mathbf{x}_{ij^*}\|^2}{\sigma^2} \exp \left(-\frac{\|\mathbf{x}_{ij^*}\|^2}{\sigma^2} \right). \quad (3.1)$$

Here $\mathbf{x}_{ij^*} = [x \ y]^T$ are the local pixel locations¹ for the neighborhood ij^* , $(\bullet)^T$ is the vector transpose, $\|\bullet\|$ is the vector norm and $\nabla^2(\bullet)$ the Laplace operator, for an example see Figure 3.3e.

The first term at the right-hand side of Equation 3.1 integrates the intensity values and smooths out any detail smaller than the width σ . The second term in Equation 3.1 integrates contrast for objects larger than $\sim 2\sigma$ and penalizes the surrounding

¹In the current chapter, all image processing is performed on the corrected image coordinates of Chapter 2, therefore we drop the redundant notation $(\hat{\bullet})$ for the dewarped image position $\hat{\mathbf{x}} = [\hat{x} \ \hat{y}]^T$.

area. As the two terms in Equation 3.1 integrate 0 the image convolution suppresses objects larger than σ . Hence h_{mex} enhances the appearance for objects of width σ , see the variation in fine detail at the top row in Figure 3.3d.

DOWNGRADING THE IMAGE RESOLUTION

Secondly, we introduce a box filter h_{box} to integrate the image intensity values and down-sample the image resolution. The result of this procedure can be seen along the column space of Figure 3.3d. Together, combining the two approaches by applying different consecutive combinations of h_{box} and h_{mex} presents a flexible method to reveal different levels of detail S_{ij}^σ from the background-subtracted image S_{ij}^n . For example see (b3,h2) in Figure 3.3d as we enhance the image contrast for larger predators in the foreground, as is used to track the group of tuna fish in Chapter 2.

3.3.3. ELLIPSE IMAGE CONVOLUTION

We continue considering the shape and orientation of the fish in the object domain and the corresponding projection. We approximate the fish in the camera images as elliptical silhouettes. This provides two advantages. First, in the framework of projective geometry (Chapter 2) an ellipsoid in the object domain projects as an ellipse in the image [69], with a corresponding forward light cone through object space [68]. This naturally embeds the optical transfer [66] for a pinhole camera. Second, an ellipse has several useful parametrizations and can be cast into a sequence of linear image filters.

IMAGE CONIC CONTOUR FUNCTION

We express the ellipse contour function as the conic section in the image as is conventional in projective geometry:

$$\tilde{\mathbf{x}}^T C \tilde{\mathbf{x}} = 0 \text{ with } C = \begin{bmatrix} c_1 & c_2/2 & c_4/2 \\ c_2/2 & c_3 & c_5/2 \\ c_4/2 & c_5/2 & c_6 \end{bmatrix}. \quad (3.2)$$

Here $\tilde{\mathbf{x}} = [x \ y \ k]^T$ is the augmented image coordinate ($k = 1$) using the calibration described in Chapter 2, and C is the symmetric conic coefficient matrix. The six coefficients in Equation 3.2 correspond to five independent parameters: the ellipse semi-axes and orientation, the image position, and a scale that can be normalized [68].

Equation 3.2 can be written as a generic 2nd order polynomial function $f(x, y)$ that is segmented at 0:

$$f(x, y) = \tilde{\mathbf{x}}^T C \tilde{\mathbf{x}} = c_1 x^2 + c_2 x y + c_3 y^2 + c_4 x + c_5 y + c_6 = 0. \quad (3.3)$$

Here the coefficients c_k can be stored in a vector $\mathbf{c} = [c_1 \ c_2 \ c_3 \ c_4 \ c_5 \ c_6]^T$ corresponding to the different terms x^2, xy, y^2, x, y , and 1.

FITTING OF THE CONTOUR FUNCTION

We can directly obtain the coefficients c_k through fitting the polynomial function of Equation 3.3 to the scale-enhanced image² S_{ij}^σ of Section 3.3.2 on a predefined pixel

²In the case of a Gaussian point spread function $I \sim \exp(\tilde{\mathbf{x}}^T C \tilde{\mathbf{x}})$ for the particle image projection [30] one can fit the log-normalized particle image $I^* = \log(I) \sim \tilde{\mathbf{x}}^T C \tilde{\mathbf{x}}$. This is further used to suppress strong reflections from imaging the underwater environment.

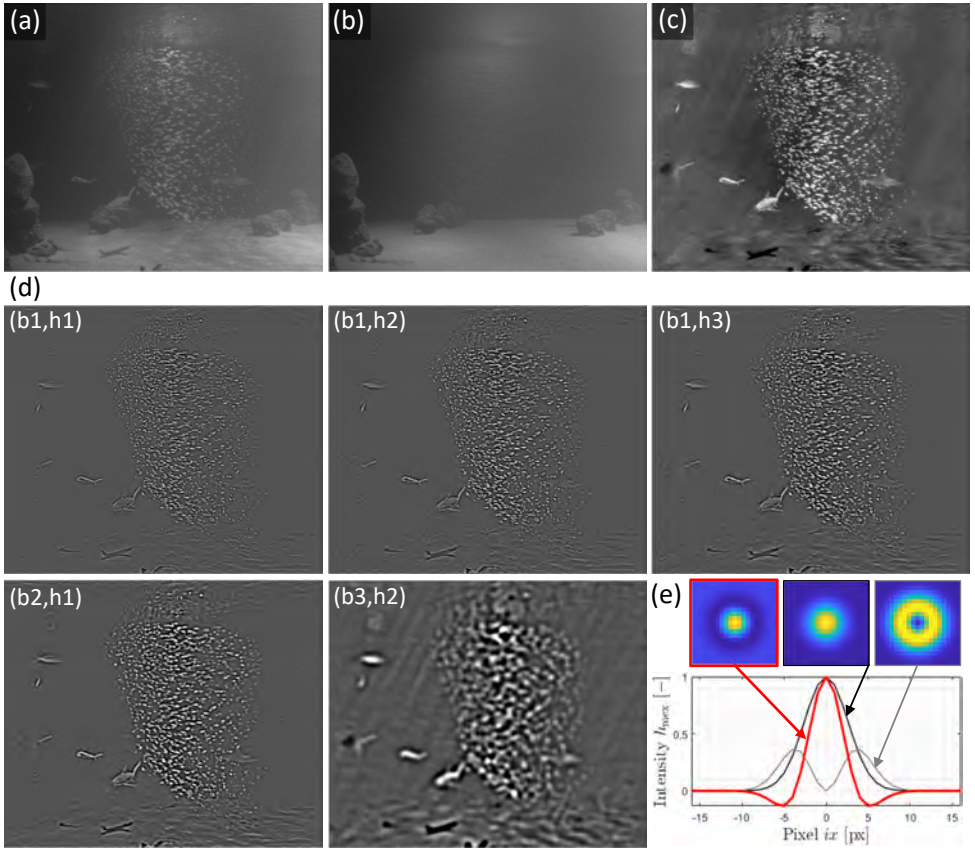


Figure 3.3: Background removal and multi-resolution image contrast. a) Raw image I_{ij}^n from view (3) in Figure 3.1a. b) Patched background image B_{ij} , see also Appendix B.1. c) Best fit background subtracted image S_{ij}^n from (a) and (b), note the light rays cast from the water surface. d) Along the column space of the page, h1–h3 present image convolution with the Mexican-hat image filter (e) at increasing scale $\sigma \sim 2, 3, 4$ px. Along the row space, b1 and b2 present a downgraded image resolution using a 2×2 box filter; (b3,h2) present a result for three consecutive image resolutions. e) Mexican hat image filter (top-left inset, red curve) in its parts: top-middle the convolution kernel for smaller detail in the foreground (black curve), top-right image filter that penalizes the image background (grey curve).

neighborhood ij^* . This can be achieved through a Savinstky-Golay smoothing and differentiation filter [70] that constitutes a separate image convolution kernel h_k (higher-order gradient) to each coefficient c_k . The details are provided in Appendix B.2.

Matching the pixel neighborhood ij^* with the associated scale of interest by $2\sigma + 1$ we convolute the images S_{ij}^σ with h_k and obtain the coefficients c_{ij}^k for each pixel location ij . In Figure 3.4a we present results obtained for the multiple image convolutions for a single scale $\sigma \sim 3$ px similar to (b1,h2) in Figure 3.3d. We now classify the resulting contour function by interpreting the coefficient values.

CLASSIFICATION OF THE CONTOUR FUNCTION

To identify whether the fitted coefficients c_{ij}^k for the 2nd-order polynomial function of Equation 3.3 belong to a local image peak, valley, or saddle point, we classify its critical point. We deduce the location of the critical point by extremizing the value of the polynomial function $f(x, y)$:

$$\nabla f(x, y) = 0 \rightarrow \underbrace{\begin{bmatrix} 2c_1 & c_2 \\ c_2 & 2c_3 \end{bmatrix}}_H \underbrace{\begin{bmatrix} x \\ y \end{bmatrix}}_x = - \underbrace{\begin{bmatrix} c_4 \\ c_5 \end{bmatrix}}_g \rightarrow \mathbf{x} = -H \setminus \mathbf{g}. \quad (3.4)$$

Here \mathbf{g} is the local image gradient and H is the image Hessian.

Based on the trace and determinant of the image Hessian H (left of Figure 3.4a) we determine in Table 3.1 whether the critical point is a local maximum (peak), minimum (valley), or saddle point. We restrict the current work to local image maxima as valid fish positions in the image foreground. This will be of use in Section 3.3.4.

determinant	trace	result
$\det(H) > 0$	$\text{tr}(H) > 0$	image minimum
$\det(H) > 0$	$\text{tr}(H) < 0$	image maximum
$\det(H) < 0$	-	saddle point

Table 3.1: Evaluation criteria for the level-set of Equation 3.3 by the determinant $\det(H)$ and trace $\text{tr}(H)$ of the local image Hessian H .

ESTIMATE OF OPTICAL FLOW

We further use the relatively high frame rate of the image data to compute the displacement of the contour function of Equation 3.3 from one frame to the next one. This presents two additional advantages. First, we improve the fit of the polynomial by integrating temporal information for our sequence of image filters. Secondly, we estimate the optical flow from the image sequence which helps initiate the tracking.

We include an optical flow vector $\mathbf{u} = [u \ v]^T$ which displacement $\mathbf{u}\Delta t$ over Δt we add inside the contour function of Equation 3.3:

$$f(x - u\Delta t, y - v\Delta t, \Delta t) = c_1(x - u\Delta t)^2 + c_2(x - u\Delta t)(y - v\Delta t) + c_3(y - v\Delta t)^2 + c_4(x - u\Delta t) + c_5(y - v\Delta t) + c_6 + c_7^* \Delta t + c_8^* \Delta t^2, \quad (3.5)$$

where the terms $\Delta t, \Delta t^2$ are added to include image intensity variation. Expanding each term in Equation 3.5 and regrouping $x^2, xy, \dots, \Delta t^2$, we write another function $g(x, y, \Delta t)$ of same order that is fitted to the pixel neighborhood ijn^* over several frames n :

$$g(x, y, \Delta t) = c_1x^2 + c_2xy + c_3y^2 + c_4x + c_5y + c_6 + c_7x\Delta t + c_8y\Delta t + c_9\Delta t + c_{10}\Delta t^2. \quad (3.6)$$

Comparing the terms $x\Delta t$ and $y\Delta t$ for Equation 3.5 and Equation 3.6 in Table 3.2 the

optical flow \mathbf{u} is obtained by inverting of a set of linear equations:

$$\underbrace{\begin{bmatrix} 2c_1 & c_2 \\ c_2 & 2c_3 \end{bmatrix}}_H \underbrace{\begin{bmatrix} u \\ v \end{bmatrix}}_{\mathbf{u}} = - \underbrace{\begin{bmatrix} c_7 \\ c_8 \end{bmatrix}}_{\partial_t \mathbf{g}} \rightarrow \mathbf{u} = -H \setminus \partial_t \mathbf{g}, \quad (3.7)$$

with $\partial_t \mathbf{g}$ defined as the time derivative of the image gradient. Note that further modeling a rigid body motion for the ellipse allows including the rotation, acceleration *etc.*, and extend Table 3.2. However, this remains beyond the scope of the current work.

term	$f(x - u\Delta t, y - v\Delta t, \Delta t)$	$g(x, y, \Delta t)$
x^2	c_1	c_1
xy	c_2	c_2
y^2	c_3	c_3
x	c_4	c_4
y	c_5	c_5
1	c_6	c_6
$x\Delta t$	$-2c_1 u - c_2 v$	c_7
$y\Delta t$	$-c_2 u - 2c_3 v$	c_8
Δt	$c_7^* + c_4 u - c_5 v$	c_9
Δt^2	$c_8^* + c_1 u^2 + c_2 uv + c_3 v^2$	c_{10}

Table 3.2: Ellipse image displacement from a term-by-term comparison of the expanded polynomial function $f(x - u\Delta t, y - v\Delta t, \Delta t)$ and its fitted form $g(x, y, \Delta t)$.

3.3.4. IMAGE SEGMENTATION AND IDENTIFICATION

At this stage of the image processing we have removed the image background, enhanced the image contrast at scale σ , and extracted the coefficients c_{ij}^k that give the conic contour function and optical flow. We now use the image classification criteria of the previous subsection to cluster ellipse shapes corresponding to the fish images.

IMAGE SEGMENTATION

Given a scale σ we identify for each pixel ij if the pixel neighborhood ijn^* belongs to a fish. First, we segment the fish in the image foreground by $S_{ij}^\sigma > 0$. Secondly, we complement the segmentation with the criteria $\det(H_{ij}) > 0$ and $\text{tr}(H_{ij}) < 0$ for the image Hessian, see Table 3.1. In addition, we demand that the critical point \mathbf{x}_{ij} of Equation 3.4 lies within the pixel neighborhood by $\|\mathbf{x}_{ij}^*\| < \sigma$ away from ij . Similarly, we constrain the optical flow vector \mathbf{u}_{ij} of Equation 3.7 within the same range by $\|\mathbf{u}_{ij}^*\| < \sigma/\Delta t$.

For practical purposes, such as changing lighting conditions, we introduce variable image segmentation levels ϵ_σ , ϵ_{\det} and ϵ_{tr} and define the segmentation mask M_{ij} :

$$\begin{cases} M_{ij} = 1 \text{ when } S_{ij}^\sigma > \epsilon_\sigma \text{ and } \det(H_{ij}) > \epsilon_{\det} \text{ and } \text{tr}(H_{ij}) < \epsilon_{\text{tr}} \\ \quad \text{and } \|\mathbf{x}_{ij}^*\| < \sigma \text{ and } \|\mathbf{u}_{ij}^*\| < \sigma/\Delta t, \\ M_{ij} = 0 \text{ otherwise.} \end{cases} \quad (3.8)$$

The segmentation levels ϵ are based on mean and standard deviation statistics and can be restricted/relaxed depending on the image quality. A result is shown in Figure 3.4c.

VOTING AND ELLIPSE IDENTIFICATION

Having segmented the image in Figure 3.4c, we identify pixels that correspond to the same ellipse. Inspired by the image Hough transform we define a ‘voting map’ V_{ij} that bins the number of critical points \mathbf{x}_{ij} that correspond to the same pixel indices ij . The result of this process is shown in Figure 3.4d and f, where we further pinpoint the location of distinguishable fish images.

Finally, we extract connected regions from the voting map V_{ij} and perform a weighted average to cluster c_{ij}^k for contour functions that approximate the same fish image. In Figure 3.4e and g, we illustrate a correct segmentation. Each individual fish image is associated with a single ellipse \mathbf{c}_p where $p = 1 \cdots P$ lists the number of identifications. Finally, we recover the shape of the ellipse through Appendix B.3 and provide useful manipulations in Appendix B.4 which we use in the remainder of this chapter.

3.3.5. CONTRAST MAXIMIZATION

In Figure 3.4 we identify 1379 fish over a single scale σ for the school of ± 2000 fish. Although not all fish are visible in the image, and many may be in occlusion, we continue to raise the number of identifications over a range of scales and decide the most representative contour function. For this purpose, we evaluate the peak value of the extracted polynomial function fitted to the enhanced image brightness and maximize the local image contrast per unit area.

First, in Figure 3.5a, we enhance the image contrast for the smallest scale (b1,h1) of Figure 3.3d to extract the set of ellipses \mathbf{c}_p . Secondly, in Figure 3.5b, we process the next length-scale (b1,h2) of Figure 3.3d and obtain the ellipses \mathbf{c}_q . The two consecutive image scales present a high degree of overlap. This is shown in Figure 3.5c-1 and c-3 which we overlay in c-2. We compute the degree of overlap from the ellipse contours and corresponding midpoints \mathbf{x}_p and \mathbf{x}_q (Appendix B.3) by the normalized (point-point) ellipse distance $d_{pq} = d(\mathbf{c}_p, \mathbf{x}_q)$ of Appendix B.5.

Computing the degree of overlap back-forth between the image scales from interchanging p and q , we construct the rectangular bi-adjacency (indicator) matrix B_{pq} :

$$\begin{cases} B_{pq} = 1 \text{ when } d(\mathbf{c}_p, \mathbf{x}_q) \leq 1 \text{ and } d(\mathbf{c}_q, \mathbf{x}_p) \leq 1, \\ B_{pq} = 0 \text{ otherwise.} \end{cases} \quad (3.9)$$

This gives a bipartite graph that pairs p with q , when $B_{pq} = 1$ the ellipses consistently overlap, while $B_{pq} = 0$ indicates otherwise.

Evaluating the peak value of the polynomial we keep the contour function of maximum intensity per unit area by the ellipse semi-axis (Appendix B.3). In this way, we distinguish between two paired ellipses p and q that belong to a single fish and two ellipses that represent partially overlapping fish images. This process is shown in Figure 3.5c-1 to c-3 with a result in c-7 zoomed in from Figure 3.5d. Subsequently, we update an image mask (Figure 3.5c-6) and remove fish through inward interpolation (image flood-fill) in c-8. This image is input to the next scale in Figure 3.5c-5 and we repeat the process (c-9 and c-10) to identify 1729 fish at maximum image contrast in Figure 3.5e.

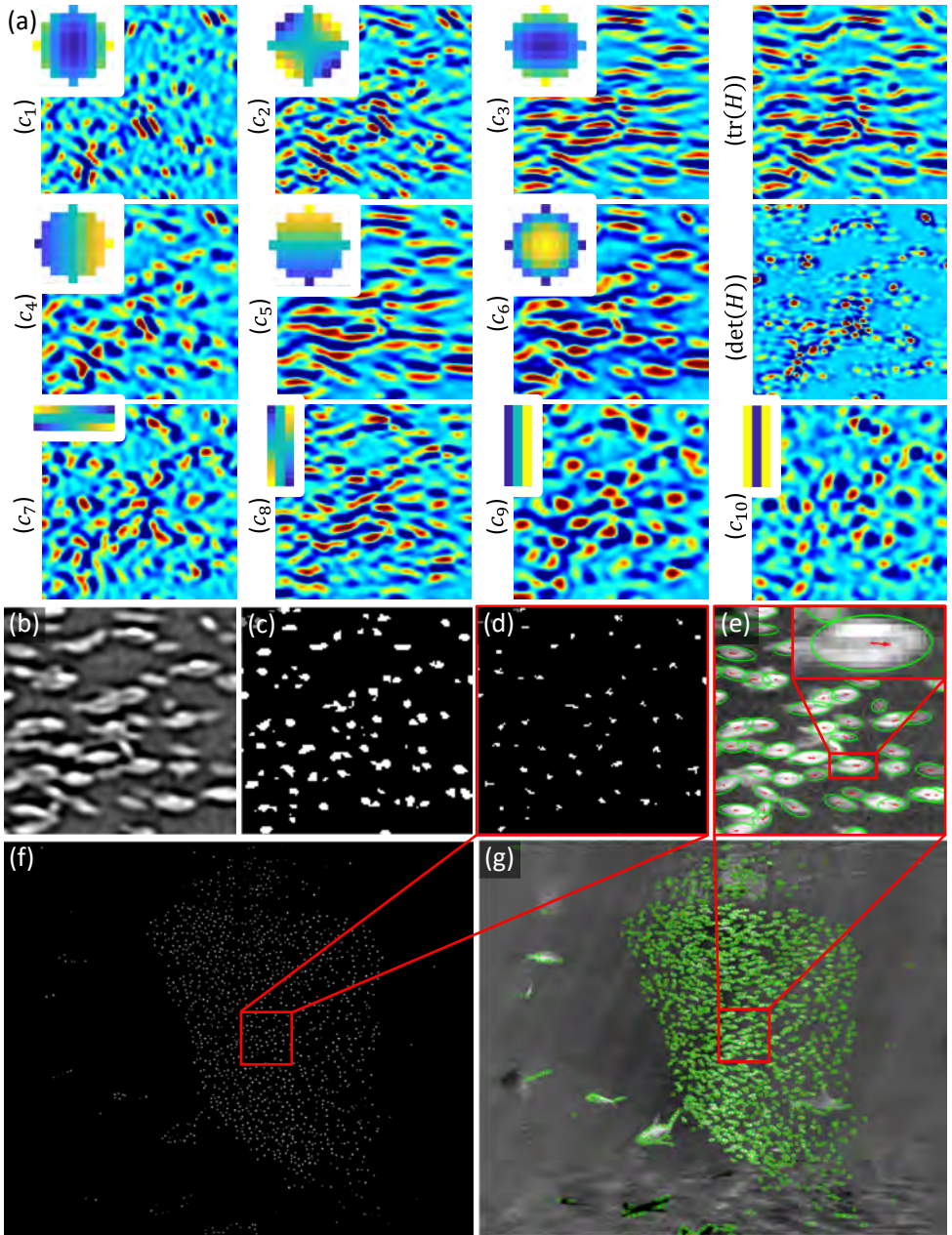


Figure 3.4: Fish image ellipse detection. a) The coefficient values c_k from the convolution filters h_k (inset, top-left) corresponding to Equation 3.6 (pattern recognition): the second and mixed image derivatives (c_1, c_2, c_3), the image gradients (c_4, c_5), the parabolic convolution filter (c_6), the image gradient time derivatives (c_7, c_8), the image time derivative (c_9), and second derivative (c_{10}); the image trace $\text{tr}(H)$ and determinant $\det(H)$. b) Input image S_{ij}^σ from Figure 3.3d (b1,h2) with scale $\sigma \sim 3 \text{ px}$. c) Segmented image M_{ij} from the criteria of Equation 3.8. d) Voting map V_{ij} , binning the midpoint from the image ellipse at the input resolution. e) Resulting ellipse identification \mathbf{c}_p from the image processing routine (a)–(d). f) Full image (d) for the voting map V_{ij} . g) Full image (e) for the resulting ellipse identification \mathbf{c}_p with 1379 identified fish.

It is noteworthy that looping over multiple scales reduces the chance of missing a fish by variable image segmentation levels of Equation 3.8; compare the insets in Figure 3.5a and b that together make Figure 3.5d. This in principle improves the robustness of the described fish identification algorithms. Finally, we note that spurious fish identification (sharks, sand floor, water surface, *etc.*) will largely lack correspondence and be removed when matching among views in the next section.

3.3.6. CAMERA TRACKING

We initiate the tracking of fish in the camera views by linking the image identification between image frames n and $n + 1$. Using the optical flow vectors \mathbf{u}_p and \mathbf{u}_q we align the quantities at $t_{n+1/2}$ by Appendix B.4. We determine the overlap by the normalized ellipse distance d_{pq} and compute the bi-adjacency matrix B_{pq} :

$$\begin{cases} B_{pq} = 1 & \text{when } d(\mathbf{c}_p^{n+1/2}, \mathbf{x}_q^{n+1/2}) \leq 1 \text{ and } d(\mathbf{c}_q^{n+1/2}, \mathbf{x}_p^{n+1/2}) \leq 1, \\ B_{pq} = 0 & \text{otherwise.} \end{cases} \quad (3.10)$$

The result of the camera tracking can be found in Figure 3.6 for 10 consecutive frames output from Figure 3.5. Ellipses that uniquely connect across multiple frames correspond to a segment of a projected trajectory, while connections with multiplicity are stored as indexed correspondences that either go into or come out of occlusion, see the diagrams in Figure 3.6c.

Figure 3.6a and b present a sparse set of fish images on the side of the school revealing long track segments (red) for the high degree of image overlap. Figure 3.6d and e present results obtained in the middle of the school. Here a continuous rate of fish images going into and coming out of occlusion disrupts the image analysis and breaks the fish tracks into smaller segments. This introduces significant uncertainty in the image.

Fish do not always remain tracked. In particular in the presence of large occlusions, see Figure 3.1b (snapshot 2), and when the fish lose contrast or disappear in the background. It is noteworthy that the graph between different frames is not limited to consecutive images, but can also be constructed by skipping a few. This will be continued in Section 3.5 when tracking from different camera views.

3.4. CORRESPONDENCE MATCHING AND TRIANGULATION

We proceed to match the identified fish projections in the different views and triangulate their position. First, we link stereoscopic correspondences between different camera pairs by using the ray-tracing framework of projective geometry introduced in Chapter 2. Secondly, we associate stereoscopic correspondences that image the same object coordinate by matching the complete cluster graph between multiple views. This essentially introduces a combinatorial problem with a large number of candidates. We end this section by optimizing the object triangulation that uniquely fits the identified ellipses using a simple strategy to minimize the total reprojection error.

3.4.1. LINKING STEREOSCOPIC CORRESPONDENCES

We start with linking stereoscopic correspondences between different views using ray-tracing geometry. The ellipse midpoint \mathbf{x}_p in camera c defines a ray through the object

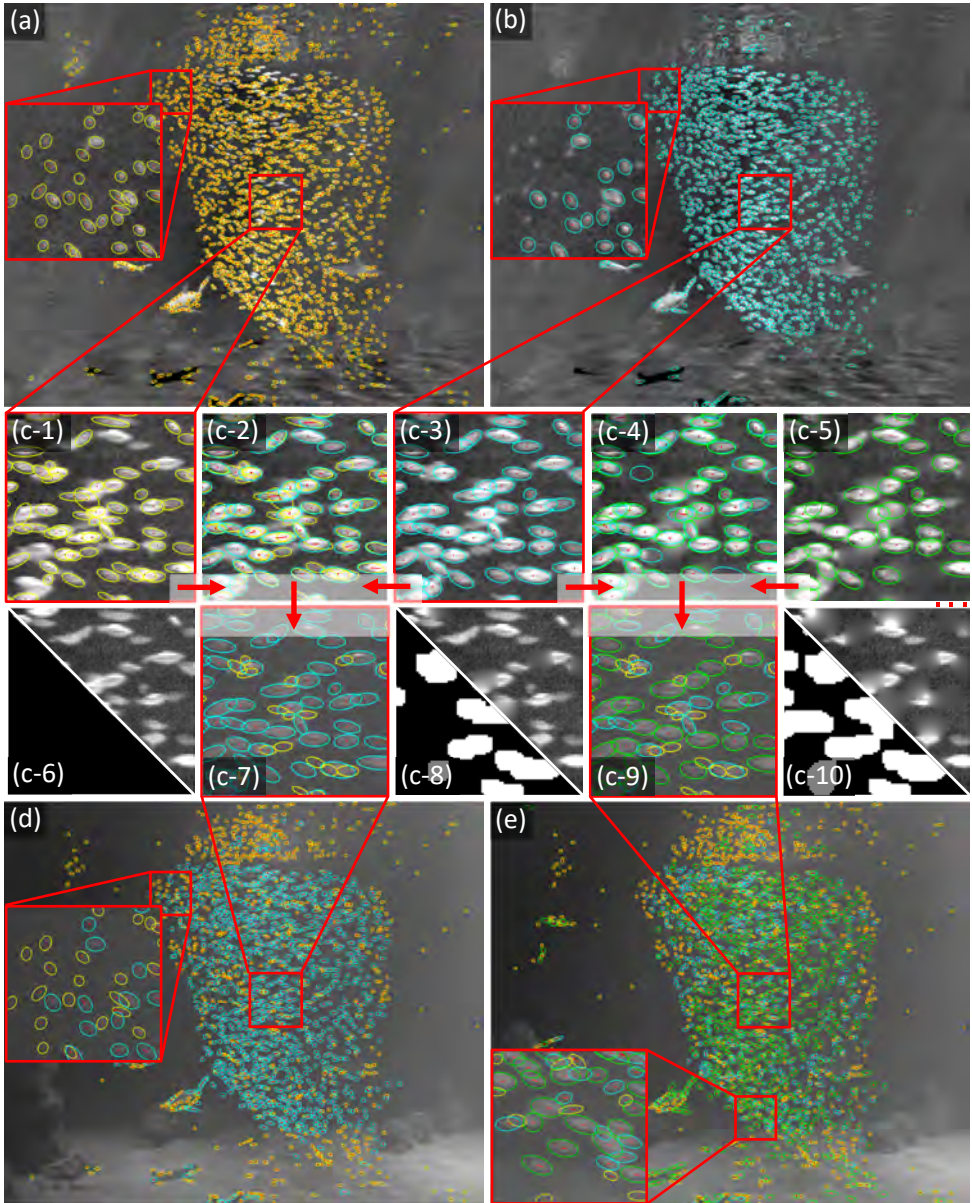


Figure 3.5: Ellipse identification over multiple scales. a) Ellipse detection for the image (b1,h1) of Figure 3.3; identifying small fish images at the edge of the school (inset). b) Ellipse detection for the image (b1,h2) of Figure 3.3; emphasizing larger fish images, while losing the fish at the edges of the school. c) Contrast maximization: close-up image (c-1) from (a) and (c-3) from (b), combined overlay (c-2) from (c-1) and (c-3) with (c-3) to (c-5) analogous for consecutive image scales, original input image with empty mask (c-6), best ellipse identification (c-7) through maximizing the contrast of (c-2), updated mask (c-8) and fish image removal from (c-7), the repeated process for (c-9) and (c-10). d) Ellipse identification through contrast maximization of (a) and (b), inset the combined ellipse identification at the edge of the school. e) Repeated process for (a) and (b) and the next image scale (b1,h3) of Figure 3.3, inset a close-up at the bottom of the school. In total, we identify 1729 fish images looping over multiple scales. All color coding is consistent.

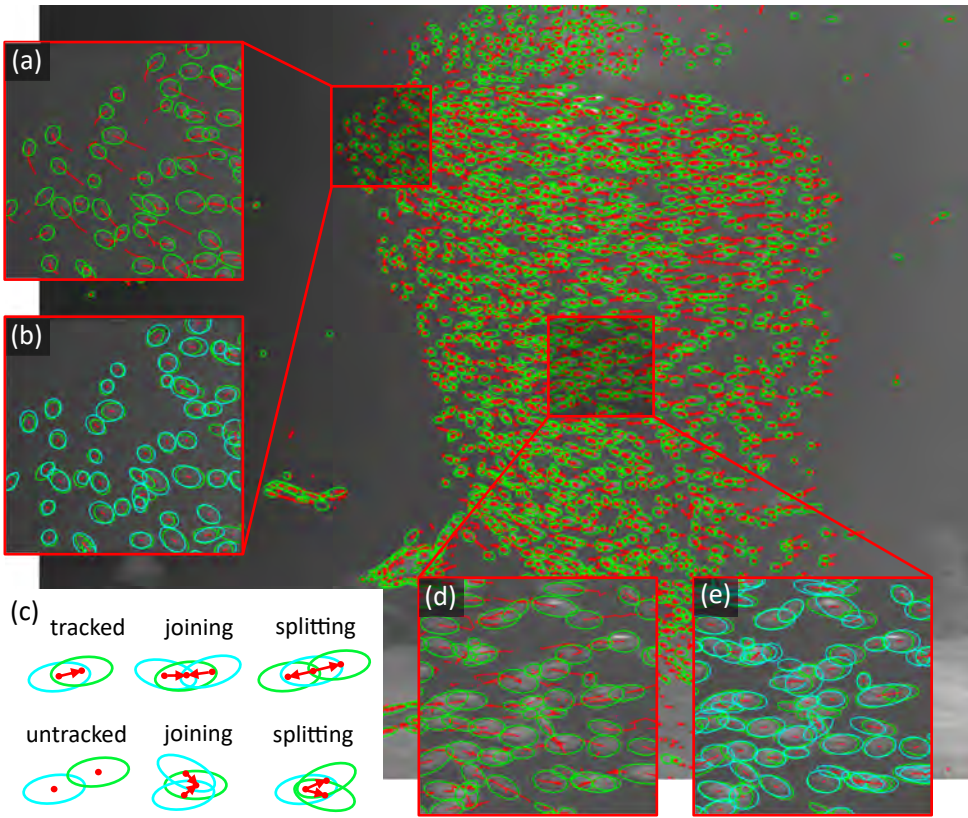


Figure 3.6: Tracking in the camera image. a) Close-up at the side of the school, showing smooth connected tracks for a sparse group of fish. b) Consecutive fish ellipse image overlap (cyan to green) that defines the track links. c) The track linking graph using the ellipse image contour and displacement vectors. A ‘tracked’ ellipse for a unique track segment and an ‘untracked’ ellipse leaving an image point without connectivity. Two ellipses that are ‘joining’ into one and end their tracks going into occlusion. One ellipse ‘splitting’ into two and defining two new track segments. d and e) Similar close-up as in (a) and (b), however, with lesser track quality due to an increasing rate of occlusions.

domain that can be projected on another view c' using the fundamental matrix³ F between the views, and yields the epipolar line \mathbf{l}'_p on the view c' :

$$\mathbf{l}'_p = F\mathbf{x}_p, \tag{3.11}$$

where other way around a point \mathbf{x}'_q in view c' projects an epipolar line by $\mathbf{l}_q = F^T \mathbf{x}'_q$ on view c , consistently using the superscript $(\bullet)'$. This process is illustrated in Figure 3.7a and b where we cast a red point in view c to a line in c' and a cyan point from c' to a line in c , and mark the consistent ray-crossing.

³The fundamental matrix F follows from the projection matrices $P^c = [R^c \mathbf{t}^c]$ of Chapter 2 by $F = [\mathbf{e}'^\dagger]_\times P^{c'} P^{c\dagger}$ where $(\bullet)^\dagger$ is the pseudo inverse and \mathbf{e}' the epipolar line that follows from the null space of $P^{c'}$ with $[\bullet]_\times$ the matrix cross product; for a full construction see Hartley and Zisserman [68].

STEREOSCOPIC BI-ADJACENCY AND INCIDENCE MATRICES

From the epipolar lines \mathbf{l}'_p projected from camera c onto c' , the ellipse contours \mathbf{c}'_q in camera c' , and the reverse projection of camera c' onto c , we find the ellipses \mathbf{c}_p and \mathbf{c}'_q that are in stereoscopic correspondence. We compute the point-line distance $d_{pq} = d(\mathbf{c}_p, \mathbf{l}'_q)$ of Appendix B.5, and the reverse, and define the bi-adjacency B_{pq} :

$$\begin{cases} B_{pq}^{cc'} = 1 & \text{when } d(\mathbf{c}_p, \mathbf{l}'_q) \leq 2 \text{ and } d(\mathbf{c}'_q, \mathbf{l}'_p) \leq 2, \\ B_{pq}^{cc'} = 0 & \text{otherwise,} \end{cases} \quad (3.12)$$

segmenting ≤ 2 as the associated object position is expected to project halfway between the point and line.

From the stereoscopic linking from $B_{pq}^{cc'} = 1$, we list a large number⁴ of $l = 1 \cdots L$ correspondences for the consistent ray-crossing. We define the (sparse) incidence matrices J_{pl}^c and $J_{ql}^{c'}$ that connect the l stereoscopic correspondences to the image ellipse identification p and q in views c and c' . These matrices formally decompose the bi-adjacency matrix of Equation 3.12 as $B_{pq}^{cc'} = J_{pl}^c J_{lq}^{c'}$ where we sum over the repeated indices.

INTEGRATION OF THE PROJECTIVE GEOMETRY

At this point, the integration of the ray-tracing geometry and the ellipse identification in Equation 3.12 has two advantages. First, evaluating the distance on the ellipse contour we normalize the image resolution for the varying fish image projection (Section 3.2.2). In fact, Equation 3.12 includes the shape of the forward projected light-cone [68] that varies with the position and orientation of the fish and includes the optical transfer [66] from the image to the object domain (Figure 3.8a and c). Secondly, we take into account the error from the calibration of Chapter 2. This is achieved by including a uniform expansion (Appendix B.4) for the ellipse contour as shown in Figure 3.7c.

In this way, we allow a physically grounded variation in the pixel reprojection error and include relevant sources of uncertainty to match correspondences at a ‘subfish’ accuracy; independent of the camera configuration (relative positions and viewing angle). This presents a robust segmentation to find stereoscopic correspondences between the views as we image fish of various sizes that are swimming over large distances.

3.4.2. F-FOCAL CORRESPONDENCE MATCHING

There are two fundamental stereoscopic ambiguities that compromise the validity of many stereoscopic correspondences found in the previous subsection. Both these artifacts are illustrated in the ray-tracing diagram of Figure 3.8d for the multiple cameras c , c' , and c'' in a top view.

Firstly, a pair of stereoscopic cameras c and c' triangulate so-called ghost-particles [30], or ‘ghost-fish’ in the current scope, see the green squares. Here, the optical rays from one camera c may project similar epipolar lines and match two points in view c' , and yield a multiplicity of four object triangulation that share the plane from the camera

⁴The number of points $q = 1 \cdots Q$ in view c' that match with a single ray $p = 1 \cdots P$ projected from c scales by $\sim \sqrt{Q}$. Taking $P \sim Q$ the bi-adjacency matrix of Equation 3.12 is therefore populated by $L \sim \mathcal{O}(P^{3/2})$ correspondences versus a total number of $\mathcal{O}(P^2)$ elements.

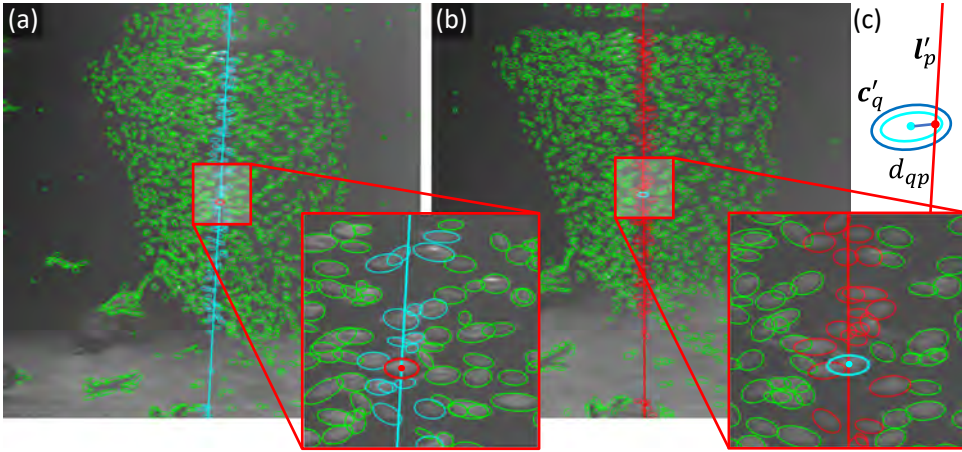


Figure 3.7: Linking of stereoscopic correspondences for Figure 3.1a. a) Ellipse identification in view (3), here taken as c , and in cyan, a selected ray cast from view (4), matching with the red marked ellipse, also see the inset. b) Ellipse identification view (4), here taken as c' , with in red the matched ray cast from view (3) consistently matching with the cyan marked ellipse, also see the inset. c) Point-line distance d_{qp} in view c' between the ellipse c'_q and the projected line l'_p from c consistent in color-code from the inset of (b). The rays traced in (a) and (b) yield a multiplicity of 121 stereoscopic correspondences (cyan and red ellipses).

centers [68]. Secondly, a set of three views c , c' , and c'' , may triangulate the same point multiple times, see the green triangles in Figure 3.8d. Here, the stereoscopic triangulation for one camera pair c and c' will share the view c' with the triangulation of another camera pair c' and c'' . We now cluster these stereoscopic correspondences and suppress the appearance of ‘ghost-fish’ in the next subsection.

MATCHING STEREOSCOPIC CORRESPONDENCES VIA GRAPH CLUSTERING

We extract l linked stereoscopic correspondences between the views of Figure 3.8a and proceed to connect their graph in Figure 3.8b. For this purpose, we continue to raise the number of views to match in a camera pool. We indicate the camera pool by $f = 2, 3, \dots, F$ that we call the camera focality; here up to a quadrifocal camera pool $F = 4$. We permute through all possible combinations of cameras $F!/(f!(F-f)!)$ and extract complete cluster graphs composed of $(f^2 - f)/2$ stereoscopic links.

Starting from the first diagram in Figure 3.8b we link the stereoscopic correspondences l between the views c and c' with another set of correspondence h between views c' and c'' from the incidence matrices $J_{pl}^{cc'}$ and $J_{pl}^{c'c''}$ that share view c' . Then, for the trifocal camera pool ($f = 3$) in the second diagram, we find the cyclic graph between views c , c' , and c'' that represent a trifocal correspondence match (red), while we ignore links that do not connect consistently (grey).

Following these steps, we repeat this process for the second diagram in Figure 3.8b and link the matched trifocal correspondences l in views c , c' and c'' with to the correspondences h between views c' , c'' and c''' in a perfect overlap $(f - 1)$ in views c' and c'' . From the graph cycle between different trifocal correspondences, we find the complete cluster graph (red) for stereoscopic links that define a quadrifocal correspondence

match ($f = 4$) in the third diagram, while we do not consider the incomplete graph clique (grey). Further raising the camera focality f , this procedure generalizes to any number of views. Further detail is given in Appendix B.6.

CAMERA INCIDENCE MATRIX, OBJECT TRIANGULATION, AND REPROJECTION ERROR

Having matched all possible correspondences l at increasing focality f we define the camera incidence matrix J_{pl} with the image identification p running over all camera views c . The camera incidence matrix naturally encodes the camera overlap for the matched correspondences and we triangulate (Appendix A.5) the associated object position $\mathbf{X}_l = [X \ Y \ Z]^T$, and the velocity $\mathbf{U}_l = [U \ V \ W]^T$ from the optical flow.

Finally we compute the average normalized reprojection error $\varepsilon_{pl} = d(\mathbf{c}_p, [R^c \ \mathbf{t}^c] \tilde{\mathbf{X}}_l)$ along the object displacement $\mathbf{X}_l + \mathbf{U}_l \Delta t$ over the frame sequence used for the image processing (Section 3.3). When the reprojection error is violated outside the expanded and displaced ellipse contours ($\varepsilon > 1$), we refine the camera incidence matrix J_{pl} :

$$\begin{cases} J_{pl} = 1 & \text{when } \varepsilon_{pl} \leq 1, \\ J_{pl} = 0 & \text{otherwise.} \end{cases} \quad (3.13)$$

Remark that the argument of Equation 3.13 can be complemented by restricting the depth of field and other user-specific criteria (*e.g.* object skew, velocity, acceleration, coherence, *etc.*). In Figure B.3 of Appendix B.6 we provide triangulated examples for a number of consecutive camera pools with 337400 stereoscopic, 213306 trifocal, and 49699 quadrifocal correspondence matches; imaging at narrow camera angles and limited baseline.

3.4.3. COST-FUNCTION OPTIMIZATION

We optimize the object triangulation that best fits the image identification in the different camera views. This is achieved by writing a constrained integer assignment over the matched correspondences of the previous subsection. The solution to the integer assignment greatly reduces the number of correspondences and filters the majority of spurious matches from the object triangulation presented in Appendix B.6. The results here will be input to the recursive branching of trajectories in the next section.

CONSTRAINED INTEGER ASSIGNMENT

We define an integer assignment by writing a solution vector λ_l that is either 1 or 0. This solution vector selects the object triangulation that best fits the image and runs over all stereoscopic, trifocal, and quadrifocal camera pools. We score the fit by the average projection errors $\varepsilon_l = \sum_p \varepsilon_{pl} / \sum_p J_{pl} \in [0 \ 1]$ and enforce a unique solution by constraining the incidence matrix J_{pl} back to the image.

Computing the total error by summation over ε_l and the solution vector λ_l for the repeated index, and imposing the constraint in the same way, we formally write:

$$\begin{aligned} & \min_{\lambda_l} \varepsilon_l \lambda_l \\ & \text{subject to } J_{pl} \lambda_l \geq 1. \end{aligned} \quad (3.14)$$

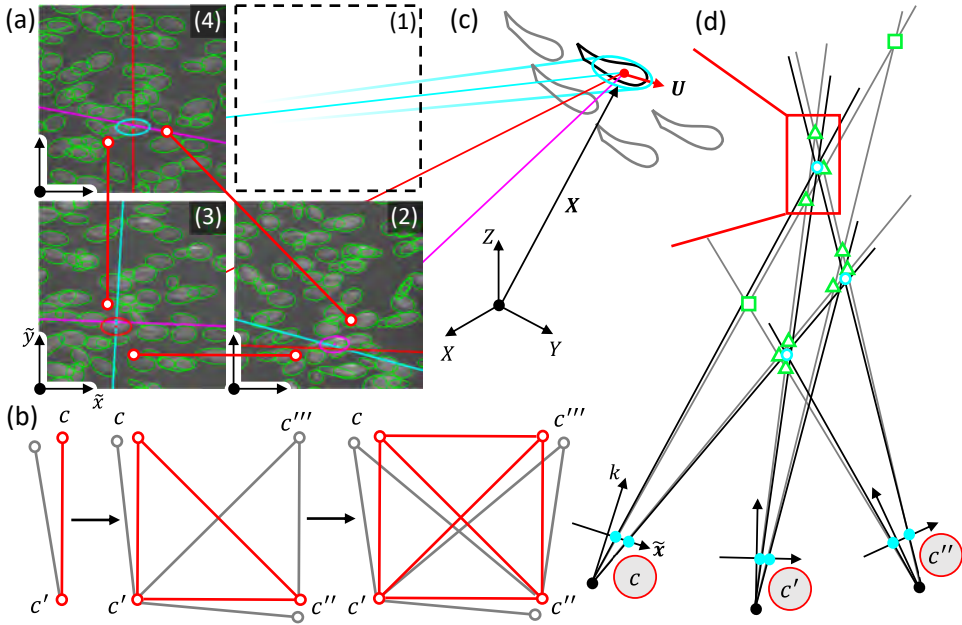


Figure 3.8: Matching of f -focal correspondences. a) A set of zoomed-in trifocal views (2)–(4) extending from Figure 3.7a and b, with consistent color-coding; in red the extraction of stereoscopic links between the views. b) Clustering of stereoscopic correspondences into trifocal and quadrifocal complete cluster graphs (red), and ignoring the incomplete ones (grey). c) The ray-tracing geometry used for triangulation of the three-dimensional fish position \mathbf{X}_I and velocity \mathbf{U}_I in the object space; in cyan the forward projected ellipse contour. d) Illustration of the trifocal triangulation and the stereoscopic ambiguity, where an increasing number of views can be used to improve the accuracy and test the validity of triangulated objects. For real examples see Figure B.3.

The inequality constraint $J_{pl}\lambda_l \geq 1$ picks each image identification p at least once. This relaxes a strict equality $J_{pl}\lambda_l = 1$ for occluded⁵ image identifications that may correspond to multiple object points.

Minimizing the total reprojection error, the solution vector λ_l is forced to pick the minimum number of object positions that fill the images by the incidence matrix J_{pl} . Therefore Equation 3.14 inherently rewards a large camera cover $w_l = \sum_p J_{pl}$ for the matched correspondence of the previous subsection. We obtain a unique solution since ε_l uniquely weights each associated object triangulation, and when including more views in trade-off with an elevated reprojection error (over-determined).

DIRECT SOLUTION THROUGH COST-FUNCTION SORTATION

In the current work, we solve the integer assignment of Equation 3.14 using a cost-function sortation that provides a direct solution. We first sort the largest camera cover w_l in descending order (4,3,2) and subsequently sort the minimum reprojection error ε_l within the camera cover. We then select the solution $\lambda_l = 1$ for the entries of the index p that appear first in the sorted incidence matrix J_{pl} . In the presence of limited

⁵Augmenting additional upper-bound constraints $J_{pl}\lambda_l \leq 1, 2, 3, \dots$ in Equation 3.14 can enforce a strict camera incidence or be used for ‘pruning’ of matches [48] and limit the number of allowed occlusions.

camera angles and baseline, this approach can easily handle large collections of input correspondence matches such as presented in Appendix B.6.

The cost-function sortation presents a simple solution strategy, where we aim to achieve a triangulation that best fills the images at a minimum reprojection error and is based on the greedy algorithm. The direct solution strategy does not guarantee a global minimum [4, 12, 15] but is robust against (integer-)solver error. More sophisticated solution strategies may, in principle, represent different triangulation algorithms [43, 48, 61].

3

RESULT FOR THE OBJECT TRIANGULATION

A result is provided in Figure 3.9 with the quadrifocal object positions in red, the trifocal correspondences in green, and the remaining stereoscopic triangulation in cyan. In Figure 3.9a and b we plot the sorted cost-function and the resulting error distributions which slightly elevate when including more views. In Figure 3.9c–f, we plot the obtained object triangulation and reprojection on the images. We obtain a total of 3511 triangulated object points. This number approaches the school of ± 2000 fish and clearly resembles its silhouette within the varying camera overlap, although some noise remains.

The current framework is flexible for missing data among views and does not require prior knowledge of the camera overlap as is common to tomographic methods [39, 40, 66]. Furthermore, we greatly reduce the number of triangulated correspondences presented in Figure B.3 of Appendix B.6. Lastly, in practice, there will always be ‘ghost-fish’ due to spurious ellipse identifications, errors by noise in the image, and errors from the camera calibration of Chapter 2.

3.5. THREE-DIMENSIONAL TIME-RESOLVED TRACKING

From the camera tracking of Section 3.3.6 and the correspondence matching of Section 3.4.3, we integrate the time domain between the object space and different camera views. Thereby, we include the shape of the trajectories from the camera images [2, 5, 11, 12, 15] in the three-dimensional reconstruction to perform the time-resolved tracking [34, 35, 43] of the fish in the school. For this purpose, we track the fish simultaneously in the camera images and the object domain. We branch multiple feasible trajectories using a series of steps [43] and extend our integer solution strategy [15] to find the candidate tracks that remain in a best-fit correspondence.

3.5.1. BRANCHING AND SMOOTHING OF FEASIBLE TRAJECTORIES

Starting from the first frame in the recording in Figure 3.10a, we initiate a new set of trajectories l that are ‘seeded’ from the triangulated correspondence matching (Section 3.4.3) for each frame $n = 1 \cdots N$. We then ‘branch’ these trajectories l by the camera tracking (Section 3.3.6) from the current frame n into the next frame $n + 1$ and define a set of multiple feasible trajectories extensions $l^* = 1 \cdots L^*$, and triangulate their position $\mathbf{X}_{l^*}^n$ and velocity $\mathbf{U}_{l^*}^n$.

FITTING OF TRAJECTORIES

In face of significant uncertainty from the image processing and tracking, we simultaneously integrate the knowledge of the position and velocity in the camera image and

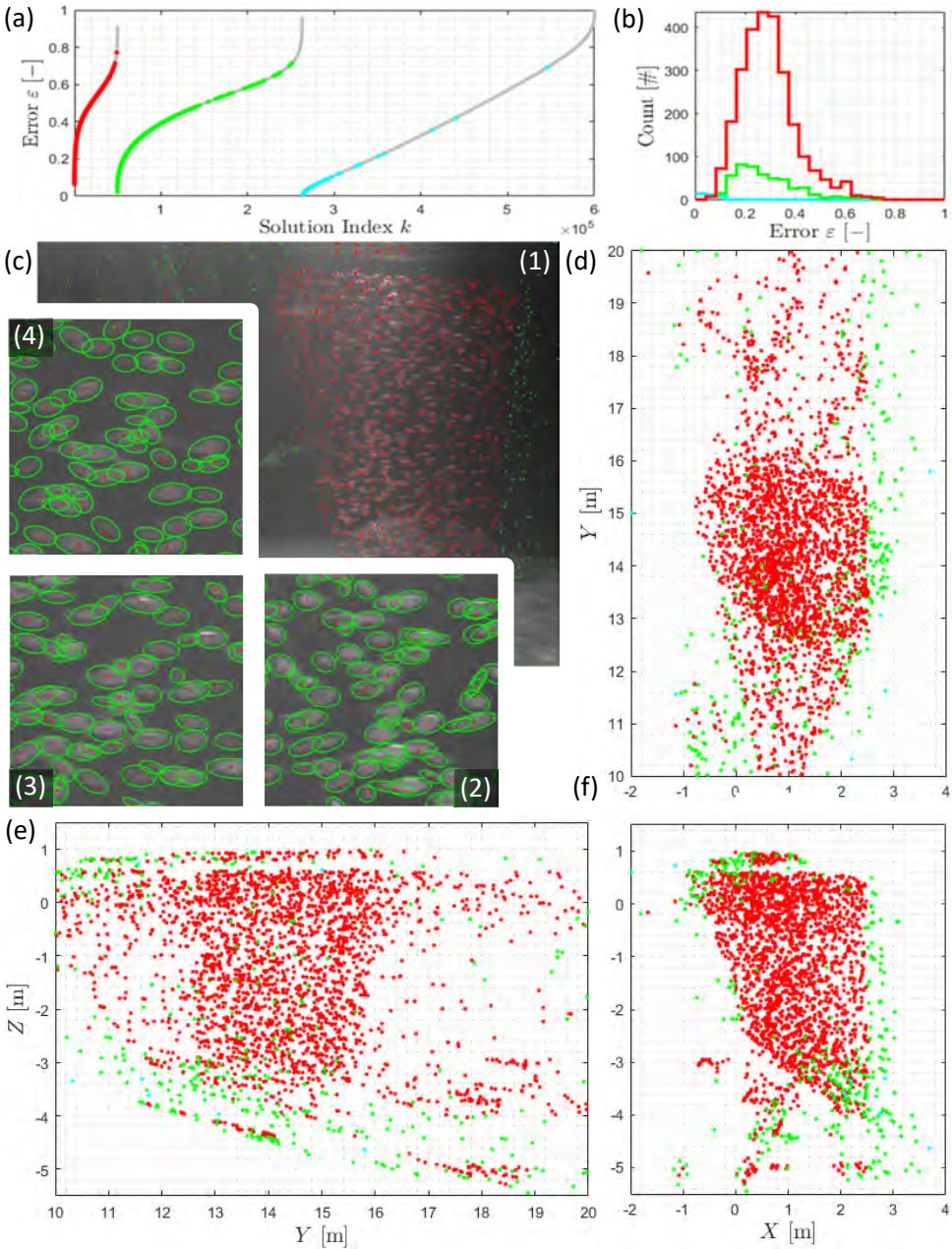


Figure 3.9: Cost-function optimization. a) Cost-function sorting for the camera cover and the reprojection. In grey is the available sorted solution vector for the input triangulation of Figure B.3 and overlaid the selected solution for the quadrifocal (red), trifocal (green), and residual stereoscopic correspondences (cyan). b) The distribution of the reprojection error for the optimized solution, for the quadrifocal (red), trifocal (green), and stereoscopic correspondences (cyan). c) Reprojected solution in view (1) of Figure 3.1a, on the right we find trifocal camera overlap (green) for the part of the school outside of view (2). d–f) A top-, side- and front view of the resulting object triangulation with a total of 3155 correspondences, clearly marking the position of the school and camera cover, with consistent color code.

object domain. This is achieved by introducing a trajectory model $\gamma(t)$. Here we use a polynomial basis function expansion:

$$\gamma(t) = \sum_k \mathbf{c}_k t^k = \mathbf{c}_0 + \mathbf{c}_1 t + \mathbf{c}_2 t^2 + \mathbf{c}_3 t^3 + \text{h.o.t.}, \quad (3.15)$$

with unknown vector coefficients \mathbf{c}_k in two, and three dimensions, for the camera image and object domain, respectively.

We fit $\gamma(t)$ to the tracking data on a predefined stencil n^* that runs over a span of neighboring frames⁶:

$$\min_{\mathbf{c}_k} \sum_{n \in n^*} \|\mathbf{X}^n - \gamma(t^n; \mathbf{c}_k)\|^2 \quad \forall l \text{ or } l^*, \quad (3.16)$$

and substitute the object coordinate \mathbf{X}^n with the image position \mathbf{x}_c^n when fitting in the camera view c .

Equation 3.16 can be efficiently solved by vectorization for a large set of trajectories l , or their branched extensions l^* , in the presence of non-uniform data in n^* . For the current work, we use a linear line fit [48] for Equation 3.15 which integrates the position and velocity [32, 34, 35] into a smooth signal [42, 43].

PREDICTION, CORRECTION, AND EXTENSION

We first use the trajectory fit in the images to improve and augment image processing and camera tracking. This is shown for the separate steps [43, 48] in Figure 3.10b:

1. ‘Predict’ new image positions for trajectory l from the fitting, and track the (green) ellipse for l^* that may have been outside the full overlap. This complements possible spurious camera tracking (shown in red).
2. ‘Correct’ a consistent value for the image position and velocity, and average the ellipse shape to recursively improve (occluded) image identifications for the newly branched camera tracking l^* (from green to yellow).
3. ‘Extend’ the image position for an existing trajectory l as we extrapolate the fit in case no image identification is available in the succeeding frames (cyan to yellow), here up to the bounds of the stencil n^* .

An example of this process is shown in Figure 3.10c with consistent color coding. The correction step suppresses noise and smooths the image identification in the presence of fish going into and coming out of occlusion (Section 3.3.6). Therefore, in the current work, the correction step is an integral part of the time-resolved tracking [43, 48]. From the corrected image processing we re-triangulate the object position and velocity and correct the trajectories in the object domain in the same way.

Marching forward (green) and backward (red) over the frames n within the processing window W of Figure 3.10a the correction step recursively interpolates the predicted and current measurement, and prevents a growing phase lag. This helps the tracking converge to smooth trajectories in face of a varying reconstruction uncertainty for the

⁶We define $n^* = n - N \dots n$ when tracking forward from frame n to $n + 1$, and the reverse $n^* = n \dots n + N$ when tracking in backward from n to $n - 1$, where N is the number of neighboring frames.

added degrees of freedom in object space. Finally, we compute the reprojection errors $\varepsilon_{pl^*}^n$ and camera incidence matrix $J_{pl^*}^n$ for the feasible trajectories l^* and account for the error from the calibration the same as in Section 3.4.1.

It is noteworthy that one is free to include higher order curve fitting for Equation 3.15. For example, augmenting the acceleration, curvature, torsion, and/or integrating independent measurements of these signals by the image processing (see remark Section 3.3.3). This would require additional modeling and for example extend the implementation to (non-linear) Kalman-filtering techniques [73], which can also include the error from the calibration [43, 65]. However, this is beyond the current scope.

3.5.2. SPLITTING AND MERGING OF FEASIBLE TRAJECTORIES

When the reprojection error $\varepsilon_{pl^*}^n$ for the newly branched trajectories l^* is violated, as is illustrated in Figure 3.10d by the red dot in view (2), we relax the incidence matrix $J_{pl^*}^n$ for the current correspondence match at frame n and reprocess its complete subgraphs of focality $f - 1$, see diagram Figure 3.10e. This breaks the trajectory extension l^* into multiple feasible branches. We refer to this process as ‘splitting’.

Subsequently, we find trajectories that meet in complete overlap for the current correspondences at frame n by the associated incidence matrices and find all combinations of their trajectories from the corresponding graph adjacency. This process we refer to as ‘merging’. We append to the feasible trajectories l^* and consistently reprocess the smoothing in object space.

FEASIBLE TRAJECTORY INCIDENCE

We repeat the splitting and merging process until no reprojection error is violated and append the multiple branches to the feasible trajectories l^* . Finally, we define the feasible trajectory incidence matrix F_{ll^*} between the trajectory l and its ‘branched’, ‘split’, and ‘merged’ extensions l^* as:

$$\begin{cases} F_{ll^*} = 1 \text{ when } l^* \text{ is branched, split, or merged from } l, \\ F_{ll^*} = 0 \text{ otherwise.} \end{cases} \quad (3.17)$$

This incidence matrix formally expresses the relation between existing trajectories l and new feasible extension l^* . This will be of use in the next part.

Moving forward and backward over the image frames, the splitting and merging make the tracking robust against error and allow us to find the missing ‘link’ and reward the matching of track segments [15]. When the reprojection error is continuously violated for the newly branched trajectories l^* , the splitting eventually terminates the extensions that decorrelate from the camera images [59]. Thereby, the integration of the time domain suppresses the tracking of triangulated ‘ghost-fish’ of Section 3.4.

3.5.3. COST-FUNCTION OPTIMIZATION

From the ‘seeding’, ‘branching’, ‘splitting’, and ‘merging’ of feasible trajectories l^* we optimize the (single) best extension l^* to l initiated from the triangulated correspondence matches. For this purpose, we extend the integer assignment of Equation 3.14 and find the trajectories in the object domain that best fit the simultaneous tracking in the images from the average projection error along the track [5, 11, 15].

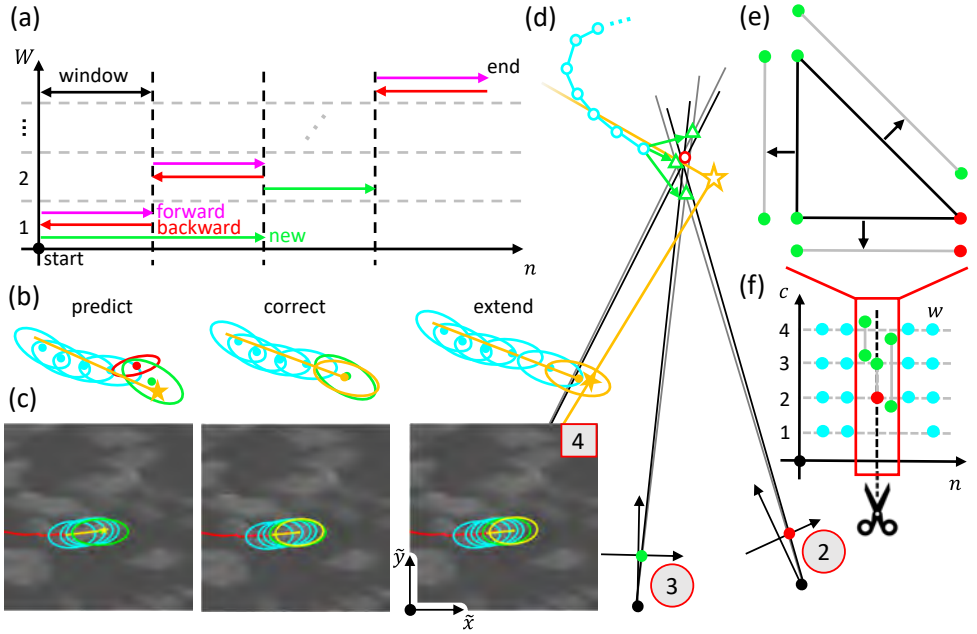


Figure 3.10: Simultaneous image and object tracking. a) Windowed data processing for the frames n in the window stepping W . In green, newly appended frames, in red, backward tracked frames, and in magenta, the second forward tracking step. b) Branching of tracks in the individual camera views. First, we ‘predict’ new track positions using the tracking (Figure 3.6) and a trajectory fit (yellow), matching new positions (green) and ignoring the spurious ellipse in red. Second, we ‘correct’ newly appended track positions averaging the ellipses in the trajectory fit (yellow). Third, we ‘extend’ the trajectory in case of missing image data and test the track for the reprojection of the object position (yellow star). c) Example of the track branching algorithm, providing a real case for the prediction, correction, and extension, with consistent color coding. d) Track branching in the object space, undergoing the same steps as for the camera views of (b). e) Relaxing of a trifocal set into its stereoscopic subgraph when violating the reprojection error (red dot). f) Diagram for the camera cover along the frame-set n that defines the weight function w .

AUGMENTED INTEGER ASSIGNMENT

To find the best feasible trajectory extension we extend the integer assignment of Equation 3.14. First we substitute $\varepsilon_{l^*} = \sum_{pn} \varepsilon_{pl^*}^n / \sum_{pn} J_{pl^*}^n \in [0, 1]$ and write the integer solution vector λ_{l^*} that is either 1 or 0. Secondly, we constrain the integer solution λ_{l^*} back to the image identification p for each frame n by the incidence matrix $J_{pl^*}^n$. We then augment the constraints the feasible trajectory incidence F_{ll^*} of Equation 3.17 and constrain an upper bound for the object trajectories l and their extensions l^* :

$$\begin{aligned} \min_{\lambda_{l^*}} \quad & \varepsilon_{l^*} \lambda_{l^*} \\ \text{subject to} \quad & J_{pl^*}^n \lambda_{l^*} \geq 1 \\ & F_{ll^*} \lambda_{l^*} \leq 1. \end{aligned} \quad (3.18)$$

The added constraint $F_{ll^*} \leq 1$ in Equation 3.18 ensures that the trajectories l do not split into multiple extensions l^* as we enforce picking a single one. Like before, the total

summation over λ_{l^*} ensures that we select a minimal number of solutions, where we now simultaneously maximize the camera cover and trajectory length, while ϵ_{l^*} rewards a unique solution at the minimal tracking error.

COST-FUNCTION SORTATION AND ITERATIVE SOLUTION STRATEGY

We now devise a similar cost-function solution strategy as in Section 3.4.3. First, we sort the starting frame $N_{l^*}^{\text{start}}$ in l^* , and subsequently, the end frame $N_{l^*}^{\text{end}}$ ascending. Thereby we reward long tracking sequences for l^* in forward tracking mode. Secondly, we define a weighting function $w_{l^*} = \sum_{pn} J_{pl^*}^n$ that rewards the matched number of image identification p and frames n . Lastly, we sort for the reprojection error ϵ_{l^*} .

We obtain a solution by an iterative ‘Divide-and-Conquer’ strategy [15], for further detail see Appendix B.7. Relaxing the second constraint in Equation 3.18 when l^* is solved for l , we remove ‘ghost-fish’ trajectories by solving only the first constraint, without user-defined filtering [43, 51]. We track the fish l within the processing window W of Figure 3.10a forward (green), backward (red), and again forward (magenta) to connect to the next window. Evaluating Equation 3.18 for each frame n , we keep the feasible trajectories l^* bounded within the computer memory, preventing an exponential number of candidates. This gives a set of trajectories that can be further evaluated.

RESULT FOR THE TIME-RESOLVED TRACKING

The results of this process are shown in Figure 3.11 over a processing window W of 50 frames. Figure 3.11a and b plot the sortation in track-length, the weighting- and cost-function similar to Figure 3.9a. Figure 3.11c–f color-code 1-second long tracks in the object domain with the average reprojection error $\epsilon_l^n = \sum_p \epsilon_{pl}^n / \sum_p J_{pl}^n$ which may extend over several pixels; we reproject tracks on the image like in Figure 3.6.

Figure 3.11g plots the distribution in track length in forward and backward tracking mode. First, newly appended frames (green) quickly drop off with 1350 tracks in the long tail, indicating broken trajectory segments. Secondly, 4266 fish are tracked backward over the window W , approximately twice the amount of ± 2000 fish. Finally, tracking again forward to connect to the next processing window, a correct amount of 2297 fish remain; removing the doubly-tracked fish, see also Figure B.4 of Appendix B.7.

In the current implementation forward, backward, and again forward tracking is crucial to obtaining long trajectories. In principle, this process can be further iterated to improve the reconstruction. Applying more sophisticated solution strategies⁷ may further achieve a lower cost value with possibly better object tracking.

3.6. OBJECT RECONSTRUCTION AND POST-PROCESSING

Having processed the images in Section 3.3, matched correspondences in Section 3.4, and tracked the fish simultaneously in the images and object domain in Section 3.5 we output the three-dimensional reconstruction for analysis. First, we perform a last step to fully integrate the framework of projective geometry in tracking the fish. Secondly,

⁷For example, one could sort the frame span $N_{l^*}^{\text{end}} + 1 - N_{l^*}^{\text{start}}$ instead of the start and end frame separately, or solely rely on the weighting function w_{l^*} , for example, over the whole recording sequence without the windowed processing.

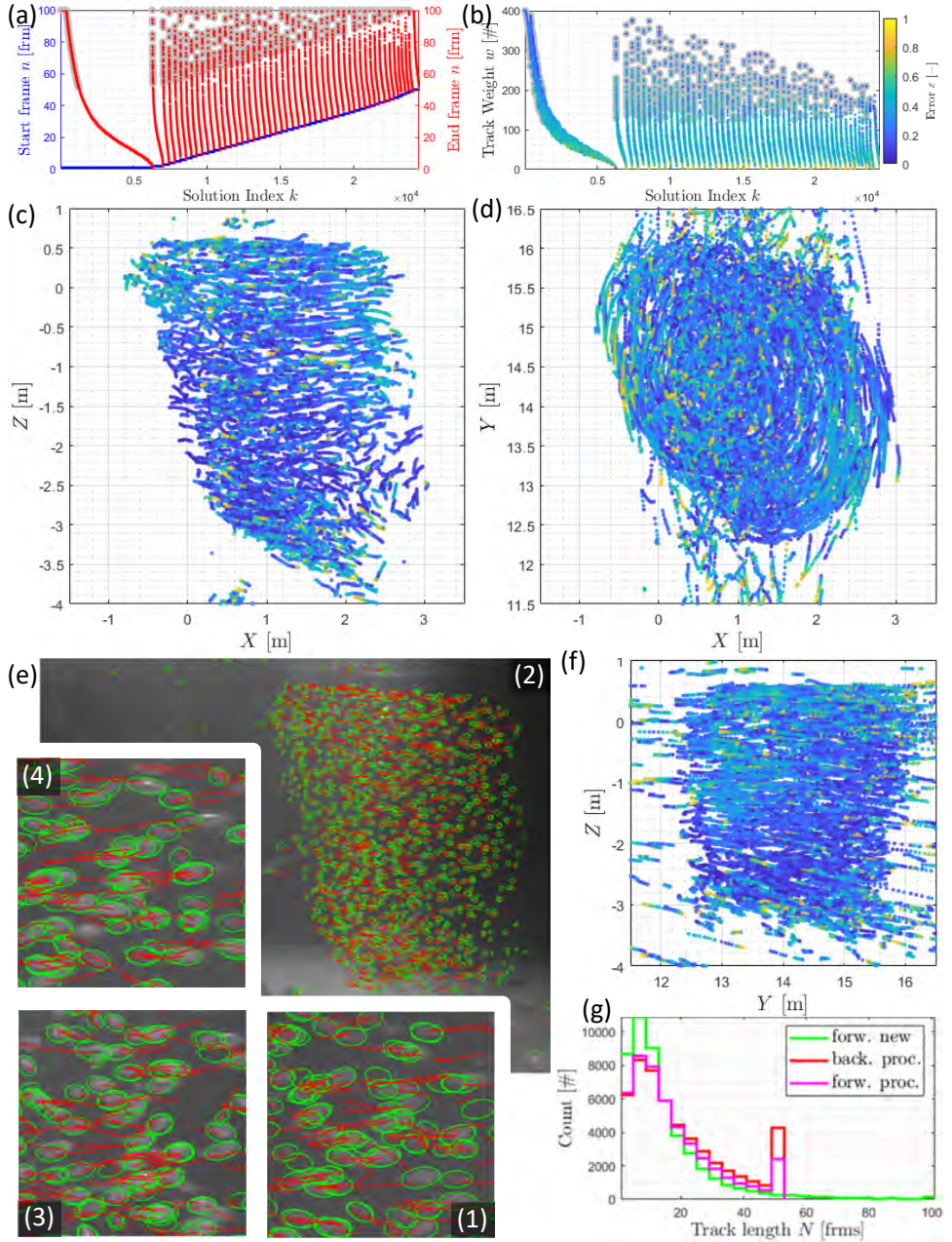


Figure 3.11: Time-resolved tracking. a) Start and end frames prioritized in the cost-function sortation. b) Weight function w_{l^*} for the camera cover, with the color-code the reprojection error ϵ_{l^*} . c, d, and f) The three-dimensional tracking data for 1-second long tracks. e) Reprojected tracks from object space, similar to Figure 3.6. g) Track-length distribution for the different steps in the processing window. In green the forward tracking appending new frames with 1350 tracks in the long tail, in red the backward tracking with 4266 doubly-track fish, in magenta the forward tracking with 2297 tracks; showing the correct number of ± 2000 tracked fish across the window. For (a) and (b) we mark the plotted trajectories of (c)–(f) for the cost-function solution in grey shading. All tracks are of greater or equal length than the window of 50 frames.

we filter the object tracking as partially performed in Figure 3.11, and post-process the tracking data in the object domain.

3.6.1. QUADRIC RECONSTRUCTION

We compute the object ellipsoid corresponding to the image processing to include the size of the fish in the object domain. Similar to the conic contour function (Section 3.3.3) an ellipsoid in the object domain is naturally expressed as a quadric surface [68]:

$$\tilde{\mathbf{X}}^T Q \tilde{\mathbf{X}} = 0 \text{ with } Q = \begin{bmatrix} q_1 & q_2/2 & q_4/2 & q_7/2 \\ q_2/2 & q_3 & q_5/2 & q_8/2 \\ q_4/2 & q_5/2 & q_6 & q_9/2 \\ q_7/2 & q_8/2 & q_9/2 & q_{10} \end{bmatrix}. \quad (3.19)$$

Here $\tilde{\mathbf{X}} = [X \ Y \ Z \ 1]^T$ is the augmented object coordinate (Chapter 2), and Q is the quadric coefficient matrix.

We reconstruct the quadric from the dual-space representation [69] in Appendix B.8. This naturally embeds the optical transfer from the object domain to the image and reverses the forward projection in Section 3.4.1 back to the image. This finalizes the integration of the framework of projective geometry. Note that the quadric reconstruction can be further used for the recursive branching of trajectories. For example, one can integrate the image processing across views and/or find the greater displacement of a fish group using correlation techniques [30, 31]; for further remarks see the end of Appendix B.8.

3.6.2. CLEANING AND FILTERING OF TRAJECTORIES

All data are processed with a window W of 50 frames, a linear trajectory fit of 5 frames (within one fish displacement), with minimum focality of $f \geq 3$ cameras and a maximum number of 3 frames to predict when data is missing in the images. To clean the obtained tracking data we first filter tracking sequences with length $T_l = N_l^{\text{end}} + 1 - N_l^{\text{start}}$ by restricting a minimum number of frames $T_l \geq \Delta T_{\text{min}}$ and remove shorter tracking. Secondly, we remove points along trajectories l by limiting the reprojection error $\varepsilon_l^n \leq \mathcal{E}_{\text{max}}$. For an illustration of this process see Supplementary-Figure B.6 of Appendix B.

We further add user-defined and dynamic filtering criteria. Firstly, we remove outliers in the positions by restricting the measurement volume for the recording sequence and remove outliers in the velocity data by limiting the physical value. Secondly, we remove positions that are outside the span of the fish school that freely relocates within the bounds of the (restricted) measurement domain. Finally, we restrict high signal derivatives such as the velocity and acceleration magnitude, and their value in the direction of the depth of field of the cameras.

All data is post-processed using a third-order trajectory (Equation 3.15), and missing data can be interpolated [34, 74, 75]. A post-processed result is shown in Figure 3.12 for the rapid escape response of Figure 3.1b. Reprojecting the trajectories on the dewarped images (Chapter 2), it is clear that we track the fish over a large distance in the different parts of the image as discussed in Section 3.2.2. Furthermore, from the inset camera views of Chapter 2 we track fish at narrow camera viewing angles, and the tracking re-

mains in the presence of large occlusions, see supplementary figures B.7 and B.8 for large occlusions and a set of super-wide-angle lenses.

3.7. PERFORMANCE ASSESSMENT

We continue to assess the performance of our tracking algorithms. We compute several quality metrics that help understand the reliability of the post-processed tracking data. First, we identify the main input parameters to the tracking and plot distribution in reprojection errors and track length. Secondly, we inspect the distribution of the probability of finding a fish in the next frame and present boundaries and operating conditions for the tracking. Subsequently, we plot a tracking reliability function from the track length distribution [30] and extract a tracking efficacy parameter. Finally, we relate the tracking efficacy back to the input parameters and present an overview of the tracked number of objects against the average track length [15].

3.7.1. PARAMETERS OF MAIN INPUT

We identify the image source density and time resolution of Section 3.2.2 as the main input parameters to the three-dimensional tracking algorithms. We start with estimating the image density surrounding a focal fish l in the cameras. We compute the average neighbor distance D_{pl}^n in the image over 18 nearest⁸ neighbors l^* by the normalized ellipse distance $d(\mathbf{c}_{pl}^n, \mathbf{x}_{pl^*}^n)$ of Appendix B.5 back-forth by swapping l and l^* . Likewise, we estimate the time resolution by the frame-to-frame image overlap O_{pl}^n from the average distances $d(\mathbf{c}_{pl}^n, \mathbf{x}_{pl}^{n-1})$ from the previous to the current ($n-1, n$), and $d(\mathbf{c}_{pl}^n, \mathbf{x}_{pl}^{n+1})$ the current to the next frames ($n, n+1$), and in reverse (swapping $n-1, n, n+1$).

When the image distance D_{pl}^n between two fish and overlap O_{pl}^n along a fish track are below 1 their value corresponds to images that are overlapping more than half their body length. When the distance functions are of value 2, images are exactly adjacent, and for values greater than > 2 , images are fully separated. Finally, based on a hexagonal sphere packing with a maximum packing density of $\pi\sqrt{3}/6 \approx 0.9069$ in the plane, we relate the image distance back to the image source density by $0.9069D_{pl}^{n-2}$ expressed in ‘fish-image-per-pixel’ (fipp), while the overlap O_{pl}^n between frames is directly read as a ‘fish-swim-per-frame’ (fspf).

REPROJECTION ERROR AND TRACK-LENGTH DISTRIBUTION

We start with quantifying the variation of the normalized reprojection error ε_{pl}^n used to optimize the tracking of Section 3.5. We plot the average value of the reprojection error $\varepsilon(O, D)$ as a function of the image distance D and overlap O . In Figure 3.13a, we find lowest reprojection errors ε within the range $O \leq 3/4$ fspf and $D \geq 2$ with a density less than 0.227 fipp, and optimal values above $D \geq 3$, or 0.101 fipp, attaining a minimal value of $\varepsilon \approx 0.25$. These bounds locate an overall minimum and thereby isolate the best tracking for the input parameters.

This is reassured by the track length T_l^n . In Figure 3.13b we plot the distribution

⁸By the ray-tracing geometry of Figure 3.7 that can connect over $d_{pq} \leq 2$ neighboring fish in another view, we select the number of neighbors based on a hexagonal packing with two radial shells (*i.e.* $6 + 12$).

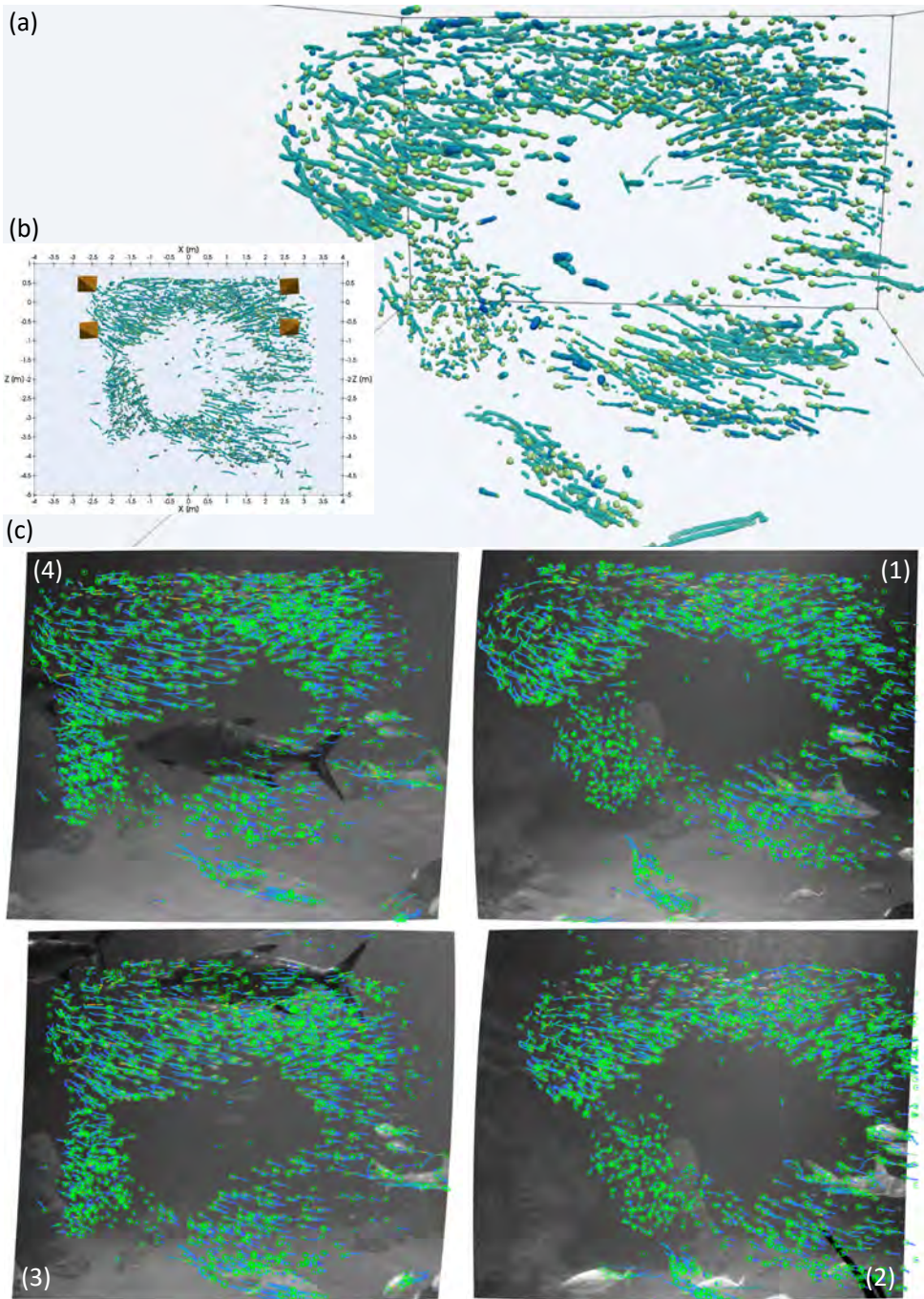


Figure 3.12: Render of snapshot (2) of Figure 3.1b. a) 'Birds-eye' view for post-processed fish tracking. In green the ellipsoid (quadric) reconstruction with the trajectories color-coded with the linear velocity for 1-second long tracks. b) Front view aligned with the camera views, showing the positions of the calibrated cameras with narrow camera baselines and angles (Chapter 2). c) The four views imaging the fish school, overlaid the projected object ellipsoids and the fish trajectories with consistent color-code from (a) and (b) for 1/2-second long tracks to prevent overcrowding the images.

$T(O, D)$ by the input parameters O and D . We find that a maximum length of $\Delta T \sim 160$ frames (~ 4 seconds at 40 fps in Figure 3.12) is obtained for $O \leq 1/2$ and $D \geq 4$ (or 0.057 fipp). Outside this region, we find that the track length distribution drops where the reprojection error is elevated in Figure 3.13a. Finally, the tracking methods start to break down for $D \leq 2$ when going into a heavy occlusion number ($D \rightarrow 1$) and approaching an ‘optical-limit’ (1 fipp). However, below $D \leq 2$ (i.e. > 0.227 fipp), it may be in question what is actually tracked, lacking a well-defined image correspondence; resulting in patched object tracks with a high degree of noise.

3

3.7.2. COIN TOSS: PROBABILITY TRACKING INTO THE NEXT FRAME

From the track length distribution, we now ask: ‘What is the probability of tracking a fish from the previous into the next frame?’. For this purpose, we bookkeep a ‘coin toss’ for the indexed fish tracks l over the frame set n . We either document a ‘heads’ $P^{\text{NF}} = 1$ when the current tracking index exists in the previous and next frame or a (complimentary) ‘tails’ $P^{\text{NF}} = 0$ when the current index neither occurs in the previous nor next frame. Bookkeeping this ‘coin toss’ we then compute the average probability from the number of ‘heads’ and ‘tails’ by the total number of draws over multiple data sets.

RELIABILITY BOUNDARIES AND OPERATING CONDITIONS

Firstly, in Figure 3.13c, we plot the joint probability distribution $P^{\text{NF}}(O, D)$ by the image distance D and overlap O . Reliable tracking $P^{\text{NF}} \rightarrow 1$ (dark red) is obtained for an upper bound in the image overlap of $O \leq 1/2$ and a lower bound in image density of $D \geq 3$. Outside this region, the tracking reliability rapidly degrades for an image overlap $1/2 \leq O \leq 1$ to $P^{\text{NF}} \approx 0.6$, while for an image density below $D < 3$, the probability drops to $P^{\text{NF}} \approx 0.9$ which, in principle, reduces the reliability to a few tens of frames. Furthermore, no data is obtained below the line $D = 2O$ through the origin. Here the tracking algorithms fail to extract the tracking data.

Secondly, in Figure 3.13d, we plot the joint probability distribution of $P^{\text{NF}}(O, \varepsilon)$ by the image overlap O and (normalized) reprojection error ε . Here we find that for moderate reprojection error up to $\varepsilon \leq 0.3$ the tracking reliability remains unchanged and that for $0.3 < \varepsilon \leq 0.8$ the upper bound for the image overlap gradually restricts the reliability. At last, only for high reprojection error $\varepsilon > 0.8$ the reliability rapidly degrades.

Having analyzed reliability bounds, our tracking data are not restricted within these domains. In Figure 3.13e and f, we plot the joint distributions $f(O, D)$ and $f(O, \varepsilon)$ by the input parameters O and D and reprojection error ε . Most of our data are within an overlap $O \leq 1/2$, image distance $2 \leq D \leq 8$, and reprojection error $\varepsilon \leq 0.8$ which may vary over a number of pixels. According to Figure 3.13c and d, these numbers are within range of reliable tracking. Only from Figure 3.13b the image density seems to pose the major challenge to obtaining longer tracks since the best results are obtained for $D > 4$.

A local image source density above 0.101 up to 0.227 fipp pushes the implementation of the current tracking algorithms. Such images densities are common to current works in experimental fluid-mechanics [43, 46, 48, 51, 52] and expressed in ‘particle-per-pixel’ (ppp) are known to be challenging beyond ~ 0.05 up to 0.125 ppp (although numbers may differ from application to application). This confirms the challenges as introduced in Section 3.2 in obtaining long tracks in three dimensions.

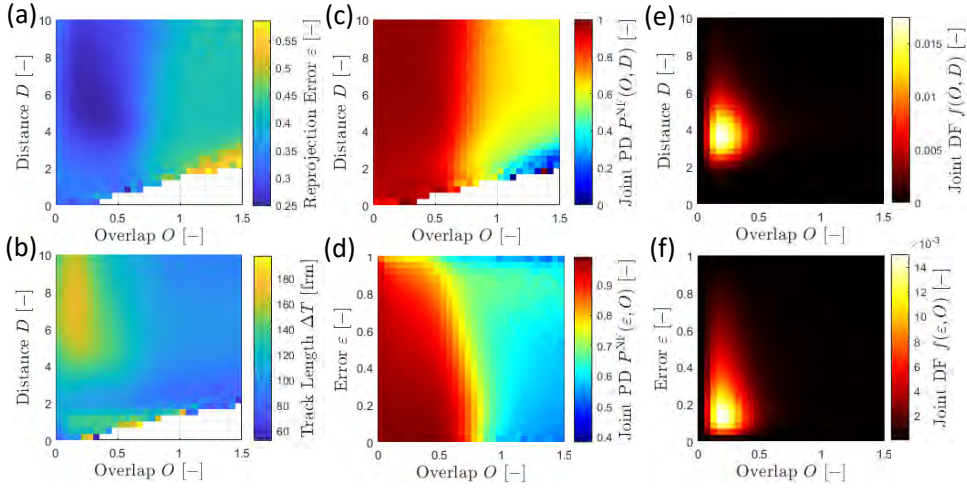


Figure 3.13: Tracking performance by input parameters. a) Average reprojection error $\varepsilon(O, D)$ by image overlap O and distance D . b) Average track length $T(O, D)$ by image overlap O and distance D . c) Joint probability distribution $P^{\text{NF}}(O, D)$ by image overlap O and distance D . d) Joint probability distribution $P^{\text{NF}}(O, \varepsilon)$ by image overlap O and reprojection error ε . e) Joint distribution function $f(O, D)$ by image overlap O and distance D . f) Joint distribution function $f(O, \varepsilon)$ by image overlap O and variation in reprojection error ε .

3.7.3. TRACK-LENGTH DISTRIBUTION AND TRACKING EFFICACY

Since the track length ΔT greatly varies with the input image data, we now would like to know what percentage of the school remains tracked at a certain number of frames. For this purpose, we consider a tracking reliability function [30] for which we identify a single tracking efficacy parameter.

We formally express the percentage of the school that remains tracked by the complementary cumulative probability distribution function of finding a track of length T greater or equal to ΔT :

$$F^{\text{NF}}(T \geq \Delta T) = \eta_{\text{NF}}^{\Delta T}. \quad (3.20)$$

Equation 3.20 is a monotonically decreasing function of the distribution in track length ΔT . Therefore, on the right-hand side, we compare its decay against the tracking efficacy parameter η_{NF} that we can extract from the tracking data.

EXTRACTION OF THE TRACKING EFFICACY PARAMETER

Considering the tracking data of Figure 3.12, we first draw distributions in track length ΔT independently for each frame n to correctly sample the occurrence of trajectories through the image data. In Figure 3.14a, we plot the conditional probability density function $f(F^{\text{NF}}(T \geq \Delta T)|\Delta T)$ against the track-length ΔT and obtain the percentage of the school that remains tracked. Here we find that, after the post-processing steps, the minimum track length of 80 frames rapidly drops off on a semi-logarithmic scale along the x -axis, and compared to the inset sample curves for different reliability of Equation 3.20 we read a tracking efficacy bound between $0.99 < \eta_{\text{NF}} < 0.999$.

To obtain a better picture of the variation in the tracking efficacy we invert Equation 3.20 by $\eta_{\text{NF}} = F(T \geq \Delta T)^{1/\Delta T}$ and compute the conditional probability density func-

tion for $f(\eta_{\text{NF}}(\Delta T)|\Delta T)$ from the distribution in track length ΔT . In Figure 3.14b, we find that the initial tracking efficacy rapidly drops off from $\eta_{\text{NF}} \approx 0.999$ and that after this drop we obtain a more or less stable value of $\eta_{\text{NF}} \approx 0.994$. We keep the extraction of η_{NF} as the reliability estimate, where from Equation 3.20 we can infer the percentage of the school tracked $F(T \geq \Delta T)$ at certain track length ΔT .

INTERRELATING THE TRACKING EFFICACY AND THE PROBABILITY NEXT FRAME

We end this section by interrelating the tracking efficacy η_{NF} back to the input parameters and presenting an overview of the tracking reliability. The probability of tracking into the next frame was found to go up with the distance in the image D , and down with increasing reprojection error ε and image overlap O . Therefore, we expect the tracking efficacy η_{NF} to go down for increasing ε/D and O/D . This motivates an ad hoc downward scaling for the group $\varepsilon O/D^2$, multiplying the validity of the calibration (Chapter 2), the ‘fish-swim-per-frame’, and the number of ‘fish-image-per-pixel’.

In Figure 3.14c, we extract the tracking efficacy η_{NF} and plot against the group $\varepsilon O/D^2$ for the multiple data sets underlying Figure 3.13. Indeed, the efficacy η_{NF} drops off with these parameters. As is expected the best tracking is obtained for the lower reprojection error (best calibration), the highest time resolution (lowest ‘fish-swim-per-frame’), and is rewarded for sparse fish schooling (least ‘fish-image-per-pixel’). Drawing the overall correspondence between we find that our tracking algorithm provides high efficacy numbers ranging well above $\eta_{\text{NF}} > 0.985$ for the current data, although operating at relatively high image density (beyond 0.101 fipp).

Finally, we compute the average number of tracked objects $L_{\text{obj}} = \sum_n L^n/N$, with L^n the number of trajectories and N the total number of frames, and plot against the average number of tracked frames $T_{\text{obj}} = \sum_{nl} T_l^n/L^n/N$. In Figure 3.14d we track approximately 1500 to 2500 fish with an average track length of 100 to 175 frames where we color code the tracking efficacy parameter η_{NF} [15]. We find that a higher tracking efficacy promotes longer track length, with a slight bias to obtaining a larger number of objects tracked. Here the school of ± 2000 fish may partly be out of view, in heavy occlusion, or in parts of the fish tank that are poorly illuminated. Together, these numbers now provide reference values for the final part of this thesis.

3.8. CONCLUSIONS

In this chapter, we demonstrated the application of tracking algorithms from experimental fluid mechanics in combination with previous efforts from field measurements to track and triangulate schooling fish in three dimensions over a large distance. Imaging inside a complex underwater environment, we discussed several elements of and challenges to tracking fish inside the large ocean aquarium at the Rotterdam zoo. We presented the necessary steps involved in processing the image data, including background removal and the extraction of fish images at different length-scale using a series of convolution filters. In particular, we fully integrated the framework of projective geometry starting from image identification, and included the directional dependent projection of fish. This makes the current work robust against variation in the reprojection error and remaining errors from calibration, here imaging at narrow camera angles over a large measurement volume. Furthermore, the correspondence matching and triangulation

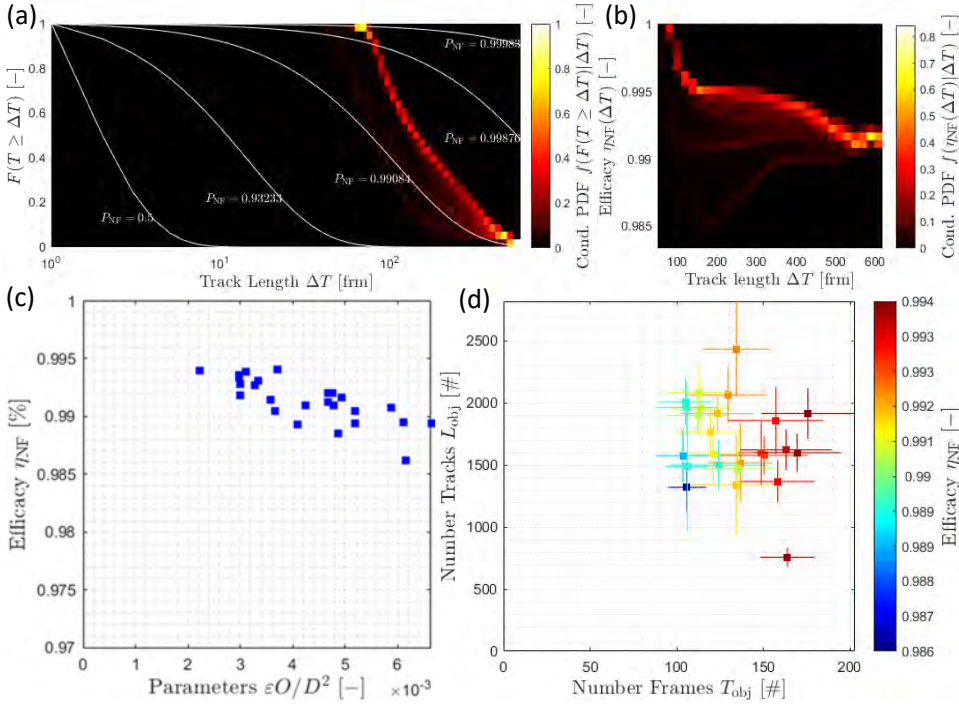


Figure 3.14: Tracking efficacy and overview. a) Reliability of tracking into the next frame for the data in Figure 3.12. b) Extraction of the tracking efficacy η_{NF} . c) Tracking efficacy against the input parameters O and D , and reprojection error ϵ . d) Overview of the tracking data, number of fish L_{obj} against the average track-length T_{obj} , the error bars indicate the variation and the color-code give the tracking efficacy parameter η_{NF} .

lation algorithms are scalable for any number of views and deal with missing data in the presence of large occlusion by solitary predators without the need for prior knowledge of camera overlap. Finally, we showed that the forward, backward, and (again) forward tracking of fish is crucial in obtaining the correct number of fish tracked within the current optimization strategy.

Subsequently, we assessed the performance of our tracking algorithms. First, we identified the main parameters of input to the fish tracking and shed light on the distribution of the reprojection error and track length. We found the lowest reprojection errors ($\epsilon \approx 0.25$) and longest tracking sequences (± 160 frames) up to an image density of 0.101 ‘fish-image-per-pixel’ (fipp) and an image overlap in consecutive frames below 0.5 ‘fish-swim-per-frame’ (fspf). Secondly, we inspected the probability of tracking a fish into the next frame. We confirmed an optimal performance in the same region, while our methods break down above 0.227 fipp local image source density. Since the tracking algorithms do not operate at optimal conditions, we subsequently asked what percentage of the school remains tracked for a number of frames. For this purpose, we constructed a reliability function and extracted a tracking efficacy parameter. We reported a tracking efficacy well above $\eta_{NF} > 0.985$ and presented a rough downward scaling at increasing

reprojection error, fish-swim-per-frame, and fish-image-per-pixel.

These quality metrics are now available for tracking data in the coming chapter. Our tracking algorithms are applicable in the broader context of time-resolved tracking of (bio-)active particles as well as the tracking of organisms, and ellipsoidal objects in three dimensions.

REFERENCES

- [1] A.-J. Buchner, K. Muller, J. Mehmood, and D. Tam, *Hopping trajectories due to long-range interactions determine surface accumulation of microalgae*, PNAS **118**, 1 (2021).
- [2] Z. Wu, N. I. Hristov, T. H. Kunz, and M. Betke, *Tracking-reconstruction or reconstruction-tracking? comparison of two multiple hypothesis tracking approaches to Interpret 3D Object Motion from Several Camera Views*, in *Workshop on Motion and Video Computing (WMVC)* (IEEE, Snowbird, UT, USA, 2009).
- [3] H. S. Wu, Q. Zhao, D. Zou, and Y. Q. Chen, *Acquiring 3D motion trajectories of large numbers of swarming animals*, in *2009 IEEE 12th International Conference on Computer Vision Workshops, ICCV Workshops 2009* (IEEE, Kyoto, 2009) pp. 593–600.
- [4] D. Zou, Q. Z. Q. Zhao, H. S. W. H. S. Wu, and Y. Q. C. Y. Q. Chen, *Reconstructing 3D motion trajectories of particle swarms by global correspondence selection*, in *12th International Conference on Computer Vision*, Vol. 1 (IEEE, Kyoto, 2009) pp. 1578–1585.
- [5] H. S. Wu, Q. Zhao, Z. Danping, and C. Yan Qiu, *Automated 3D trajectory measuring of large numbers of moving particles*, OPTICS EXPRESS **19**, 7646 (2011).
- [6] Y. Liu, H. Li, and Y. Q. Chen, *Automatic tracking of a large number of moving targets in 3D*, in *European Conference on Computer Vision*, Vol. 7575 LNCS (Springer, Berlin, Heidelberg, 2012) pp. 730–742.
- [7] A. Attanasi, A. Cavagna, L. Del Castello, I. Giardina, S. Melillo, L. Parisi, O. Pohl, B. Rossaro, E. Shen, E. Silvestri, and M. Viale, *Collective Behaviour without Collective Order in Wild Swarms of Midges*, PLoS Computational Biology **10**, 1 (2014).
- [8] K. Van Der Vaart, M. Sinhuber, A. M. Reynolds, and N. T. Ouellette, *Mechanical spectroscopy of insect swarms*, Science Advances **5**, 1 (2019).
- [9] D. Adhikari, B. J. Gemmell, M. P. Hallberg, E. K. Longmire, and E. J. Buskey, *Simultaneous measurement of 3D zooplankton trajectories and surrounding fluid velocity field in complex flows*, Journal of Experimental Biology **218**, 3534 (2015).
- [10] D. W. Murphy, D. Olsen, M. Kanagawa, R. King, S. Kawaguchi, J. Osborn, D. R. Webster, and J. Yen, *The Three Dimensional Spatial Structure of Antarctic Krill Schools in the Laboratory*, Scientific Reports **9** (2019), 10.1038/s41598-018-37379-9.
- [11] Zheng Wu, N. I. Hristov, T. L. Hedrick, T. H. Kunz, and M. Betke, *Tracking a large number of objects from multiple views*, in *12th International Conference on Computer Vision, Iccv* (IEEE, Kyoto, Japan, 2009) pp. 1546–1553.
- [12] Z. Wu, T. H. Kunz, and M. Betke, *Efficient track linking methods for track graphs using network-flow and set-cover techniques*, in *Computer Society Conference on Computer Vision and Pattern Recognition* (IEEE, Colorado Springs, CO, USA, 2011) pp. 1185–1192.

- [13] D. H. Theriault, N. W. Fuller, B. E. Jackson, E. Bluhm, D. Evangelista, Z. Wu, M. Betke, and T. L. Hedrick, *A protocol and calibration method for accurate multi-camera field videography*, *Journal of Experimental Biology* **217**, 1843 (2014).
- [14] A. Cavagna, I. Giardina, A. Orlandi, G. Parisi, A. Procaccini, M. Viale, and V. Zdravkovic, *The STARFLAG handbook on collective animal behaviour: Part I, empirical methods*, Tech. Rep. (2008).
- [15] A. Attanasi, A. Cavagna, L. Del Castello, I. Giardina, A. Jelić, S. Melillo, L. Parisi, F. Pellicani, E. Shen, E. Silvestri, and M. Viale, *GReTA-A Novel Global and Recursive Tracking Algorithm in Three Dimensions*, *IEEE Transactions on Pattern Analysis and Machine Intelligence* **37**, 2451 (2015).
- [16] B. E. Jackson, D. J. Evangelista, D. D. Ray, and T. L. Hedrick, *3D for the people: Multi-camera motion capture in the field with consumer-grade cameras and open source software*, *Biology Open* **5**, 1334 (2016).
- [17] M. Sinhuber, K. van der Vaart, R. Ni, J. G. Puckett, D. H. Kelley, and N. T. Ouellette, *Three-dimensional time-resolved trajectories from laboratory insect swarms*, *Scientific Data* **6** (2019), 10.1038/sdata.2019.36.
- [18] D. J. Evangelista, D. D. Ray, S. K. Raja, and T. L. Hedrick, *Three-dimensional trajectories and network analyses of group behaviour within chimney swift flocks during approaches to the roost*, *Proceedings of the Royal Society B: Biological Sciences* **284**, 1 (2017).
- [19] H. Ling, G. E. McLvor, G. Nagy, S. MohaimenianPour, R. T. Vaughan, A. Thornton, and N. T. Ouellette, *Simultaneous measurements of three-dimensional trajectories and wingbeat frequencies of birds in the field*, *Journal of the Royal Society Interface* **15** (2018), 10.1098/rsif.2018.0653.
- [20] A. Cavagna, S. Melillo, L. Parisi, and F. Ricci-Tersenghi, *SparTA Tracking across Occlusions via Partitioning of 3D Clouds of Points*, *IEEE Transactions on Pattern Analysis and Machine Intelligence* **43**, 1394 (2021).
- [21] A. Cavagna, X. Feng, S. Melillo, L. Parisi, L. Postiglione, and P. Villegas, *CoMo: A Novel Comoving 3D Camera System*, *IEEE Transactions on Instrumentation and Measurement* **70** (2021), 10.1109/TIM.2021.3074388.
- [22] C. K. Hemelrijk, H. Hildenbrandt, J. Reinders, and E. J. Stamhuis, *Emergence of Oblong School Shape: Models and Empirical Data of Fish*, *Ethology* **116**, 1099 (2010).
- [23] S. Butail and D. A. Paley, *Three-dimensional reconstruction of the fast-start swimming kinematics of densely schooling fish*, *Journal of the Royal Society Interface* **9**, 77 (2012).
- [24] J. Delcourt, M. Denoël, M. Ylief, and P. Poncin, *Video multitracking of fish behaviour: A synthesis and future perspectives*, *Fish and Fisheries* **14**, 186 (2013).

- [25] S. H. Wang, J. Zhao, X. Liu, Z.-M. Qian, Y. Liu, and Y. Q. Chen, *3D Tracking Swimming Fish School with Learned Kinematic Model Using LSTM Network*, in *International Conference on Acoustics, Speech and Signal Processing (ICASSP)* (IEEE, New Orleans, LA, USA, 2017) pp. 1068–1072.
- [26] M. Romensky, J. E. Herbert-Read, C. C. Ioannou, A. Szorkovszky, A. J. Ward, and D. J. Sumpter, *Quantifying the structure and dynamics of fish shoals under predation threat in three dimensions*, *Behavioral Ecology* **31**, 311 (2020).
- [27] N. Chenouard, I. Smal, F. De Chaumont, M. Maška, I. F. Sbalzarini, Y. Gong, J. Cardinale, C. Carthel, S. Coraluppi, M. Winter, A. R. Cohen, W. J. Godinez, K. Rohr, Y. Kalaidzidis, L. Liang, J. Duncan, H. Shen, Y. Xu, K. E. Magnusson, J. Jaldén, H. M. Blau, P. Paul-Gilloteaux, P. Roudot, C. Kervrann, F. Waharte, J. Y. Tinevez, S. L. Shorte, J. Willemse, K. Celler, G. P. Van Wezel, H. W. Dan, Y. S. Tsai, C. O. De Solórzano, J. C. Olivo-Marin, and E. Meijering, *Objective comparison of particle tracking methods*, *Nature Methods* **11**, 281 (2014).
- [28] M. Patel, S. E. Leggett, A. K. Landauer, I. Y. Wong, and C. Franck, *Rapid, topology-based particle tracking for high-resolution measurements of large complex 3D motion fields*, *Scientific Reports* **8** (2018), 10.1038/s41598-018-23488-y.
- [29] A. La Porta, G. A. Voth, A. M. Crawford, and E. Bodenschatz, *Fluid particle accelerations in fully developed turbulence*, *Nature* **409**, 1017 (2001).
- [30] R. Adrian and J. Westerweel, *Particle Image Velocimetry* (Cambridge University Press, Cambridge, 2011).
- [31] M. Raffel, C. Willert, F. Scarano, C. Kähler, S. Wereley, and J. Kompenhans, *Particle Image Velocimetry: A Practical Guide*, 3rd ed. (Springer, 2018).
- [32] J. Willneff and A. Gruen, *A New Spatio-Temporal Matching Algorithm For 3D-Particle Tracking Velocimetry*, in *The 9th of International Symposium on Transport Phenomena and Dynamics of Rotating Machinery* (ETH Zurich, Institute of Geodesy and Photogrammetry, Honolulu, Hawaii, 2002) pp. 1–7.
- [33] F. Pereira, H. Stürer, E. C. Graft, and M. Gharib, *Two-frame 3D particle tracking*, *Measurement Science and Technology* **17**, 1680 (2006).
- [34] N. T. Ouellette, H. Xu, and E. Bodenschatz, *A quantitative study of three-dimensional Lagrangian particle tracking algorithms*, *Experiments in Fluids* **40**, 301 (2006).
- [35] H. Xu, *Tracking Lagrangian trajectories in position-velocity space*, *Measurement Science and Technology* **19** (2008), 10.1088/0957-0233/19/7/075105.
- [36] D. Doh, D. Kim, K. Cho, Y. Cho, W. Lee, T. Saga, and T. Kobayashi, *Development of genetic algorithm based 3D-PTV technique*, *Journal of Visualization* **5**, 243 (2002).

- [37] Y. Ge, S. S. Cha, and J.-H. Park, *Study of particle tracking algorithms based on neural networks for stereoscopic tracking velocimetry*, *Optics and Lasers in Engineering* **44**, 623 (2006).
- [38] S. P. Panday, K. Ohmi, and K. Nose, *An ant colony optimization based stereoscopic particle pairing algorithm for three-dimensional particle tracking velocimetry*, *Flow Measurement and Instrumentation* **22**, 86 (2011).
- [39] G. E. Elsinga, F. Scarano, B. Wieneke, and B. W. Van Oudheusden, *Tomographic particle image velocimetry*, *Experiments in Fluids* **41**, 933 (2006).
- [40] C. Atkinson and J. Soria, *An efficient simultaneous reconstruction technique for tomographic particle image velocimetry*, *Experiments in Fluids* **47**, 553 (2009).
- [41] J. Westerweel, G. E. Elsinga, and R. J. Adrian, *Particle Image Velocimetry for Complex and Turbulent Flows*, *Annu. Rev. Fluid Mech* **45**, 409 (2013).
- [42] D. Schanz, A. Schröder, S. Gesemann, and B. Wieneke, *'Shake the box': Lagrangian particle tracking in densely seeded flows at high spatial resolution*, in *9th International Symposium on Turbulence and Shear Flow Phenomena*, Vol. 3 (Melbourne, 2015).
- [43] D. Schanz, S. Gesemann, and A. Schröder, *Shake-The-Box: Lagrangian particle tracking at high particle image densities*, *Experiments in Fluids* **57**, 1 (2016).
- [44] F. Huhn, D. Schanz, S. Gesemann, and A. Schröder, *FFT integration of instantaneous 3D pressure gradient fields measured by Lagrangian particle tracking in turbulent flows*, *Experiments in Fluids* **57** (2016), 10.1007/s00348-016-2236-3.
- [45] J. F. Schneiders and F. Scarano, *Dense velocity reconstruction from tomographic PTV with material derivatives*, *Experiments in Fluids* **57** (2016), 10.1007/s00348-016-2225-6.
- [46] A. Rubbert and W. Schröder, *Iterative particle matching for three-dimensional particle-tracking velocimetry*, *Experiments in Fluids* **61** (2020), 10.1007/s00348-020-2891-2.
- [47] K. Mallery, S. Shao, and J. Hong, *Dense particle tracking using a learned predictive model*, *Experiments in Fluids* **61**, 1 (2020).
- [48] S. Tan, A. Salibindla, A. U. M. Masuk, and R. Ni, *Introducing OpenLPT: new method of removing ghost particles and high-concentration particle shadow tracking*, *Experiments in Fluids* **61**, 1 (2020).
- [49] Y. Gim, D. K. Jang, D. K. Sohn, H. Kim, and H. S. Ko, *Three-dimensional particle tracking velocimetry using shallow neural network for real-time analysis*, *Experiments in Fluids* **61**, 1 (2020).
- [50] A. R. Khojasteh, Y. Yang, D. Heitz, and S. Laizet, *Lagrangian coherent track initialization*, *Physics of Fluids* **33** (2021), 10.1063/5.0060644.

- [51] T. Jahn, D. Schanz, and A. Schröder, *Advanced iterative particle reconstruction for Lagrangian particle tracking*, Experiments in Fluids **62** (2021), 10.1007/s00348-021-03276-7.
- [52] Y. Yang and D. Heitz, *Kernelized Lagrangian particle tracking*, Experiments in Fluids **62** (2021), 10.1007/s00348-021-03340-2.
- [53] H. G. Maas, A. Gruen, and D. Papantoniou, *Particle tracking velocimetry in 3-dimensional flows. 1. Photogrammetric determination of particle coordinates*, Experiments in Fluids **15**, 133 (1993).
- [54] N. A. Malik, T. Dracos, and D. A. Papantoniou, *Particle tracking velocimetry in three-dimensional flows - Part II: Particle tracking*, Experiments in Fluids **15**, 279 (1993).
- [55] Y. G. Guezennec, R. S. Brodkey, N. Trigui, and J. C. Kent, *Algorithms for fully automated three-dimensional particle tracking velocimetry*, Experiments in Fluids **17**, 209 (1994).
- [56] M. Novara, K. J. Batenburg, and F. Scarano, *Motion tracking-enhanced MART for tomographic PIV*, Measurement Science and Technology **21** (2010), 10.1088/0957-0233/21/3/035401.
- [57] K. Lynch and F. Scarano, *A high-order time-accurate interrogation method for time-resolved PIV*, Measurement Science and Technology **24** (2013), 10.1088/0957-0233/24/3/035305.
- [58] K. P. Lynch and F. Scarano, *An efficient and accurate approach to MTE-MART for time-resolved tomographic PIV*, Experiments in Fluids **56** (2015), 10.1007/s00348-015-1934-6.
- [59] G. E. Elsinga and S. Tokgoz, *Ghost hunting - An assessment of ghost particle detection and removal methods for tomographic-PIV*, Measurement Science and Technology **25** (2014), 10.1088/0957-0233/25/8/084004.
- [60] D. Verhoeven, *Limited-data computed tomography algorithms for the physical sciences*, APPLIED OPTICS **32**, 3736 (1993).
- [61] B. Wieneke, *Iterative reconstruction of volumetric particle distribution*, Measurement Science and Technology **24** (2013), 10.1088/0957-0233/24/2/024008.
- [62] M. Novara, D. Schanz, N. Reuther, C. J. Kähler, and A. Schröder, *Lagrangian 3D particle tracking in high-speed flows: Shake-The-Box for multi-pulse systems*, Experiments in Fluids **57**, 1 (2016).
- [63] S. M. Soloff, R. J. Adrian, and Z. C. Liu, *Distortion compensation for generalized stereoscopic particle image velocimetry*, Measurement Science and Technology **8**, 1441 (1997).
- [64] B. Wieneke, *Volume self-calibration for 3D particle image velocimetry*, Experiments in Fluids **45**, 549 (2008).

- [65] B. Wieneke, *Improvements for volume self-calibration*, Measurement Science and Technology **29** (2018), 10.1088/1361-6501/aacd45.
- [66] D. Schanz, S. Gesemann, A. Schröder, B. Wieneke, and M. Novara, *Non-uniform optical transfer functions in particle imaging: Calibration and application to tomographic reconstruction*, Measurement Science and Technology **24** (2013), 10.1088/0957-0233/24/2/024009.
- [67] G. Bertens, G. Bagheri, H. Xu, E. Bodenschatz, and J. Moláček, *In situ cloud particle tracking experiment*, Review of Scientific Instruments **92** (2021), 10.1063/5.0065806.
- [68] R. Hartley and A. Zisserman, *Multiple view geometry in computer vision*, 2nd ed. (Cambridge University Press, Cambridge, 2004).
- [69] G. Cross and A. Zisserman, *Quadric Reconstruction from Dual-Space Geometry*, in *Sixth International Conference on Computer Vision* (IEEE, Bombay, India, 1998) pp. 1–7.
- [70] P. Meer and I. Weiss, *Smoothed differentiation filters for images*, Journal of Visual Communication and Image Representation **3**, 58 (1992).
- [71] T. Lindeberg, *Image Matching Using Generalized Scale-Space Interest Points*, Journal of Mathematical Imaging and Vision **52**, 3 (2015).
- [72] P. Viola and M. Jones, *Rapid Object Detection using a Boosted Cascade of Simple Features*, in *Computer Society Conference on Computer Vision and Pattern Recognition* (IEEE, Kauai, HI, USA, 2001).
- [73] M. M. Verhaegen and V. Verdult, *Filtering and system identification: a least squares approach* (Cambridge University Press, 2007).
- [74] S. Gesemann, F. Huhn, D. Schanz, and A. Schröder, *From Noisy Particle Tracks to Velocity, Acceleration and Pressure Fields using B-splines and Penalties*, in *18th International Symposium on the Application of Laser and Imaging Techniques to Fluid Mechanics* (Lisbon, Portugal, 2016).
- [75] J. M. Lawson, E. Bodenschatz, C. C. Lalescu, and M. Wilczek, *Bias in particle tracking acceleration measurement*, Experiments in Fluids **59**, 1 (2018).

4

INNER STRUCTURE AND KINEMATICS OF THREE-DIMENSIONAL FISH SCHOOLS

This chapter demonstrates the application of the measurement technique of Chapter 2 and the tracking algorithms of Chapter 3 to extract the full three-dimensional tracking data of the schooling fish inside the ocean aquarium of the Rotterdam zoo. We start this chapter by providing an overview of the data sets recorded over different measurement weeks. We identify a variety of schooling behaviors by visual inspection of the shape and motion of the school. Subsequently, we extract statistical distributions from the position and velocity of the fish. We present several quantitative metrics to analyze the variability of the school in terms of geometry, shape, and internal structure. For this, we consider the time evolution of the volume and aspect ratio(s) of the school, and the local fish density. We characterize the radial distribution of the fish in the school by computing the spatial moments. The radial distribution reveals a bimodality where the fish either cluster to form a cohesive group or redistribute towards the boundary of the school. This redistribution towards the boundary of the school is found to be characteristic of a predator attack. Next, for the school kinematics, we investigate the time series of the distribution of fish velocity in the school, local polarization of heading, the velocity of the school center of mass, angular momentum, and volume rate-of-change. We partition the total kinetic energy in the school and derive a set of dimensionless kinematic parameters. These parameters describe several elementary motions from which we construct a ternary diagram for the distribution of kinetic energy in the school. For the different kinematics and geometries of the school, we compare local state variables for the swimming velocity, local heading polarization, and fish density. Our results suggest an underlying relationship between these local state variables. Their actual interrelations open many future research directions into the three-dimensional dynamics of fish schooling.

4.1. TRACKING DATA ACQUIRED AT THE ROTTERDAM ZOO

To begin, we provide an overview of the tracking data acquired at the Rotterdam zoo. We review the different measurement weeks and discuss the environmental conditions relevant to the data collection. We present examples representative of the large variety of schooling behaviors observed in the fish tank. From these examples, we categorize the schooling behaviors following the work by Pitcher and Wyche [1] for a school of 250 (salt water) sand-eels, and Magurran and Pitcher [2] for a school up to 50 (sweet water) mullets, for further reading see [3–5]. Categorizing the behavior of the schooling fish, we introduce the relevant terminology.

4.1.1. MEASUREMENTS AT THE OCEANIUM AQUARIUM

A total of 6 measurement weeks were performed over 4 years to acquire image data of a large school of ± 2000 *Harengula clupei* (false herring) located in the Oceanium aquarium at the Rotterdam zoo. The measurement weeks occurred between August 2017 and January 2020 during off-season visitor summer and winter months with 6-month intervals. The measurement volume is $20 \times 20 \times 6 \text{ m}^3$ as introduced in Chapter 1. Only a few studies have conducted experiments at such length-scale [6, 7] and the number of fish is substantially more than previous fish tracking work in two [8–16] and three dimensions [17–24] in a laboratory setting.

The fish swim counter-clockwise in the tank when viewed from the top. The water circulation is clockwise, hence the fish swim against the flow. The climate control in the tank simulates a semi-natural habitat with seasonal and daytime effects. These effects include variations in the water quality (temperature, oxygen concentration, and salinity) and lighting conditions. This, in turn, affects the fish behavior and activity (day/night, summer/winter, predation, breeding, *etc.*), and visibility by the water turbidity and illumination. For further details see Chapter 1.

During each measurement period, we acquired ± 150 high-quality multiple-camera video recordings, amounting to ~ 40 TB of raw image data. For the first measurement week, we used a set of wide-angle lenses (NIKKOR AF-24mm), while for the rest, we used super-wide-angle lenses (VENUS OPTICS LAOWA 7.5mm MFT) with a greater field of view, see Supplementary-Figure B.8. To position the school within our camera views, the curators trained the fish to feed within a designated area. This was achieved by placing the feeding machine above the tank (Chapter 1) at a given position in front of the large window that provides the optical access (Chapter 2), see top Figure 4.1.

All image data of the fish school were acquired during the daytime. No data were recorded during nighttime due to a lack of illumination inside the tank. By the day and nighttime cycle inside the fish tank and variation in ambient light, all data sets have varying lighting conditions and fish behavior. Therefore, to capture a wide variety of schooling dynamics inside the tank, we adapted the camera frame rate between 20 and 70 *Hz* with different exposure times between 10 and 40 *ms*.

DATA SELECTION

The measurement technique described in Chapter 2 and the implementation of the tracking algorithms described in Chapter 3, allow us to extract the three-dimensional trajectories of the fish from the images recorded with the 4 synchronized cameras. From

each measurement week, we processed a subset of approximately ~ 20 – 25 data sets. The selected data sets were chosen uniformly throughout the measurement week(s) and day-time to be representative of the fish behavior.

We particularly focused on data sets in which the school resides in a milling configuration. This behavior is also seen in the natural environment [25–28], and has been described as a torus and (bait-)ball shape, and is assumed to be a natural state for the school. To investigate the variability in the schooling behavior, we also selected data to include avoidance responses such as sudden expansions and splitting behaviors [1, 2] arising from interaction with other fish species. A full data descriptor is found in Appendix C.1 for the processed camera calibration, and in Appendix C.2 for the processed tracking data.

4.1.2. MILLING, PREDATORY ESCAPE, SHOALING, AND FORAGING

In figures 4.1 to 4.3, we plot the results obtained from the three-dimensional tracking. We provide 1-second long tracks of the fish position in the tank height (Z), width (X), and visual-depth (Y) coordinate (meters) that is pointing away from the camera setup. Each track is color-coded with the magnitude of the swimming velocity U . The coordinates $X = 0$ and $Z = 0$ m correspond to positions in front of the camera setup, the water surface is located between $Z = 1$ and 1.5 m, and the bottom of the tank is located between $Z = -4.5$ and -4 m. We find a broad variety of behaviors for the schooling fish. These include multiple (single, double, triple) fish mills positioned next to each other, cruising and foraging groups that swim freely through the tank, and an extensive range of escape behaviors triggered by a predator; all documented in Table C.2 of Appendix C.2.

MILLING

Figure 4.1 presents a set of four differently shaped fish schools where the fish swim in a milling configuration [25–28] and turn counter-clockwise in a single rotating ‘fish-vortex’ or ‘fish-tornado’ as viewed from above. Here, the continuous rotation naturally fixes the school’s center of mass while the fish swim at an approximately constant velocity. This behavior occurs when the fish do not actively engage with a predator.

In Figure 4.1a, we show three examples of a ‘surface mill’ formed below the water surface. Here the shape of the fish mill is flattened at the location of the feeding machine. From left to right, we find three typical shapes: (1) The school accumulates underneath the surface, changes its shape, and spreads into a flat ‘pancake’ close to the water’s surface. This shape is observed during the daytime feeding of the fish. (2) The mill is shaped like a droplet that resides below the water surface in a hemisphere. (3) One part of the school remains milling under the water surface, while the rest extends deeper into the fish tank like a ‘droplet’ pinch-off.

In Figure 4.1b, we present examples of fish mills that are freely swimming below the water surface. Again we identify three shapes: (1) A cylindrical-shaped mill (left). (2) A large ‘fish ball’ (center). (3) A ball-shaped mill is located towards the bottom of the fish tank (right). Unlike the hemisphere-shaped surface mill of Figure 4.1a, the milling school at the bottom of the tank (-4 m) does not form a dome. Instead, the mill remains spherically shaped, although the school slightly flattens.

Large deformation may develop within fish mills with a cylindrical shape. Figure 4.1c

presents three increasingly deformed fish mills. In such mills, we observe that the cohesion between the top and bottom parts may get broken. Here, the irregular shape slowly drifts and splits into multiple mills, which can be next or on top of each other and eventually rejoin later (not shown).

Finally, we show several examples of slender tornado-shaped fish mills in Figure 4.1d. These shapes extend from the top to the bottom of the fish tank and are vertically skewed, like in Figure 4.1c. Although the fish mills in figures 4.1c and d are strongly skewed in shape, the fish still swim close to a circular motion on a tilted plane. Note that this plane may be at a different angle from the vertical direction than its skewed shape.

ESCAPE RESPONSES

4

In Figure 4.2, we present several escape responses of the harengulas during a predatory attack. Typically, the predator fish (and cohabitant species) approach the fish school from the front or back with respect to the overall viewing direction of the camera setup. This approach direction aligns with our optical setup and is advantageous in experiments tracking the escape response. The broad range of escape maneuvers provides a large set of extreme events and is a natural framework to study the inner kinematics of the fish school when not milling.

First, in Figure 4.2a, we show the fish school in response to a predator swimming in the vicinity of the cylindrical mill. As the predator does not appear to pose a direct threat we find that the schooling fish avoid the approaching predator or ‘herd’ away [1, 2]. Depending on the predator’s location, we find that the school either develops a characteristic sideways dent (left) or dents from below (center). In contrast, on the right of Figure 4.2a, the ‘dented’ mill avoids the passing predator without losing cohesion.

Secondly, in Figure 4.2b, we present three examples of a trespassing predator while the fish school does not lose cohesion. When the predator comes closer to the school in Figure 4.2c, we observe a diverse range of complex dynamics and rapid escape responses. Following Magurran and Pitcher [2], the predator creates an empty space or ‘vacuole’ when passing through (also see Pitcher and Wyche [1]), here triggering ‘donut’ and ‘star’-like dynamic shapes, including sudden flash expansions as the fish startle and flee away (on the right). The predator interaction interrupts the mill that eventually breaks cohesion as the school occasionally splits into parts due to the predator’s near presence. With increasing intensity of the predator attack, we find that the motion restores to milling after multiple turns, splits, and rejoining with an occasional ‘hourglass’-like shape [1, 2] (omitted here) when evading the predator’s threat.

Finally, in Figure 4.2d, we show three examples of collective responses as the fish in the school become increasingly agitated. On the left of the page, we first find a rising school that is fleeing a predator. Secondly, to the right of the page, we find a mill escaping a predator. Here the school is forced to the bottom and assumes the shape of an ‘angled torus’ like motion (center). Finally, we show a ‘collective downdraft’ in which the school rapidly dives (right); similar diving responses have also been reported in the field [29].

SHOALING AND FORAGING

In Figure 4.3, we present several examples of less frequent collective behavior that occur when the fish are not under immediate predation. Although these behaviors are

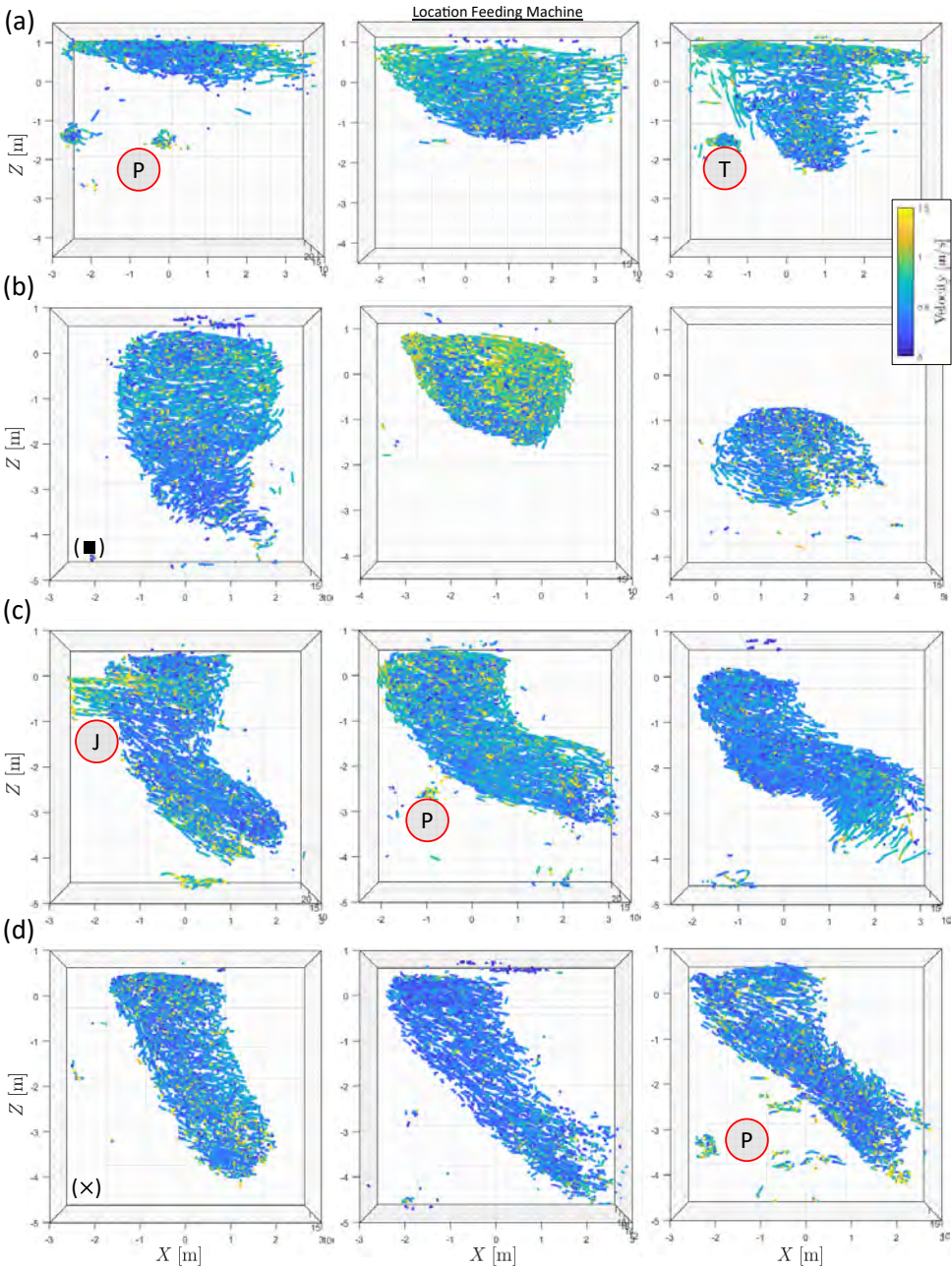


Figure 4.1: Milling behavior. Along the height of the page, a 3×4 grid of snapshots of differently shaped fish mills (left, center, right). a) A surface mill that is flattened into a ‘pancake’-like shape (left), grouping in a hemisphere at the water surface of the fish tank (center), and a ‘droplet’ pinch-off (right). b) A cylindrical fish mill (left), a large fish ball (center), and a ball-shaped mill near the bottom of the fish tank (right). c) A cylindrical fish mill deforming over the height of the fish tank; on the left, a group of fish joins the school. d) A slender, ‘tornado’-shaped cylindrical fish mill that stretches far down the bottom of the fish tank at an increasing angle from the vertical direction (towards the right). We indicate the location of the feeding machine on top, the predator (P), the turtle (T), and joining a fish group (J), and give the data (\times , \blacksquare) marked in Figure 4.5a.

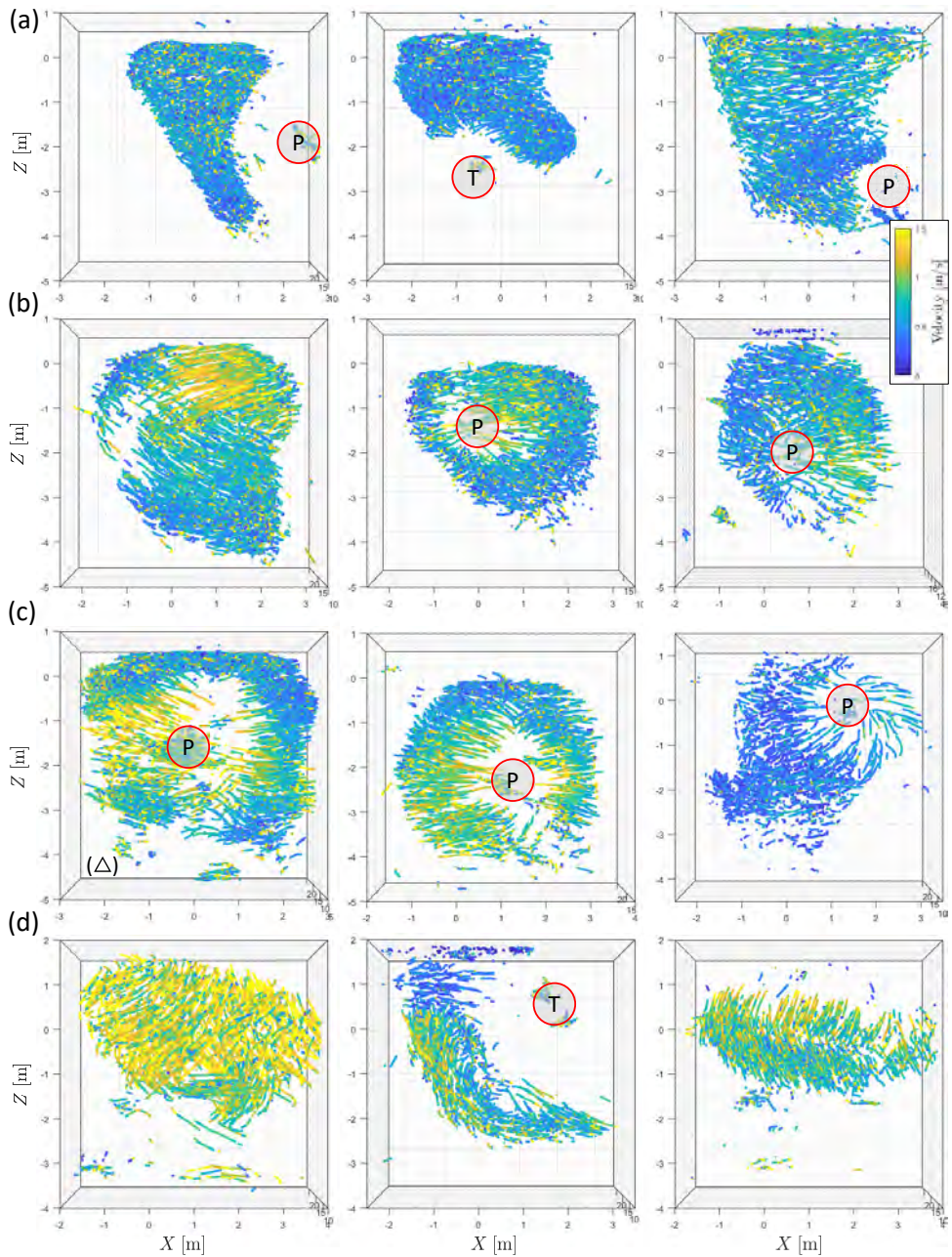


Figure 4.2: Escape responses. From top to bottom, at increasing agitation, a 3×4 grid of snapshots of different escape responses and their complex features (left, center, right). a) A dented fish mill that avoids and is herded by a predator passing sideways. b) An approaching predator that triggers an avoidance response, exciting the school. c) Escape responses: complex splitting, a 'donut/star'-shaped escape response, and a rapid flash expansion (from left to right). d) Other escape responses: a collective uprising towards the surface (left), severe deformation into an angled torus (center), and a collective downdraft or dive (right). We indicate the location of the predator (P) and the turtle (T) and give the time series data (Δ) from Figure 4.4 onward, as also marked in Figure 4.5a.

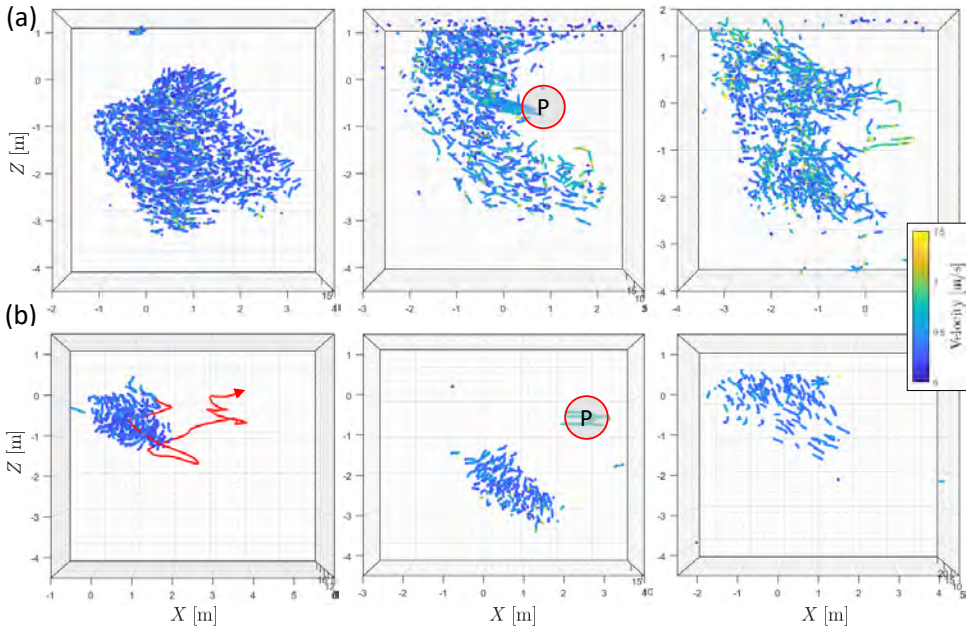


Figure 4.3: Shoaling and foraging. From top to bottom in a 3×2 grid of different snapshots (left, center, right). a) Fish milling in a slower shoal (left), a swarming-like shoal (middle), and a fish shoal that displays a ‘chaotic-darting’ type motion for the individual fish (right). b) Several foraging schools that are separated from the large fish mill and are freely cruising through the fish tank. On the left is a path of a foraging school (red); for its time series see figures C.8 and C.9 in Appendix C. We indicate the location of the predator (P).

observed less often, they have been consistently identified during each measurement week, over the course of the 4-year period.

In Figure 4.3a, we show three different examples of fish mills ranging from a swarming aggregation on the left to a disorganized state on the right. Following Pitcher [3], we suggest that this behavior may be referred to as ‘shoaling’, which presents a broader category and relaxes strong requirements on the degree of polarization (alignment) for schooling. Sorted in decreasing number of fish, we find a slowly evolving fish mill that includes non-circular deformations (left), a fish school that seems to be in a disorganized state (center), and on the right, we find a fish shoal that is displaying a ‘chaotic-darting’ type of (swarming) motion for the individual fish in the school.

In Figure 4.3b presents three different examples of fish groups that separated from the main school. These schools are freely swimming or ‘cruising’ [1, 2] in a uni-directional motion through the large ocean aquarium, see inset red path (left). We call this behavior ‘foraging’. This behavior occurs when the fish are exploring the semi-natural habitat searching for food. Here the fish school constantly relocates its position with short intermediate moments of milling (left Figure 4.3b).

4.2. SCHOOL SHAPE AND DISTRIBUTION OF FISH

We proceed to extract quantitative statistics describing the shape of the school from the many examples presented in the previous section and reported in Appendix C.2. For the remainder of this chapter, we aim to extract meaningful and descriptive statistics that can be used for reference to improve our understanding of schooling behavior.

First, we present examples of the time evolution of the volume and aspect ratios of the school in the presence of predators as well as other cohabiting species and record the local fish density in the neighborhood of each fish. These metrics are common to the study of three-dimensional bird flocks [30, 31], fish schools [17, 18, 23], and schooling simulations [32–34], and help characterize variations in the school shape.

Secondly, building on previous work [17, 18, 30, 31], we characterize the distribution of fish in the school. For this, we compute spatial moments of the radial fish distribution and report temporal variations for the moment mean, standard deviation, and skewness. We show that these moments capture essential changes in the internal configuration of the school. Finally, we study the variability of the shape parameters and the spatial moments across multiple data sets and show that the moment skewness reveals a bimodality during predator interaction.

4

4.2.1. SCHOOL CENTER OF MASS, SEMI-AXES AND LOCAL FISH DENSITY

We characterize the instantaneous shape of the school by extracting geometric parameters from the distribution of fish positions. We write the position of the i^{th} fish in the school as the vector $\mathbf{X}_i(t) = [X_i \ Y_i \ Z_i]^T$ for $i = 1 \cdots I$ with I the total number of fish, and $(\bullet)^T$ the vector transpose. For the remainder of this chapter, we only consider data sets that contain a single school or a part of it, and exclude cases when the school is split into multiple groups, see Table C.2 in Appendix C.2. All fish trajectory data are post-processed with the smoothing and differentiation methods introduced in Chapter 3.

DEFINITION OF THE SCHOOL CENTER OF MASS AND VOLUME, AND LOCAL FISH DENSITY
Assuming unit mass for each fish, we compute the center of mass of the school $\langle \mathbf{X}_i \rangle = \mathbf{X}_M = \sum_{i=1}^I \mathbf{X}_i / I$, where bracket notation $\langle \bullet \rangle$ is used to average over all fish in the school. Next, we define a bounding ellipse to represent the school shape and we use it to infer the volume and geometry. First, we compute the directions of the principal axes of the school by performing a singular value decomposition that gives an orthonormal vector basis $\{\mathbf{e}_1, \mathbf{e}_2, \mathbf{e}_3\}$. Secondly, along each principal axis, we define the length $\lambda_1 > \lambda_2 > \lambda_3$ for the semi-major, intermediate, and semi-minor axis, to include most of the fish distributed within the school as the mean value of absolute fish position plus two standard deviations. The detail of the definition is provided in Appendix C.3.

The bounding ellipse represents to a good approximation the shape of the fish school (see diagram and examples in Figure C.1 of Appendix C.3) and the semi-axis provide an elementary description of the school shape, comparable to previous approaches [18, 30, 31]. We use the semi-axes values to estimate the volume of the school as $\mathcal{V} = 4\pi/3 \lambda_1 \lambda_2 \lambda_3$. In addition, the ratios between the semi-axes approximate the aspect ratios of the three-dimensional fish school. We call $\eta_1 = \lambda_1/\lambda_3$ the dominant aspect ratio between the semi-major and semi-minor axis, and $\eta_2 = \lambda_2/\lambda_3$ the subdominant aspect ratio between the intermediate and semi-minor axis.

We also define the local fish density $\rho_i(t)$ for each fish i in the school by considering the J closest neighboring fish [34]. The local fish density is computed as $\rho_i(t) = J/(4\pi/3(\langle d_{ij}(t) \rangle_{j \in J})^3)$, where $\langle d_{ij}(t) \rangle_{j \in J}$ is the average distance between the fish i and its J closest neighbors. Here we choose $J = 10$. This is more than a single nearest neighbor ($J = 1$) and provides robustness against noise averaging over a number of tracked fish positions while remaining to be smaller than a subgroup ($J \sim 100$) for the school of ± 2000 fish. The local density gives the number of fish (#) per cubic meter (m^{-3}) and characterizes the compactness in the fish vicinity. We note that different J may give different density estimates [35] and that we include more fish than a supposed interaction range reported for birds [36]. Finally, we report the average value for the local fish density $\langle \rho_i(t) \rangle$ alongside other time series analyses.

TIME SERIES OF THE VOLUME, DENSITY, ASPECT RATIOS OF THE SCHOOL

Figure 4.4 presents our results for one particular data set corresponding to a school that is evading a predator (see Figure 4.2c, left Δ). Figure 4.4 corresponds to the same data set (C1S21 in Table C.2) as the one presented in Figure 3.1b in Chapter 3. Results for other data sets are provided in supplementary figures C.4 to C.9 at the end of Appendix C and include the different schooling behaviors presented in Section 4.1.

In Figure 4.4a, the recording starts with a predator attack ($t = 0$). The school expands as it escapes the predator, see snapshot (1) at $t = 1.5$ s. This expansion leaves an empty space inside the school, which is referred to as a ‘vacuole’ in the literature [1, 2]. Subsequently, the school rejoins, see snapshot (2) from $t = 5$ to $t \sim 10$ s, and returns to a cohesive fish mill in snapshot (3) from $t = 13$ s onward. Figure 4.4b, c, e, and f give the time evolution of the volume $\mathcal{V}(t)$, the average value for the local fish density $\langle \rho_i(t) \rangle$ and the dominant and subdominant aspect ratios $\eta_1(t)$, and $\eta_2(t)$.

At $t = 1.5$ s, the volume of the school is large, $\mathcal{V} \sim 120$ m^3 , corresponding to a typical school diameter of 6 m . From $t = 5$ to $t = 13$ s, the volume of the school decreases to ~ 40 m^3 corresponding to a diameter of ~ 3 m . For a school of ± 2000 fish, these variations in the volume would correspond to a significant decrease in the average spacing between fish from ~ 40 to 27 cm . However, these fish spacing are not observed for the evolution in average local fish density $\langle \rho_i(t) \rangle$ that we report on a different y-axis with units m^{-3} in blue (on the right).

The average local fish density is initially close to $\langle \rho_i \rangle \sim 80$ m^{-3} at $t = 1.5$ s and increases to $\langle \rho_i \rangle \sim 110$ m^{-3} for $t = 13$ s. These values correspond to distances between fish ranging from ~ 27 and 31 cm , which is significantly smaller than the distances inferred from the volume alone. The difference in respective fish spacing obviously comes from the large vacuole that is not included in the computation of the local fish density $\rho_i(t)$, despite its variation roughly following the volume evolution $\mathcal{V}(t)$ of the school.

In Figure 4.4c, we plot both the dominant and subdominant aspect ratios [31]. During the escape maneuver at $t = 1.5$ s, the semi-axes are nearly equal ($\eta_1 \simeq \eta_2 \sim 1.5$), and the shape of the school is nearly spherical. From $t = 5$ to $t \sim 10$ s, we find that the dominant and subdominant aspect ratios reach different values of $\eta_1 \simeq 2$, and $\eta_2 \simeq 1$, indicating a change in the shape of the school. Eventually, the school takes a nearly cylindrical shape at $t = 13$ s, and the aspect ratios remain different with $\eta_1 \simeq 2.5$, and $\eta_2 \simeq 1.5$. Finally, we show in Figure 4.4f the change in aspect ratios with the volume of the school.

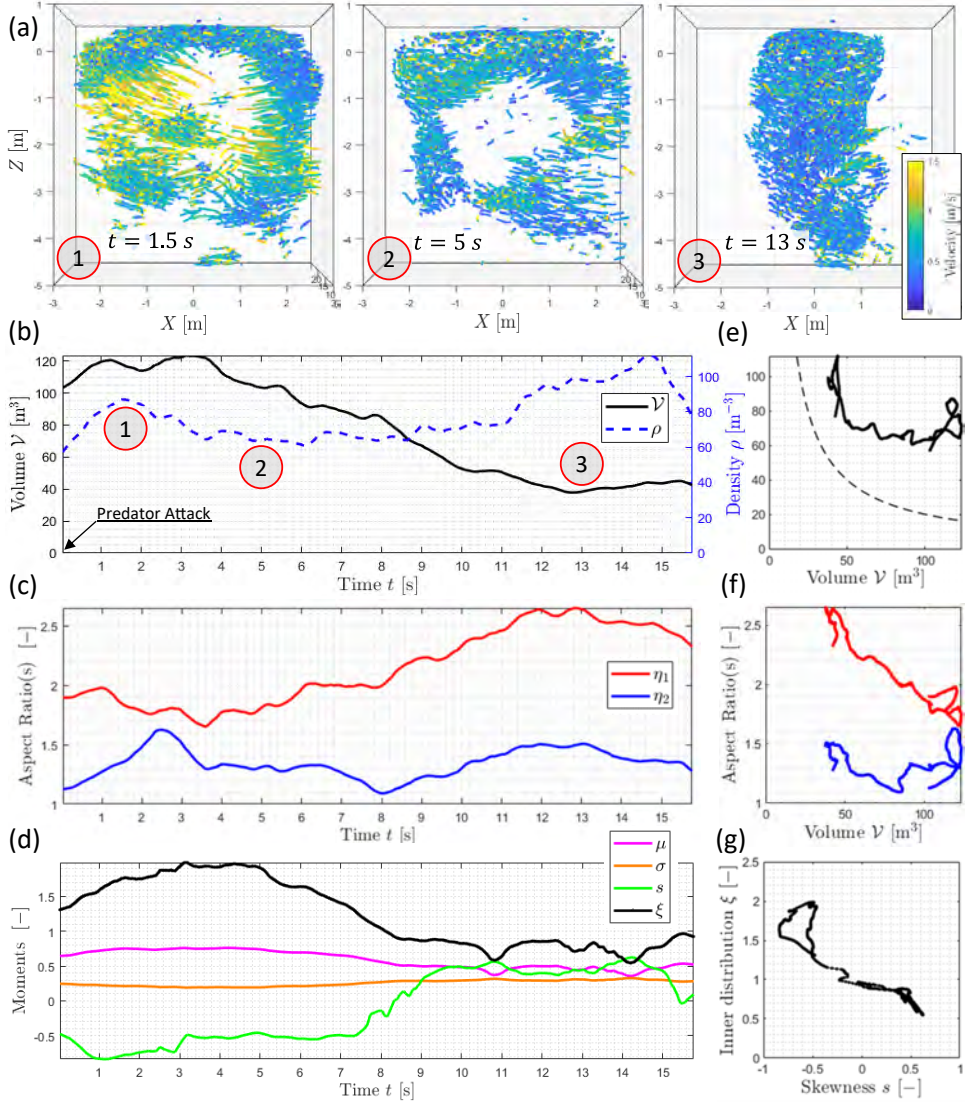


Figure 4.4: Shape, density, and inner fish distribution during a predator attack. a) Three snapshots of the fish school: (1) rapid escape from a predator leaving a vacuole at $t = 1.5$ s, (2) the school rejoins after the attack $t = 5$ to $t \sim 10$ s, (3) the school returns to a cohesive mill from $t = 13$ s onward. b) Time series of the volume $\mathcal{V}(t)$ (black) and of the average local fish density $\langle \rho_i(t) \rangle$ (blue dashes), inset the time snapshots of (a). c) Time series of the dominant aspect ratio $\eta_1(t)$ (red), and the subdominant aspect ratio $\eta_2(t)$ (blue). d) Time series of the moment mean $\mu(t)$ (magenta), standard deviation $\sigma(t)$ (orange) and skewness $s(t)$ (green), and the inner distribution parameter $\xi(t) = \mu/2\sigma$ (black). e) The relation between the average density $\langle \rho_i(t) \rangle$ and the volume $\mathcal{V}(t)$ of (b), the black dashed line indicates a uniform density for a school of ± 2000 fish. f) The relation between the aspect ratios $\eta_1(t)$ (red) and $\eta_2(t)$ (blue) of (c) and the volume $\mathcal{V}(t)$ of (b). g) The locus drawn by the skewness $s(t)$ and the inner fish distribution parameter $\xi(t)$ from (f). We indicate (b) the predator attack at $t = 0$.

4.2.2. INNER DISTRIBUTION OF FISH IN THE SCHOOL

The shape of the school and the distribution of fish vary significantly both within one data set and between different data sets. These variations in shape often overshadow more fundamental differences in the distributions and schooling behavior. For example, Figure 4.1 highlights that milling can occur in a school of widely different shapes.

In order to quantify the distribution of fish positions and provide a meaningful comparison between schools of different shapes, we rescale the position data and introduce a new coordinate system for the school. We place the origin at the center of mass \mathbf{X}_M and align the coordinate system with the principal axis $\{\mathbf{e}_1, \mathbf{e}_2, \mathbf{e}_3\}$ defined previously. We then normalize the coordinates with the values of the semi-axis $(\lambda_1, \lambda_2, \lambda_3)$ such that the bounding ellipsoid is rescaled to the unit sphere.

The change in the coordinate system involves a linear transformation composed of a translation, a rotation, and the rescaling of the axes. The rotation matrix from the principal axis to the global coordinates is simply $R = [\mathbf{e}_1 \ \mathbf{e}_2 \ \mathbf{e}_3]$. We call $\Lambda = \text{diag}([\lambda_1 \ \lambda_2 \ \lambda_3])$ the scaling matrix, which scales the unit sphere to the computed ellipsoid. We then define $\tilde{\mathbf{X}}_{i/M}$ the rescaled position of fish i with respect to the center of mass:

$$\tilde{\mathbf{X}}_{i/M} = \Lambda^{-1} R^T (\mathbf{X}_i - \mathbf{X}_M), \quad (4.1)$$

where $(\bullet)^{-1}$ is the matrix inverse, and $(\bullet)^T$ the matrix transpose.

The rescaled coordinates facilitate the comparison between the distribution of fish for schools with different volume and aspect ratios. We now consider the radial distribution of fish in rescaled coordinates and compute the spatial moments of this distribution. The spatial moments characterize important features of the internal distribution of fish in the school and help identify whether fish are distributed uniformly within the school or, for example, accumulate radially at the edges.

COMPUTATION OF THE SPATIAL MOMENTS

We compute the radial position of the fish $r_i = \|\tilde{\mathbf{X}}_{i/M}\|$ and deduce the radial distribution function $f(r)$. Examples of distributions are represented in Figure C.2 of Appendix C.4. The radial distribution is characterized by computing the moments of the distribution. We compute the 1st, 2nd and 3rd central moment, corresponding to the mean, the standard deviation, and the skewness of the distribution $f(r)$:

$$\text{mean: } \mu = \int_0^\infty r f(r) dr, \quad (4.2)$$

$$\text{standard deviation: } \sigma = \sqrt{\int_0^\infty (r - \mu)^2 f(r) dr}, \quad (4.3)$$

$$\text{and normalized skewness: } s = \left(\int_0^\infty \left(\frac{r - \mu}{\sigma} \right)^3 f(r) dr \right)^{1/3}. \quad (4.4)$$

The moments μ , σ , and s are explicitly computed by summations over the radial fish positions. We estimate their value over a finite interval that we truncate $r \leq 3/2$ for practical purposes. In this way, we limit the domain and remove positions that are not part of the school ($r \gg 1$) such as solitary fish and/or excessive irregularity in the school shape. All detail is given in Appendix C.4.

The mean μ and standard deviation σ in equations 4.2 and 4.3 characterize the location and width for the peak value of the radial distribution $f(r)$. For reference, the uniform distribution ($f(r) = 1$ when $0 \leq r < 1$ and $f(r) = 0$ otherwise) has a mean value of $\mu = 1/2$ and a standard deviation of $\sigma = \sqrt{1/12} \approx 0.29$.

The normalized skewness s in Equation 4.4, on the other hand, quantifies the degree of asymmetry in the radial distribution normalized by σ . When the peak of the distribution is symmetric the skew is zero ($s = 0$). When the peak of the distribution is increasingly biased towards the origin $r = 0$ (left) the skew is increasingly positive ($s > 0$), and when biased in the positive r direction (right) the skew is negative ($s < 0$).

TIME SERIES FOR THE MOMENT MEAN, STANDARD DEVIATION AND SKEWNESS

In Figure 4.4d we present the time evolution for the mean μ , the standard deviation σ , and skewness s for the same data set as in Figure 4.4a. These time series are also presented for different data sets in the appendix, see supplementary figures C.4, C.6, and C.8 in Appendix C.

We find that the value for the skewness s is initially negative ($s < 0$) from $t = 0$ to $t = 8.5$ s. This indicates that the fish are mostly distributed at the edge of the school, far from the center of mass. After the predator has passed and the school rejoins, the skew changes sign to a positive value $s > 0$ from $t = 8.5$ s onward. This indicates that the fish cluster into a cohesive group. Our results suggest that the skewness of the fish distribution provides a clear distinction between an escape maneuver from a predator and the rest state of the school.

We turn to the values for the mean μ and standard deviation σ . From $t = 0$ to $t = 8.5$ s, the mean approaches $\mu \rightarrow 1$ with a low standard deviation $\sigma \sim 0.25$. This is consistent with the value of the skewness s and is characteristic of the fish being distributed in a narrow peak at the edges of the school (also see Figure C.2d in Appendix C.4). Then, from $t = 8.5$ s onward the mean decreases to $\mu \sim 0.5$ while the standard deviation slightly increased to $\sigma \sim 0.3$. Hence, when the school rejoins into a cohesive group following the attack, the fish distribute more or less uniformly ($\mu = 1/2$ and $\sigma = \sqrt{1/12} \approx 0.29$).

DEGREE OF INTERNAL DISTRIBUTION OF FISH IN THE SCHOOL

We continue to investigate the degree of redistribution of fish towards the edge of the school when the predator attacks. For this purpose, we define a single — inner distribution parameter $\xi = \mu/2\sigma$ — that expresses the moment mean μ in units standard deviation σ like the normalized skewness (Equation 4.4). For a uniform distribution ($\mu = 1/2$ and $\sigma = \sqrt{1/12}$) the inner distribution parameter reads $\xi = \sqrt{3/4} \approx 0.87$; when $\xi \geq 0.87$ the fish redistribute towards the edge, and when $\xi \leq 0.87$ towards the origin.

In Figure 4.4d, we plot the inner distribution parameter in black. Initially, the value of the black curve is close to $\xi \rightarrow 2$ when the fish are sharply distributed at the edge of the school in snapshot (1) up to $t = 8.5$ s. Thereafter, its value drops down to $\xi \sim 1$ and the school approaches a uniform distribution. Finally, we find in Figure 4.4g that the inner distribution parameter ξ and skewness s together develop a curious locus in the $s\xi$ -plane; drawing the connection between the skewness and fish distribution.

4.2.3. VARIABILITY IN SCHOOL SHAPE AND BIMODAL FISH DISTRIBUTION

In the previous subsection, we developed metrics to characterize the geometry of the school and focused on one particular data set of a predator escape. In this subsection, we investigate the relevance of these shape parameters for several data sets that capture different events of schooling behavior as presented in figures 4.1 to 4.3 and in Table C.2 of Appendix C.2. We quantify the variability from statistical distributions of the shape parameters and radial distribution and examine the relations between them.

DOMINANT, SUBDOMINANT ASPECT RATIO, VOLUME, AND FISH DENSITY

In Figure 4.5a, we plot the (non-dimensional) dominant aspect ratio η_1 and the subdominant aspect ratio η_2 of the school against the volume \mathcal{V} . The different points represent different data sets and the error bars indicate the variation in the time series (e.g. Figure 4.4). The dominant aspect ratio varies over a range of $1.5 < \eta_1 < 4$ (red), while the subdominant aspect ratio η_2 varies within a smaller range $1 < \eta_2 < 2$ (blue).

The differences in the aspect ratios are expected since the dominant aspect ratio is larger than the subdominant aspect ratio by construction. These numbers now provide reference values for the dominant features in the shape of the school. For example, we mark three particular data sets: the slender mill (\times) in Figure 4.1d, a circular mill (\blacksquare) of Figure 4.1b, and the escape response (Δ) of Figure 4.2c.

In Figure 4.5b, we plot the joint distribution for the average value of the local fish density $\langle \rho_i \rangle$ and the volume \mathcal{V} . This distribution is obtained by accumulating the data included in figure Figure 4.4e over all data sets. We find that this distribution has a roughly triangular shape. For comparison, we plot the school density $\rho = 2000/\mathcal{V}$, which is directly related to the volume, see cyan dashes in Figure 4.5b.

One interpretation is as follows. For small volumes $\mathcal{V} < 40 \text{ m}^3$, we find that the volume scaling represents a lower bound for the average local density. In contrast, for larger volumes $\mathcal{V} > 40 \text{ m}^3$, the density is contained above a lower bound $\rho > 50 \text{ m}^{-3}$ (yellow dashes). Therefore the local fish density does not simply scale with the volume of the school, instead it approaches a constant level away from the intersection point where the two curves cross (yellow/cyan dashes).

SKEWNESS AND DISTRIBUTION OF FISH IN THE SCHOOL

Since the aspect ratio and volume only capture elementary features of the school geometry, we continue to focus on the distribution of fish in a school. Figure 4.5c plots the joint distribution density of the inner distribution parameter ξ and the normalized skewness s . Interestingly, the internal distribution of the fish in the school is bimodal with two distinct peaks: one with a negative skew for $s \approx -0.5$ and $\xi \approx 0.9$, and the other with a positive skew for $s \approx 0.5$ and $\xi \approx 0.8$. These peaks sit just above and below the value for a uniform distribution $\xi = \sqrt{3}/4 \approx 0.87$.

The two peaks in Figure 4.5c correspond to two different schooling behavior. First, for the peak with a negative skew, $s \sim -0.5$, the fish are more densely distributed towards the edge of the school. This skewed distribution is a possible signature of an escape maneuver, see Figure 4.4a, d, and g. The escape response is then further characterized by the (long) upward tail in the joint distribution $f(s, \xi)$ for $s = -0.5$ and $\xi \gg 0.87$, and provides the degree of redistribution. Second, for the peak with a positive skew $s \sim 0.5$,

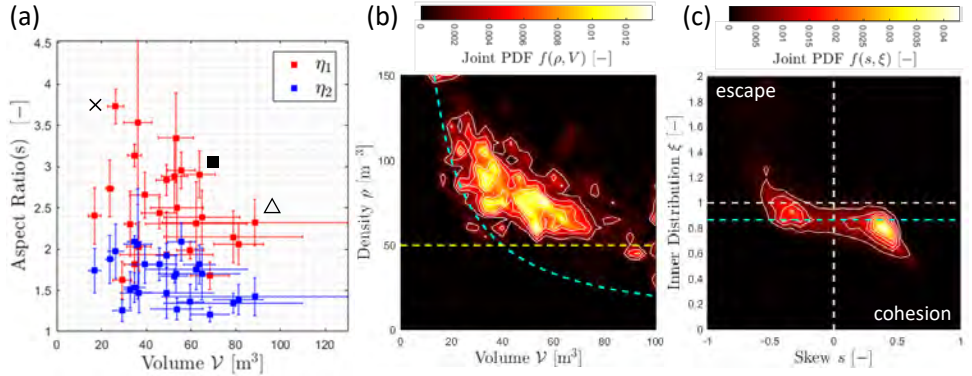


Figure 4.5: Variability of the shape, density, and inner fish distribution. a) Dominant and subdominant aspect ratios of the school η_1 (red), and η_2 (blue) against the volume \mathcal{V} for different data sets. The error bars indicate the variation over the time series. We mark the data (\times , \blacksquare , \triangle) in figures 4.1 and 4.2. b) Joint probability density $f(\langle \rho_i \rangle, \mathcal{V})$ for the mean fish density $\langle \rho_i \rangle$ and the volume \mathcal{V} , in cyan a uniform density for 2000 fish, and in yellow a lower bound at higher volume. c) Joint probability density $f(s, \xi)$ for the moment skew s and inner distribution parameter ξ ; the white dashes indicate the zero and unit crossing for s and ξ , the uniform distribution $\xi = \sqrt{3}/4$ is in cyan. We indicate extremes for escape and cohesion (white text).

the fish cluster towards the center of the school and form a cohesive group. This peak is characteristic of the absence of predation.

These results agree with the example time series of Figure 4.4d. In particular, the change in the sign of s characterizes a transition between the milling rest state and escape maneuvers, while ξ can be used to measure the degree to which the fish cluster into a cohesive mill or are (re-)distributed towards the boundary.

4.3. KINEMATICS OF FISH SCHOOLING

To this point, we have only considered the fish position from which we have deduced the fish distribution within the school. We now consider the distribution of fish velocity and characterize the kinematics of the school for the different schooling behavior introduced in Section 4.1. First, we extract statistics from the distribution of swimming velocity and the local polarization inside the school, and we compute the motion of the center of mass [17, 18, 23]. Then, we compute mixed spatial moments of the velocity distribution at the location of the center of mass and quantify the average angular momentum and volume rate-of-change of the school. These metrics provide measures for translation, rotation, and volumetric changes in the school, see previous experimental [13] and simulation work [37–43].

We also define a kinematic decomposition of the fish velocity in the coordinate system introduced in Section 4.2.2 and extend on previous experimental work in two dimensions [13]. We partition the kinetic energy of each fish and derive a set of interrelated non-dimensional kinematic parameters. With these non-dimensional numbers, we quantify the degree of ‘foraging’, ‘milling’, and ‘dilation’, in three dimensions. Finally, we present the variability in the kinematics of fish schools for the numerous data sets presented in this thesis and define a ternary diagram for the school kinematics.

4.3.1. VELOCITY, POLARIZATION, ANGULAR MOMENTUM, AND DILATION

We begin by computing the velocity of each fish as the time derivative of the position vector $\mathbf{U}_i(t) = d\mathbf{X}_i(t)/dt$ for the i^{th} fish in the school and we write the swimming speed as $U_i(t) = \|\mathbf{U}_i\|$. We compute the velocity vector using the smoothing and differentiation filters introduced in Chapter 3 to filter noise and outliers.

To monitor changes in the distribution of velocity in the school, we compute the average swimming speed $\bar{U}(t) = \langle U_i(t) \rangle$ and standard deviation $\sigma_U(t) = \sqrt{\langle (U_i(t) - \bar{U}(t))^2 \rangle}$; for a discussion of the velocity distribution see Appendix C.5. Furthermore, we express the fish heading vector $\hat{\mathbf{h}}_i = \mathbf{U}_i/U_i$ in direction of swimming and compute the local polarization $\phi_i(t) = \|\langle \hat{\mathbf{h}}_j \rangle_{j \in J}\|$ by averaging $j \in J$ in the neighborhood of fish i similar to the local fish density in Section 4.2.1; for related work see [13, 17, 33, 44].

The polarization ϕ_i is a localized state variable representing the alignment of fish in the school. When $\phi_i = 1$, neighboring fish $j \in J$ swim exactly in the same direction as the focal fish i , hence the school is in a locally polarized state. On the other hand, when $\phi = 0$ fish swim in different directions, hence the school is in a locally disorganized state. We report the average polarization $\langle \phi_i(t) \rangle$ alongside other time series analyses.

The school is observed to rotate, translate, and undergo changes in volume and shape. To characterize these different dynamics, we define mixed spatial moments of the velocity distribution and fish position. We compute the velocity of the center of mass $\mathbf{U}_M(t) = d\mathbf{X}_M(t)/dt = \langle \mathbf{U}_i \rangle$ as well as:

$$\text{average angular momentum } \mathbf{L} = 2\pi \langle (\mathbf{X}_i - \mathbf{X}_M) \times (\mathbf{U}_i - \mathbf{U}_M) \rangle, \quad (4.5)$$

$$\text{and total volume rate-of-change } \mathcal{V}_C = 4\pi \langle \|\mathbf{X}_i - \mathbf{X}_M\| (\mathbf{X}_i - \mathbf{X}_M) \cdot (\mathbf{U}_i - \mathbf{U}_M) \rangle. \quad (4.6)$$

Here the prefactor 2π in Equation 4.5 provides scaling for the angular revolution, and the prefactor 4π in Equation 4.6 is a scaling constant for the surface area of the sphere; connecting the volume rate-of-change \mathcal{V}_C to the evolution of volume \mathcal{V} of the equivalent ellipsoid¹ of Section 4.2.1.

The excitation of the fish in the school is captured by the distribution of speed $U_i(t)$ and the local polarization $\phi_i(t)$. $\mathbf{U}_M(t)$ on the other hand represents the average displacement of the school as a whole, while the average angular momentum $\mathbf{L}(t)$ and the volume rate-of-change $\mathcal{V}_C(t)$ represent the average rotation and change in volume. $\mathbf{L}(t)$ and $\mathcal{V}_C(t)$ have units of m^2/s , and m^3/s respectively.

FISH VELOCITY AND POLARIZATION

In Figure 4.6b, we plot together the time series of the average swimming velocity $\bar{U}(t)$ (magenta), the standard deviation of the velocity distribution $\sigma_U(t)$ (orange) and the average local polarization $\langle \phi_i(t) \rangle$ (blue) for the same data set used in Figure 4.4a. Initially, the average swimming velocity increases to $\bar{U}(t) \sim 0.7 \text{ m/s}$ until $t = 1.5 \text{ s}$. After the attack, the velocity gradually decreases to $\bar{U} \rightarrow 0.4 \text{ m/s}$ as the school rejoins between $t = 5$ to $t \sim 10 \text{ s}$. Next, the school returns to a cohesive mill at $t = 13 \text{ s}$ with a short increase in the swimming speed and similar changes in the standard deviation $\sigma_U(t)$. Although

¹Directly differentiating the ellipsoidal volume evolution $d\mathcal{V}/dt = 4\pi/3 d/dt[\lambda_1 \lambda_2 \lambda_3]$ yields a complex expression by the semi-axes. Taking the geometric mean $\tilde{\lambda} = (\lambda_1 \lambda_2 \lambda_3)^{1/3}$ simplifies the notation to $4\pi/3 d/dt[\tilde{\lambda}^3] = 4\pi \tilde{\lambda}^2 \dot{\tilde{\lambda}}$, which in Equation 4.6 we subsequently approximate $\tilde{\lambda}^2 \dot{\tilde{\lambda}}$ at the right-hand side.

the velocity changes over the events this suggests that its distribution is little affected by a predator engaging in an attack, also see Appendix C.5 and Figure C.3.

Figure 4.6b presents the time series of the average local polarization $\langle \phi_i(t) \rangle$, with a different non-dimensional y-axis in blue (on the right). For this data set, the average polarization remains large, between $0.7 < \langle \phi_i(t) \rangle < 0.8$, and does not seem to change significantly. The polarization provides the local structural alignment in the school. To investigate whether there is a non-trivial interrelation between fish speed and alignment we plot in Figure 4.6e the average polarization $\langle \phi_i(t) \rangle$ against the average velocity $\bar{U}(t)$. However, at this point, we find no definite signature over the escape event.

VELOCITY OF CENTER OF MASS AND ANGULAR MOMENTUM

Figure 4.6c represents the time evolution of the velocity of the center of mass $U_M(t) = \|\mathbf{U}_M(t)\|$ and of the magnitude of the angular momentum $L(t) = \|\mathbf{L}(t)\|$. These metrics provide a global measurement for the degree of translation and rotation of the school.

Until $t = 3$ s, the center of mass of the school is moving at a speed up to $U_M \simeq 0.3$ m/s, during the predator escape maneuver. After the predator has passed at $t \sim 5$ s, the school remains at a fixed position, with $U_M \leq 0.1$ m/s. When the school returns to a cohesive mill, $t \sim 13$ s, the speed of the center of mass increases again to $U_M \simeq 0.2$ m/s. The relative variations in $U_M(t)$ are more pronounced than those in swimming speed $\bar{U}(t)$. However, changes in the position of the center of mass do not uniquely characterize escape maneuvers, since U_M is also higher between $t = 13$ and $t = 15$ s when the school reforms into a cohesive fish mill in absence of a direct predator attack.

In Figure 4.6c we plot the average angular momentum $L(t)$ with a different y-axis (units m^2/s) in blue. During the avoidance maneuver, from $t = 1.5$ s to $t \sim 10$ s, the average angular momentum elevates to a value of $L \simeq 4$ m^2/s . Returning to the rotating milling state, the angular momentum decreases to $L \simeq 1$ m^2/s . Thus the angular momentum does not reach a maximum when the school is rotating in a milling motion.

The initial increase in the angular momentum $L(t)$ is due to the increase in volume and the change in the inner distribution of fish (see Figure 4.4b and d). After returning to a cohesive mill, the value of the angular momentum $L(t)$ decreases because the fish cluster in a cohesive group. Therefore, the value of $L(t)$ is not directly indicative of milling as reported in previous laboratory experiments on smaller planar fish schools [13] and simulation work [37–43].

VOLUME RATE-OF-CHANGE AND INTERRELATIONS

In Figure 4.6d, we plot the volume rate-of-change $\mathcal{V}_C(t)$, computed from Equation 4.6. Initially, the school rapidly enlarges to reach a peak value of $\mathcal{V}_C \rightarrow 20$ m^3/s during the predator attack from $t = 0$ until $t = 1.5$ s. Subsequently, the volume gradually decreases, at a slower rate between $-10 < \mathcal{V}_C < -5$ m^3/s from $t = 5$ s until the school is in a cohesive group, consistent with the volume evolution in Figure 4.4b. Unlike the center of mass velocity $U_M(t)$ and angular momentum $L(t)$, these rapid fluctuations in the volume rate-of-change $\mathcal{V}_C(t)$ help differentiate the predatory attack from the milling school.

Finally, in Figure 4.6f and g, we consider the relation between $U_M(t)$, $L(t)$, and $\mathcal{V}_C(t)$. We find that $U_M(t)$ and $L(t)$ draw a loop that displays distinct dynamic features present in the predatory attack. Similarly, we plot the volume rate-of-change $\mathcal{V}_C(t)$ against the velocity of the center of mass $U_M(t)$ drawing a loop with a large variation. Such large

variations have not been observed in previous laboratory scale experiments [13, 17, 24]. In the current work, only the volume rate-of-change brings a pronounced signature for the interaction with the predator [45].

4.3.2. KINEMATIC DECOMPOSITION AND PARTITION IN KINETIC ENERGY

We now introduce a different framework to decompose the kinematics while ignoring the school shape. We express a relative rate of deformation over the finite-sized school by normalizing the velocity in the rescaled coordinate system of Section 4.2.2. We compute the kinematic decomposition and partition the kinetic energy to derive three distinct kinematic schooling parameters. These dimensionless kinematic parameters characterize the kinematic state (or ‘phase’) of the school [13]. We further express a global rotation and total expansion rate within the current framework.

AXES RESCALING AND KINEMATIC DECOMPOSITION

We define a normalized relative velocity $\tilde{\mathbf{U}}_{i/M}$ for each fish i in the instantaneous frame centered at $\mathbf{X}_M(t)$ and moving at $\mathbf{U}_M(t)$. In addition, we rescale the velocity along the semi-axis $(\lambda_1, \lambda_2, \lambda_3)$ in the same way as previously done in Equation 4.1:

$$\tilde{\mathbf{U}}_{i/M} = \Lambda^{-1} R^T (\mathbf{U}_i - \mathbf{U}_M) = \tilde{\mathbf{U}}_i - \tilde{\mathbf{U}}_M. \quad (4.7)$$

This definition expresses the fish velocity components in terms of the rate-of-change of the finite-sized school. At the right-hand side of Equation 4.7 $\tilde{\mathbf{U}}_i$ is the rescaled swimming velocity and $\tilde{\mathbf{U}}_M$ is the normalized velocity of the center of mass.

It bears to emphasize that the normalized relative velocity has units $1/s$ and $\tilde{\mathbf{U}}_{i/M} \neq d\tilde{\mathbf{x}}_{i/M}(t)/dt$ as we assume instantaneity for axes rescaling of Equation 4.1. This rescaling normalizes the large variation in the aspect ratio of the school (Figure 4.5a) and removes a straining component for the velocity field in case the mill is rotating and shearing in an elliptical cross-section. The distribution of the velocity components at the semi-axis rescaling is further discussed in Appendix C.5.

We use an orthogonal decomposition of the normalized relative velocity $\tilde{\mathbf{U}}_{i/M}$, which we write as the sum of a radial component $\tilde{\mathbf{U}}_{i/M}^\perp$ in the radial direction $\hat{\mathbf{r}}_i = \tilde{\mathbf{x}}_{i/M}/r_i$ and an orthogonal component $\tilde{\mathbf{U}}_{i/M}^\parallel = \tilde{\mathbf{U}}_{i/M} - \tilde{\mathbf{U}}_{i/M}^\perp$ in the direction tangent to the sphere. Reordering the terms on the left- and right-hand side in Equation 4.7, we write the kinematic decomposition of the rescaled swimming velocity:

$$\tilde{\mathbf{U}}_i = \tilde{\mathbf{U}}_M + \tilde{\mathbf{U}}_{i/M}^\parallel + \tilde{\mathbf{U}}_{i/M}^\perp. \quad (4.8)$$

This decomposes the fish kinematics into the motion of the center of mass and its parallel, and perpendicular components in the frame moving with the school.

PARTITIONING OF THE INTERNAL KINETIC ENERGY IN THE SCHOOL

We now write the total kinetic energy summing over all fish $\sum_i U_i^2$ and partition its value. Using the kinematic decomposition of Equation 4.8, the total kinetic energy yields a simple expression:

$$\sum_{i=1}^I \tilde{U}_i^2 = \sum_{i=1}^I \tilde{U}_M^2 + \sum_{i=1}^I \tilde{U}_{i/M}^\parallel{}^2 + \sum_{i=1}^I \tilde{U}_{i/M}^\perp{}^2. \quad (4.9)$$

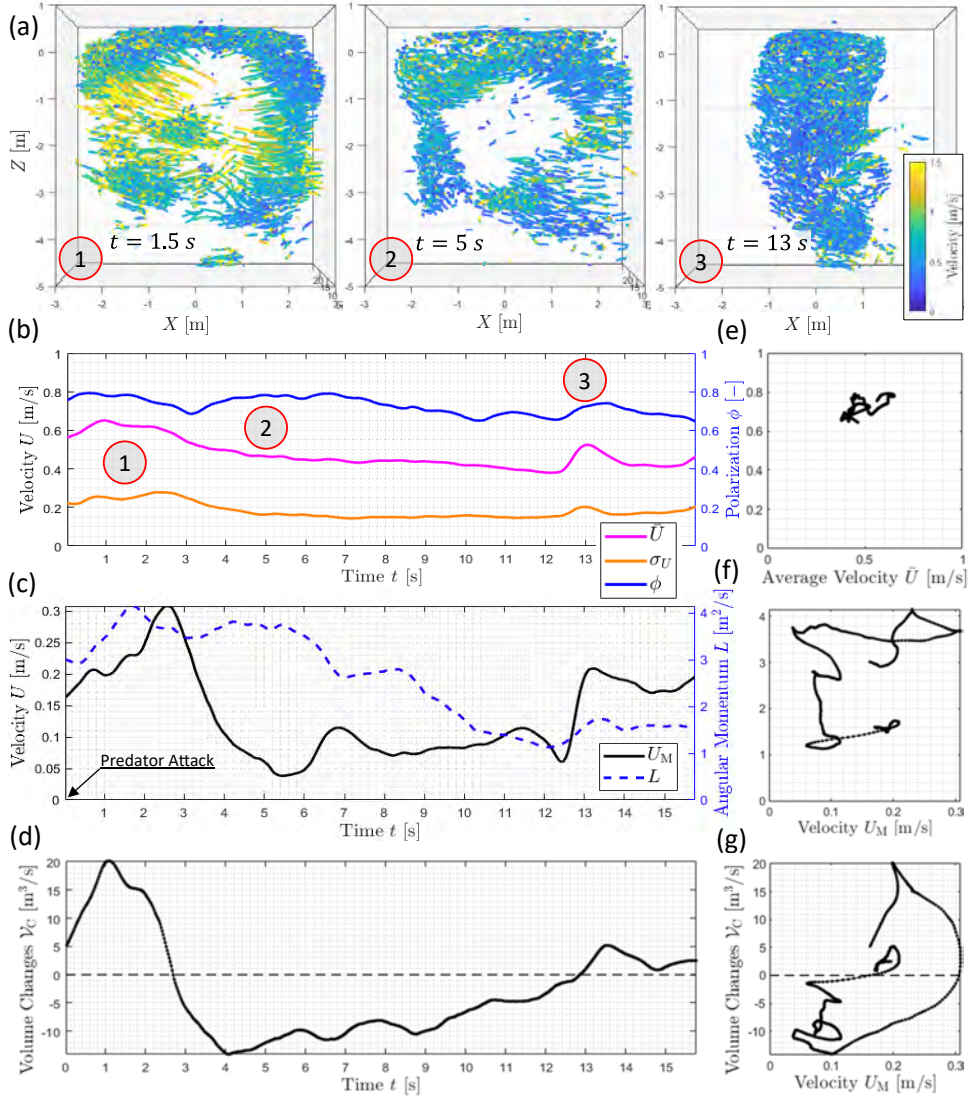


Figure 4.6: Velocity, polarization, angular momentum, and volumetric changes at predator attack. a) The snapshots of Figure 4.4: (1) rapid escape leaving a vacuole at $t = 1.5$ s, (2) the school rejoins after predator intervention $t = 5$ to $t \sim 10$ s, (3) the school returns to a cohesive mill from $t = 13$ s onward. b) Time series for the average fish velocity $\bar{U}(t)$ (magenta) and the standard deviation $\sigma_U(t)$ of the fish velocity distribution (orange) alongside the local fish polarization $\langle \phi_i(t) \rangle$ (blue). c) Time series for the velocity of the center of mass $U_M(t)$ of the school (black) and the angular momentum $L(t)$ around the center of mass (blue dashes). d) Time series for the volume rate-of-change $\mathcal{V}_C(t)$ away from the center of mass. e) The polarization $\langle \phi_i(t) \rangle$ against the average velocity $\bar{U}(t)$ from (b). f) The locus drawn by the velocity of the center of mass $U_M(t)$ and the angular momentum $L(t)$ of (c). g) The locus by the velocity of the center of mass $U_M(t)$ and the volume rate-of-change $\mathcal{V}_C(t)$ of (d) when evading the predator. We indicate (c) the predator attack at $t = 0$.

There are no cross terms in Equation 4.9 in the binomial expansion as $\tilde{\mathbf{U}}_{i/M}^{\parallel}$ and $\tilde{\mathbf{U}}_{i/M}^{\perp}$ are orthogonal and the summation $\sum_i \tilde{\mathbf{U}}_M^T (\tilde{\mathbf{U}}_{i/M}^{\parallel} + \tilde{\mathbf{U}}_{i/M}^{\perp}) = \tilde{\mathbf{U}}_M^T \sum_i \tilde{\mathbf{U}}_{i/M} = 0$.

The left-hand side of Equation 4.9 provides the total kinetic energy of the fish school from the summation over the individual fish i . The right-hand side highlights three contributions to the energy budget. From left to right we have the kinetic energy: (1) of the center of mass, (2) of the angular velocity of the fish around the center of mass, and (3) of the radial in/outward motion of the fish (school dilation). Equation 4.9 does not provide a conservation law but provides a well-defined basis to quantify how the kinetic energy is distributed between the different components of the fish motion in the school.

FORAGING, MILLING, AND DILATION IN THREE DIMENSIONS

We now use the decomposition of the kinetic energy to characterize the kinematics of the school using three dimensionless kinematic parameters. We normalize each component of the kinetic energy inside the school with the average kinetic energy $\langle \tilde{U}_i^2 \rangle$ of the fish. The three terms in the partition of the kinetic energy of Equation 4.9 define three non-dimensional numbers:

$$\text{foraging number } F = \frac{\tilde{U}_M^2}{\langle \tilde{U}_i^2 \rangle}, \quad (4.10)$$

$$\text{milling number } M = \frac{\langle \tilde{U}_{i/M}^{\parallel 2} \rangle}{\langle \tilde{U}_i^2 \rangle} \quad (4.11)$$

$$\text{and dilation number } D = \frac{\langle \tilde{U}_{i/M}^{\perp 2} \rangle}{\langle \tilde{U}_i^2 \rangle}. \quad (4.12)$$

Finally, Equation 4.9 can then be rewritten in terms of F , M , and D , and provides the total partitioning:

$$F + M + D = 1. \quad (4.13)$$

The ‘foraging number’ F measures the relative importance of the normalized velocity of the center of mass relative to the normalized velocity of the fish. For $F = 0$, the center of mass is fixed and the school remains at a fixed position in the fish tank. On the other hand, when $F = 1$ the school undergoes a pure translation.

A uni-directional motion, corresponding to $F = 1$, is not compatible with the steady rotation of a fish mill. The ‘milling number’ M quantifies the kinetic energy in the rotation motion of the school around the center of mass. When $M = 0$, no fish swims around the center of mass, while for $M = 1$, all fish swim with a perfect rotation.

Finally, the ‘dilation number’ D corresponds to the kinetic energy associated with the radial motion of fish towards and away from the center of mass. When $D = 0$ the school neither expands nor contracts and when $D = 1$ all fish move radially with respect to the center of mass.

PURE EXPANSION, ISOCHORIC DEFORMATION, AND PURE ROTATION

The foraging and milling numbers F , and M are closely related to common definitions for the total polarization, and rotational order parameters (see *e.g.* [13, 37, 39, 41]). The

dilation number D , on the other hand, expands on previous experimental work in two dimensions [13] and completes the decomposition of the kinetic energy. We now subdivide the dilation number D into two parts, namely the:

$$\text{expansion number } E = \frac{\langle \tilde{U}_{i/M}^\perp | \tilde{U}_{i/M}^\perp | \rangle}{\langle \tilde{U}_i^2 \rangle} \quad (4.14)$$

$$\text{and isochoric number } I = D - |E|, \quad (4.15)$$

where $|\cdot|$ denotes the absolute value.

The ‘expansion number’ E expresses the average signed value of the radial velocity component \tilde{U}_i^\perp . The sign of E keeps track of whether the school is expanding ($E > 0$) or contracting ($E < 0$), similar to the volume rate-of-change of Equation 4.6. The ‘isochoric number’ I is the difference with the total dilation D . This number represents the amount of kinetic energy in the radial distribution which does not contribute to any change in volume because an equal number of fish swim inwards and outwards.

The milling number M does not measure the total rotation about a single rotation axis. To illustrate how the milling number M is related to the rotational order parameters in [13, 37, 39, 41], we define a rotation number R . For this, we compute the angular momentum vector in the rescaled coordinates $\tilde{\mathbf{L}} = 2\pi(\tilde{\mathbf{X}}_{i/M} \times \tilde{\mathbf{U}}_{i/M})$, define the rotation axis $\hat{\boldsymbol{\omega}} = \tilde{\mathbf{L}}/\|\tilde{\mathbf{L}}\|$ and deduce the circumferential (or hoop) direction as $\hat{\boldsymbol{\theta}}_i = \hat{\boldsymbol{\omega}} \times \hat{\mathbf{r}}_i / \|\hat{\boldsymbol{\omega}} \times \hat{\mathbf{r}}_i\|$. We project the velocity $\tilde{\mathbf{U}}_{i/M}$ on $\hat{\boldsymbol{\theta}}_i$ and compute the rotation number:

$$\text{rotation number } R = \frac{\langle \hat{\boldsymbol{\theta}}_i \cdot \tilde{\mathbf{U}}_{i/M} | \hat{\boldsymbol{\theta}}_i \cdot \tilde{\mathbf{U}}_{i/M} | \rangle}{\langle \tilde{U}_i^2 \rangle}, \quad (4.16)$$

normalizing similarly to equations 4.10 to 4.15. The rotation number gives the total kinetic energy in rotation around $\hat{\boldsymbol{\omega}}$ and keeps track of the sign similarly to Equation 4.14.

TIME SERIES FOR THE KINEMATIC PARAMETERS

We consider the same escape response as in figures 4.4 and 4.6 and plot the time evolution of the kinematic parameters M , F , D , E , I and R . Figure 4.7b represent over time the milling number $M(t)$ (red) and the foraging number $F(t)$ (green). The dilation number $D(t)$ is represented in cyan when $E > 0$ and the school expands, and in blue when $E < 0$ and the school contracts. The subdivision for the isochoric number $I(t)$ is in orange and the rotation number $R(t)$ is in magenta. For more examples of milling and foraging schools see supplementary figures C.5, C.7, and C.9 in Appendix C.

The value of the milling number $M(t)$ ranges between $0.6 < M < 0.75$ and remains more or less unchanged during the predator attack. Compared with the range of the angular momentum $L(t)$ in Figure 4.6c, the amplitude of $M(t)$ is smaller between $t = 1$ s and $t = 13$ s, and the associated kinetic energy is relatively unaffected. Furthermore, the average degree of dilation $D(t)$ fluctuates in a narrow range around $D \sim 0.3$. Because the sum of M , F , and D equals one, the increase in one is always balanced by a decrease in another. Figure 4.7 shows that most of the milling number $M(t)$ varies complementary to the foraging number $F(t)$ between $0 \leq F < 0.2$.

We further investigate the milling number $M(t)$ over time and how it relates to the rotation number $R(t)$ in Figure 4.7b. The rotation number has a much lower value of $R \sim 0.4$ compared to the milling number $0.6 < M < 0.75$, and these values are correlated. This indicates that little over half of the kinetic energy in milling is distributed in a pure rotation. Therefore the motion of the school is far from a perfect cylindrical rotation, even when the school returns to a cohesive mill.

This discrepancy is due to, fish swimming in different planes over the height of the school, misalignment of the rotation axis, and a percentage of fish swimming against the dominant direction of rotation. In Figure 4.7e we further show that the degree of pure rotation R corresponds to an increase with the degree of milling M . Thus, when the milling number increases, the rotational order in the school is increasingly cylindrical, as may be expected for the correlated variations.

Next, we consider the time series of the dilation number $D(t)$. The pure expansion rate can be deduced from the difference $|E| = D - I$ and it varies between $-0.2 < E < 0.2$, during which the isochoric number decreases from $I \sim 0.2$ to 0.1 . The relation between the expansion number $E(t)$ and dilation number $D(t)$ is summarized in Figure 4.7f. Although the changes in the dilation number are small, the values are in direct correspondence with outward expansion and inward contraction.

The variations of E are consistent with the volume rate-of-change of Equation 4.6. At $t = 1.5$ s, the school is in a rapid expansion $E \approx 0.2$. Around $t = 3$ s, the center of mass moves leading to an increase of the foraging number to a maximum value of $F \approx 0.2$. From $t = 3$ s onward, the school goes into a lasting contraction $E \approx -0.2$. The relation between the expansion number E and foraging number F are represented in Figure 4.7g, and together they account for ~ 20 % of the total kinetic energy in the school when evading the predator.

Finally, the distribution of the kinetic energy over milling, foraging, and dilation, is summarized in Figure 4.7c as we draw the locus of M , F , and D on the plane defined by $M + F + D = 1$. Here, the plane $M + F + D = 1$ allows us to visualize the schooling dynamics in a ternary diagram, plotted in percentages in Figure 4.7d. This graphic representation provides a comprehensive picture of the kinematics of the fish school, where we color code the time in seconds.

4.3.3. VARIABILITY AND DISTRIBUTION OF KINETIC ENERGY

To this point, we have considered the kinematic parameters over time for one specific data set. We now investigate the relevance of these parameters for multiple data-sets recorded for the measurement weeks described in Appendix C.2. We first plot joint distributions for milling M , foraging F , and dilation D on the ternary diagram introduced in Figure 4.7d. This gives insight into the partitioning of the kinetic energy over a range of schooling behaviors [13]. We then plot the degree of rotation R as a function of the milling number M , and the dilation D as a function of the expansion number E to further elucidate the associated schooling kinematics.

TERNARY DIAGRAM AND KINEMATIC STATE

We construct the ternary diagram for the coupled variables M , F , and D from the kinematic decomposition on the plane $M + F + D = 1$, and report the partitioning of the ki-

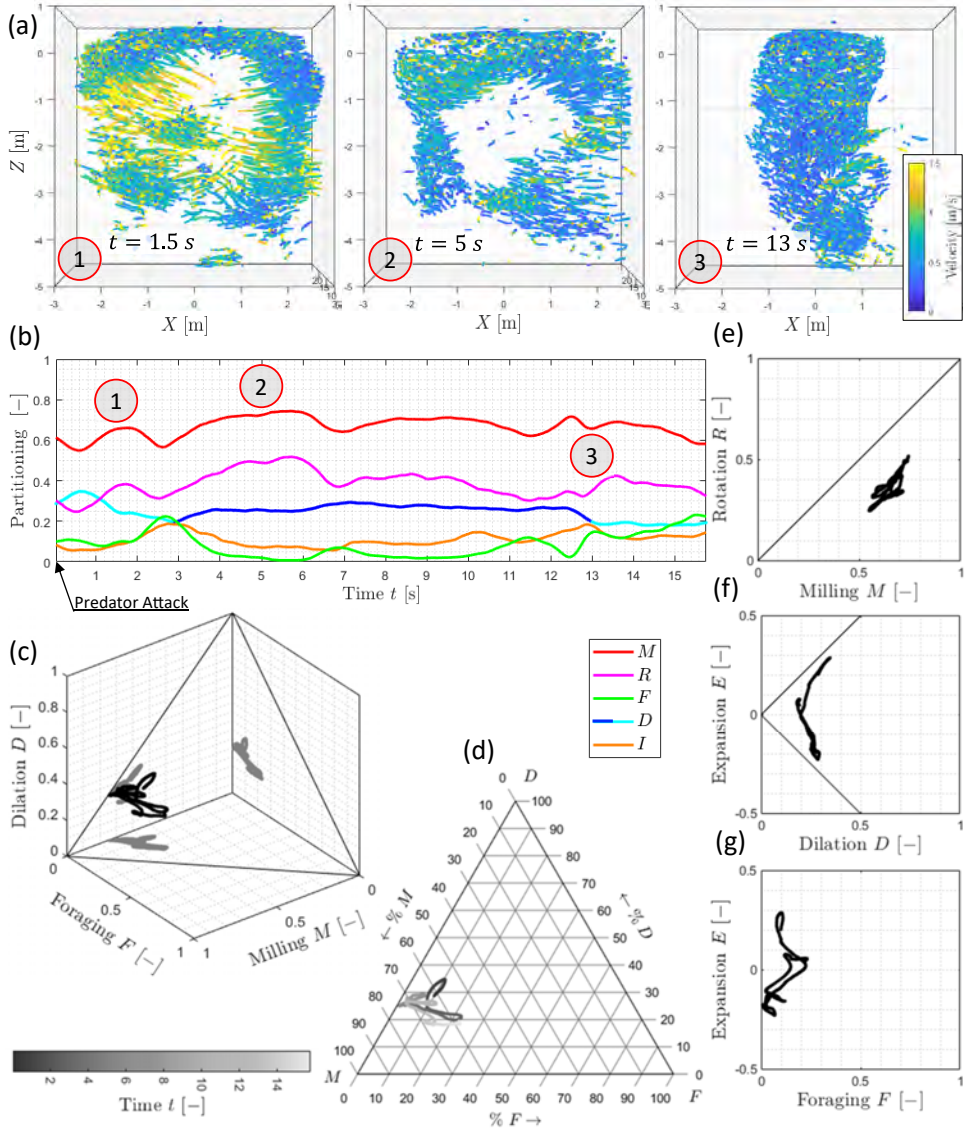


Figure 4.7: Partitioning of the kinematics of the fish school. a) The snapshots of Figure 4.4 and Figure 4.6: (1) rapid escape at $t = 2.5$ s, (2) rejoining from $t \sim 5$ to 10 s, (3) cohesive mill from $t = 13$ s onward. b) Time series milling number $M(t)$ (red), rotation number $R(t)$ (magenta), foraging number $F(t)$ (green), dilation number $D(t)$ (cyan for $E > 0$ and blue for $E < 0$), isochoric number $I(t)$ (orange) accompanying the snapshots of (a). c) Phase portrait of transient schooling dynamics drawn by the milling number $M(t)$, foraging number $F(t)$, and dilation number $D(t)$, inset the plane $M + F + D = 1$ that joins through the axes values 1. d) The ternary diagram that is extracted from the plane $M + F + D = 1$ from (c), the grey shading indicates time t . e) Rotation number $R(t)$ against milling number $M(t)$, the black line gives the upper bound $R = M$. f) Expansion number $E(t)$ against the dilation number $D(t)$, the black line gives the lower and upper bounds $D = |E|$. g) Expansion number $E(t)$ against foraging number $F(t)$. We indicate (b) the predator attack at $t = 0$.

netic energy in percentages. In Figure 4.8a, we plot the joint distribution $f(M, F, D)$ for the kinematic schooling parameters which include data from all our data sets. The distribution presents a clear peak, which corresponds to a partition $M : F : D / 75 : 5 : 20 \%$, and this peak is consistent with a milling state. Therefore, our quantitative characterization of kinematic modes agrees with our experimental observation of the prevalence of milling in the Rotterdam zoo.

An over-representation of milling throughout all data sets may mask subtle features in the schooling kinematics away from milling. Therefore we normalize the distribution for each value of M and plot the conditional distribution of F and D knowing the degree of milling M as $f(F, D|M) = f(F, D, M)/f(M)$, see Figure 4.8b. While both the degree of milling and foraging vary over a wide range of values from close to 0 to almost 100 %, the degree of dilation remains limited to values smaller than 30 %. We find that most of the fish schooling data clusters around a single trend that determines the relative degree of milling, foraging, and dilation, with constant ratio $D/M \propto 30/70$ in direction of foraging (yellow trend-line Figure 4.8b).

In addition, we insert the average partition of milling, foraging, and dilation for selected data sets. With this, we demonstrate how the M, F, D -partition can be used to classify the schooling behavior identified in Section 4.1 for the measurement weeks listed in Appendix C.2. Firstly, data sets that are classified as milling range above $\sim 60 \%$ milling number M (cyan circles). Secondly, the escape responses of the school in response to predators (magenta stars) range F between ~ 10 and 50% and M between ~ 40 and 70% . Finally, we inset two data sets that are solely classified as foraging (green squares). They indeed have a high foraging number F above $\sim 50 \%$ (see also Supplementary-Figure C.9).

PURE ROTATION AND PURE EXPANSION

Next, we investigate what happens when the school approaches a pure milling state $M \rightarrow 100 \%$ away from the peak position $M : F : D / 75 : 5 : 20 \%$ of Figure 4.8a. For this, we plot the conditional distribution $f(R|M) = f(R, M)/f(M)$ in rotation number R for an increasing degree of milling M in Figure 4.8c, see also Figure 4.7e. We find that for $M > 0.7$, the degree of pure rotation R is proportional to the milling number M and the school approaches a pure rotation state $R \rightarrow 1$ for $M \rightarrow 1$ (yellow trend-line). Hence for an increasing degree of milling M , we find that the school is increasingly rotating around a single axis.

We continue to consider the variation in the dilation by the expansion of the school, characteristic of a predator escape. We plot the distribution of the dilation number D conditional to the degree of expansion E by the conditional distribution function $f(D|E) = f(D, E)/f(E)$. Figure 4.8d reveals a crescent moon-like shape that is similar in signature to Figure 4.7f. The dilation number varies between $D \simeq 0.2$ when $E = 0$ up to $D \simeq 0.4$ when $|E| \rightarrow 0.3$. This captures the redistribution of kinetic energy. When $E = 0$ the isochoric number $I = D \simeq 0.2$ and when $|E| = 0.3$ its value decreases to $I = D - |E| = 0.1$ and approaches a pure expansion/contraction by the cyan dashes. Offsetting the absolute value $D = |E|$ for $E = 0$ we inset a few ad hoc reference curves $D = \sqrt{E^2 + I_0^2}$ (white dashes) with $I_0 \sim 0.25$ joining the data points in yellow; bridging their connection.

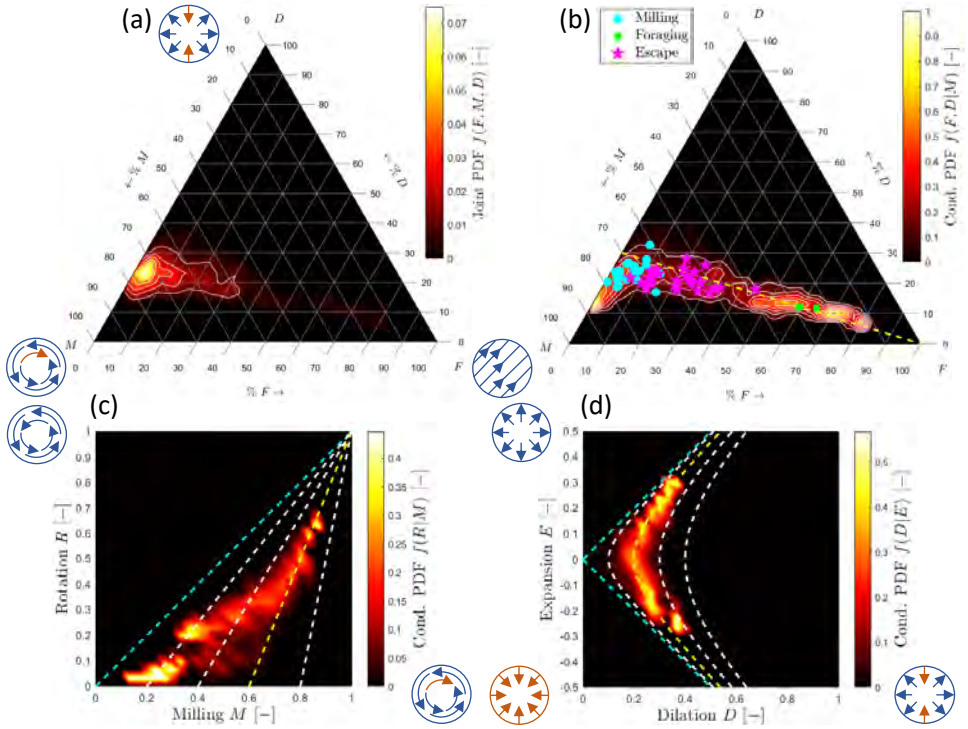


Figure 4.8: Variability of the fish school kinematics. a) Joint probability density $f(M, F, D)$ at the plane $M + F + D = 1$ that defines the ternary diagram for the milling, foraging, and dilation number M , F , and D . b) Conditional probability density $f(F, D|M)$ for the ternary diagram of (a), mediating between dilation D and foraging F , conditional to the degree of milling M , the colored markers inset the most dominant behaviors for some of the data sets. c) The rotation number R conditional to the milling number M , inset several reference lines for constant R/M (white) with the upper bound $R = M$ in cyan and in yellow the best fit to the data for $M \rightarrow 1$. d) The expansion number E plotted against the dilation number D , inset in cyan the lower and upper bound(s) $D = |E|$, several sample curves for $D = (E^2 + I_0^2)^{1/2}$ (white) and in yellow the curve that best joins the data. The inset pictograms illustrate the different elementary schooling motions.

4.4. SHAPE, KINEMATICS, AND LOCAL STATE VARIABLES

In the previous two sections, we introduced quantitative parameters to characterize fish schooling behavior. We focused on the time series and investigated the variability in the geometry (Section 4.2) and the kinematics of fish schooling (Section 4.3). Continuum models of group dynamics require the definition of equations of states to establish the relation between local state variables. One common example, from the modeling of traffic flow, is the relationship between driving speed and traffic density [46, 47]. Here, we consider local state variables characteristic of schooling fish namely, the swimming velocity, the local heading polarization, and fish density [9, 34].

For the current discussion, we restrict our focus to the 2017 measurement week of Table C.2 in Appendix C.2 which presents the greater variation in schooling behavior and is recorded at the highest resolution for similar time sequences. First, we plot the swimming velocity, the averaged local polarization, and fish density against the kine-

matic schooling parameters [13]. Second, we plot these local state variables against the obtained geometric parameters. The results here suggest a relationship between swimming velocity, local polarization, and fish density. This opens new directions for future research on fish schooling dynamics.

4.4.1. KINEMATIC STATE, FISH VELOCITY, POLARIZATION, AND DENSITY

A change in local schooling behavior, here expressed by the swimming velocity, local polarization of heading, and fish density can imply a global change in the resulting kinematic state. Therefore, we compute the average swimming velocity of the fish U , heading polarization ϕ , and fish density ρ as a function of the milling M , foraging F , and dilation D numbers [13], and present our results on the ternary diagram of Figure 4.8.

In Figure 4.9a, we plot the average swimming velocity U as a function of the kinematics schooling parameters. The velocity is a distinctive feature of the swimming behavior of the fish. One may expect notably different fish swimming activities for the different kinematics of the school. In our experiments, the swimming velocity does not provide a well-defined signature for the different schooling modes of milling, foraging, and dilation. The velocity remains mostly constant, except for a limited increase in the swimming velocity when the schooling behavior approaches pure milling ($M \rightarrow 100\%$) or foraging ($F \rightarrow 100\%$) kinematics, see isocontours in Figure 4.9a.

Figure 4.9b presents the average value for polarization ϕ as a function of M , F , and D . Here, we do find a distinct signature for the value of ϕ . Close to the peak position $M : F : D / 75 : 5 : 20\%$ (Figure 4.8a) the polarization takes a minimum value of $\phi \simeq 0.6$ and increases when the school kinematics moves closer to pure milling $M \rightarrow 100\%$ and foraging state $F \rightarrow 100\%$ with $\phi \rightarrow 0.85$. Therefore, away from the peak position in the ternary diagram (Figure 4.8a), the polarization suggests two different extremes for the school. The school either forms a fully polarized fish mill, or the school emerges to a pure foraging state and swims uni-directional through the fish tank.

We continue to compute the average value for the local fish density ρ against the kinematic schooling parameters M , F , and D in Figure 4.9c. The maximum fish density ($\rho \sim 100 \text{ m}^{-3}$) is reached just above the peak position in Figure 4.8a and the school is in a cohesive mill. Away from the peak position the school is generally sparser ($\rho \rightarrow 50 \text{ m}^{-3}$) in the direction of pure milling and foraging. Overall, the fish density varies more gradually and is more broadly distributed compared to the polarization.

4.4.2. SCHOOL GEOMETRY, FISH VELOCITY, POLARIZATION, AND DENSITY

Unique to the large ocean aquarium is that the fish swim in a relatively unconstrained environment and the school is free to undergo complex changes in shape. In Section 4.1 we presented various schooling behavior including elongated mills and rapidly expanding schools when escaping a predator (figures 4.1 to 4.3). Here, the variety in the shape of the school and internal distribution of fish is best captured by the dominant aspect ratio η_1 and inner distribution parameter ξ (Section 4.2). Therefore we continue to compare the average swimming velocity U , local polarization ϕ , and fish density ρ for these geometric parameters.

Figure 4.9d plots the swimming average velocity U of fish in the school against the dominant aspect ratio η_1 and the inner distribution variable ξ . We see a clear increase

from $U \sim 0.45$ to 0.6 m/s when the fish redistribute towards the edge of the school in the range of $1 < \xi < 2$, corresponding to a negative skewness ($s < 0$) for $\xi > 0.87$ (Figure 4.5c). These values are typical of an escape response, see the time series of figures 4.4 and 4.6, and supplementary figures C.4 to C.9 in Appendix C. In addition, we find that the swimming velocity decreases from $U \sim 0.45$ to 0.3 m/s when the dominant aspect ratio increases within $1 < \eta_1 < 5$. These data points correspond to highly elongated fish mills, such as those presented in Figure 4.1d. Hence our results suggest that the swimming velocity decreases with the effective reduction in the diameter of the school.

In Figure 4.9e, we proceed by plotting the local heading polarization against the dominant aspect ratio η_1 and the inner fish distribution parameter ξ . The heading polarization ϕ follows from the fish velocity U and when the fish redistribute towards the boundary of the school ($1 < \xi < 2$) its value increases from $\phi \sim 0.7$ to $\phi \sim 0.85$ accordingly. On the other hand, when the fish are distributed towards the center of the school for $\xi < 1$, the polarization remains approximately constant below $\phi < 0.7$ for different values of the dominant aspect ratio $1 < \eta_1 < 5$, and no changes are observed.

In Figure 4.9f, we present the average local density ρ against the dominant aspect ratio η_1 and inner fish distribution ξ . Contrary to the velocity and polarization, we find that the local density decreases when the fish redistribute towards the boundary for larger $\xi \rightarrow 2$, while its value remains unaffected by η_1 . Naively, this decrease in density when the fish redistribute towards the boundary may be interpreted as inevitable, the size of the school enlarges and thereby the density diminishes due to the expanding geometry. However, this interpretation may lack actual physical grounding. The shape of the school is thought to emerge from the dynamics and interaction among the fish [32–34], from the bottom-up, and not the other way around, top-down, see also previous experimental work [18].

FISH TRAFFIC: INTERRELATIONS BETWEEN LOCAL STATE VARIABLES

Considering all our observations from Figure 4.9, a general picture emerges. We find that when the fish density increases, the swimming velocity decreases, and when the polarization increases the swimming velocity increases, for all resulting kinematics and features in the shape. Such a relationship between the velocity, the local density, and the local polarization is central to modeling and predicting group dynamics, see for example simple equations of state for the continuum modeling of traffic flow [47–49].

Moreover, an inverse relationship between density and velocity is a primary mechanism responsible for the formation of shock waves, leading to traffic jams in traffic flow problems. Our findings suggest that such (non-linear) wave propagation mechanisms may too exist for schooling fish in three dimensions. Such mechanisms have previously been studied in fish schooling models by a limited perception range [32–34], and have as well been reported in experiments [9, 17, 18] and field observation [50–52], and underlie to different mechanisms of information transfer [15, 53, 54].

4.5. SUMMARY AND CONCLUSIONS

In this chapter, we have demonstrated the application of the measurement technique detailed in Chapter 2 and the tracking algorithms presented in Chapter 3. We presented how we extract quantitative measures from the full three-dimensional tracking data of

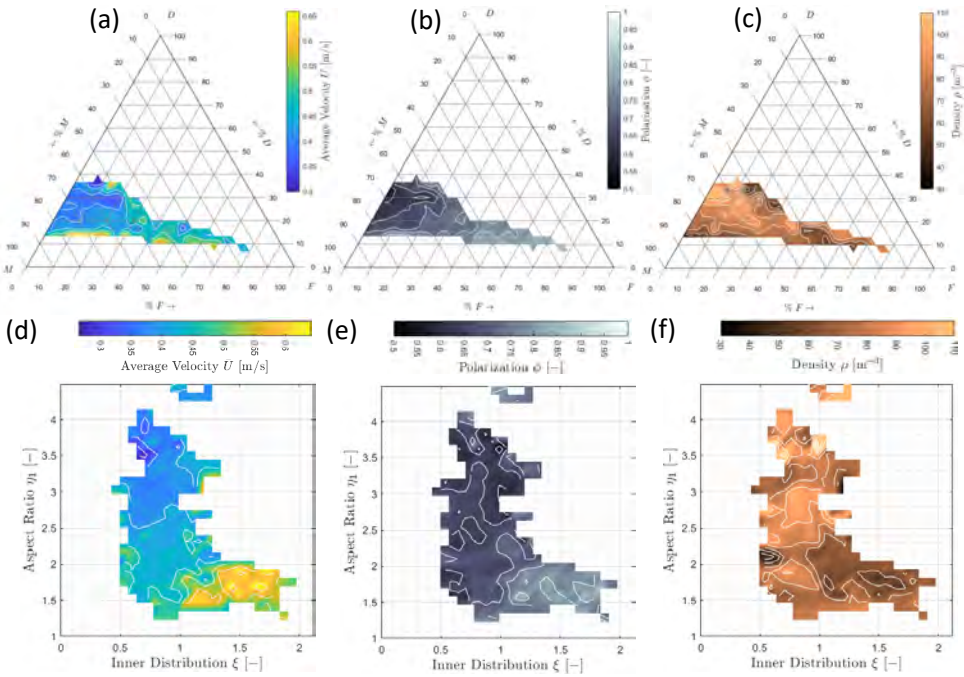


Figure 4.9: Local fish density, polarization, and velocity against the kinematic and geometric schooling parameters. a–c) The swimming velocity U of the fish, the local heading polarization ϕ and the average fish density ρ plotted against the kinematics schooling parameters for milling M , foraging F , and dilation D . d–f) The average swimming velocity U of the fish, the local heading polarization ϕ and the average fish density ρ plotted against the inner distribution parameter ξ , and dominant aspect ratio η_1 of the school.

the fish inside the large school at the Rotterdam zoo.

In Section 4.1, we presented an overview of the tracking data. We found that, in absence of a predator, the school is milling counter-clockwise in the fish tank. This behavior was observed consistently for all 6 measurement weeks over 4 years, with a large variety of school shapes, including surface accumulation, cylindrical, skewed, and elongated fish mills. Furthermore, upon interaction with a predator fish, we found many behaviors in qualitative agreement with the work by Pitcher and Wyche [1] and Magurran and Pitcher [2] including splitting (and joining), vacuole, rapid flash expansion, cruising, as well as, a collective downdraft, or dive [29], among many.

In Section 4.2, we performed the first quantitative assessment and studied the geometric properties of the school. We selected a specific data set corresponding to a time series for a rapid escape response. For this data set, we presented the time evolution of the volume, the density, and the aspect ratios of the school. We also defined the spatial moments for the internal distribution of fish in the school and presented the evolution for the moment mean, standard deviation, and skew for the same data set. In particular, we showed that the skew switches sign when the fish redistribute towards the edges, where the inner fish distribution parameter quantifies its degree.

Following this analysis, we continued to consider all of the data sets available and

studied the variability of the school shape and inner distribution parameters, and presented their statistical distribution. We quantified the large variation in overall shape by the aspect ratio(s) of the school. At higher school volumes, we found that the local density of fish does not follow a uniform scaling and approaches a constant level. Moreover, we found a bimodality for the parameters of skew and inner distribution which the fish either cluster toward the origin of the school or redistribute at the edges, suggesting a predator attack.

In Section 4.3, we quantified the kinematics of schooling fish. We first considered the evolution of the velocity, local polarization, and mixed spatial moments. Here we found little differences in the velocity distribution when the school is interacting with a predator or not. Furthermore, we demonstrated that the velocity of the center of mass and the angular momentum do not provide a comprehensive picture of schooling behavior. Therefore, we computed the kinematic decomposition on our rescaled set of axes in the reference frame of the school. Partitioning the kinetic energy, we characterized the motion of the school with several kinematic parameters quantifying the degree of milling, foraging, and dilation. We further subdivided the milling number in a pure rotation and dilation in pure expansion which helped further analyze the school kinematics.

Starting with time series analyses we continued to investigate the variability in the kinematics of the school. We presented the joint distribution functions at the ternary diagram for milling, foraging, and dilation, and showed that most of the data sets are in a milling state at a partition $M : F : D / 75 : 5 : 20$ %. Presenting the conditional probability density function against milling we found that away from the milling position, the school mediates between pure milling and foraging following a single trend line. We also quantified the distribution of the kinetic energy in the direction of pure milling. Here the school increasingly rotates around a single axis. Furthermore, we quantified the redistribution of kinetic energy when the school dilates. Here we found the school to approach a pure expansion in escape.

In Section 4.4, we compared the swimming velocity, the local polarization, and fish density for the kinematic schooling parameters, shape, and inner fish distribution. Firstly, we found little variation in fish swimming velocity for the kinematic schooling parameters. Secondly, we observed a well-defined minimum in fish polarization when the fish are in a cohesive mill and multi-modality towards pure milling and foraging, with a more gradual variation in fish density. Next, we found a jump in the swimming velocity when the fish redistribute towards the edges of the school ($\xi > 0.87$) and a gradual drop when the school elongates ($\eta_1 \gg 1$) into a slender cohesive mill ($\xi < 0.87$). Moreover, the local fish polarization sharply increases when the fish redistribute towards the boundary while the fish density decreases. The actual dynamic interaction between fish and relations between these variables open a broad range of future research directions, stretching beyond the scope of the current thesis.

The parameters and analyses defined in this chapter are now available as reference values for the shape and kinematics of different schooling data sets and behaviors. Altogether, we demonstrated their use in the different analyses and provided new insight into the inner working of three-dimensional fish schools.

REFERENCES

- [1] T. J. Pitcher and C. J. Wyche, *Predator-avoidance behaviours of sand-eel schools: why schools seldom split*, in *Predators and prey in fishes*, Vol. 2 (Springer, Dordrecht, 1983) pp. 193–204.
- [2] A. E. Magurran and T. J. Pitcher, *Provenance, shoal size and the sociobiology of predator-evasion behaviour in minnow shoals*, *Proc. R. Soc. Lond.* **229**, 439 (1987).
- [3] T. J. Pitcher, *Heuristics Definitions of Fish Shoaling Behavior*, *Animal Behavior*, 611 (1982).
- [4] A. E. Magurran, *The Adaptive Significance of Schooling as an Anti-predator Defence in Fish*, *Ann. Zool. Fennici* **27**, 51 (1990).
- [5] T. J. Pitcher and J. K. Parrish, *Functions of Shoaling Behaviour in Teleost*, 2nd ed., edited by T. J. Pitcher, Vol. 7 (Chapman & Hall, London, 1993) pp. 364–438.
- [6] S. Marras, R. S. Batty, and P. Domenici, *Information transfer and antipredator maneuvers in schooling herring*, *Adaptive Behavior* **20**, 44 (2011).
- [7] G. Rieucau, A. J. Holmin, J. C. Castillo, I. D. Couzin, and N. O. Handegard, *School level structural and dynamic adjustments to risk promote information transfer and collective evasion in herring*, *Animal Behaviour* **117**, 69 (2016).
- [8] P. Domenici and R. S. Batty, *Escape behaviour of solitary herring (*Clupea harengus*) and comparisons with schooling individuals*, *Marine Biology* **128**, 29 (1997).
- [9] C. Becco, N. Vandewalle, J. Delcourt, and P. Poncin, *Experimental evidences of a structural and dynamical transition in fish school*, *Physica A: Statistical Mechanics and its Applications* **367**, 487 (2006).
- [10] J. E. Herbert-Read, A. Perna, R. P. Mann, T. M. Schaerf, D. J. T. Sumpter, A. J. W. Ward, and H.-R. Performed, *Inferring the rules of interaction of shoaling fish*, *PNAS* **108**, 18726 (2011).
- [11] Y. Katz, K. Tunstrøm, C. C. Ioannou, C. Huepe, I. D. Couzin, S. A. Levin, I. D. C. Designed, and I. D. C. Performed, *Inferring the structure and dynamics of interactions in schooling fish*, *PNAS* **108**, 18720 (2011).
- [12] S. Marras and P. Domenici, *Schooling Fish Under Attack Are Not All Equal: Some Lead, Others Follow*, *PLoS ONE* **8**, 1 (2013).
- [13] K. Tunstrøm, Y. Katz, C. C. Ioannou, C. Huepe, M. J. Lutz, and I. D. Couzin, *Collective States, Multistability and Transitional Behavior in Schooling Fish*, *PLoS Computational Biology* **9**, 1 (2013).
- [14] A. Berdahl, C. J. Torney, C. C. Ioannou, J. J. Faria, and I. D. Couzin, *Emergent Sensing of Complex Environments by Mobile Animal Groups*, *Science* **339**, 574 (2013).

- [15] S. B. Rosenthal, C. R. Twomey, A. T. Hartnett, H. S. Wu, and I. D. Couzin, *Revealing the hidden networks of interaction in mobile animal groups allows prediction of complex behavioral contagion*, Proceedings of the National Academy of Sciences of the United States of America **112**, 4690 (2015).
- [16] J. Jhawar, R. G. Morris, U. R. Amith-Kumar, M. Danny Raj, T. Rogers, H. Rajendran, and V. Guttal, *Noise-induced schooling of fish*, Nature Physics **16**, 488 (2020).
- [17] S. V. Viscido, J. K. Parrish, and D. Grünbaum, *Individual behavior and emergent properties of fish schools: a comparison of observation and theory*, Source: Marine Ecology Progress Series **273**, 239 (2004).
- [18] C. K. Hemelrijk, H. Hildenbrandt, J. Reinders, and E. J. Stamhuis, *Emergence of Ob-long School Shape: Models and Empirical Data of Fish*, Ethology **116**, 1099 (2010).
- [19] S. Butail and D. A. Paley, *Three-dimensional reconstruction of the fast-start swimming kinematics of densely schooling fish*, Journal of the Royal Society Interface **9**, 77 (2012).
- [20] J. Delcourt, M. Denoël, M. Ylief, and P. Poncin, *Video multitracking of fish behaviour: A synthesis and future perspectives*, Fish and Fisheries **14**, 186 (2013).
- [21] S. H. Wang, J. Zhao, X. Liu, Z.-M. Qian, Y. Liu, and Y. Q. Chen, *3D Tracking Swimming Fish School with Learned Kinematic Model Using LSTM Network*, in *International Conference on Acoustics, Speech and Signal Processing (ICASSP)* (IEEE, New Orleans, LA, USA, 2017) pp. 1068–1072.
- [22] I. Watts, M. Nagy, R. I. Holbrook, D. Biro, and T. Burt de Perera, *Validating two-dimensional leadership models on three-dimensionally structured fish schools*, Royal Society Open Science **4** (2017), 10.1098/rsos.160804.
- [23] A. J. Ward, T. M. Schaerf, J. E. Herbert-Read, L. Morrell, D. J. Sumpter, and M. M. Webster, *Local interactions and global properties of wild, free-ranging stickleback shoals*, Royal Society Open Science **4** (2017), 10.1098/rsos.170043.
- [24] M. Romenskyy, J. E. Herbert-Read, C. C. Ioannou, A. Szorkovszky, A. J. Ward, and D. J. Sumpter, *Quantifying the structure and dynamics of fish shoals under predation threat in three dimensions*, Behavioral Ecology **31**, 311 (2020).
- [25] J. K. Parrish and L. Edelstein-Keshet, *Complexity, Pattern, and Evolutionary Trade-Offs in Animal Aggregation*, Science **284**, 99 (1999).
- [26] D. J. T. Sumpter, *The principles of collective animal behaviour*, Philosophical Transactions of the Royal Society B: Biological Sciences **361**, 5 (2006).
- [27] U. Lopez, J. Gautrais, I. D. Couzin, and G. Theraulaz, *From behavioural analyses to models of collective motion in fish schools*, Interface Focus **2**, 693 (2012).
- [28] J. Delcourt, N. W. Bode, and M. Denoël, *Collective vortex behaviors: Diversity, proximate, and ultimate causes of circular animal group movements*, Quarterly Review of Biology **91**, 1 (2016).

- [29] L. Nøttestad and B. E. Axelsen, *Herring schooling manoeuvres in response to killer whale attacks*, Canadian Journal of Zoology **77**, 1540 (1999).
- [30] A. Cavagna, I. Giardina, A. Orlandi, G. Parisi, and A. Procaccini, *The STARFLAG handbook on collective animal behaviour: Part II, three-dimensional analysis*, Tech. Rep. (2008).
- [31] M. Ballerini, N. Cabibbo, R. Candelier, A. Cavagna, E. Cisbani, I. Giardina, A. Orlandi, G. Parisi, A. Procaccini, M. Viale, and V. Zdravkovic, *Empirical investigation of starling flocks: a benchmark study in collective animal behaviour*, Animal Behaviour **76**, 201 (2008).
- [32] H. Kunz and C. K. Hemelrijk, *Artificial fish schools: collective effects of school size, body size, and body form*. Artificial Life **9**, 237 (2003).
- [33] C. K. Hemelrijk and H. Kunz, *Density distribution and size sorting in fish schools: An individual-based model*, Behavioral Ecology **16**, 178 (2005).
- [34] C. K. Hemelrijk and H. Hildenbrandt, *Self-organized shape and frontal density of fish schools*, Ethology **114**, 245 (2008).
- [35] A. Cavagna, A. Cimarelli, I. Giardina, A. Orlandi, G. Parisi, A. Procaccini, R. Santagati, and F. Stefanini, *New statistical tools for analyzing the structure of animal groups*, Mathematical Biosciences **214**, 32 (2008).
- [36] M. Ballerini, N. Cabibbo, R. Candelier, A. Cavagna, E. Cisbani, I. Giardina, V. Lecomte, and A. Orlandi, *Interaction ruling animal collective behavior depends on topological rather than metric distance: Evidence from a field study*, PNAS **105**, 1232 (2008).
- [37] I. D. Couzin, J. Krause, R. James, G. D. Ruxton, and N. R. Franks, *Collective Memory and Spatial Sorting in Animal Groups*, J. theor. Biol **218**, 1 (2002).
- [38] J. Gautrais, C. Jost, and G. Theraulaz, *Key behavioural factors in a self-organised fish school model*, Ann. Zool. Fennici **45**, 415 (2008).
- [39] D. S. Calovi, U. Lopez, S. Ngo, C. Sire, H. Chaté, and G. Theraulaz, *Swarming, schooling, milling: Phase diagram of a data-driven fish school model*, New Journal of Physics **16**, 1 (2014).
- [40] A. Filella, F. Nadal, C. Sire, E. Kanso, and C. Eloy, *Model of Collective Fish Behavior with Hydrodynamic Interactions*, Physical Review Letters **120**, 1 (2018).
- [41] A. Costanzo and C. K. Hemelrijk, *Spontaneous emergence of milling (vortex state) in a Vicsek-like model*, Journal of Physics D: Applied Physics **51**, 1 (2018).
- [42] A. Costanzo, *Milling-induction and milling-destruction in a Vicsek-like binary-mixture model*, EPL **125** (2019), 10.1209/0295-5075/125/20008.
- [43] A. Costanzo, E. Van Haeringen, and C. K. Hemelrijk, *Effect of time-delayed interactions on milling: A minimal model*, EPL **138**, 1 (2022).

- [44] A. Cavagna, I. Giardina, and T. S. Grigera, *The physics of flocking: Correlation as a compass from experiments to theory*, *Physics Reports* **728**, 1 (2018).
- [45] N. O. Handegard, K. M. Boswell, C. C. Ioannou, S. P. Leblanc, D. B. Tjostheim, and I. D. Couzin, *The dynamics of coordinated group hunting and collective information transfer among schooling prey*, *Current Biology* **22**, 1213 (2012).
- [46] M. J. Lighthill and G. B. Whitham, *On kinematic waves II. A theory of traffic flow on long crowded roads*, *Proceeding of the Royal Society A* **229**, 317 (1955).
- [47] G. B. Whitham, *Linear and Nonlinear Waves*, 2nd ed. (WILEY, New York, 1974).
- [48] R. Haberman, *Partial differential equations*, 5th ed. (Pearson, 2012).
- [49] V. L. Knoop, *Traffic Flow Theory: An introduction with exercises*, 3rd ed. (TU Delft Open, Delft, 2020).
- [50] F. Gerlotto, S. Bertrand, N. Bez, and M. Gutierrez, *Waves of agitation inside anchovy schools observed with multibeam sonar: a way to transmit information in response to predation*, *ICES Journal of Marine Science* **63**, 1405 (2006).
- [51] A. Procaccini, A. Orlandi, A. Cavagna, I. Giardina, F. Zoratto, D. Santucci, F. Chiarotti, C. K. Hemelrijk, E. Alleva, G. Parisi, and C. Carere, *Propagating waves in starling, *Sturnus vulgaris*, flocks under predation*, *Animal Behaviour* **82**, 759 (2011).
- [52] C. K. Hemelrijk, A. Costanzo, H. Hildenbrandt, and C. Carere, *Damping of waves of agitation in starling flocks*, *Behavioral Ecology and Sociobiology* **73** (2019), 10.1007/s00265-019-2734-4.
- [53] A. Attanasi, A. Cavagna, L. Del Castello, I. Giardina, T. S. Grigera, A. Jelić, S. Melillo, L. Parisi, O. Pohl, E. Shen, and M. Viale, *Information transfer and behavioural inertia in starling flocks*, *Nature physics* **10**, 691 (2014).
- [54] V. Lecheval, L. Jiang, P. Tichit, C. Sire, C. K. Hemelrijk, and G. Theraulaz, *Social conformity and propagation of information in collective u-turns of fish schools*, *Proceedings of the Royal Society B: Biological Sciences* **285**, 1 (2018).

5

CONCLUSIONS AND RECOMMENDATIONS

This thesis presented results in tracking a large school of ± 2000 *Harengula clupei* (false herring) swimming in three dimensions in a semi-natural habitat at the large-scale public ocean aquarium of the Rotterdam zoo. We summarize the main conclusions of this thesis and make several recommendations for future research avenues.

Chapter 2 presented our measurement technique to image fish swimming in a large tank in three dimensions. We first introduced our imaging setup located behind a large window that allowed us to optically access the underwater environment in the fish tank. Secondly, we introduced our calibration technique and explained the implementation of projective geometry and linear ray-tracing in the presence of significant optical distortion imaging from air to water. Combining non-linear camera mappings commonly used in experimental fluid mechanics with methods from computer vision we alleviated the requirement of a large calibration target to be moved with known displacements. Rather, we used a freely moving calibration target that is much smaller than the measurement domain itself and can be positioned at random positions and orientations over large distances by a team of divers.

We continued characterizing the performance of our calibration method. We validated a precision below 2 % of the calibration target dimension ($30 \times 30 \text{ cm}^2$ checkerboard tile), corresponding to a triangulation accuracy below 1 *cm* over the entire measurement volume. Correcting the optical distortion across the refractive interface from air to water, the calibration method correctly captures the intrinsic camera properties such as the focal length of the lenses and the extrinsic camera positioning and orientations. An assessment of the robustness and convergence of our camera calibration method revealed that a minimum of 15 calibration images is required to obtain a valid camera calibration. Increasing the number of calibration images better samples the measurement domain and improves spatial accuracy. Finally, tracking a group of tuna fish over a large distance demonstrated the application of our camera calibration to biological fluid mechanics and the tracking of fish in three spatial dimensions.

Chapter 3 introduced algorithms used to perform time-resolved three-dimensional tracking of fish in a large school. We first explained several challenges in imaging a complex underwater environment and described the directional dependent (anisotropic) projection of the fish by their position, and orientation. Subsequently, we presented image processing routines to remove the image background and introduced several image convolution filters to identify the fish over multiple scales by an elliptical contour function in the individual camera views. From the identified ellipse contour, we presented a full integration of the framework of projective geometry to make our methods robust against variations in the reprojection error over large distances. Using linear ray-tracing, we showed how we match fish in stereoscopic correspondence and construct trifocal and quadrifocal camera matches. We defined an integer assignment and presented a direct solution strategy to find matches that best fit the different camera images. We expanded this integer assignment to include recent advances in particle tracking from experimental fluid mechanics and fitting of trajectories to perform the time-resolved tracking of fish. Finally, we showed that forward, backward, and (again) forward tracking in time is crucial in obtaining long trajectories in the face of missing data, including the tracking of fish behind large occlusions from surrounding predators.

5

We then presented the steps involved in post-processing and cleaning the tracking data. We first filtered noise from elevated reprojection errors and segmented the data to select long trajectories. Following the post-processing, we characterized the performance of our tracking algorithms. First, we identified the fish image density and frame displacement as the main parameters of input to the tracking algorithms. Expressing the image density in ‘fish-image-per-pixel’ (fipp) and the frame displacement as ‘fish-swimmer-frame’ (fspf), we obtained the lowest reprojection errors (~ 0.25 fish image) and the longest tracks (± 160 frames) below 0.101 fipp and 0.5 fspf. Secondly, we computed the probability of tracking into the next frame. We marked sharp boundaries for the image displacement in the same region, while our methods break down after 0.227 fipp local image source density. Finally, we further investigated the reliability of the tracking into the next frame and extracted a single tracking efficacy parameter. We obtained high tracking reliability above an efficacy of 0.985, which drops off with increasing image displacement and density, and error from the calibration while tracking at sub-optimal imaging conditions.

Chapter 4 presented results obtained from the measurement technique and tracking algorithms introduced in this thesis. From the multiple measurement weeks that were performed over the course of four years, we first showcased a qualitative overview of the tracking data. These included different schooling behaviors, with multiple modes of milling, foraging, and a large variety of school shapes and escape responses including rapid (flash) expansions.

Subsequently, we proceeded with a quantitative analysis of the school shape and internal distribution of fish. We started by identifying the center of gravity of the school and compared the time series for school volume, the local fish density, and the dominant, and subdominant aspect ratios. We then compared the variation of the aspect ratios of the school for multiple data sets and revealed that the fish density in the school does not simply scale with the volume but rather reached a constant density at higher volumes. Subsequently, we continued to analyze time series for spatial moments of the

radial fish distribution and showed that fish redistribute to the edges, suggesting a predator attack. Finally, we revealed a bimodality for the distribution of fish in the school as the fish either distribute uniformly when in a cohesive mill or strongly redistribute towards the boundary when in escape.

Next, we turned our attention to the kinematics of the fish school. We started by presenting time series for the distribution of fish velocity and local polarization alongside time series for the velocity of the school center of mass and mixed spatial moments. Here we showed that the angular momentum of the school about its center of gravity is inconclusive for the degree of milling while the volumetric rate-of-change is mostly indicative of evading a predator. We then investigated the distribution of the kinetic energy inside the school. From the kinematic decomposition, we identified three kinematic parameters that correspond to three types of distinct behavior namely, foraging (uniform translation), milling (rotation), and dilation (radial in/outward motion). We presented a ternary diagram for the kinematics of the school and presented a unique signature that predominantly resides between milling and foraging. Furthermore, for an increasing degree of milling, the school increasingly rotates around a single axis, and for the degree of dilation, the school approaches a pure expansion when in escape.

The final part of this thesis further discussed our results in relation to local state variables of fish swimming velocity, local polarization of heading, and fish density. Most notably, when the fish redistribute toward the edge of the school the swimming velocity and local polarization increase, while the density decreases. Although this may be inevitable from the expanding geometry of the school, a more sophisticated point-of-view actually hints at a hidden dependency between velocity, fish density, and polarization. Such a functional dependency is at the heart of transport models in traffic flow modeling. This suggests that similar mechanisms may too exist for schooling fish in three dimensions; with many directions for future research.

5.1. OUTLOOK TO FUTURE WORK

Having unlocked the third dimension for the shape and kinematics of a realistically sized fish school, swimming unconstrained in a semi-natural habitat, we have yet scratched the surface. We hope that the current thesis will provide a foundation for future research, for which we make several recommendations to improve and build on this thesis.

Firstly, the measurement technique of Chapter 2 and the subsequent tracking algorithms are flexible to include more than four cameras. Although the current work has been implemented to make optimal use of existing facilities and lighting conditions with the least intrusion to the fish in the tank, the camera configuration has been greatly limited to narrow camera angles and baselines down to $\sim 5^\circ$ and $\sim 1\text{ m}$, respectively. Such limitations obviously restrict the accuracy of the tracking data and may introduce bias in the velocity and acceleration statistics, although extensively validated. Therefore one improvement could be made by imaging at a greater variation in camera positions ranging beyond the span of the large window used to optically access the fish tank. This could for example be achieved by installing camera positions above the tank or possibly using waterproof camera equipment to image the fish throughout the tank.

Such improvements are not at all a trivial task. They may require a great deal of design iteration and experimentation. For example, imaging above the water surface down

into the tank specific care should be taken for disturbances from the water surface. Here one solution could be to use long focal-length lenses and position the cameras away to limit the effective distortion in the image. On the other hand, one may decide to install optical boxes. Such can in turn be (partially) submerged to carry existing camera equipment. However, viewing from different angles the fish may appear camouflaged or poorly visible due to a lack of light. Furthermore, such additional hardware may require special care for animal safety. Potential hazards may include fish jamming into equipment, use of electricity underwater, corrosion, the beak of a curious sea turtle, and may require the use of durable materials (*e.g.* from food processing).

Secondly, the application of the tracking algorithms of Chapter 3 can be further improved with current advances in imaging. Here the multi-resolution wavelet and ellipse identification image filters may be extended to include the increasingly complex and fine features of the fish image projection. For example, considering high-order shape functions. Furthermore, elaborating sophisticated solution strategies to solve the integer assignment for matching and tracking fish in three dimensions still carries the potential to extract longer trajectories in the object domain. Moreover, advanced Kalman filters could improve the accuracy of fish trajectories in the presence of significant uncertainty and noise. For example, one could further integrate dual-space geometry and solve the greater fish group displacement using object correlation routines. Finally, as not implemented in the current work, one could as well update and correct the camera calibration which may deflect and vibrate over the course of a measurement week.

Regarding the tracking of fish, perhaps more exciting would be to track the large variety of predator and cohabitant fish, and their complex body pose, and motion. One could explore novelties in machine learning and neural networks to fully resolve the shape and motion of swimming sharks, as well as the fast start of a barracuda fish, and the highly synchronous swimming kinematics of hunting tuna in a group, to name a few. Such developments in existing and future (high-resolution) image data, could explore novel questions on the interaction of the school with a shark and its tail-fin motion, as well as the interaction between the school and the waving flipper of a sea turtle.

Finally, for the analysis presented in Chapter 4 we hope that the geometric and kinematics parameters will provide a systematic framework to characterize the behavior of future schools in three dimensions. With preliminary analysis that remained beyond the scope of the current work: ‘What is the spatial distribution of velocity around the center of rotation in a milling fish school, is it a solid-body rotation or an (irrotational) fluid-like vortex motion, or something in between?’, ‘Is a milling fish school fully correlated in all three spatial dimensions, or is there a hidden anisotropy in which the school is for example stratified in planar layers?’, ‘What is the apparent interaction between the fish swimming velocity, local density, and polarization, and what is the implication for the school’s cohesion?’, ‘What is the inner structure of the fish neighborhood (nearest neighbors, residence time, mean free path, *etc.*), do fish lock on to preferential positions in each other’s wake?’, ‘What is the evolution in distance between identified fish pairs, and can we extract a meaningful interaction (or social force) from their relative approach and departure?’. Facing such questions, this thesis contributes frameworks to analyze the shape and kinematics, which may find future use in, for example, delineating the predator attack from the milling state of the school.

5.2. SCIENTIFIC CONTRIBUTION AND IMPACT

Although this thesis extensively focused on harvesting the three-dimensional tracking data, its novelty is leveraged by its application to a realistic quasi-field setting. In particular, the unique ocean aquarium facility present at the Rotterdam zoo has allowed the tracking of fish in a relatively unconstrained and semi-natural habitat. This has not only presented the tracking of an increased number of fish at a length scale much larger than previously attempted but as well supported a natural schooling behavior at a scale that is hardly possible in a laboratory setting. Therefore, the novelty of the current contribution provides a first measurement of a realistically sized fish school, in a realistic environment. This has a direct impact to further our knowledge and fundamental understanding of the collective behavior and social self-organization of fish schooling as well as the associated biomechanics and fluid dynamics.

For example, we have shown that the school of fish in the Rotterdam zoo is not simply uniformly distributed in space. Actually, the distribution of fish within the school evolves and progresses when interacting with a predator. This not only provides new insight into the variety in school shape but also gives new insight into the internal cohesion of the fish school, which is free to split and distribute throughout the large tank. This result has been obtained in the unconstrained environment of the large ocean aquarium of the Rotterdam zoo. It could hardly have been obtained in a laboratory setting because of the physical constraints represented by the length scale of the school, and the impossibility of supporting a natural schooling behavior.

In addition, we extensively investigated the three-dimensional kinematics of the fish school, while ignoring its shape. Up to this point experimental work on variability of collective states and associated transitional behavior had been limited to two dimensions in a laboratory setting. In our work, we found that conventional metrics to quantify the global order of the school are only partially relevant in an unconstrained three-dimensional quasi-field setting. Therefore, we extended the previous work to include the expansion and contraction of the school, which can only be studied in a large enough fish tank such as the one present in the Rotterdam zoo. Since our framework relies solely on partitioning the kinetic energy of the animal group, it provides a general framework to compare with other model systems such as swarming midges, birds flocking in the field, and other species that display collective behavior.

In a final discussion of this thesis, we focused on the variability in the schooling dynamics against our kinematic and shape parameters. Here we found that the schooling fish display an interaction between local state variables in relation to the global shape and kinematics state of the school. As the shape and structure of the school are thought to emerge from the interactions among the fish, this provides new insight into the dynamics and social self-organization of a realistically sized fish school. Moreover, a coupling between the local fish interaction and the global structure over the full extent of the school is not at all a trivial result. Here lie open questions beyond the physical range of the current experiment, for example, what sets the system size of a finite school?

This thesis work provides a new and unique availability of empirical tracking data for schooling fish in three dimensions. Such availability has a direct impact on the extraction of the underlying social rules and for example, improves the modeling of social forces in three dimensions. Moreover, allowing the comparative biology between differ-

ent model systems of collective behavior, such as insect swarming, bird flocking, and fish schooling for the current work, helps deepen our understanding of different crowd dynamics. This has a direct impact on crowd control, the biomimetics of robotic schooling, and collective flight, as well as in improving traffic flow, and potentially contributing to our understanding of active fluids such as those found at the micron-scale. It is our hope that the availability of the novel three-dimensional tracking data for the complex unconstrained dynamics of schooling fish brings a new paradigm where some of the inherent assumptions in our understanding of planar fish schools may need to be readdressed.

A

APPENDIX

This appendix belongs primarily to Chapter 2.

A.1. OPTICAL DISTORTION ACROSS AN INTERFACE

Refraction across an interface between two media of different refractive indexes is governed by Snell's law:

$$\frac{\sin(\theta_2)}{\sin(\theta_1)} = \tilde{n}, \quad (\text{A.1})$$

where $\tilde{n} = n_1/n_2$ with n the refractive index, θ_1 is the incident angle and θ_2 is the exit angle to the normal vector on the interface. For a flat interface, the image plane of a camera can be warped parallel to the interface by the linear image mapping H :

$$H = \begin{bmatrix} A & \mathbf{p} \\ \mathbf{v}^T & 1 \end{bmatrix}, \quad (\text{A.2})$$

where A is a 2×2 matrix that describes an affine image transformation that changes the aspect ratio and skew of the image, \mathbf{p} centers the image at the principle ray, and \mathbf{v}^T describes a perspective change [1]. With these notations, the distortion mapping can be written as:

$$\hat{\mathbf{x}} = \frac{A\mathbf{x} + \mathbf{p}}{\sqrt{\lambda \|A\mathbf{x} + \mathbf{p}\|^2 + (\mathbf{v}^T\mathbf{x} + 1)^2}}, \quad (\text{A.3})$$

where $\lambda = (1 - \tilde{n}^2)/f^2$ with f the focal-length in pixels dimensions, and can be simplified to the division model by Taylor expansion of the denominator [2].

A.2. RELATIVE CAMERA POSITIONS FROM CALIBRATED VIEWS

We determine the rigid body motion from a view c to another view c' , by first finding the best rotation, using the Kabsch algorithm [3]. We first compute the cross-covariance

matrix $A = \sum_{n,j} \mathbf{X}_j^{n,c'} (\mathbf{X}_j^{n,c})^T$ using the paired object coordinates $\mathbf{X}_j^{n,c}$ and $\mathbf{X}_j^{n,c'}$ from multiple checkerboards. We then compute the singular value decomposition of the cross-covariance matrix $A = USV^T$ and extract the best rotation matrix $R^{c,c'}$ as:

$$R^{c,c'} = U \begin{bmatrix} 1 & 0 & 0 \\ 0 & 1 & 0 \\ 0 & 0 & \det(UV^T) \end{bmatrix} V^T. \quad (\text{A.4})$$

Knowing $R^{c,c'}$, we use the rigid body motion $\mathbf{X}_j^{n,c'} = R^{c,c'} \mathbf{X}_j^{n,c} + \mathbf{t}^{c,c'}$ to compute the translation vector $\mathbf{t}^{c,c'}$ between the views.

From the relative position between the views we find a unique extrinsic camera positioning R^c , \mathbf{t}^c by taking the first view at reference and solving the minimization problem for the translation \mathbf{t}^c ,

$$\begin{aligned} \min_{\mathbf{t}^c} \sum_{c \neq c', c'} & \left\| R^{c,c'} \mathbf{t}^{c'} - \mathbf{t}^{c,c'} - \mathbf{t}^c \right\|^2 \\ \text{subject to} & \quad \mathbf{t}^1 = \mathbf{0} \end{aligned} \quad (\text{A.5})$$

and the rotation R^c ,

$$\begin{aligned} \min_{R^c} \sum_{c \neq c', c'} & \left\| R^{c,c'} R^{c'} - R^c \right\|_F^2 \\ \text{subject to} & \quad R^1 = I, \end{aligned} \quad (\text{A.6})$$

where F is the Frobenius norm that sums over all matrix components squared and I is the identity matrix. These linear least squares problems have a direct solution using methods described in Boyd and Vanderberghe [4] and generalize to any number of views.

A.3. PROJECTED AREA OF A PLANAR OBJECT

A planar object with area $\mathcal{A}_{\text{plane}}$ and local plane coordinates $\mathbf{X} = [X \ Y \ 0]^T$ is mapped to the dewarped image-plane by $\tilde{\mathbf{x}} = p(K[R \ \mathbf{t}]\tilde{\mathbf{X}})$. The projected area in the dewarped image plane $\mathcal{A}_{\text{dewarped}}$ can be computed by integrating the determinant of the Jacobian of the projection map:

$$\mathcal{A}_{\text{dewarped}} = \int_{\mathcal{A}_{\text{plane}}} |\nabla p(X, Y)| dXdY. \quad (\text{A.7})$$

This integral can be evaluated using standard numeric integration techniques.

A.4. MAGNIFICATION OF THE DISTORTION MAP

An image is dewarped according to the distortion map $\hat{\mathbf{x}} = m(\mathbf{x})$. Similar to Appendix A.3 the area deformation of the distortion map can be computed by integrating the determinant of the Jacobian:

$$\mathcal{A}_{\text{dewarped}} = \int_{\mathcal{A}_{\text{image}}} |\nabla \mathbf{m}(\mathbf{x})| dx dy. \quad (\text{A.8})$$

This integral can be used to correct the light intensity per pixel area for the varying magnification of the distortion map. The average area expansion of the map is found by

integration over the complete image:

$$\tilde{J} = \frac{1}{\mathcal{A}_{\text{image}}} \int_{\mathcal{A}_{\text{image}}} |\nabla \mathbf{m}(\mathbf{x})| dx dy. \quad (\text{A.9})$$

A.5. POINT TRIANGULATION AND SKEWNESS

A point \mathbf{X} in the object domain is triangulated by minimizing the point-line distance to the optical rays from the different cameras. The optical rays associated with each view are computed by inverting the camera calibration matrix $K^c \setminus \tilde{\mathbf{x}}^c k^c$ where k^c scales the depth of field and $\tilde{\mathbf{x}} = [\hat{x} \ \hat{y} \ 1]^T$. The object location is then triangulated by the linear least squares problem:

$$\min_{\mathbf{X}, k^c} \sum_c^C \|K^c \setminus \tilde{\mathbf{x}}^c k^c - [R^c \ \mathbf{t}^c] \tilde{\mathbf{X}}\|^2. \quad (\text{A.10})$$

We then compute the skewness s as the average point-line distance between the optical rays and the object location by:

$$s = \frac{1}{C} \sum_c^C \|K^c \setminus \tilde{\mathbf{x}}^c k^c - [R^c \ \mathbf{t}^c] \tilde{\mathbf{X}}\|. \quad (\text{A.11})$$

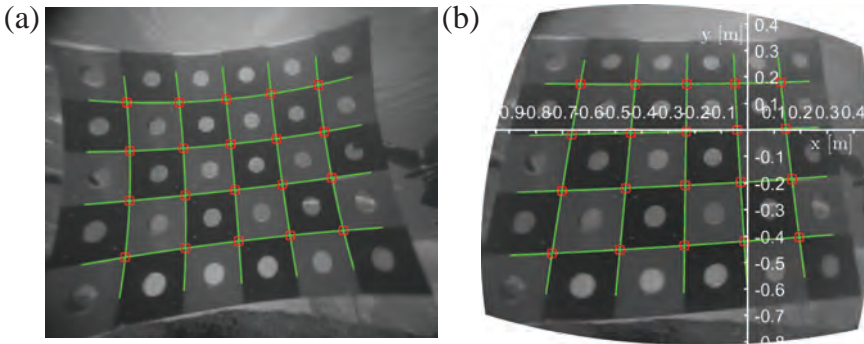


Figure A.1: **Supplementary** Optical distortions for an ultra-wide-angle lens (VENUS OPTICS LAOWA 7.5mm MFT). a) Processed calibration image with a set of curved gridlines (second-order polynomial curves) and intersections. b) Calibrated calibration image using the interface model of Appendix A.1.

REFERENCES

- [1] R. Hartley and A. Zisserman, *Multiple view geometry in computer vision*, 2nd ed. (Cambridge University Press, Cambridge, 2004).
- [2] A. W. Fitzgibbon, *Simultaneous linear estimation of multiple view geometry and lens distortion*, in *Proceedings of the 2001 IEEE Computer Society Conference on Computer Vision and Pattern Recognition. CVPR 2001* (IEEE, Kauai, HI, USA, 2001) pp. 125–132.
- [3] W. Kabsch, *A discussion of the solution for the best rotation to relate two sets of vectors*, *Acta Cryst.* **32**, 922 (1976).
- [4] S. Boyd and L. Vanderberghe, *Convex Optimization*, 1st ed., 471 (Cambridge University Press, Cambridge, 2004).

B

APPENDIX

This appendix belongs primarily to Chapter 3.

B.1. PATCHING A BACKGROUND IMAGE

We patch a still background image across the image frames $n = 1 \cdots N$ for each camera c separately. We first initiate an empty background image $B_{ij} = 1$ for each pixel position $\mathbf{x}_{ij} = [x \ y]^T$ where i and j are the pixel indices along x , and y , with $(\bullet)^T$ the vector transpose. We then recursively update the background image B_{ij} and suppress non-stationary artifacts that move in the image foreground by randomly permuting the frames n and drawing single images without multiplicity by the following steps:

1. We select an available input image I_{ij}^n from the frame-set, see Figure B.1a.
2. We fit the current image background B_{ij} to the input image I_{ij}^n by rescaling the intensity values using a polynomial basis function expansion $f(\mathbf{x}_{ij}) = \sum_k c_k \phi_k(\mathbf{x}_{ij})$ with terms $\phi_k(\mathbf{x}_{ij}) = 1, x, yx^2, xy, \dots$ by a weighted regression:

$$\min_{c_k} \sum_{ij} B_{ij}^{-2} (I_{ij} - f(\mathbf{x}_{ij}; c_k) B_{ij})^2, \quad (\text{B.1})$$

This is equivalent to fitting $f(\mathbf{x}_{ij})$ to the image background division I_{ij}^n/B_{ij} , see Figure B.1b for a 2nd order polynomial basis function $f(\mathbf{x}_{ij})$ that resolves the average variation in image intensity for the first iteration (top row).

3. We subtract the rescaled image background B_{ij} from the input image I_{ij}^n and compute the residual variation $I_{ij}^* = I_{ij}^n - f(\mathbf{x}_{ij})B_{ij}$ that we segment within a confidence bound b for the standard deviation $\sigma = \sum_{ij} (I_{ij}^*)^2 / IJ$ over image resolution IJ by $-b\sigma \leq I_{ij}^* \leq +b\sigma$, see Figure B.1c.
4. From the rescaled image background $f(\mathbf{x}_{ij})B_{ij}$ and the segmented residual variation I_{ij}^* we update the image background by $B_{ij}^{w+1} \leftarrow (wf(\mathbf{x}_{ij})B_{ij}^w + I_{ij}^*) / (w +$

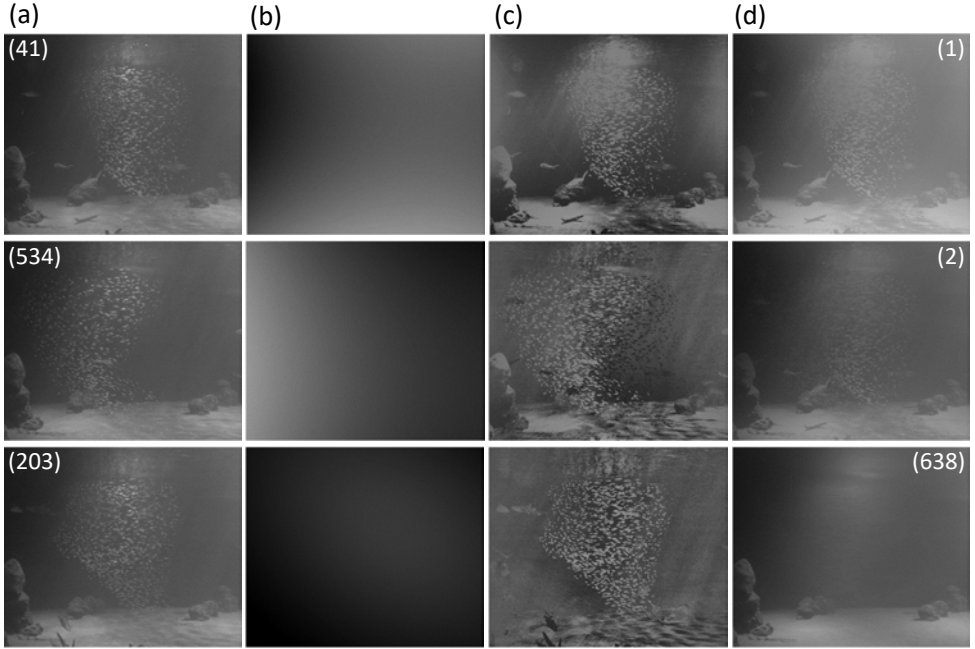


Figure B.1: Patching a background image for view (3) of Figure 3.3. Along the column space of the page: a) Raw input images for randomly selected image frame $n = 41, 534$ and finally 203 for the first, second and final iteration ($N = 638$). b) The fitted polynomial basis function $f(\mathbf{x}_{ij})$ for rescaling the current image background. c) Segmentation of the residual variation I_{ij}^* . d) The updated background image B_{ij} . Along the row space, we start at frame $n = 41$ in (a) and define a first iteration for a background image in (d), and repeat this process randomly permuting through the frame-set ($n = 41, 534, \dots, 203$), and finally separating the foreground from the image background (iteration 638).

1) where w counts the iteration number and computes the average image background for the w^{th} frame in the recursion, see Figure B.1d.

Steps (1) to (4) are repeated until we obtain a desirable result, separating the image foreground from the image background, see the bottom row of Figure B.1. In step (3) one can also define an image mask and use the inward interpolation (image flood-fill) of Section 3.3.5 to remove fish in the foreground.

B.2. IMAGE SMOOTHING AND DIFFERENTIATION FILTERS

We derive the Savitsky-Golay image smoothing and differentiation kernels [1] as a set of convolution filters that are used for fitting a generic polynomial basis function expansion $f(\mathbf{x}_{ij^*}) = \sum_k c_k \phi_k(\mathbf{x}_{ij^*})$ to a predefined (arbitrary) pixel neighborhood ij^* at the pixel location ij . Similar to Equation B.1 the fitting of the basis function expansion $f(\mathbf{x}_{ij^*})$ on the pixel neighborhood ij^* can be written as:

$$\min_{c_k} \sum_{ij^*} \left(I_{ij^*} - \sum_k c_k \phi_k(\mathbf{x}_{ij^*}) \right)^2 \quad \forall ij. \quad (\text{B.2})$$

We vectorize Equation B.2 and define the coefficient vector $\mathbf{c} = [c_1 \cdots c_k]^T$, the (local) image vector $\mathbf{I} = [I_1 \ I_2 \ \cdots \ I_{ij^*}]^T$, and construct the Vandermonde-matrix M for the basis functions $\phi(\mathbf{x}_{ij^*})$,

$$M = \begin{bmatrix} 1 & x_1 & y_1 & x_1^2 & x_1 y_1 & \cdots & \phi_k(\mathbf{x}_1) \\ 1 & x_2 & y_2 & x_2^2 & x_2 y_2 & \cdots & \phi_k(\mathbf{x}_2) \\ \vdots & \vdots & \vdots & \vdots & \vdots & \ddots & \vdots \\ 1 & x_{ij^*} & y_{ij^*} & x_{ij^*}^2 & x_{ij^*} y_{ij^*} & \cdots & \phi_k(\mathbf{x}_{ij^*}) \end{bmatrix}, \quad (\text{B.3})$$

resulting in:

$$\min_{\mathbf{c}} \|\mathbf{I} - M\mathbf{c}\|^2, \quad (\text{B.4})$$

with $\|\bullet\|$ the 2nd-norm over the vector entries. Equation B.4 has a direct solution through the normal equations [2]:

$$\mathbf{c} = (M^T M) \setminus M^T \mathbf{I}, \quad (\text{B.5})$$

where $(\bullet)^T$ is the matrix transpose.

The solution for the coefficients c_k can be written as a set of convolution filters h_k from the row-space of $(M^T M) \setminus M^T$ resulting in the image convolution $c_{ij}^k = h_k \circ I_{ij}$, where \circ stands for the convolution operator and where the pixel, and coefficient indexing, ij , and k , distribute naturally. We remark that the pixel neighborhood ij^* can include multiple images over n image frames by ijn^* .

B.3. SHAPE PARAMETERS FROM THE ELLIPSE CONTOUR

Recall the definition of the (conic) contour function from Section 3.3.3 for the augmented image coordinate $\tilde{\mathbf{x}} = [x \ y \ 1]^T$:

$$\tilde{\mathbf{x}}^T C \tilde{\mathbf{x}} = \begin{bmatrix} x \\ y \\ 1 \end{bmatrix}^T \begin{bmatrix} c_1 & c_2/2 & c_4/2 \\ c_2/2 & c_3 & c_5/2 \\ c_4/2 & c_5/2 & c_6 \end{bmatrix} \begin{bmatrix} x \\ y \\ 1 \end{bmatrix} = 0 \text{ with } C = \begin{bmatrix} \frac{1}{2}H & \frac{1}{2}\mathbf{g} \\ \frac{1}{2}\mathbf{g}^T & s \end{bmatrix}, \quad (\text{B.6})$$

where c_k are the coefficients of the symmetric conic matrix C with coefficient vector $\mathbf{c} = [c_1 \ c_2 \ c_3 \ c_4 \ c_5 \ c_6]^T$, and where \mathbf{g} is the image gradient, H the image Hessian, s the scale, and we call $\mathbf{x} = -H \setminus \mathbf{g}$ the midpoint. We now recover the shape parameters in case Equation B.6 describes an ellipse contour.

Consider an ellipse contour $(x/a)^2 + (y/b)^2 = 1$ with semi-axes of size $a \geq b > 0$ along the x and y axes and situated at the origin in the xy -plane. Homogenizing the expression by $(x/a)^2 + (y/b)^2 - 1 = 0$ we define the diagonal matrix $\Lambda = \text{diag}([a^2 \ b^2]^T)$ and write the expression in the form of Equation B.6 giving $\tilde{\mathbf{x}}^T \Lambda^{-1} \tilde{\mathbf{x}} = 0$. Subsequently, we write the rigid body transformation $\mathbf{x}' = R\mathbf{x} + \mathbf{t}$ with rotation matrix R and translation vector \mathbf{t} , and invert $\mathbf{x} = R^T \mathbf{x}' - R^T \mathbf{t}$. We substitute the homogeneous coordinates and obtain:

$$C = \begin{bmatrix} R^T & -R^T \mathbf{t} \\ \mathbf{0}^T & 1 \end{bmatrix}^T \begin{bmatrix} \Lambda^{-1} & \mathbf{0} \\ \mathbf{0} & -1 \end{bmatrix} \begin{bmatrix} R^T & -R^T \mathbf{t} \\ \mathbf{0}^T & 1 \end{bmatrix} = \begin{bmatrix} R\Lambda^{-1}R^T & -R\Lambda^{-1}R^T \mathbf{t} \\ -\mathbf{t}^T R\Lambda^{-1}R^T & -1 + \mathbf{t}^T R\Lambda^{-1}R^T \mathbf{t} \end{bmatrix}. \quad (\text{B.7})$$

From Equation B.7 it is clear that we can decompose the shape from the Hessian by the Schur decomposition $H = R\Lambda^{-1}R^T$, where the shape can be obtained from Λ and the

orientation from the (unitary) rotation matrix R . The translation vector \mathbf{t} is consistent with the midpoint definition of Equation B.6, and $2s = -1 + \mathbf{t}^T R \Lambda R^T \mathbf{t}$ gives the scale.

B.4. MANIPULATIONS TO AN ELLIPSE CONTOUR

In Figure B.2a to c we present three elementary manipulations of the position and shape of an ellipse contour function. First, we displace and enlarge the ellipse rescaling its size. This is achieved through a simple linear transformation $\tilde{\mathbf{x}}' = T\tilde{\mathbf{x}}$ with:

$$T = \begin{bmatrix} 1/a & 0 & d_x \\ 0 & 1/a & d_y \\ 0 & 0 & 1 \end{bmatrix}, \quad (\text{B.8})$$

where a is the scaling factor, and d_x , and d_y are the components of the displacement vector $\mathbf{d} = [d_x \ d_y]^T$, see Figure B.2a and b. Through substitution of $\tilde{\mathbf{x}} = T^{-1}\tilde{\mathbf{x}}'$ into the contour function for the image conic of Equation B.6, we obtain:

$$C' = T^{-T} C T^{-1}, \quad (\text{B.9})$$

with $(\bullet)^{-1}$ the matrix inverse. Alternatively, the rescaling is achieved by modifying the scale $s' = a^2 s - (1 - a^2)/2\mathbf{g}^T \mathbf{x}$; adjusting the value of the polynomial function instead of rescaling the Hessian matrix.

Secondly, we perform a uniform expansion ε of the ellipse contour in Figure B.2c. First, we decompose the conic matrix C in its parts (Equation B.6). We shift its midpoint $\mathbf{x} = -H \setminus \mathbf{g}$ at the origin and subsequently normalize the scale s . We perform the Schur-decomposition $H = R\Lambda^{-1}R^T$ to extract Λ , and add the uniform expansion ε :

$$\Lambda' = (\Lambda^{-1/2} + \varepsilon)^{-2}, \quad (\text{B.10})$$

which we transform back through Equation B.7.

B.5. DISTANCE FUNCTIONS ON THE ELLIPSE CONTOUR

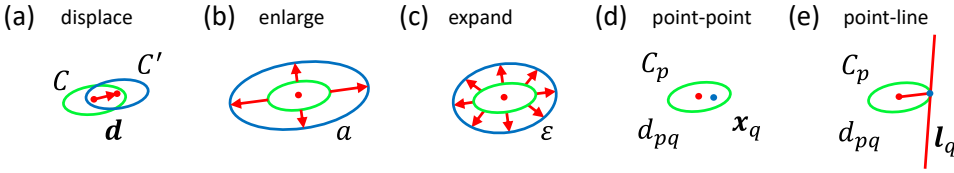
Consider an ellipse contour function $\tilde{\mathbf{x}}^T C_p \tilde{\mathbf{x}} = 0$ and its coefficient vector \mathbf{c}_p . To test whether an adjacent point $\mathbf{x}_q = [x \ y]^T$, or line $\tilde{\mathbf{l}}_q = [a \ b \ c]^T$ with coefficient a, b, c in homogeneous coordinates [3], falls within, or passes through, the span of \mathbf{c}_p , as is illustrated in Figure B.2d and e, we present two elementary distance functions d_{pq} .

POINT-POINT DISTANCE

The distance of the point \mathbf{x}_q to the midpoint \mathbf{x}_p on the span of the ellipse C_p can be naturally evaluated on the quadratic polynomial function:

$$d_{pq} = d(\mathbf{c}_p, \mathbf{x}_q) = \sqrt{1 - \frac{\tilde{\mathbf{x}}_q^T C_p \tilde{\mathbf{x}}_q}{\tilde{\mathbf{x}}_p^T C_p \tilde{\mathbf{x}}_p}}. \quad (\text{B.11})$$

The numerator in Equation B.11 evaluates the value of the polynomial for the coefficient vector \mathbf{c}_p at the location of \mathbf{x}_q while the denominator normalizes the peak value for the



B

Figure B.2: Diagrams for different ellipse manipulations. a) Displacement $\mathbf{d} = [d_x \ d_y]^T$ (red) of the ellipse C (green) to the new location C' (blue). b) Enlargement of the ellipse rescaling its semi-axis by the scaling factor a (green to blue). c) Uniform expansion of the ellipse by the value ϵ , with consistent color-code to (a) and (b). d) Ellipse point-to-point distance d_{pq} , in blue the position \mathbf{x}_q at the interior of the contour function $d_{pq} \leq 1$. e) Ellipse point-line distance d_{pq} , in blue the point \mathbf{y}_q at the perimeter of the ellipse contour at $d_{pq} = 1$.

polynomial function at \mathbf{x}_p . When the location of $\mathbf{x}_q = \mathbf{x}_p$, the fraction inside the square root is 1 and the distance d_{pq} gives 0. When the location of \mathbf{x}_q is at the perimeter of the ellipse, the contour function gives $\tilde{\mathbf{x}}_q^T C_p \tilde{\mathbf{x}}_q = 0$ and the distance is 1. The square root rescales the quadratic value to a linear distance $d_{pq} \in [0, \infty)$ that is positive definite.

POINT-LINE DISTANCE

We evaluate the minimum distance between a line \mathbf{l}_q and the midpoint \mathbf{x}_p on the level-set contour for \mathbf{c}_p . The closest point \mathbf{y}_q along \mathbf{l}_q is found by minimizing the constrained distance on the polynomial function,

$$\begin{aligned} \min_{\tilde{\mathbf{y}}_q} (\tilde{\mathbf{x}}_p - \tilde{\mathbf{y}}_q)^T C_p (\tilde{\mathbf{x}}_p - \tilde{\mathbf{y}}_q) \\ \text{subject to } \tilde{\mathbf{l}}_q^T \tilde{\mathbf{y}}_q = 0. \end{aligned} \quad (\text{B.12})$$

Introducing a Lagrange multiplier we solve a linear system of equations [2]:

$$\mathbf{y}_q = -H_p \setminus \mathbf{g}_p - H_p \setminus \mathbf{l}_q \frac{1 - \mathbf{l}_q^T H_p \setminus \mathbf{g}_p}{\mathbf{l}_q^T H_p \setminus \mathbf{l}_q}, \quad (\text{B.13})$$

and the distance function d_{pq} reads,

$$d_{pq} = d(\mathbf{c}_p, \mathbf{l}_q) = \sqrt{\frac{(1 - \mathbf{l}_q^T H_p \setminus \mathbf{g}_p)^2}{\mathbf{l}_q^T H_p \setminus \mathbf{l}_q (\mathbf{g}_p^T H_p \setminus \mathbf{g}_p - 2s_p)}}, \quad (\text{B.14})$$

where $\mathbf{l}_q = [a/c \ b/c]^T$ is the in-homogeneous line definition. When $d_{pq} = 0$ the line \mathbf{l}_q matches the midpoint \mathbf{x}_p within the ellipse contour ($d_{pq} \leq 1$) and when $d_{pq} > 1$ the passes outside the ellipse perimeter on the positive definite domain $d_{pq} \in [0, \infty)$.

B.6. CLUSTERING OF STEREOSCOPIC CORRESPONDENCES

Given the incidence matrices J_{pl}^c and $J_{ql}^{c'}$ for the stereoscopic linking of Section 3.4.1 we perform the f -focal correspondence matching of Section 3.4.2 and extract the complete cluster graph between views from graph cycles.

LINKING OF CORRESPONDENCES

Starting with the stereoscopic camera pool of focality $f = 2$ we concatenate the stereoscopic correspondences l to the views c and c' into one incidence matrix $J_{pl}^{cc'}$, where the image index p runs over all cameras. Subsequently, we link the stereoscopic correspondences between three views c , c' , and c'' . We select another set of stereoscopic correspondences h in an adjacent camera pair c' and c'' with incidence matrix $J_{ph}^{c'c''}$. We then compute the bi-adjacency matrix $B_{lh}^{c'}$ in the shared view c' that links the stereoscopic correspondences in a perfect connectivity $f - 1$:

$$\begin{cases} B_{lh}^{c'} = 1 & \text{when } J_{lp}^{cc'} J_{ph}^{c'c''} = (f - 1), \\ B_{lh}^{c'} = 0 & \text{otherwise,} \end{cases} \quad (\text{B.15})$$

where we sum the repeated indices, and c' indicates the overlapping view.

Equation B.15 generalizes to linking correspondences between any number of cameras in a pool of focality f . First, for a trifocal correspondence with $f = 3$, we define the incidence matrix $J_{pl}^{cc'c''}$. Subsequently, we compute the overlap with an adjacent set h in a trifocal camera pool c', c'', c''' where the overlapping indices from $J_{ph}^{c'c''c'''}$ in the shared view c', c'' naturally count $f - 1 = 2$ and gives the perfect connectivity for the bi-adjacency $B_{lh}^{c'c''}$. We then raise the camera pool to the next one $f + 1$ and repeat this process to the pairing quadrifocal correspondences.

CONSTRAINING OF GRAPH CYCLES

Returning to the stereoscopic camera pool $f = 2$, the linked correspondences l and h between views c , c' , and c'' that join in view c' may further connect by a set of stereoscopic correspondences m in views c and c'' presenting a cyclic graph. We further limit the bi-adjacency matrix $B_{lh}^{c'}$ of Equation B.15 to a cyclic graph by the associated matrices B_{lm}^c and $B_{hm}^{c''}$ of the camera pool:

$$\begin{cases} B_{hl}^{c'} = 1 & \text{when } B_{hl}^{c'} = 1 \text{ and } B_{lm}^c B_{mh}^{c''} = 1, \\ B_{hl}^{c'} = 0 & \text{otherwise,} \end{cases} \quad (\text{B.16})$$

for all l , h and m . Equation B.16 can be updated by the matrix multiplication.

The same process holds for a trifocal camera pool $f = 3$. Here two trifocal correspondence sets l and h , in views c , c' , c'' , and c', c'', c''' connect in perfect overlap in views c', c'' via $B_{lh}^{c'c''}$. Following, they either form a cyclic graph via m in views c , c', c''' or c', c'', c''' , and Equation B.16 naturally applies to the associated bi-adjacency matrices. Continuing to a quadrifocal camera pool $f = 4$ this process again generalizes.

EXTRACTION OF THE COMPLETE CLUSTER GRAPH

Returning to the stereoscopic camera pool $f = 2$, we extract the clustered stereoscopic correspondences from the bi-adjacency matrix $B_{lh}^{c'}$ of Equation B.16. As the bi-adjacency matrix $B_{lh}^{c'}$ is part of a graph cycle for the next focality $f + 1 = 3$, we read the trifocal match directly from $B_{lh}^{c'} = 1$ and list $s = 1 \cdots S$ trifocal correspondences. Subsequently,

we decompose the bi-adjacency matrix $B_{lh}^{c'} = J_{ls}^{c'} J_{sh}^{c'}$ and extract the incidence matrices $J_{ls}^{c'}$, and $J_{hs}^{c'}$ from the trifocal correspondence match s to the stereoscopic links l and h . Finally, we relate these incidence matrices back to the images by $J_{ps}^{cc'} = J_{pl}^{c'} J_{ls}^{c'}$ and $J_{ps}^{c''} = J_{ph}^{c''} J_{hs}^{c'}$ which we concatenate into the single output incidence matrix $J_{ps}^{cc'c''}$.

We repeat this process for the remaining bi-adjacency matrices B_{lm}^c and $B_{hm}^{c''}$. Within the segmentation of the stereoscopic correspondence, we generate all possible correspondence matches. Again this process naturally carries over to any number of views, where quadrifocal matches from the trifocal camera pool $f = 3$ can be clustered analog.

We finally extract complete cluster graphs from the input stereoscopic correspondences by the diagrams in Figure 3.8b of Section 3.4.2. A result is shown in Figure B.3 starting from 337400 stereoscopic correspondences ($f = 2$) and generating 213306 trifocal, and 49699 quadrifocal correspondences at increasing focality $f = 3, 4$.

B.7. ITERATIVE COST-FUNCTION SOLUTION

We devise a ‘Divide and Conquer’ strategy to solve the integer assignment in Section 3.5.3 for the cost-function sortation in l^* . For a data frame n we select $\lambda_{l^*} = 1$ for:

1. The feasible extensions l^* that first appear in the incidence F_{ll^*} (‘Divide’).
2. The subset of unique l^* that uniquely fills the image from $J_{pl^*}^n$ (‘Conquer’).

We then repeat these two steps until no more entries are available in the constraints, and every trajectory l is in its best extensions l^* . Secondly, we relax step one and solve step two solely for the unique trajectories l^* for $J_{pl^*}^n \lambda_{l^*} \geq 1$. In this way, we automatically reject ‘ghost-fish’ trajectories since they do not uniquely fill the image.

Seeding new tracks L by the predefined frame rate we march forward, backward, and forward again over the images in the processing window W . We first apply our optimization strategy to each frame n . In this way, we prevent branching an exponentially growing number of feasible trajectories (roughly $L^* \sim \mathcal{O}(L \exp(N))$) and remain bounded in the computer memory (roughly $L^* \sim \mathcal{O}(L)$). Secondly, we solve all available frames altogether and suppress any remaining ghosts.

In Figure B.4 we show the resulting tracking during this process. First, in Figure B.4a, we track 1350 segments of broken trajectories of the school in forward mode, giving only a partial solution to the fish tracking. Secondly, in Figure B.4b, we track 4266 fish backward. This is twice the amount of ± 2000 fish that can be observed, and we find doubly-tracked fish that yet uniquely fill the images. Finally, in Figure B.4c, we track 2297 fish forward again and remove many of the fish doubles.

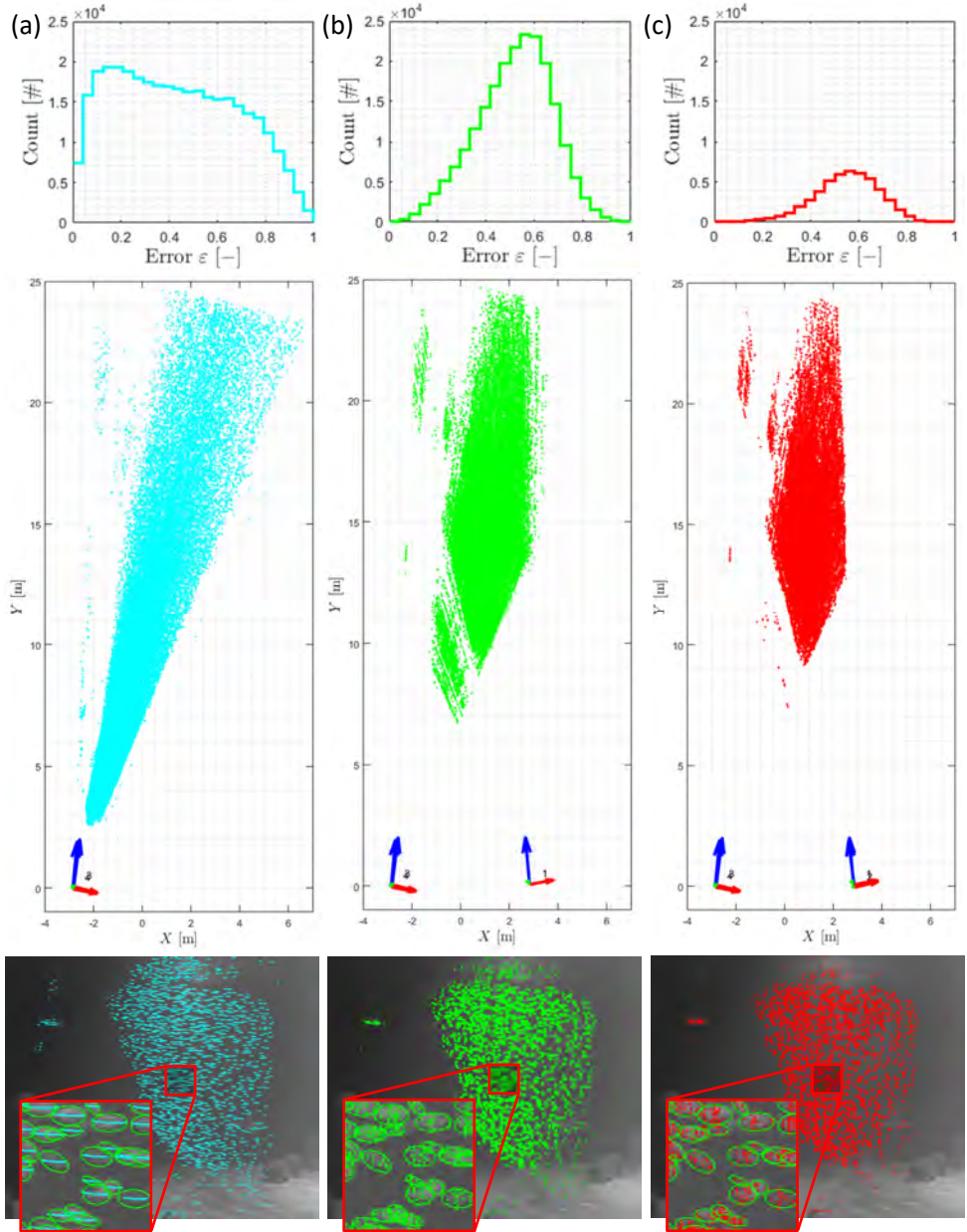


Figure B.3: Triangulated correspondence matches. a) Stereoscopic triangulation between views (3) and (4) of Figure 3.1a with a total of 337400 correspondences at narrow viewing angles (degeneracy). b) Trifocal triangulation from views (2), (3), and (4) with a total of 213306 correspondences. c) Quadrifocal triangulation for view (1)–(4) with a total of 49699 correspondences. On the top row of the page, we plot the distributions of reproduction error, in the middle the object triangulation, on the bottom we reproject view (3), inset a close-up. The (narrow) camera baselines and angles are indicated by the plotted camera position and orientation. Note that the peak in the error distribution elevates when the triangulation includes more views.

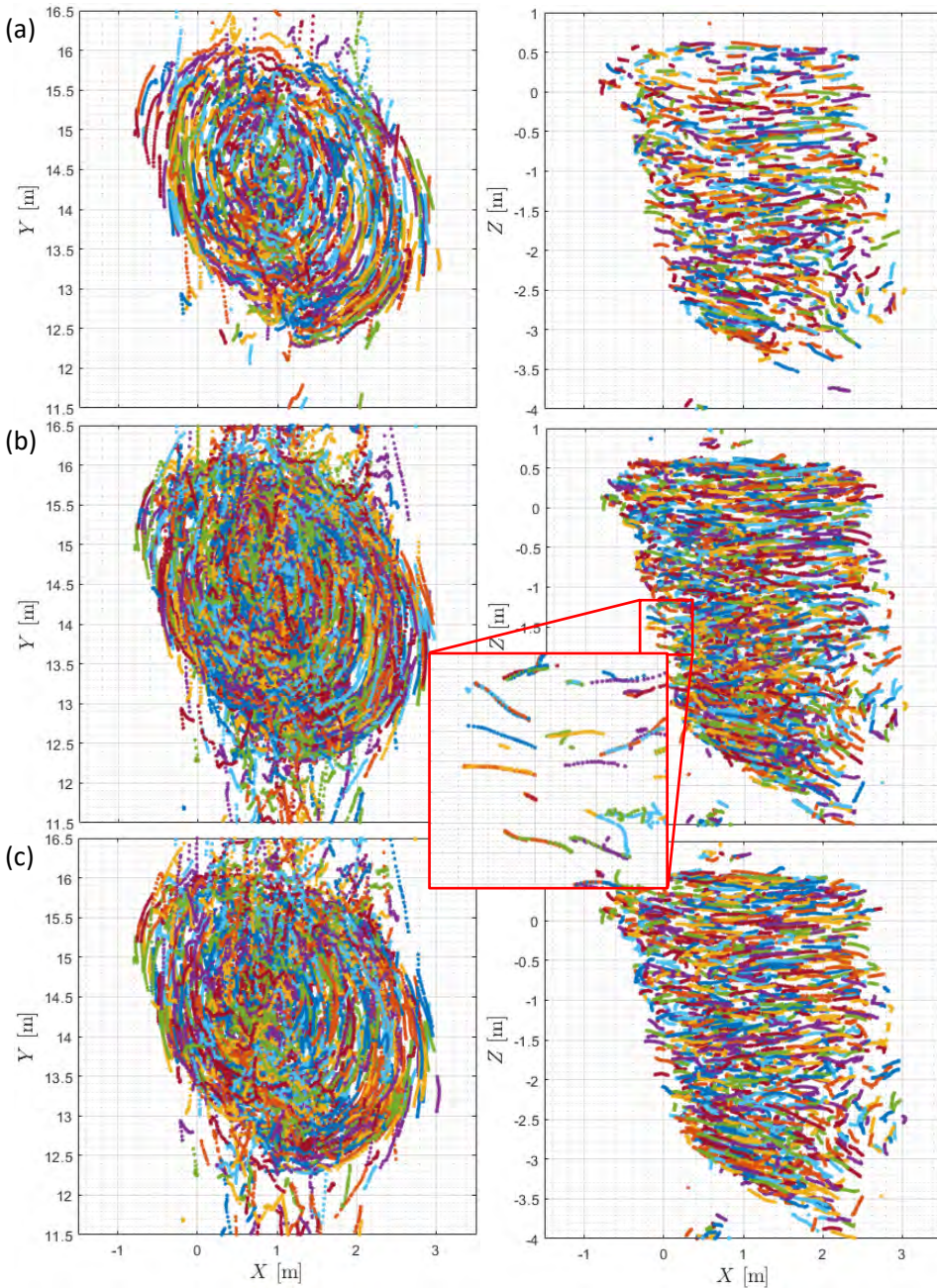


Figure B.4: Windowed processing of the tracking data. a) Forward tracking appending newly processed image frames starting from the object triangulation with a total of 1350 tracks. b) Backward tracking of the existing time series, displaying doubly-tracked fish with a total of 4266 tracks. c) Forward tracking of the existing time series, removing the majority of the fish doubles resulting in a total of 2297 tracks. All tracks shown here have a length greater or equal to 50 frames.

B.8. QUADRIC RECONSTRUCTION BY DUAL-SPACE GEOMETRY

An ellipsoid in object space is naturally expressed as a quadric surface [3] in the augmented object coordinate $\tilde{\mathbf{X}} = [X \ Y \ Z \ 1]^T$:

$$\tilde{\mathbf{X}}^T Q \tilde{\mathbf{X}} = \begin{bmatrix} X \\ Y \\ Z \\ 1 \end{bmatrix}^T \begin{bmatrix} q_1 & q_2/2 & q_4/2 & q_7/2 \\ q_2/2 & q_3 & q_5/2 & q_8/2 \\ q_4/2 & q_5/2 & q_6 & q_9/2 \\ q_7/2 & q_8/2 & q_9/2 & q_{10} \end{bmatrix} \begin{bmatrix} X \\ Y \\ Z \\ 1 \end{bmatrix} = 0 \text{ with } Q = \begin{bmatrix} \frac{1}{2} H_{3 \times 3} & \frac{1}{2} \mathbf{G} \\ \frac{1}{2} \mathbf{G}^T & S \end{bmatrix}. \quad (\text{B.17})$$

Here the coefficients q_k of the 4×4 symmetric quadric matrix Q are stored in the coefficient vector $\mathbf{q} = [q_1 \ q_2 \ \dots \ q_{10}]^T$, and analog to Equation B.6 we have the gradient vector \mathbf{G} , the Hessian matrix $H_{3 \times 3}$, the midpoint $\mathbf{X} = -H_{3 \times 3} \backslash \mathbf{G}$, and the scale $S = q_{10}$.

Following Cross and Zisserman [4], the coefficients q_k in the quadric matrix Q can be reconstructed using the dual-space geometry:

$$\min_{q_k^c, \lambda^c} \sum_c \left\| \lambda^c C^{*c} - P^c Q^* P^{cT} \right\|^2. \quad (\text{B.18})$$

Here $P^c Q^* P^{cT}$ is the quadric projection in dual-space with $C^* = C^{-T}$ and $Q^* = Q^{-T}$ the (dual) adjoint inverse [3] of the conic and quadric matrix C and Q , and λ^c is a scaling factor to each view c .

Due to the number of independent parameters for q_k (*i.e.* $10 - 1$) and λ_c we need to solve for $(10 - 1) + C$ unknowns¹, therefore Equation B.18 can be solved for a minimum of 3 independent viewing angles with $(6 - 1)C$ knowns [4] through direct solution strategies [2]. An example for 4 synthetic views is given in Figure B.5b to d.

We reconstruct the object quadric Q by first triangulating the midpoint \mathbf{X} to align the forward projection $Q^{fo} = P^c{}^T C^c P^c$ [3] by displacing the conics C^c for each view c in face of finite reprojection errors, see diagram Figure B.5a. To prevent severe elongation in the depth of field for limited/insufficient (or degenerate [4]) viewing angles, we further constrain the triangulation vector \mathbf{X} for the midpoint of the dual quadric Q^* :

$$Q^* = \begin{bmatrix} R & -\mathbf{X} \\ \mathbf{0}^T & 1 \end{bmatrix} \begin{bmatrix} \Lambda_{3 \times 3} & \mathbf{0} \\ \mathbf{0}^T & -1 \end{bmatrix} \begin{bmatrix} R & -\mathbf{X} \\ \mathbf{0}^T & 1 \end{bmatrix}^T = \begin{bmatrix} \mathbf{X}\mathbf{X}^T + Q_{3 \times 3}^* & \mathbf{X} \\ \mathbf{X}^T & -1 \end{bmatrix}, \quad (\text{B.19})$$

where the diagonal matrix $\Lambda_{3 \times 3}$ encodes the shape and R an unknown rotation matrix resulting in $Q_{3 \times 3}^*$, and we solve for a spherical shape² by,

$$Q_{3 \times 3}^* = q^* I_{3 \times 3}, \quad (\text{B.20})$$

with a single size q^* , an example is shown in Figure B.5c.

Equations B.19 and B.20 relax requirements on the minimum number of 3 views, needing only to solve for the coefficients in $Q_{3 \times 3}^*$ and reducing the number of unknowns to $6 + C$ with a minimum of 2 views; other approaches [4] may constrain a marked point

¹The number of independent parameters in projective geometry excludes parameters related to the scale, for further reading see Hartley and Zisserman [3].

²Solely constraining the midpoint makes the quadric solution susceptible to being a ruled hyperboloid.

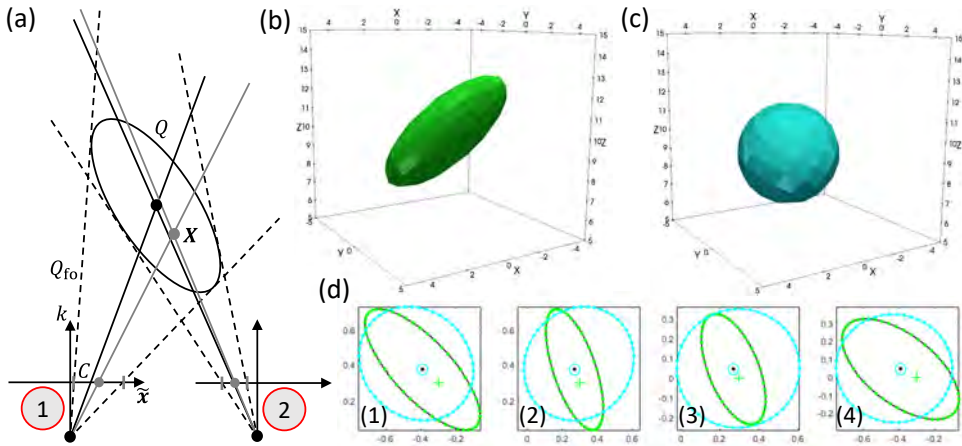


Figure B.5: Quadric reconstruction. a) Diagram for the object quadric Q , the conic projection $C^* = PQ^*P^T$ to the image plane, and the forward quadric $Q^{fo} = P^T C P$ or light-cone (dashed lines) from the projection matrix P ; exaggerated, the difference between the midpoint triangulation X and quadric reconstruction Q to elucidate sources of absolute error for the ray-tracing geometry. b) Ellipsoid reconstruction from synthetic data. c) Spherical reconstruction with a constrained triangulation. d) Four views reprojected on the synthetic image conics (black), with views (1) and (2) consistent with (a). In green the reprojection quadric contour and midpoint (green cross), in cyan the reprojected sphere where the constrained midpoint correctly encircles the conic midpoint in the projection (cyan circle). For (b) and (c) we render 1000 (approximate) equidistant points on the unit sphere (Fibonacci sequence).

or provide (in-)equality constraints on the trace and determinant of $Q_{3 \times 3}^*$. We then regularize the unconstrained quadric reconstruction Q_{unc} of Equation B.18 by the spherical shape Q_{sph} of Equation B.20 using an ad hoc weighting function for the polynomial function in the object domain by $Q' = (1 - 1/f)Q_{unc} + (1/f)Q_{sph}$ with f the focality number.

We remark that all operations of appendices B.3 to B.5 for image conic apply to the quadric surface. For the general purpose of imaging in three dimensions, the quadric reconstruction integrates the full knowledge of projective geometry and embeds the optical transfer [5] for a pinhole camera. This provides added knowledge of the bounding shape parameters in object space, here within the accuracy limits of the imaging system. By the linearity of Equation B.18 the implementation is easily vectorized, and scales without effort up to 10^4 – 10^5 positions as is common to particle tracking [6].

Finally, the polynomial function of Equation B.17 can be evaluated as a quadratic kernel inside a Gaussian to apply correlation techniques in the object domain [7], for example, to find the greater displacement of a fish group. Here the analytic representation avoids voxelizing vast volumes of empty space when spanning a large length scale. However, due to the high time resolution of our image data, such further integration remains beyond the need of the current thesis.

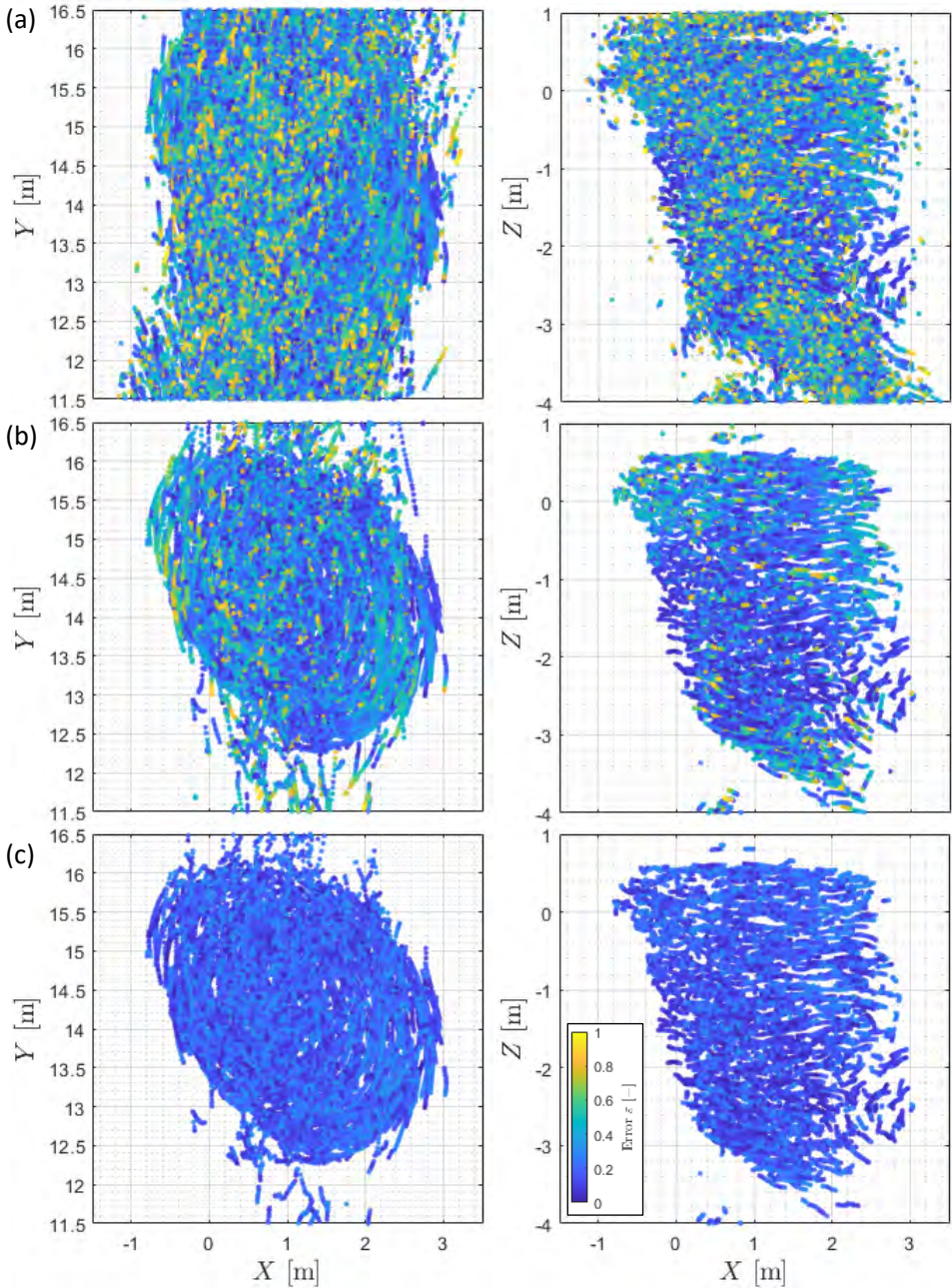


Figure B.6: **Supplementary** Segmentation of the final tracking data. a) The raw tracking data from the recursive track branching. b) Segmentation of the track length $\Delta T \geq 50$. c) Further segmentation of the normalized re-projection error $\epsilon \leq 1/3$. For (a)–(c) we present 1-second long tracks (20 frames) and color-code the normalized re-projection error $\epsilon \in [0, 1]$.

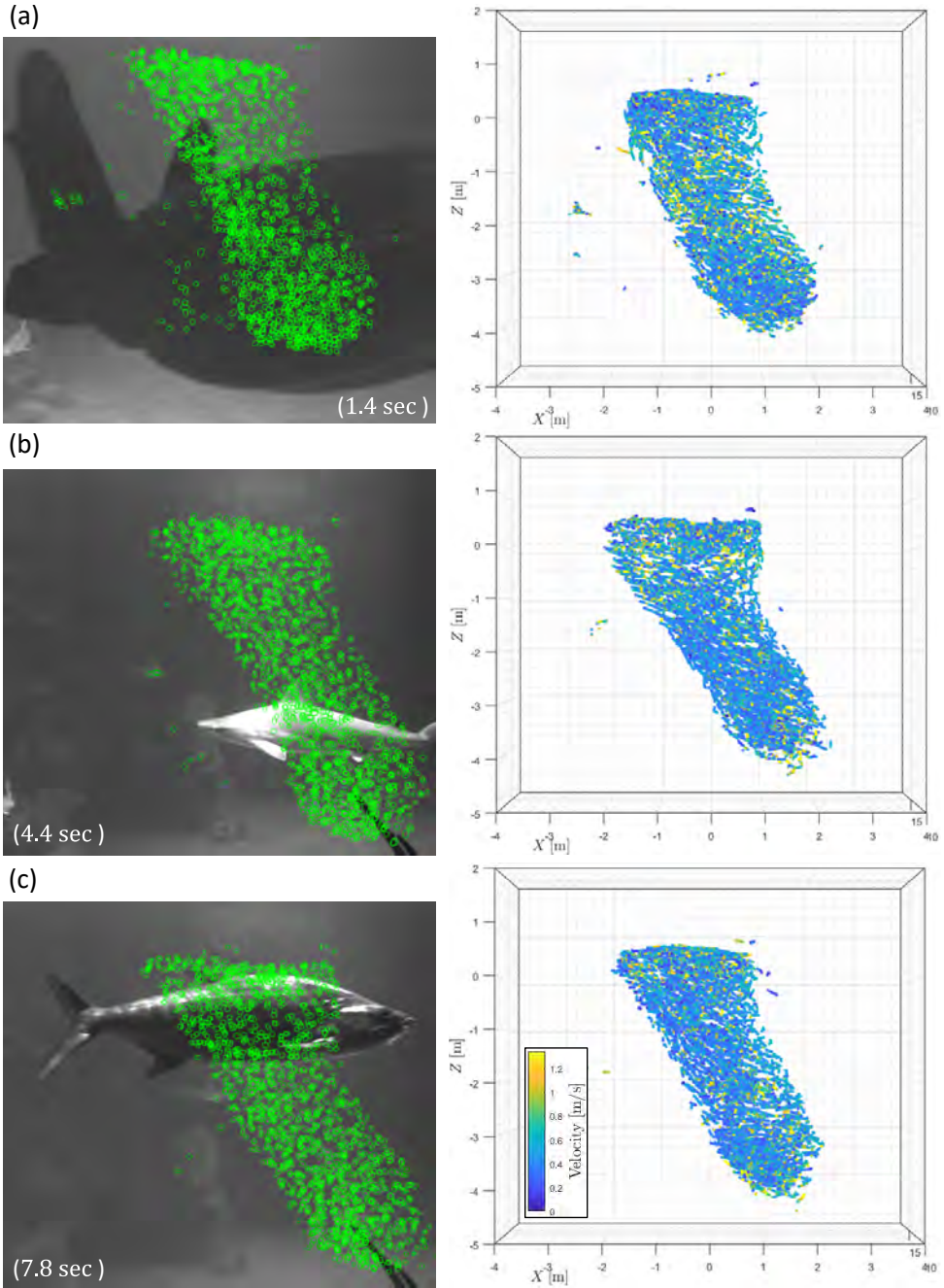


Figure B.7: **Supplementary** Resolving of large occlusions. a) A turtle passing, completely blocking the view. b) A shark swimming in front of the school. c) A tarpon fish occluding the top of the school. All of the events have little to no effect on the three-dimensional tracking, see the right column of the page.

B

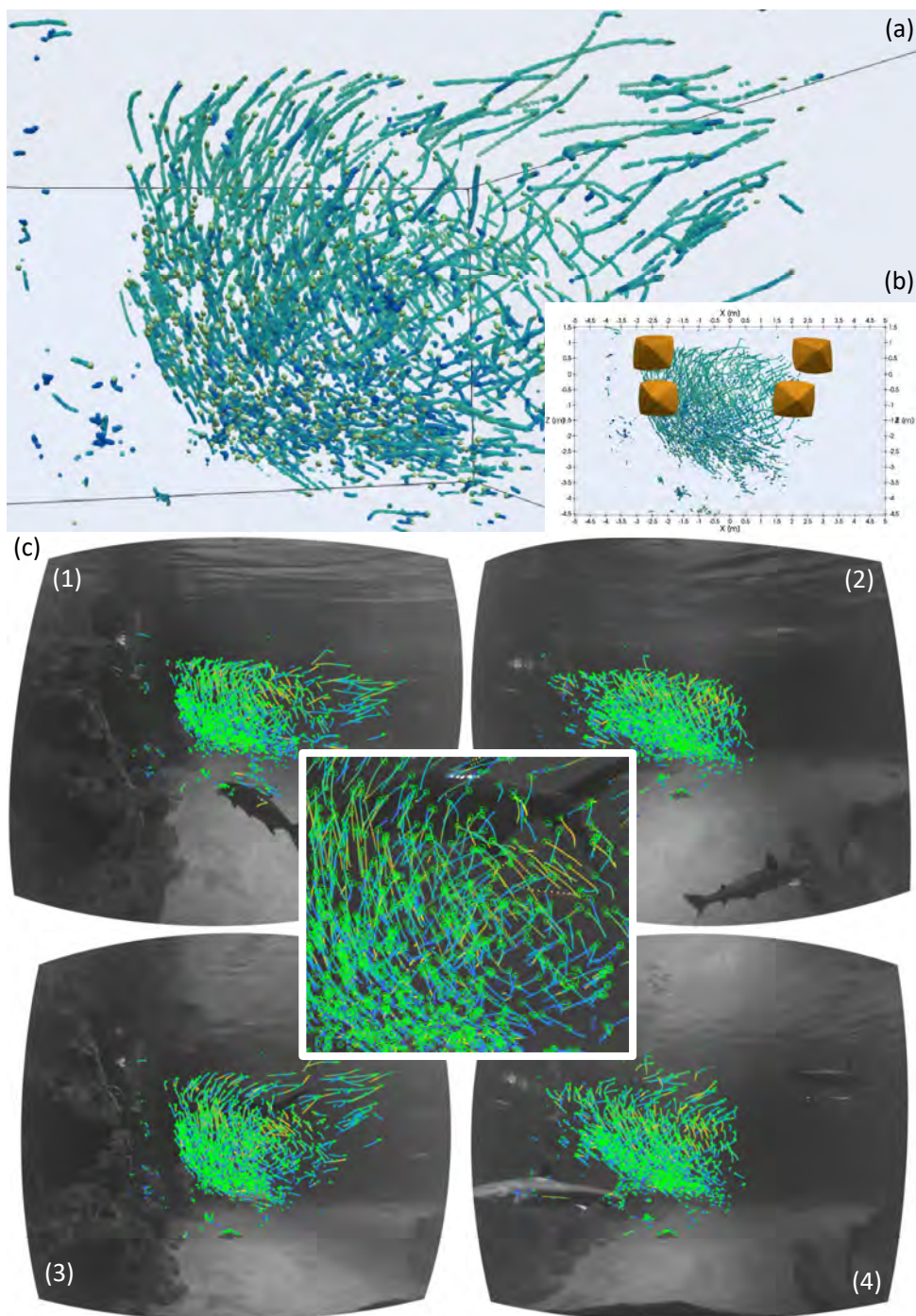


Figure B.8: **Supplementary** Tracking results for a set of ultra-wide-angle lenses (VENUS OPTICS LAOWA 7.5mm MFT). a) 'Birds-eye' render for post-processed 1-second long fish tracks. b) Front view aligned with the camera views, showing the positions of the calibrated cameras from Chapter 2. c) The four views imaging the fish school, overlaid the projected object ellipsoids for 1/2-second long tracks to prevent overcrowding the images; including a close-up view from camera 3 in the middle. Note the shape of the camera calibration in (b) for the high optical distortion in (c).

REFERENCES

- [1] P. Meer and I. Weiss, *Smoothed differentiation filters for images*, Journal of Visual Communication and Image Representation **3**, 58 (1992).
- [2] S. Boyd and L. Vanderberghe, *Convex Optimization*, 1st ed., 471 (Cambridge University Press, Cambridge, 2004).
- [3] R. Hartley and A. Zisserman, *Multiple view geometry in computer vision*, 2nd ed. (Cambridge University Press, Cambridge, 2004).
- [4] G. Cross and A. Zisserman, *Quadric Reconstruction from Dual-Space Geometry*, in *Sixth International Conference on Computer Vision* (IEEE, Bombay, India, 1998) pp. 1–7.
- [5] D. Schanz, S. Gesemann, A. Schröder, B. Wieneke, and M. Novara, *Non-uniform optical transfer functions in particle imaging: Calibration and application to tomographic reconstruction*, Measurement Science and Technology **24** (2013), 10.1088/0957-0233/24/2/024009.
- [6] D. Schanz, S. Gesemann, and A. Schröder, *Shake-The-Box: Lagrangian particle tracking at high particle image densities*, Experiments in Fluids **57**, 1 (2016).
- [7] G. E. Elsinga, F. Scarano, B. Wieneke, and B. W. Van Oudheusden, *Tomographic particle image velocimetry*, Experiments in Fluids **41**, 933 (2006).

C

APPENDIX

This appendix belongs primarily to Chapter 4.

C.1. DATA DESCRIPTOR: CAMERA CALIBRATION

Table C.1 contains a simplified overview of the processed camera calibration data using the methods described in Chapter 2. For the first measurement week (2017) we used a set of NIKKOR AF-24mm lenses and from 2018 onward we switched to a set of VENUS OPTICS LAOWA 7.5mm MFT with a greater field of view. All cameras have been calibrated with the window model of Appendix A.1 substituted into a 3rd-order mapping to introduce extra correction terms.

C.2. DATA DESCRIPTOR: PROCESSED TRACKING

All tracking data has been processed on different WINDOWS- and LINUX-based computer clusters (INTEL as well as AMD-Opteron) with a large number of CPUs (between 8–256) and sufficient internal memory (64–512GB). Each node was set up to process different data sets in parallel and to have at least the equivalent computing power of an INTEL CORE 4th Generation i7 laptop with 8–16GB of internal memory, as was partially used for code development.

Table C.2 contains the results of the processed tracking data. From left to right we review for each measurement week the fish schooling behavior following [1, 2]. We report the recording settings including the (cropped) image resolution, number of frames, the camera frame rate, and exposure time. Furthermore, we present the quality rating of Chapter 3 that includes the tracked number of objects L_{obj} , the average number of tracked frames T_{obj} , the efficacy of tracking into the next frame η_{NF} , and finally a quality assessment based on a final visual inspection of the tracking data. Example time series are presented in supplementary figures C.4 to C.9.

Data-set		Calibration							Accuracy			No.		
ID	Date	View	Positions			Orientation			Focal	Error			Skew	
□ (C#S#)	(y-m-d)	[#]	X [m]	Y [m]	Z [m]	α [°]	β [°]	γ [°]	f_{eff} [mm]	ϵ [%]	ϵ^* [px]	s [cm]	[#]	
Measurement Week August 2017														
✓	C1S1	2017-08-09	1	2.830	0.058	0.596	10.00	-9.21	-3.45	24.85	2.04	2.22	1.31	333
✓	C1S2	2017-08-14	2	2.865	-0.058	-0.587	13.89	-3.34	-2.03	25.08	1.79	2.02	1.30	300
			3	-2.825	0.051	-0.673	-14.20	0.31	-3.79	24.64	1.56	1.72	1.33	418
			4	-2.869	-0.051	0.664	-10.48	-7.91	0.24	24.83	1.67	2.17	1.36	388
Measurement Week January 2018														
✓	C2S1	2018-01-08	1	-2.618	-0.002	0.899	-7.62	-7.35	-2.06	11.32	2.91	1.27	1.24	193
X	(C2S2)	2018-01-01	2	2.866	0.002	0.775	9.97	-8.05	2.25	11.26	3.25	1.94	1.43	198
			3	-2.439	0.002	-0.821	-10.21	3.27	0.68	11.26	2.67	1.17	1.23	197
			4	2.191	-0.002	-0.853	6.39	3.85	2.81	10.77	2.67	1.50	1.33	229
Measurement Week August 2018														
✓	C3S1	2018-08-17	1	-2.668	0.004	0.899	-9.34	-6.60	3.19	10.79	2.99	1.41	1.11	221
			2	2.876	-0.005	0.796	6.93	-8.59	2.70	10.68	3.14	1.53	1.14	196
			3	-2.395	-0.005	-0.833	-5.63	0.85	-1.36	10.80	3.00	1.45	1.14	214
			4	2.188	0.006	-0.862	-0.32	9.57	0.36	10.50	3.09	1.61	1.18	223
Measurement Week January 2019														
✓	C4S1	2019-01-25	1	-2.728	0.016	0.908	-8.22	-12.03	1.36	10.60	2.89	1.52	1.13	405
✓	C4S2	2019-01-30	2	3.030	-0.017	0.766	14.84	-2.87	0.52	10.89	3.39	1.71	1.05	416
			3	-2.636	-0.018	-0.818	-9.09	10.81	3.36	10.18	3.00	1.42	1.18	398
			4	2.334	0.019	-0.856	14.92	9.73	4.19	10.28	3.04	1.45	1.07	374
Measurement Week October 2019														
✓	C5S1	2019-10-21	1	-2.602	0.022	0.918	-9.54	-2.93	2.08	10.56	3.26	1.59	1.25	488
✓	C5S2	2019-10-25	2	2.964	-0.024	0.735	10.76	-3.87	-0.61	10.69	3.07	1.50	1.18	468
			3	-2.651	-0.025	-0.808	-10.30	4.62	-0.02	10.62	2.58	1.18	1.19	475
			4	2.289	0.027	-0.844	11.72	3.89	-0.83	10.14	2.68	1.28	1.18	497
Measurement Week February 2020														
✓	C6S1	2020-02-24	1	-2.634	0.035	0.901	-18.46	-7.79	-3.18	10.86	4.30	2.02	1.25	419
✓	C6S2	2020-02-28	2	2.906	-0.037	0.775	13.27	-2.01	3.34	10.59	4.22	2.05	1.34	407
			3	-2.500	-0.042	-0.815	-11.81	7.36	-0.06	10.51	3.78	1.89	1.28	439
			4	2.227	0.043	-0.860	4.73	2.34	2.12	10.12	4.38	2.05	1.42	431

Table C.1: **Data Descriptor** Processed calibration data. All included data is indicated by a check mark (✓) and excluded data by a cross mark (X). From left to right we find the data set identifier (ID), the date of the calibration data, the camera number (1–4), the computed camera positions X , Y , and Z , the (yaw-pitch-roll) orientation angles α , β , and γ , the effective focal-length f_{eff} , and the accuracy assessment of Chapter 2 including the: the average reprojection error ϵ in percentage and ϵ^* in pixel dimension, the skew error s in centimeter, the number of used calibration images (No.). Justification of disregarded data is marked by (···).



Data-set ID (C#S#)	Date (y-m-d)	Time (h:m)	Behavior		Attacks		Resp.	Shape	No. [#]	Recording Sequence		Fr.-rate [fps]	Exposure [μs]	Tracking Data		Efficacy η_{NF} [-]	Qual.
			School	Shape	Predator	Frames [frm]				Resolution [px]	No. [#]			No. L_{obj} [#]	Frames T_{obj} [#]		
Measurement Week August 2017																	
✓ C1S1	2017-08-08	16:30	M	SK	1	S	A	D	1	2560x2160	626	39.84	15000	1591	122	0.9909	+/-
X C1S2	2017-08-09	17:00	M	S	1	T	A	D	1	2560x2160	639	39.84	15000	1575	102	0.9886	(-)
✓ C1S3	2017-08-09	21:30	M	C	1	TG	A	D	1	2560x2160	628	19.96	40000	1499	125	0.9893	+
✓ C1S4	2017-08-09	22:16	SC	CP	1	T	FE	V	1	2560x2160	628	39.84	15000	757	163	0.9939	+
X C1S5	2017-08-10	8:30	M	S	1	S	A	S	1	2560x2160	628	39.84	15000	1342	128	0.9915	(-)
✓ C1S6	2017-08-10	8:30	M	S	1	S	A	V	1	2560x2160	628	19.96	40000	1767	118	0.9913	+
✓ C1S7	2017-08-10	12:30	M	C	1	S	A	D	1	2560x2160	635	19.96	40000	1959	113	0.9909	++
✓ C1S8	2017-08-10	19:00	M	C	1	S	A	D	1	2560x2160	638	19.96	40000	2064	128	0.992	++
✓ C1S9	2017-08-10	20:40	SC	CP	1	T/S	FE	V	2	2560x2160	635	39.84	15000	1517	134	0.9918	++
✓ C1S10	2017-08-10	21:20	M	C	1	T	E	V	1	2560x2160	635	39.84	15000	1367	157	0.9934	++
✓ C1S11	2017-08-11	10:50	M	C	1	TG	A	D	1	2560x2160	623	19.96	40000	1914	124	0.9916	++
✓ C1S12	2017-08-11	15:00	M	C	1	T/S	E	H/D	2	2560x2160	623	19.96	40000	2009	105	0.9894	+
✓ C1S13	2017-08-11	19:45	M	B	1	S	E	S	1	2560x2160	663	19.96	40000	1320	106	0.9862	+/-
✓ C1S14	2017-08-11	21:50	M	SK	1	S	A	V	1	2560x2160	662	19.96	40000	1898	112	0.9905	+
✓ C1S15	2017-08-12	11:00	M	CP	1	TT/S	A	CP	1	2560x2160	633	39.84	15000	2434	134	0.992	+/-
✓ C1S16	2017-08-12	19:00	M	SK	1	T	E	V	1	2560x2160	630	19.96	40000	1964	105	0.9895	++
✓ C1S17	2017-08-12	20:00	M	C	1	S/TT/TG	E	S	2	2560x2160	630	19.96	40000	1487	105	0.9894	+
✓ C1S18	2017-08-12	21:30	M	C	1	S	A	D	1	2560x2160	630	39.84	15000	1915	174	0.9941	+
✓ C1S19	2017-08-13	12:40	M	SL	1	-	-	-	-	2560x2160	628	39.84	15000	1578	149	0.9927	+
✓ C1S20	2017-08-13	12:55	M	SL	1	-	J	HO	-	2560x2160	628	39.84	15000	1622	161	0.9936	+
✓ C1S21	2017-08-13	13:20	M	CP	1	S	FE	V	1	2560x2160	628	39.84	15000	1858	156	0.9931	+
✓ C1S22	2017-08-13	20:30	M	C	1	T	A	D	1	2560x2160	628	39.84	15000	1600	147	0.9928	++
✓ C1S23	2017-08-13	21:45	M	B	1	S	E	V	1	2560x2160	628	39.84	15000	1599	170	0.9939	++
✓ C1S24	2017-08-14	7:10	SC/F	CP	1	T	E	S	1	2560x2160	628	39.84	15000	1475	136	0.9905	+/-
✓ C1S25	2017-08-14	10:30	M	SK	1	T	A	D	-	2560x2160	628	19.96	40000	2081	112	0.9908	++
Measurement Week January 2018																	
X C2S1	2018-01-07	11:30	M	S	1	S/B	A	D	2	1600x1360	1600	60.79	10000	1869	128	0.9841	(-)
✓ C2S2	2018-01-07	11:40	M	B	1	T	A	D	1	1600x1360	1650	37.81	20000	1231	139	0.988	+
✓ C2S3	2018-01-07	14:55	M	S	1	T/S	A	D	4	960x1000	3800	40.32	20000	1035	190	0.9876	+/-
✓ C2S4	2018-01-07	16:10	M	S	1	S	A	D	1	2560x1000	1440	67.58	10000	1434	195	0.9945	+

Data-set ID (C/S#)	Date (y-n-d)	Time (hr:m)	Behavior			Attacks			Recording Sequence					Tracking Data			Efficacy η_{NE} [-]	Qual.
			School	Shape	No. [#]	Predator	Resp.	Shape	No. [#]	Resolution [pxl]	Frames [frm]	Fr-rate [fps]	Exposure [μ s]	No. LoB [#]	Frames ToB [#]			
✓ C2S5	2018-01-08	10:20	M	S	1	S/T/R/TT	A	D	4	1280x1160	2428	21.96	40000	1544	127	0.9826	+	
✓ C2S6	2018-01-08	12:50	M	S	1	TT/T/S/G	A	D	3	1600x1160	1958	39.17	20000	1157	244	0.9948	++	
✓ C2S7	2018-01-08	17:30	M	S	1	TT	A	D	1	2560x1200	1200	38.89	20000	1349	251	0.996	++	
✓ C2S8	2018-01-08	17:45	M	S	1	S/H/S/TT	A	D	5	960x1200	3214	21.87	40000	1224	184	0.9931	++	
✓ C2S9	2018-01-08	18:05	M	S	1	T/S/TT	A	D	8	960x880	4387	22.6	40000	1199	210	0.9927	++	
✓ C2S10	2018-01-08	19:40	F	S	1	-	-	-	-	1280x1160	2498	64.38	10000	249	283	0.9943	+	
✓ C2S11	2018-01-08	20:25	M	UP	1	-	-	-	-	2560x2160	667	49.63	10000	1243	132	0.9916	+	
✓ C2S12	2018-01-09	12:10	M	S	1	T/S	A/I	D/V	4	1280x800	3485	22.79	40000	1078	162	0.9818	+	
✓ C2S13	2018-01-09	13:25	M	B	1	S	E	V	1	1280x1200	2400	63.63	10000	1156	120	0.9478	+/-	
X C2S14	2018-01-09	14:55	M	S	1	T/S/B	A	D/S	7	960x800	4815	22.79	40000	1201	103	0.9766	(+/-)	
X C2S15	2018-01-09	17:10	M	S	1	T/S	A	D	2	960x760	4981	42.2	20000	953	159	0.9683	(+/-)	
X C2S16	2018-01-09	17:15	M	S	1	T/S	A	S/V	7	960x760	5049	22.88	40000	1081	103	0.9685	(-)	
✓ C2S17	2018-01-09	18:05	F	S	1	-	-	-	-	1600x840	2731	41.56	20000	217	279	0.9934	++	
✓ C2S18	2018-01-10	10:25	M	C	1	-	-	-	-	1600x1200	1807	63.63	10000	1615	259	0.9955	++	
X C2S19	2018-01-10	13:05	M	S	1	T/S/TG	A	D	3	960x880	4386	70.19	10000	1193	204	0.9712	(-)	
✓ C2S20	2018-01-10	17:35	M	S	1	T/S/TG	E	D	6	960x800	4754	41.87	20000	1082	191	0.9913	+	
Measurement Week August 2018																		
X C3S1	2018-08-14	20:30	M	C/B	1/2	T/S	A/S	V/D	9	960x760	5051	22.88	40000	1400	105	0.9734	(+/-)	
X C3S2	2018-08-15	12:20	M/SC	S/B	2	-	A	-	1	1600x1240	1700	21.79	40000	839	60	0.9636	(-)	
✓ C3S3	2018-08-15	21:10	M	B	1	H/S	A	D/V	3	1280x1200	2412	38.89	20000	962	209	0.9902	+	
✓ C3S4	2018-08-15	22:55	M/SH	B	1	S	A	V	2	1600x1360	1650	37.81	20000	1127	169	0.9928	+	
✓ C3S5	2018-08-16	13:10	M	B	1	S	A	D	3	1280x1560	1793	21.11	40000	915	124	0.9765	+/-	
✓ C3S6	2018-08-16	14:00	M	C	1	T/S	A	D	2	1280x1160	2443	39.17	20000	1492	156	0.9704	+	
✓ C3S7	2018-08-16	14:20	F	S	1	-	-	-	-	1280x1160	2443	39.17	20000	136	414	0.995	++	
✓ C3S8	2018-08-16	16:05	M	SK	1	H/S	A	V	3	960x1160	3302	39.17	20000	893	201	0.991	+/-	
X C3S9	2018-08-16	16:10	M	C	1	S/B/T	A	D/V	10	640x960	6014	22.41	40000	829	154	0.9714	(-)	
X C3S10	2018-08-16	16:20	M/SC	C/B	1/2	TT/S/T	A	V/D	6	1280x960	3009	22.41	40000	740	169	0.9643	(-)	
✓ C3S11	2018-08-16	22:55	M	B	1	T/S	E	V/H	2	1280x1360	2065	37.81	20000	1215	187	0.9928	+	
✓ C3S12	2018-08-17	16:45	M	S	1	-	-	-	-	1920x1560	1217	36.54	20000	1669	214	0.9951	++	
✓ C3S13	2018-08-17	17:05	M	S	1	-	-	-	-	1920x1560	1217	21.11	40000	1950	125	0.9762	++	
✓ C3S14	2018-08-17	20:05	M	C	1/2	T/S	A	V/D	4	1280x1360	2073	21.53	40000	1041	169	0.9923	+/-	
✓ C3S15	2018-08-17	21:05	M	C	1	T	A	D	1	1920x1560	1236	36.54	20000	1073	190	0.9927	+/-	

Data-set ID □ (C/S#)	Date (y-m-d)	Time (hrm)	Behavior		Attacks			Recording Sequence Resolution [px] Frames [frm]	Fr.-rate [fps]	Exposure [μs]	Tracking Data		Efficacy η_{NF} [-]	Qual.			
			School	Shape	No. [#]	Predator	Resp.				Shape	No. [#]			Frames T_{obj} [#]		
✓ C3S16	2018-08-17	21:10	M	C	1	S	E	V	2	1280x1560	1236	57.58	10000	1136	198	0.9921	+/-
x C3S17	2018-08-17	23:00	SC	CP	1	-	-	-	-	1600x1560	1446	36.54	20000	771	63	0.9796	(-)
✓ C3S18	2018-08-18	11:10	M	S	1	TG	A	CP	1	1920x1080	1780	39.74	20000	1294	203	0.9859	++
✓ C3S19	2018-08-18	16:55	M	C	1	T/S	E	S/D	4	960x960	3960	22.41	40000	1307	125	0.982	+/-
x C3S20	2018-08-18	18:25	SH/M	C	1	S	A	S/V	6	1280x1360	2117	21.53	40000	1050	115	0.9499	(-)
✓ C3S21	2018-08-18	19:00	M	C	1	S	E	V	1	1280x1360	2117	37.81	20000	1046	190	0.9873	+/-
Measurement Week January 2019																	
✓ C4S1	2019-01-26	17:15	M	S	1	-	-	-	-	1280x1160	2442	21.96	40000	435	138	0.9477	+
✓ C4S2	2019-01-26	19:05	M	C	1	-	-	-	-	1600x1360	1471	21.53	40000	925	164	0.9752	+
✓ C4S3	2019-01-26	20:25	M	B	1	S	A	D	1	1600x1360	1703	21.53	40000	776	107	0.9699	+/-
✓ C4S4	2019-01-26	22:30	M	B	1	TG	FE	V	1	1280x1360	2129	21.53	40000	930	158	0.9826	+
✓ C4S5	2019-01-27	17:45	M	S	1	-	-	-	-	1600x1360	1663	21.53	40000	520	152	0.9874	+
✓ C4S6	2019-01-27	17:55	M	C	1	S/TG/TT	A	V	3	1600x1360	1663	21.53	40000	1119	114	0.9868	+
x C4S7	2019-01-28	11:05	M	B	1	-	-	-	-	1600x1360	1608	37.81	20000	697	152	0.9893	(-)
x C4S8	2019-01-28	21:50	SH/M	CP	1/2	S	A	D	1	1920x1560	1219	21.11	40000	917	131	0.9887	(-)
✓ C4S9	2019-01-28	22:20	SH/M	B	1	TG	A	D	1	2240x1560	1052	36.54	20000	735	157	0.9893	+/-
x C4S10	2019-01-28	22:50	SC/M	CP	2	S	A	V	1	2240x1560	1047	21.11	40000	513	98	0.9778	(+/-)
x C4S11	2019-01-29	15:20	M	B	1	T/S	A	D/V	3	1600x1160	1570	21.96	40000	1039	73	0.975	(-)
✓ C4S12	2019-01-29	17:35	M	C	1	S	A	D	1	1280x1160	2467	39.17	20000	1057	147	0.9828	+/-
✓ C4S13	2019-01-29	20:00	M	C/B	1	S	A	D	2	1600x1360	1692	21.53	40000	840	103	0.9506	+/-
x C4S14	2019-01-29	21:50	M	(D)	2	-	-	-	-	1920x1560	1230	21.11	40000	985	104	0.9882	+
x C4S15	2019-01-29	21:55	M	(D)	2	S	E	D	2	1920x1560	1230	21.11	40000	1170	100	0.9798	+/-
✓ C4S16	2019-01-29	22:15	M	SK/D	2	S/G	A	V	2	1280x1360	1230	21.53	40000	987	122	0.988	+
x C4S17	2019-01-30	12:20	M	C	1	TT/S	A	D	2	1280x1160	1667	21.96	40000	1194	84	0.9729	(-)
✓ C4S18	2019-01-30	16:30	M	C	1	S	E	V	1	2560x1160	1218	39.17	20000	1798	98	0.9799	+
✓ C4S19	2019-01-30	21:00	M	B	1	S	E	S	1	1920x1360	1410	21.53	40000	888	118	0.9882	+
✓ C4S20	2019-01-30	21:50	M	C/B/SK	1	TG	A	CP	1	1920x1360	1410	21.53	40000	847	147	0.985	+
Measurement Week October 2019																	
✓ C5S1	2019-10-21	16:35	F	B	1	-	-	-	-	1600x1360	1664	21.53	40000	81	441	0.9971	++
✓ C5S2	2019-10-21	19:55	M	C	1	S	A	D/V	2	1280x960	2994	22.41	40000	1027	127	0.9883	+



Data-set ID □ (C/S#)	Date (y-m-d)	Time (h:m)	Behavior		Attacks		Recording Sequence				Tracking Data		Efficacy η_{NE} [-]	Qual.			
			School	Shape	No. #	Predator	Resp.	Shape	No. #	Resolution [px]	Frames [frm]	Ft.-rate [fps]			Exposure [μ s]	No. L_{50} #	Frames T_{50} #
✓ C5S3	2019-10-22	9:40	M	B	1	S	A	D/V	2	1920x1560	1300	21.11	40000	1347	68	0.9822	+/-
X C5S4	2019-10-22	22:25	SH	CP	1	-	-	-	-	1600x1160	1674	37.81	20000	906	116	0.9746	(-)
X C5S5	2019-10-22	22:25	M	S	1	-	-	-	-	1600x1160	1674	37.81	20000	506	131	0.9849	(-)
X C5S6	2019-10-23	10:10	M	C	1	S	A	D/V	9	960x560	6715	23.37	40000	752	87	0.9349	(-)
✓ C5S7	2019-10-23	14:35	M	S	1	-	-	-	-	1920x1360	1500	21.53	40000	1407	150	0.9908	++
✓ C5S8	2019-10-23	16:15	M	S	1	-	-	-	-	1600x1160	1398	21.96	40000	1071	131	0.991	++
✓ C5S9	2019-10-23	19:05	M	C	1	S	A	V	1	1600x1160	1398	21.96	40000	1243	171	0.9934	+
✓ C5S10	2019-10-23	19:15	SH	CP	1	S	A	D	1	1600x1160	1398	39.17	20000	654	112	0.9876	+
✓ C5S11	2019-10-23	21:30	M	C	1	S/G	E	D/V	2	960x1160	3316	39.17	20000	743	237	0.9846	+/-
X C5S12	2019-10-24	9:50	M	B	1	S	A	D	1	1920x1360	1995	37.81	20000	883	136	0.9867	(+/-)
X C5S13	2019-10-24	11:35	M	S/B	1	S/TG	A	D	3	960x760	4965	42.2	20000	889	117	0.9581	(+/-)
✓ C5S14	2019-10-24	11:55	M	B	1	-	-	-	-	1280x960	2940	40.63	20000	1521	128	0.975	+
X C5S15	2019-10-24	17:15	M	(D/SK)	2	-	-	-	-	1280x1160	2449	39.17	20000	989	151	0.9746	(+/-)
X C5S16	2019-10-24	17:50	M/F	(D)	2	S/TG	A	D/S	5	960x760	5044	22.88	40000	744	161	0.9907	(+/-)
✓ C5S17	2019-10-25	12:30	M	B/G	1	TG	A	D	1	1280x960	2939	40.63	20000	533	116	0.9489	+/-
✓ C5S18	2019-10-25	12:50	SC	UP/DI	1	S	A	D/W	1	1280x960	2939	40.63	20000	555	99	0.9406	+/-
✓ C5S19	2019-10-25	16:45	M	B/G	1	T/S	A	D	4	1280x960	3006	22.41	40000	641	102	0.984	+/-
✓ C5S20	2019-10-25	19:40	F	S	1	G	A	D	1	1280x1160	2469	39.17	20000	301	153	0.9881	+
✓ C5S21	2019-10-25	20:25	M	S/B	1	S	A	D	2	1920x1360	2111	21.53	40000	899	146	0.9858	+
✓ C5S22	2019-10-25	21:45	M	SL	1	S	A	D/S	2	1920x1360	2070	21.53	40000	828	186	0.9821	+
✓ C5S23	2019-10-25	22:30	M	C/B	1	TG	A	D/V	4	1920x1360	1981	21.53	40000	779	195	0.9933	+
Measurement Week February 2020																	
✓ C6S1	2020-02-22	13:55	M	S	1	-	-	-	-	1600x1360	1697	21.53	40000	689	102	0.9846	+/-
X C6S2	2020-02-22	15:10	M	S	1	S	A	S/D	2	1600x1360	1701	21.53	40000	682	113	0.9785	(-)
✓ C6S3	2020-02-22	17:20	SH/F	S	1	TG/TT/S	A	S/D	3	1280x960	2979	22.41	40000	643	123	0.9708	+/-
✓ C6S4	2020-02-22	17:45	M	B	1	S/T	A	D	4	1600x1160	1993	21.96	40000	768	167	0.9923	+/-
✓ C6S5	2020-02-22	19:15	M/F	S	1	-	-	-	-	1280x560	5169	23.37	40000	170	292	0.9881	++
✓ C6S6	2020-02-23	17:00	M	B	1	T	A	D	1	960x760	5070	22.88	40000	531	128	0.9793	+
X C6S7	2020-02-24	9:25	M/F	(D)	2	-	-	-	-	1920x1160	1561	21.96	40000	557	171	0.9914	(-)
X C6S8	2020-02-24	17:10	M	(D)	2	TG/S	A	V/D	2	1920x760	2534	22.88	40000	917	143	0.9818	(-)
✓ C6S9	2020-02-24	17:40	M	B	1	H/TT/S	A	D/S	4	960x760	5071	22.88	40000	316	218	0.99	+



Data-set ID □ (C#S#)	Date (y-m-d)	Time (h:m)	Behavior		Attacks		Recording Sequence			Tracking Data						
			School	Shape	No. [#]	Predator	Resp.	Shape	No. [#]	Resolution [px]	Frames [frm]	Fr.-rate [fps]	Exposure [μ s]	No. L_{obj} [#]	Frames T_{obj} [#]	Efficacy η_{NF} [-]
X	C6S10	2020-02-25	M	(D)	2	-	J	-	2240x760	2169	22.88	40000	615	153	0.9838	+/-
✓	C6S11	2020-02-26	M	S	1	S	A	V	2240x1160	1410	21.96	40000	776	137	0.9864	++
✓	C6S12	2020-02-26	M	SK	1	TT/S	A	D/V	1280x1160	2471	21.96	40000	1044	149	0.982	+/-
X	C6S13	2020-02-26	M	(D/CP)	1/2	TT/S	A	D	2240x760	2173	22.88	40000	620	137	0.9868	(-)
✓	C6S14	2020-02-26	M	B	1	S	A	V	1280x1160	2470	21.96	40000	626	160	0.9806	+/-
✓	C6S15	2020-02-27	SH	B	1	S	A	D/V	1600x1360	1679	21.53	40000	826	115	0.9866	+
✓	C6S16	2020-02-27	M/SH	B	1	S	A	D	1600x1360	1679	37.81	20000	1109	128	0.9897	+
✓	C6S17	2020-02-27	M	S	1	-	-	-	1600x	2337	40.63	20000	971	209	0.9905	+
✓	C6S18	2020-02-28	M	B	1	-	-	-	1600x1160	1953	39.17	20000	935	175	0.9869	+
X	C6S19	2020-02-28	M	(D)	2	TT/S	A	D	2240x760	1977	22.88	40000	576	170	0.9935	+/-
✓	C6S20	2020-02-28	M	C	1	S	A	V	1600x1160	1986	39.17	20000	1091	212	0.9942	+

Table C.2.: **Data Descriptor** Processed tracking data. From left to right: data set identifier (ID), date and time, behavior, attacks, recording sequence, tracking data. For the behavior of the school we identify: milling (M), foraging (F), schooling (SC), and shoaling (SH). For the shape we identify: cylinder (C), ball (B), surface (S), skewed (SK), slender (SL), double (D), ground (G), uprising (UP), and dive (DI); and we report the number of schools (No.). For the response (Resp.) to an attack/encounter we identify: avoidance (A), escape (E), flash expansion (FE), join (J), and split (S). For the shape of the response, we identify dent (D), vacuole (V), split (S), herd (H), hourglass (HO), star (S), wave (W), and complex (CP); and we report the number of attacks (No.). For the recording sequence, we report the: cropped image resolution, the number of image frames, the camera frame rate (Fr.-rate), and exposure time. For the tracking data, we report the number of tracked fish L_{obj} ; the average track length in number of frames T_{obj} ; the tracking efficacy metric η_{NF} . For the final quality assessment (Qual.) of the data we identify: excellent (++), good (+), noisy (+/-), poor (-), and discard (--). See the overview below. All data included in this thesis we indicate by a check mark (✓) and excluded by a cross mark (X). When data is disregarded we use brackets (...) to mark its justification.

School	Shape	Predator	Response	Shape	Quality
Milling	Cylinder	Shark	Avoidance	A Dent	++
Schooling	Ball	Tarpon	Flash Expansion	FE Vacuole	+
Shoaling	Surface	Tuna Group	Escape	E Split	+/-
Foraging	Skewed	Turtle	Join	J Herd	-
	Slender	Groupier	Split	S Hourglass	HO --
	Double	Barracuda	Wave	W Star	
	Ground	Horse Jack		Wave	W
	Uprising	Ray	R	Complex	CP
	Dive				
	Complex				

C.3. PRINCIPAL SEMI-AXES AND BOUNDING ELLIPSOID

We find the principal semi-axes for an equivalent ellipsoid in Figure C.1a for the point cloud \mathbf{X}_i with positions $i = 1 \cdots I$ in three consecutive steps. First, we shift the origin of the coordinate system to the center of mass \mathbf{X}_M :

$$\mathbf{X}_{i/M} = \mathbf{X}_i - \mathbf{X}_M. \quad (\text{C.1})$$

Secondly, from the $3 \times I$ matrix $M = [\mathbf{X}_{1/M}, \mathbf{X}_{2/M}, \cdots, \mathbf{X}_{I/M}]$ we compute the singular value decomposition $M = U\Sigma V^T$ to find the unitary matrix V .

The matrix V gives a linear transformation matrix to align with the principal components of the point cloud $\mathbf{X}_{i/M}$. From V we then define a (proper) rotation matrix R :

$$R = \text{sgn}(\det|V|) V, \quad (\text{C.2})$$

where the sign function $\text{sgn}(\bullet)$ for the determinant $\det|\bullet|$ constrains $\det|R| = 1$, with similarity to the Kabsch algorithm [3]. This rotation matrix $R = [\mathbf{e}_1 \ \mathbf{e}_2 \ \mathbf{e}_3]$ provides us with a set of basis vectors in the direction of the principal components.

Subsequently, we invert the rotation matrix and compute the values $\boldsymbol{\lambda} = [\lambda_1 \ \lambda_2 \ \lambda_3]^T$ of the semi-axes from the arithmetic mean, and (twice) the standard deviation:

$$\boldsymbol{\lambda} = \langle |R^T \mathbf{X}_{i/M}| \rangle + 2\sqrt{\langle (|R^T \mathbf{X}_{i/M}| - \langle |R^T \mathbf{X}_{i/M}| \rangle)^2 \rangle}, \quad (\text{C.3})$$

where $|\bullet|$ is the absolute value, and $\langle \bullet \rangle = \sum_{i=1}^I (\bullet) / I$ are the averaging brackets.

Finally, we sort the principal axes $\{\mathbf{e}_1 \ \mathbf{e}_2 \ \mathbf{e}_3\}$ in descending order for the semi-axes values $\lambda_1 > \lambda_2 > \lambda_3$. This gives the sequence of linear transformations of an arbitrary point cloud to the unit sphere.

In Figure C.1b and c, we plot two examples of the equivalent ellipsoid that is constructed from the principal semi-axes. In Figure C.1a, we find a good representation of the aspect ratio of the school for the semi-axes $\lambda_1 > \lambda_2 > \lambda_3$. In Figure C.1b, we find a good fit for the enlarged volume of the school that is escaping from a predator for the example time series of Figure 4.4 onward. In both examples, the bounding ellipsoid encloses $71.03 \pm 2.72\%$ and $76.45 \pm 2.26\%$ of the fish in the school respectively, and provides reference imagery for interpreting the distribution of fish in the school.

C.4. MOMENTS OF THE RADIAL FISH DENSITY DISTRIBUTION

We derive the explicit expressions for the first, second, and third central moment for the radial probability density function $f(r)$ of equations 4.2–4.4 of Section 4.2.2 along the radial coordinate $r_i = \|\tilde{\mathbf{X}}_{i/M}\|$ away from the origin, see Figure C.2a. We substitute the probability $f(r_i) = 1/(4\pi f_0 r_i^2)$ of finding a position i at the spherical shell of radius r_i with $f_0 = \sum_{i=1}^I 1/(4\pi r_i^2)$ a normalization factor such that $\int_0^\infty f(r) dr = 1$, and change the

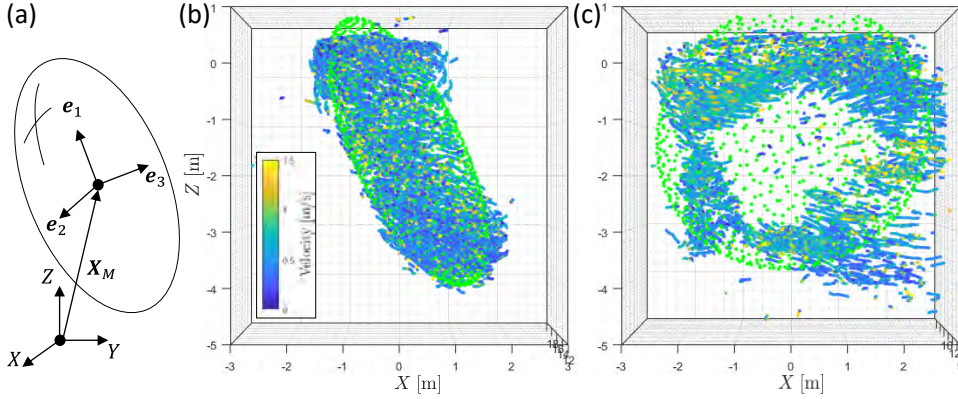


Figure C.1: Bounding ellipsoid for the fish school. a) Diagram for the bounding ellipsoid from the center of mass X_M with principle axes $\{e_1, e_2, e_3\}$. b) A slender mill (C1S19 in Table C.2): the bounding ellipsoid captures the high aspect ratio, see green dots. c) An escape response (C1S21 in Table C.2 and Figure 4.4): the bounding ellipsoid captures the enlarged volume and spherical shape of the school, see green dots.

integration to a discrete summation for the:

$$\text{mean: } \mu = \int_0^\infty r f(r) dr = \sum_{i \in I^*} \frac{r_i}{4\pi f_0 r_i^2} = \frac{\sum_{i \in I^*} 1/r_i}{\sum_{i \in I^*} 1/r_i^2}, \quad (\text{C.4})$$

$$\text{variance: } \sigma^2 = \int_0^\infty (r - \mu)^2 f(r) dr = \sum_{i \in I^*} \frac{(r_i - \mu)^2}{4\pi f_0 r_i^2} = \frac{\sum_{i \in I^*} (1 - \mu/r_i)^2}{\sum_{i \in I^*} 1/r_i^2}, \quad (\text{C.5})$$

$$\text{and skew: } s^3 = \int_0^\infty \left(\frac{r - \mu}{\sigma}\right)^3 f(r) dr = \sum_{i \in I^*} \left(\frac{r_i - \mu}{\sigma}\right)^3 \frac{1}{4\pi f_0 r_i^2} = \frac{\sum_{i \in I^*} \left(\frac{r_i - \mu}{\sigma}\right)^3 / r_i^2}{\sum_{i \in I^*} 1/r_i^2}, \quad (\text{C.6})$$

For practical purposes, we truncate the integration bounds and compute statistics over the subset $I^* = \{r_i | 0 \leq r_i \leq 3/2\}$, with upper bound $r_i \leq \mu + 2\sigma$ for the skew, and correct f_0 accordingly.

In Figure C.2b and c, we plot two reference distributions for $f(r)$ for the time series of Figure 4.4 (C1S21 in Table C.2). We inset the mean μ (magenta), the standard deviation $\mu \pm \sigma$ (orange) and skew bias $\mu + s\sigma$ (green) together with the upper integration bound $\mu + 2\sigma$ (cyan), and uniform distribution. In Figure C.2b, we plot the average radial fish distribution $f(r)$ for negative skew values ($s < 0$). Here the are redistributed towards the edges of the school ($\xi = \mu/2\sigma \sim 0.75/(2 \cdot 0.25) = 1.5 > 0.87$). In Figure C.2c, we plot the average radial fish distribution $f(r)$ for positive skew values ($s > 0$) and find a shape that clusters toward the origin of the school ($\xi = \mu/2\sigma \sim 0.5/(2 \cdot 0.35) \approx 0.71 < 0.87$).

In Figure C.2d, we plot the conditional probability density function $f(r|t)$ for the radial fish distribution $f(r)$ over the time evolution t . The axis normalization correctly normalizes the shape of the school at great variation in volume. Furthermore, the majority of the fish are found within the restricted integration bounds $\mu + 2\sigma$ which justifies its value. Finally, we improve interpretation for the skew s plotting the evolution ‘skew bias’ from the mean μ and standard deviation σ by $\mu + s\sigma \in [\mu - \sigma, \mu + \sigma]$, where the skew s is either biased positive or negative standard deviation σ .

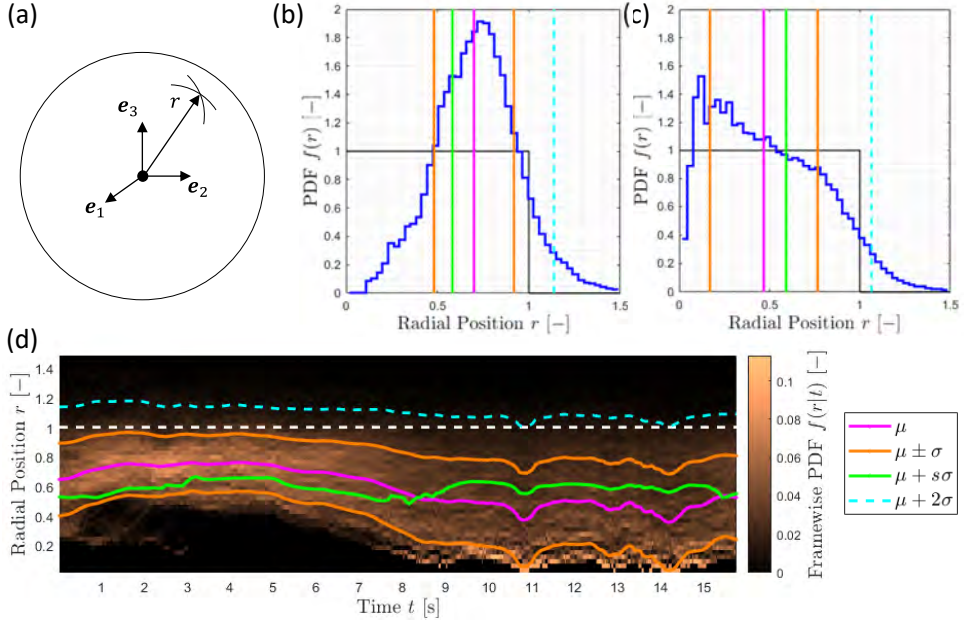


Figure C.2: The radial distribution function. a) Diagram for the radial position r at the principle axes $\{e_1, e_2, e_3\}$. b) Radial fish distribution $f(r)$ at positive skew ($s > 0$). c) Radial fish distribution $f(r)$ at negative skew ($s < 0$). In (b) and (c) are inset: a uniform density distribution (black line), the moment mean μ (magenta), standard deviation bounds $\mu \pm \sigma$ (orange), the moment skew bias $\mu + s\sigma$ (green), and the upper bound for the moment skew $\mu + 2\sigma$ (cyan dashes). d) Conditional probability density function $f(r|t)$, inset the boundary of the semi-axes (white dashes), the values for the moments with consistent color code as in (b) and (c) along the time series t . All color coding is consistent with Figure 4.4.

C.5. DISTRIBUTION OF VELOCITY INSIDE THE SCHOOL

Recall the velocity vector $\mathbf{U}_i(t) = [U_i \ V_i \ W_i]^T$ of Section 4.3.1 for the components in X , Y , and Z . We plot distributions of the components U , V and W , and the velocity magnitude $U_i(t) = \|\mathbf{U}_i(t)\|$ by the average (swimming) velocity $\bar{U}(t) = \langle U_i(t) \rangle$, median velocity $\text{Med}(U_i(t))$, and standard deviation $\sigma_U(t) = \sqrt{\langle (U_i(t) - \bar{U}(t))^2 \rangle}$.

In Figure C.3a, we plot the joint distribution function $f(U, V)$ of the in-plane velocity components U and V for the example time series of Figure 4.6 (C1S21 in Table C.2). We find that U and V are distributed in an overall ring shape for the milling school, within the accuracy range of the measurement system. In Figure C.3b, we plot the joint distribution $f(W, \sqrt{U^2 + V^2})$. Here we find that the out-of-plane component W together with the in-plane components $\sqrt{U^2 + V^2}$ construct a torus at the (plane) ring shape.

In Figure C.3c, we plot the evolution of the distribution in velocity magnitude U against time t by the conditional probability distribution $f(U|t)$. The majority of the variation is captured by the average velocity $\bar{U}(t)$ and standard deviation $\sigma_U(t)$, with little changes between the mean $\bar{U}(t)$ and median swimming velocity $\text{Med}(U_i(t))$. This suggests that the shape of the velocity distribution inside the school is little affected by the predator engaging in an attack.

We further plot the time evolution in the rescaled velocity magnitude $\tilde{U}_i(t)$ of Section 4.3.2 in Figure C.3d and normalize with the average value $\bar{\tilde{U}}(t) = \langle \tilde{U}_i(t) \rangle$. We compute similar quantities for the median rescaled velocity $\text{Med}(\tilde{U}_i(t))$ and rescaled velocity standard deviation $\sigma_{\tilde{U}}(t)$, like before. We compare results for the normalized standard deviation bounds $1 \pm \sigma_{\tilde{U}}(t)/\bar{\tilde{U}}(t)$ and median value $\text{Med}(\tilde{U}_i(t))/\bar{\tilde{U}}(t)$ with Figure C.3c and find only little variation in the rescaled velocity. This supports evidence that the overall shape of velocity distribution on the evolution of the semi-axes of the school is little affected by external interactions.

Finally, in Figure C.3e, we plot the relative density distribution $f(\tilde{U}/\bar{\tilde{U}})/f_{\text{peak}}$ of the (normalized) rescaled velocity $\tilde{U}/\bar{\tilde{U}}$, where f_{peak} normalizes the peak value of the distribution. We proceed to compare its shape against a Chi-distribution for random velocity fluctuations with zero mean and dimensionality parameter $k = 1, 2, 3, \dots$. We modify this distribution to include a (simplistic) toroidal velocity distribution¹:

$$f(U; k, \nu) \sim U^{k-1} \exp(-U^2) \exp(-\nu(\nu - 2U)). \quad (\text{C.7})$$

The extra parameter ν gives the ratio between the torus cross-section and revolution axis radii. The distribution can be properly normalized by numerical integration.

For $\nu = 0$ we obtain the Rayleigh distribution when $k = 2$ and Maxwell-Boltzmann distribution when $k = 3$, which are canonical velocity distributions in planar turbulence, and a non-interacting (ideal) gas in three dimensions. When $\nu > 0$ we set $k = 2$ and the extra exponential term $\exp(-\nu(\nu - 2U))$ raises the initial reference scaling $U^{k-1} \rightarrow U^k$ for $U < 1$, as can be shown through a 1st-order Taylor expansion $\exp(-\nu(\nu - 2U)) \stackrel{T}{\approx} \exp(-\nu^2) + 2\nu \exp(-\nu^2)U$, and decays faster for $U > 1$, by the extra exponential decaying factor. In Figure C.3e we trace a torus shape with $\nu = 4/3$ and $k = 2$ as can be seen from the inset reference lines. This captures the torus shape of Figure C.3a for the distribution of the kinetic energy over the degrees of freedom at the semi-axes.

¹We substitute the Chi-distribution $f(U; k) = \sqrt{2/\Gamma(k/2)} U^{k-1} \exp(-U^2) \sim U^{k-1} \exp(-\mathcal{L})$ with a polynomial function $\mathcal{L} = (U^2 + V^2 + W^2) + \nu(\nu - 2\sqrt{U^2 + V^2})$ for a torus in components U , V , and W . For the plane velocity magnitude U , this results in $\mathcal{L} \sim U^2 + \nu(\nu - 2U)$ and can be substituted with $k = 2$.

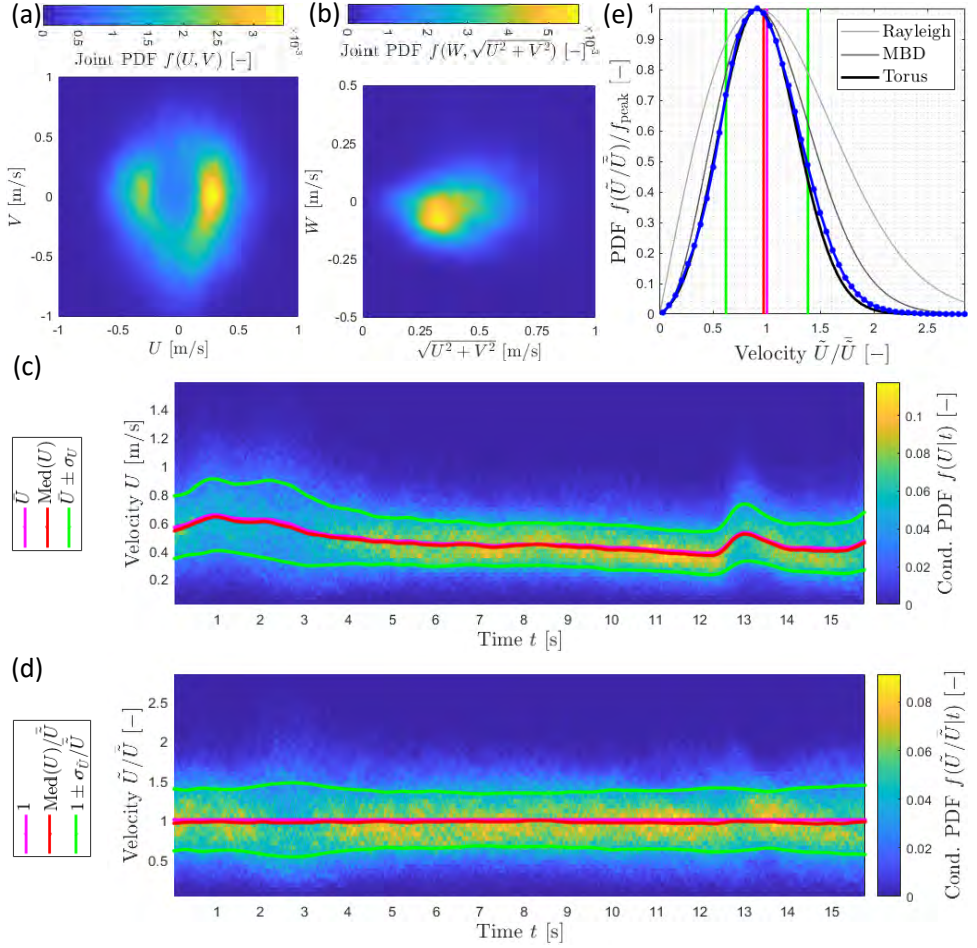


Figure C.3: Velocity distribution. a) Joint probability density function for the in-plane velocity components $f(U, V)$. b) Joint probability density function for the out-of-plane velocity component $f(W, (U^2 + V^2)^{1/2})$. c) Conditional probability density function of the linear velocity $f(U|t)$ along the time series t , inset are the mean velocity $\bar{U}(t)$ (magenta), the median velocity $\text{Med}(U_i(t))$ (red) and the standard deviation bounds $\bar{U}(t) \pm \sigma_U(t)$ (green). d) Conditional probability density of the normalized velocity at the semi-axes $f(\tilde{U}|\tilde{U}_t|t)$, along the time series t . We inset the mean velocity = 1 (magenta), median velocity $\text{Med}(\tilde{U}_i(t))/\tilde{U}_t(t)$ (red) and standard deviation bounds $1 \pm \sigma_{\tilde{U}}(t)/\tilde{U}_t(t)$ (green). e) The normalized velocity relative density distribution $f(\tilde{U}/\tilde{U}_t)/f_{\text{peak}}$. Inset the normalized statistics from (d) with consistent color-code and several sample curves for the plane Rayleigh distribution ($k = 2$, top, light grey), the Maxwell-Boltzmann distribution ($k = 3$, middle, dark grey) and the modified Chi-distribution for a Torus ($k = 2$ and $\nu = 4/3$, bottom, black). The color-coding follows Figure 4.6.

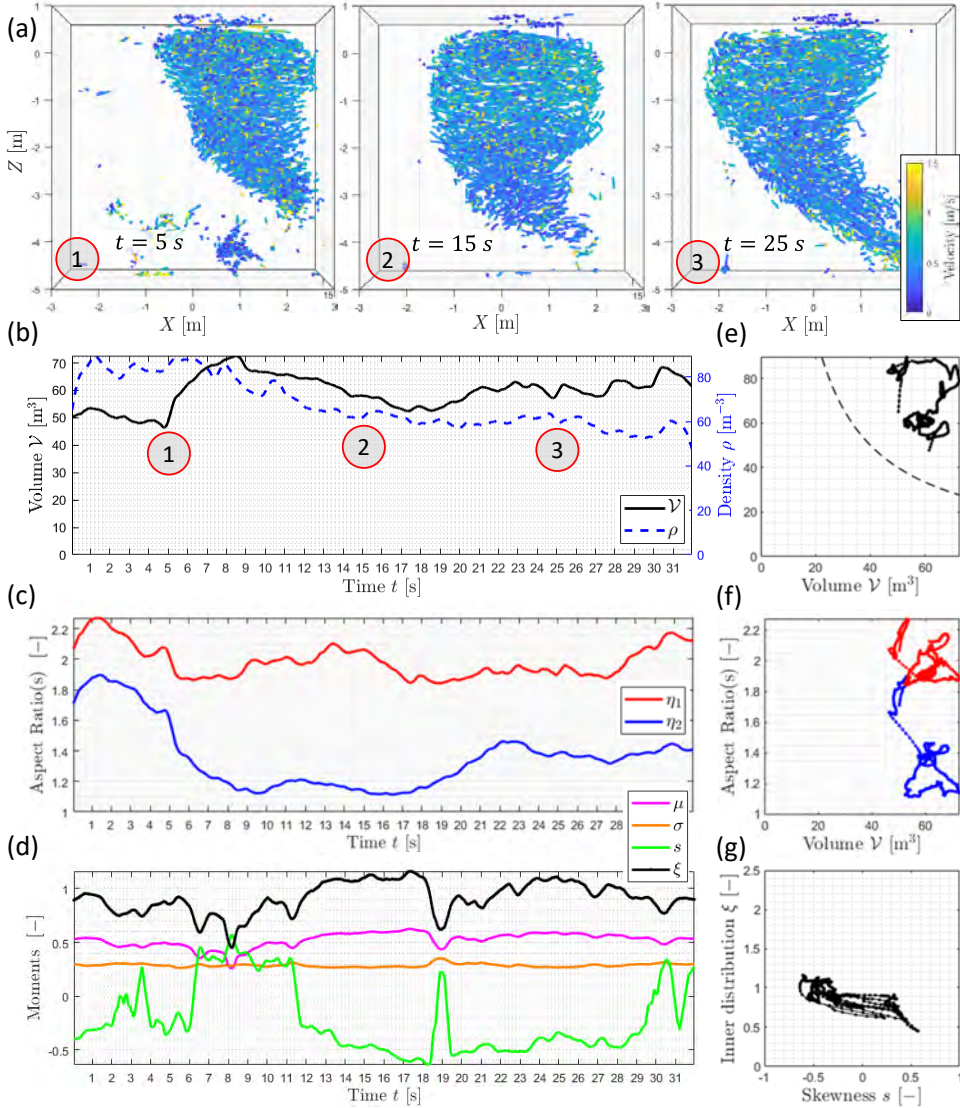


Figure C.4: **Supplementary** Shape, density, and inner fish distribution for a cylindrical fish mill (CIS8 in Table C.2 and Figure 4.1b-left). a) Three snapshots of the fish school: (1) the school is in a compact milling state $t = 5$ s, (2) the school slightly dents to avoid the predator $t \sim 5$ to 15 s, (3) the school returns to a skewed mill after the predator passes $t = 25$ s onward. b) Time series for the volume $\mathcal{V}(t)$ (black) and the average local fish density $\langle \rho_i(t) \rangle$ (blue dashes), inset the time snapshots of (a). c) Time series of the dominant aspect ratio $\eta_1(t)$ (red), and the subdominant aspect ratio $\eta_2(t)$ (blue). d) Time series for the moment mean $\mu(t)$ (magenta), standard deviation $\sigma(t)$ (orange) and skewness $s(t)$ (green), and the inner distribution parameter $\xi(t) = \mu/2\sigma$ from the spatial moments (black). e) The average local density $\langle \rho_i(t) \rangle$ plotted against the volume $\mathcal{V}(t)$ of (b), the reference line (black dashes) indicates a uniform density for a school of 2000 fish. f) Aspect ratios $\eta_1(t)$ (red) and $\eta_2(t)$ (blue) of (c) plotted against the volume $\mathcal{V}(t)$ of (b). g) Locus drawn by the skewness $s(t)$ and the inner fish distribution parameter $\xi(t)$ from (f).

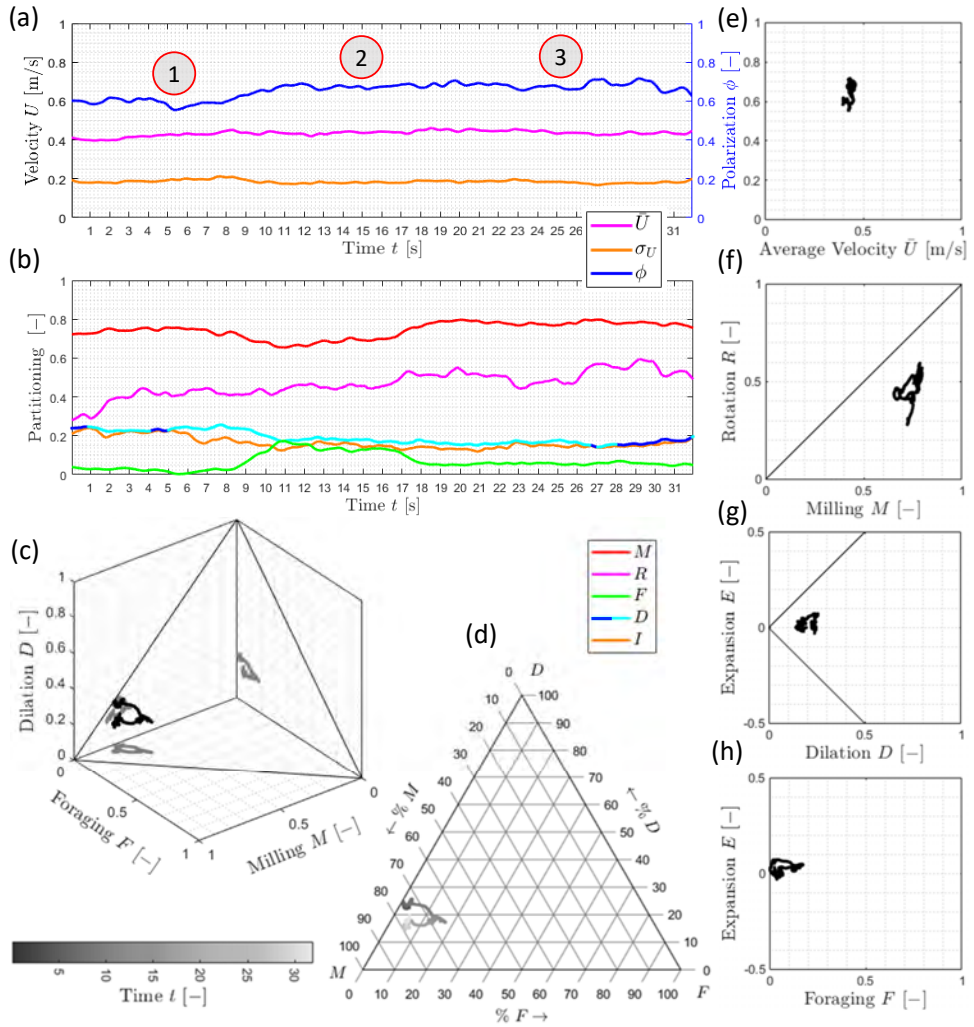


Figure C.5: **Supplementary** Velocity, polarization, and partitioning of the kinematics for the milling school of Figure C.4. a) Time series for the average fish velocity $\bar{U}(t)$ (magenta) and the standard deviation $\sigma_U(t)$ of the fish velocity distribution (orange) alongside the local fish polarization $\langle\phi_i(t)\rangle$ (blue), inset the snapshot (1)–(3). b) Time variations of the milling number $M(t)$ (red), the rotation number $R(t)$ (magenta), foraging number $F(t)$ (green), dilation number $D(t)$ (cyan for $E > 0$ and blue for $E < 0$), isochoric number $I(t)$ (orange). c) ‘Phase portrait’ drawn by the transient schooling dynamics from the milling number $M(t)$, foraging number $F(t)$, and dilation number $D(t)$, inset the plane $M + F + D = 1$ that joins through the axes values 1. d) The ternary diagram that is extracted from the plane $M + F + D = 1$ from (c), the grey shading indicates time t . e) Plotting of the polarization $\langle\phi_i(t)\rangle$ against the average velocity $\bar{U}(t)$ from (a). f) Rotation number $R(t)$ against milling number $M(t)$, the black line gives the upper bound $R = M$. g) Expansion number $E(t)$ against the dilation number $D(t)$, the black line gives the lower and upper bound(s) $D = |E|$. h) The expansion number $E(t)$ against the foraging number $F(t)$.

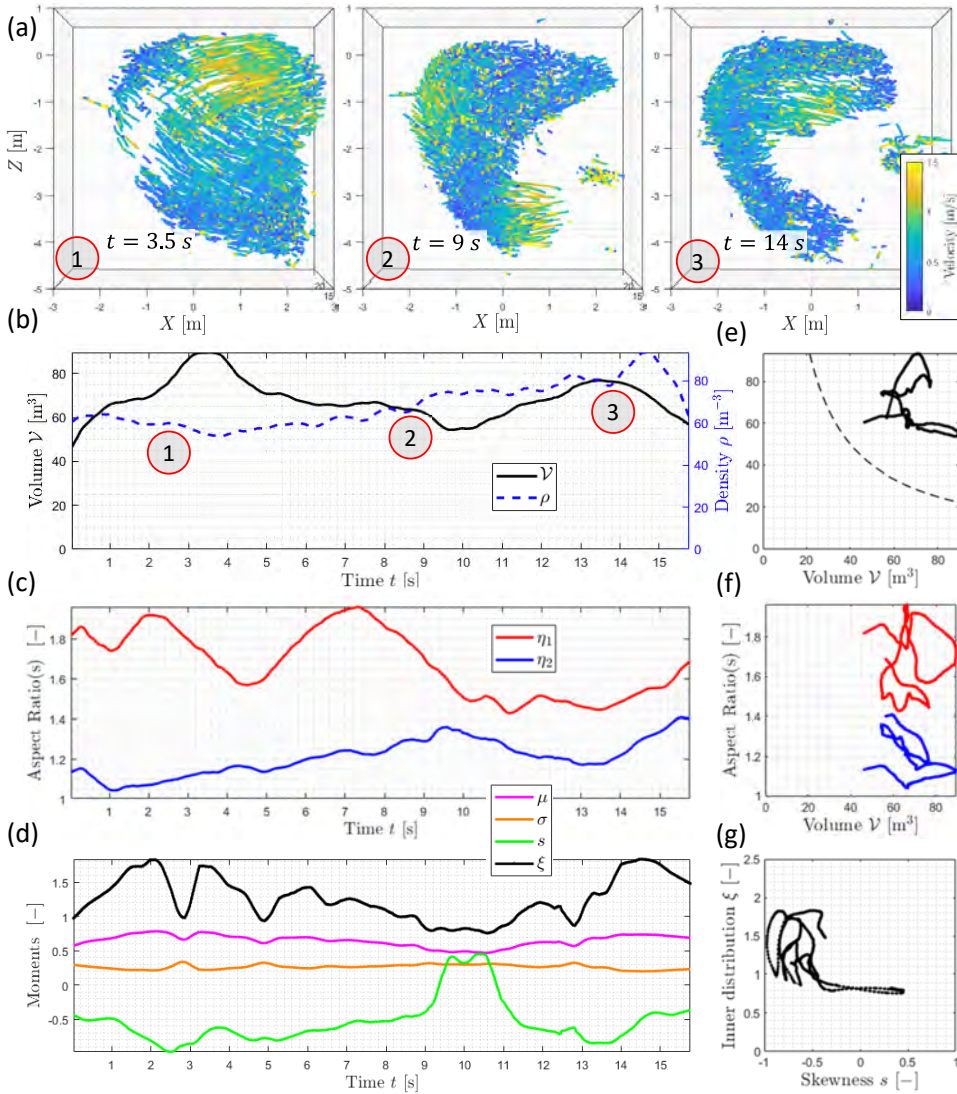


Figure C.6: **Supplementary** Shape, density, and inner fish distribution for an excited fish mill (C1S23 in Table C.2 and Figure 4.2b-left). a) Three snapshots of the fish school: (1) the school avoiding a predator $t = 3.5$ s, (2) the school denting sideways to avoid another predator $t \sim 9$ to 15 s, (3) the school avoiding a passing turtle $t = 14$ s onward. b) Time series for the volume $\mathcal{V}(t)$ (black) and the average local fish density $\langle \rho_i(t) \rangle$ (blue dashes), inset the time snapshots of (a). c) Time series of the dominant aspect ratio $\eta_1(t)$ (red), and the sub-dominant aspect ratio $\eta_2(t)$ (blue). d) Time series for the moment mean $\mu(t)$ (magenta), standard deviation $\sigma(t)$ (orange) and skew $s(t)$ (green), and the inner distribution parameter $\xi(t) = \mu/2\sigma$ from the spatial moments (black). e) The average local density $\langle \rho_i(t) \rangle$ plotted against the volume $\mathcal{V}(t)$ of (b), the reference line (black dashes) indicates a uniform density for a school of 2000 fish. f) Aspect ratios $\eta_1(t)$ (red) and $\eta_2(t)$ (blue) of (c) plotted against the volume $\mathcal{V}(t)$ of (b). g) Locus drawn by the skew $s(t)$ and the inner fish distribution parameter $\xi(t)$ from (f).

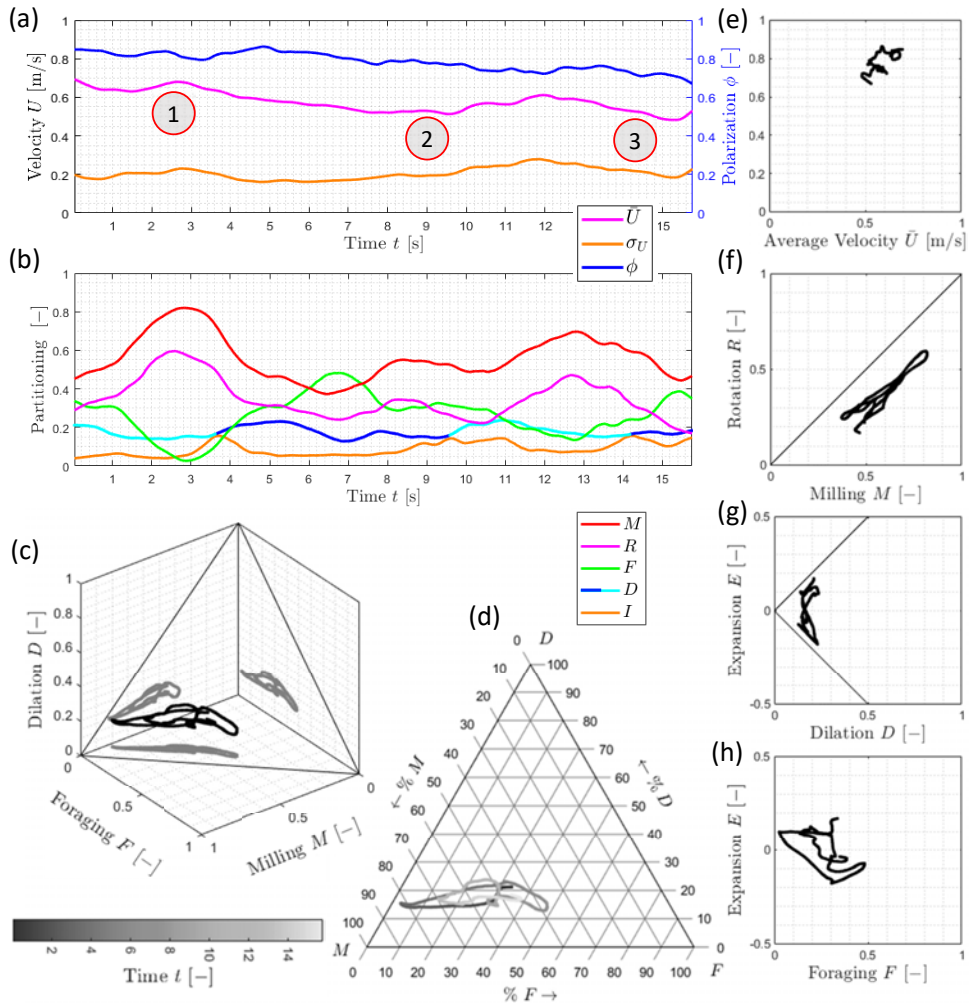


Figure C.7: **Supplementary** Velocity, polarization, and partitioning of the kinematics for the excited fish mill of Figure C.6. a) Time series for the average fish velocity $\bar{U}(t)$ (magenta) and the standard deviation $\sigma_U(t)$ of the fish velocity distribution (orange) alongside the local fish polarization $\langle\phi_i(t)\rangle$ (blue), inset the snapshot (1)–(3). b) Time variations of the milling number $M(t)$ (red), the rotation number $R(t)$ (magenta), foraging number $F(t)$ (green), dilation number $D(t)$ (cyan for $E > 0$ and blue for $E < 0$), isochoric number $I(t)$ (orange). c) ‘Phase portrait’ drawn by the transient schooling dynamics from the milling number $M(t)$, foraging number $F(t)$, and dilation number $D(t)$, inset the plane $M + F + D = 1$ that joins through the axes values 1. d) The ternary diagram that is extracted from the plane $M + F + D = 1$ from (c), the grey shading indicates time t . e) Plotting of the polarization $\langle\phi_i(t)\rangle$ against the average velocity $\bar{U}(t)$ from (a). f) Rotation number $R(t)$ against milling number $M(t)$, the black line gives the upper bound $R = M$. g) Expansion number $E(t)$ against the dilation number $D(t)$, the black line gives the lower and upper bound(s) $D = |E|$. h) The expansion number $E(t)$ against the foraging number $F(t)$.

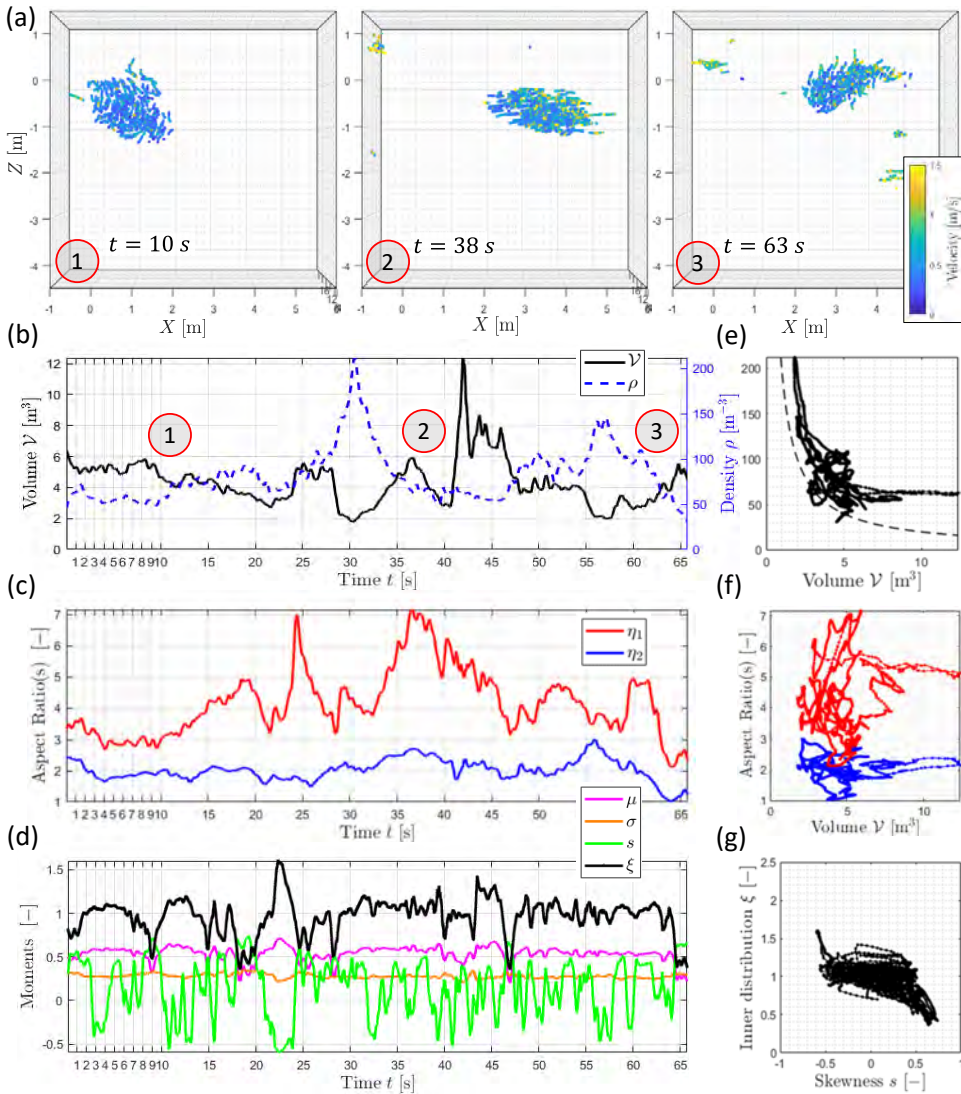


Figure C.8: **Supplementary** Shape, density, and inner fish distribution for long time-series of a small foraging school (C2S17 in Table C.2 and Figure 4.3b-left). a) Three snapshots of the fish school foraging through the large measurement domain at respective times. b) Long time-series for the volume $\mathcal{V}(t)$ (black) and the average local fish density $\langle \rho_i(t) \rangle$ (blue dashes), inset the time snapshots of (a). c) Long time-series of the dominant aspect ratio $\eta_1(t)$ (red), and the subdominant aspect ratio $\eta_2(t)$ (blue). d) Long time-series for the moment mean $\mu(t)$ (magenta), standard deviation $\sigma(t)$ (orange) and skewness $s(t)$ (green), and the inner distribution parameter $\xi(t) = \mu/2\sigma$ from the spatial moments (black). e) The average local density $\langle \rho_i(t) \rangle$ plotted against the volume $\mathcal{V}(t)$ of (b), the reference line (black dashes) indicates a uniform density for a school of 200 fish. f) Aspect ratios $\eta_1(t)$ (red) and $\eta_2(t)$ (blue) of (c) plotted against the volume $\mathcal{V}(t)$ of (b). g) Locus drawn by the skewness $s(t)$ and the inner fish distribution parameter $\xi(t)$ from (f).

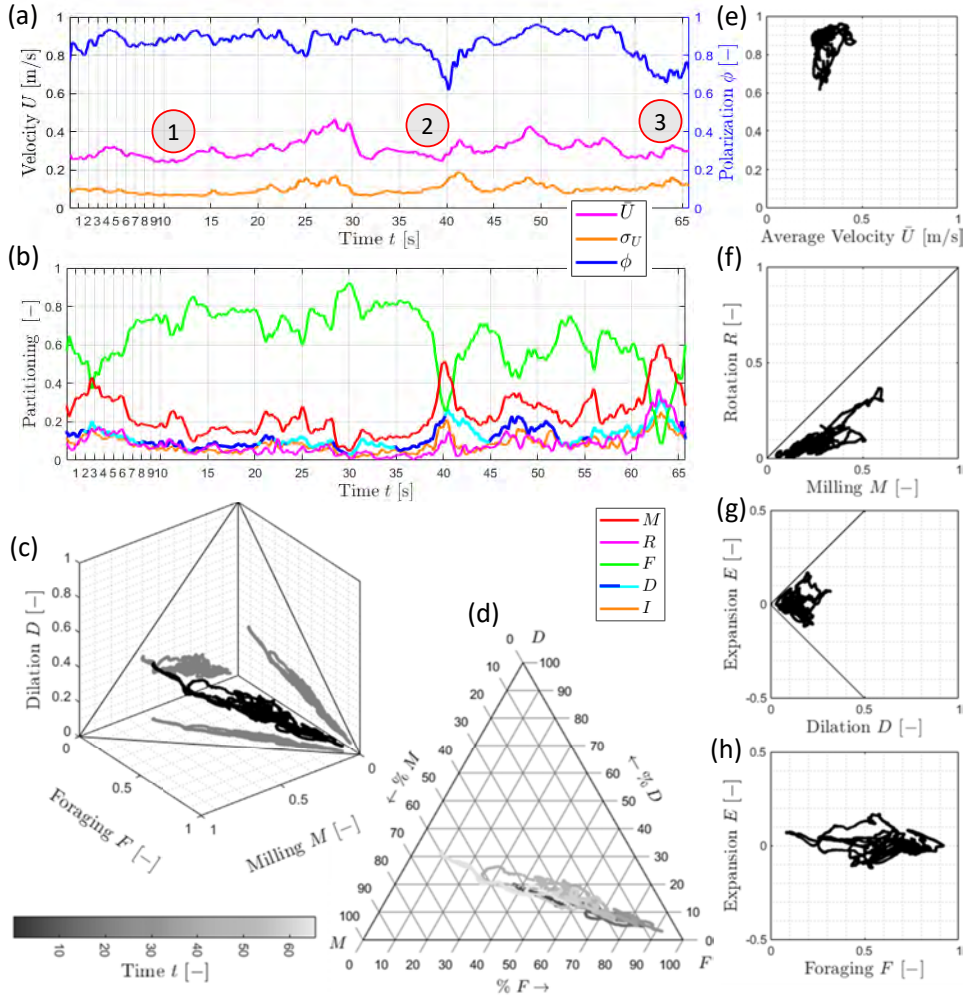


Figure C.9: **Supplementary** Velocity, polarization, and partitioning of the kinematics for the long time series foraging school of Figure C.8. a) Time series for the average fish velocity $\bar{U}(t)$ (magenta) and the standard deviation $\sigma_U(t)$ of the fish velocity distribution (orange) alongside the local fish polarization $\langle \phi_i(t) \rangle$ (blue), inset the snapshot (1)–(3). b) Time variations of the milling number $M(t)$ (red), the rotation number $R(t)$ (magenta), foraging number $F(t)$ (green), dilation number $D(t)$ (cyan for $E > 0$ and blue for $E < 0$), isochoric number $I(t)$ (orange). c) ‘Phase portrait’ drawn by the transient schooling dynamics from the milling number $M(t)$, foraging number $F(t)$, and dilation number $D(t)$, inset the plane $M + F + D = 1$ that joins through the axes values 1. d) The ternary diagram that is extracted from the plane $M + F + D = 1$ from (c), the grey shading indicates time t . e) Plotting of the polarization $\langle \phi_i(t) \rangle$ against the average velocity $\bar{U}(t)$ from (a). f) Rotation number $R(t)$ against milling number $M(t)$, the black line gives the upper bound $R = M$. g) Expansion number $E(t)$ against the dilation number $D(t)$, the black line gives the lower and upper bound(s) $D = |E|$. h) The expansion number $E(t)$ against the foraging number $F(t)$.

REFERENCES

- [1] T. J. Pitcher and C. J. Wyche, *Predator-avoidance behaviours of sand-eel schools: why schools seldom split*, in *Predators and prey in fishes*, Vol. 2 (Springer, Dordrecht, 1983) pp. 193–204.
- [2] A. E. Magurran and T. J. Pitcher, *Provenance, shoal size and the sociobiology of predator-evasion behaviour in minnow shoals*, *Proc. R. Soc. Lond.* **229**, 439 (1987).
- [3] W. Kabsch, *A discussion of the solution for the best rotation to relate two sets of vectors*, *Acta Cryst.* **32**, 922 (1976).

ACKNOWLEDGEMENTS

Having put my fullest dedication into establishing and finalizing this thesis, I would like to express a few words of my gratitude and appreciation to complete the work.

First and foremost, to my daily advisor. Daniel, you accepted me as a Ph.D. student on a truly unique position, and it has been the greatest honor to work with you and start from scratch. But perhaps you recognized my greatest milestone at the very end of my Ph.D. I remember finding a large bag with small clothes waiting on my desk at the beginning of the fall semester of 2020. This gift has been a central token of support to me, and if Sacha had not been growing so fast, I would make sure he would still be wearing these proudly today! I hope you will inspire many more students to come and continue this research forward in your footsteps. I would also like to thank my other two promoters. Jerry, if it had not been for your guidance and freedom to go down my path, I feel this work may have never been thought of conceiving. I have not only enjoyed our fruitful discussions on performing the 'Fish Image Velocimetry', but also the light-heartedness and motivating feedback, and not of less importance, a smiling sense of humor. Any challenge ahead seemed like a logical next step, instead of a daunting barrier to overcome or get involved with. I started this Ph.D. project the day after graduating with my master's and needed to rush myself to catch the first train to Groningen. Charlotte, I barged in halfway through the first lecture of 'Advanced Self-Organization of Social Systems', and what luck I ran into involve myself with such a truly interesting branch of science. I would like to thank you for all the detailed feedback we received from you during the project and our meetings, and, especially on the final thesis.

Working on this thesis was not only a golden opportunity on the scientific side, but as well as a golden chance to involve my presence at the Rotterdam zoo. I would like to thank Mark de Boer who has been of central importance in coordinating our activities around the zoo. Without your stake, this would not have been possible. It was always breathtaking to observe the school and take the data at the Oceanium, and a pleasure to see the extensive and professional dedication to animal care and facilities. In addition, would like to thank Martijn van der Veer. You were one of the first to discuss the need for our diving activities. To my happy surprise, you seemed not at all alarmed by swimming with a 'door-sized chessboard', surrounded by sharks and other looming predators. Therefore, I would like to thank all of the brave members of the diving team: Mike, Valentijn, Marieke, Jeroen, Krista, Dayenne, and Martin. My efforts to minimize the water displacement by drilling holes in our large calibration target are unmatched by the amount of physical work you have put into my thesis activities.

Next to expressing my gratitude towards my advisors and collaborators, I would like to thank a few more of my colleagues and coworkers. I would like to give a special word to Edwin Overmars. Your resourcefulness, expertise, and readiness have been crucial. I remember us practicing and building a full multi-camera setup within a 30-minute record time to film the release of the fish school, even though the catering service was

hard to impress with this number! I would like to greatly thank Mathieu Pourquie. Your knowledge and help to patch together available computational resources to process the data have been indispensable. In addition to that, I have greatly enjoyed your extensive sense of humor, which made it a pleasure to drop by for any questions. Also, I would like to particularly thank Christian Poelma for enabling me to continue my involvement in experimental fluid mechanics. Looking back at the Taylor Couette experiments I feel these are probably the most beautiful images I will ever have stitched together.

In addition, there are a few more students and staff to whom I would like to express my gratitude. John, your vibrant levels of enthusiasm were a joy to work with, and I hope many more playdates with Sacha, Stella, and Rosa will follow after the 'Kinderboeken Museum'. Junaid, working together on tracking fish and algae has greatly contributed to the quality of my work, and it was a joy to interact and have many fruitful exchanges of thought and delightful conversations. Swaraj, sharing our experience in three-dimensional imaging spiked with energy and admiration, and has been a driving force. Ankur, our first conferences became adventures, Parviz, for bringing so much joy to the lab meetings, Bob, for sharing a joking sense of humor. As well as Caroline, Gertjan, Jasper, and Jan for administrative and technical support, Guillermo, Tariq, Sowmya, Haoyu, Wout, Yavuz, Udhav, Lina, Tea, Lyke, Wouter, Nicola, Rens, Jesse, Abhirath, Arnoud, Florian, Amitosh, Sudarshan, Mike, Gem, Saad, Willian, Angeliki, Wim-Paul, Gerrit and many more all of whom I will cherish good memories.

I would like to end this acknowledgement by thanking all of my friends and my extended family for their support in chasing my academic ambitions. I would like to thank my brother and Gesa, my sister and Mark, for directing the attention away from my work, and especially Sophie, Tom, Jip, and Bo are experts in that. I would like to thank, my mother and Guido for their care and support towards the end of this project, and my father and Celine, particularly reminding me that "results have conclusions". Also, I would like to thank Leonid and Marina, and Vera, your strength of mind knows no borders; there is no better example to admire and aspire to.

Let me finally express some words that I have been waiting to put to paper. — Polina, we met at the end of December 2017 in snowy Moscow, and your first cheering appearance is still vibrantly imprinted on my eyes. Only after a few months, you told me you would be looking out to be present at my defense, and I had to reply: "Well.., let me do my best to join too!". But although I cannot get a hold of my joking remarks, you showed me a complete, and new world. Today we stand present with the three of us. Your endless trust in my aspirations makes this thesis yours, and the endless joy of having Sacha on our arms makes its celebration.

The Hague, Netherlands, 16 July '23

CURRICULUM VITÆ

Koen MULLER

14-10-1990 Born in Wageningen, The Netherlands

EDUCATION

2003–2009 Voorbereidend Wetenschappelijk Onderwijs
Het Rhedens, Velp, The Netherlands

2009–2013 Bachelor of Science Mechanical Engineering, Minor Physics
Delft University of Technology, Delft, The Netherlands

2014–2016 Master of Science Mechanical Engineering, Fluid Mechanics
Delft University of Technology, Delft, The Netherlands

ACADEMIC RESUME

2015 Visiting Student Research Collaborator, Howard Stone Lab
Princeton University, Princeton, United States

2016–2022 Doctor of Philosophy, Fluid Mechanics
Delft University of Technology, Delft, The Netherlands

2021-2022 Researcher, Multiphase Systems
Delft University of Technology, Delft, The Netherlands

2022-2023 Teacher (Docent), Energy Technology
Hogeschool Rotterdam, Rotterdam, The Netherlands

2023 Postdoctoral Researcher, Institute of Fluid Dynamics
Eidgenössische Technische Hochschule, Zürich, Switzerland

PH.D. DISSERTATION

Title: Tracking Schooling Fish in Three Dimensions: Experiments at
the Rotterdam Zoo

Promotor: Dr. Daniel See-Wai Tam

Promotor: Prof. dr. ir. Jerry Westerweel

Promotor: Prof. dr. Charlotte K. Hemelrijk

LIST OF PUBLICATIONS

JOURNAL ARTICLES

3. **Muller, K.**, Buchner, A.-J., Hemelrijk, C.K., Westerweel, J. & Tam, D.S.W. *Tracking Schooling Fish in Three Dimensions: Multi-modality and Variability in Shape, Inner Structure and Kinematics*. [IN PREPARATION]
2. **Muller, K.**, Mehmood, J., Hemelrijk, C.K., Westerweel, J. & Tam, D.S.W. *A Three-Dimensional Tracking Method for Schooling Fish in a Large Scale Experiment at the Rotterdam Zoo*. [IN PREPARATION]
1. **Muller, K.**, Hemelrijk, C.K., Westerweel, J., & Tam, D.S.W. (2020). *Calibration of Multiple Cameras for Large-Scale Experiments Using a Freely Moving Calibration Target*. *Experiments in Fluids*, 61(1):7.

CONFERENCE PROCEEDINGS

4. **Muller, K.**, Greidanus, A.J., Dash, A., & Poelma, C. (2022). *Bullet Time Taylor-Couette: Unwrapping the 360 Degree Field of View for Rheoscopic Flow Visualization*. In Proceedings of the 20th International Symposium on Application of Laser and Imaging Techniques to Fluid Mechanics (pp. 2028–2043). Instituto Superior Técnico.
3. **Muller, K.**, Westerweel, J., Hemelrijk, C.K., & Tam, D.S.W. (2019). *Tracking Fish inside a Large School*. *Statistical Physics and Soft Condensed Matter, Physics at Veldhoven (FOM)*.
2. **Muller, K.**, Westerweel, J., Hemelrijk, C.K., & Tam, D.S.W. (2018). *Three-Dimensional Tracking of Fish inside a Large School at the Rotterdam Zoo*. 71st Annual Meeting of the APS Division of Fluid Dynamics, 63(13).
1. **Muller, K.**, Tam, D.S.W., & Westerweel, J. (2018). *Multiple-View Camera Calibration for Large Scenes with Limited Spatial Access at the Rotterdam Zoo*. In Proceedings of the 19th International Symposium on Application of Laser and Imaging Techniques to Fluid Mechanics (pp. 1818-1822). Instituto Superior Técnico.

OTHER CONTRIBUTIONS

3. **Muller, K.**, Greidanus, A.J., Dash, A., & Poelma, C. *Bullet Time Taylor-Couette: Unwrapping the 360 Degree Field of View for Rheoscopic Flow Visualization*. [IN PREPARATION]
2. Buchner, A.-J., **Muller, K.**, Mehmood, J., & Tam, D.S.W. (2021). *Hopping Trajectories due to Long-Range Interactions Determine Surface Accumulation of Microalgae*. *Proceeding National Academy of Sciences*, 118(20).
1. Kim, H., **Muller, K.**, Shardt, O., Afkhami, S., & Stone, H. A. (2017). *Solutal Marangoni Flows of Miscible Liquids Drive Transport Without Surface Contamination*. *Nature Physics*, 13(1105–1110).

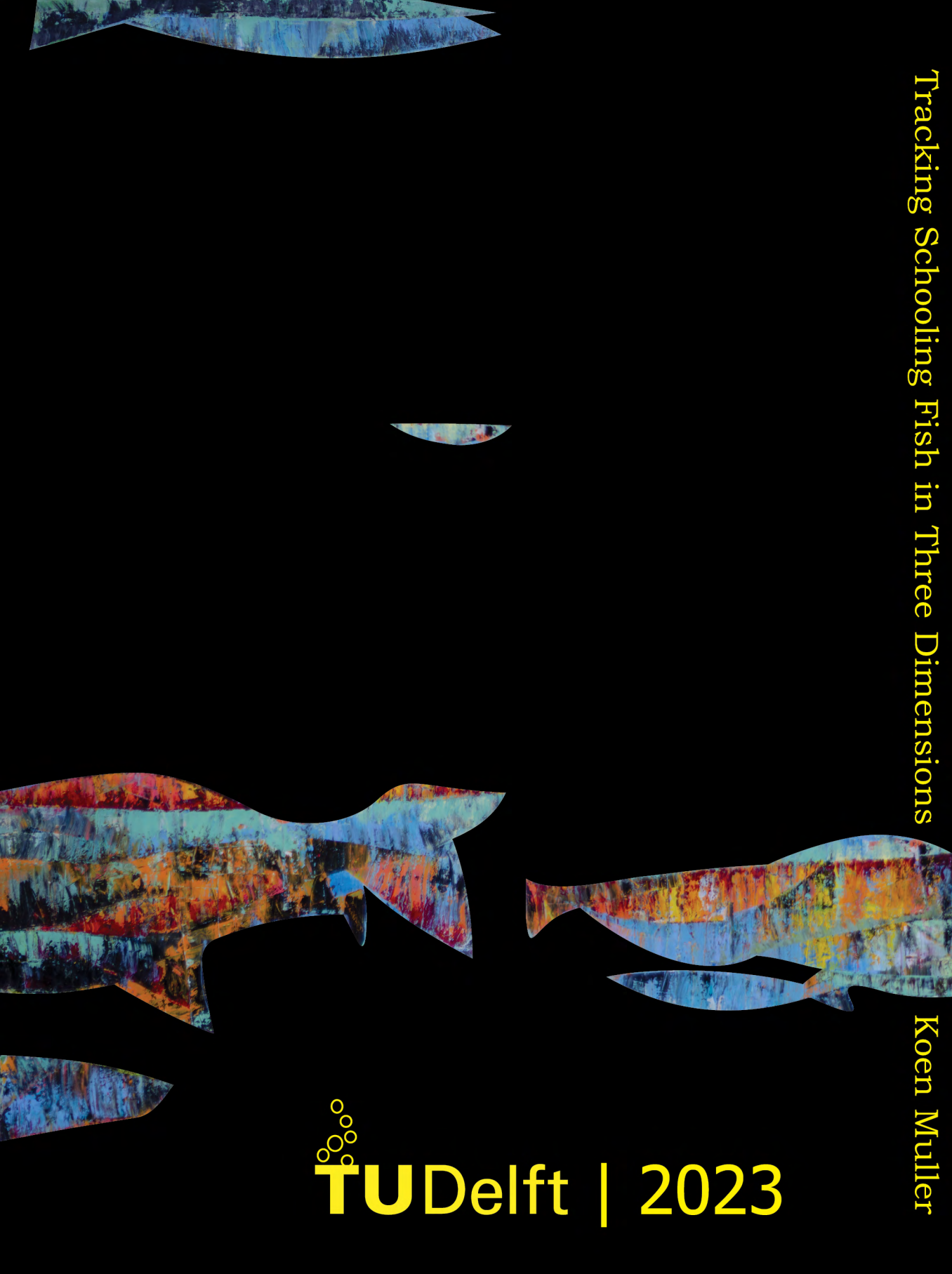
PUBLIC OUTREACH

3. *TU Delft Onderzoekt Vissenscholen in Blijdorp*. (2020). NTR: Wetenschap, NPO2, De Kennis van Nu.
2. *Draaiende Discobal*. (2020). De Giraffe, Diergaarde Blijdorp Rotterdam Zoo (pp. 20–21).
1. *Koud Bloed: Op Onderzoek naar het Gedrag van Valse Haringen*. (2018). Vriendennieuws, Vrienden van Blijdorp (pp. 18–19).



Tracking Schooling Fish in Three Dimensions

Koen Muller



 **TU Delft** | 2023